Optical performance of the reflective surface profile of a heliostat

by

Willem Adolph Landman

Dissertation presented for the degree of
Doctor of Philosophy
in the Faculty of Engineering
at Stellenbosch University

Supervisor: Prof. F. Dinter
Co-supervisor: Dr. P. Gauché

March 2017

Declaration

By submitting this dissertation electronically, I declare that the entirety of the work contained therein is my own, original work, that I am the sole author thereof (save to the extent explicitly otherwise stated), that reproduction and publication thereof by Stellenbosch University will not infringe any third party rights and that I have not previously in its entirety or in part submitted it for obtaining any qualification.

This dissertation includes one original paper published in a peer-reviewed journal. The development and writing of this paper (published) was the principal responsibility of myself and, for each of the cases where this is not the case, a declaration is included in the dissertation indicating the nature and extent of the contributions of co-authors.

March 2017

Abstract

Micro gas turbine (MGT) central receiver systems offer advantages which could improve the techno-economic viability of the next generation of concentrating solar power (CSP) plants. This relatively young technology is not yet well understood, and the optimal configurations are yet to be determined. The high flux requirements and small modular configuration suggest that the heliostat field of a MGT CSP plant may have alternative parameter sensitivities than conventional systems. The objective of this thesis is to fundamentally understand the optics of a heliostat to develop methods, models and figures of merit as tools to improve the techno-economic viability of central receiver systems with particular emphasis on MGT CSP.

A study of the fundamentals of heliostat optics shows that heliostat beam aberrations are statistically differentiated according to whether they occur consecutively or are path dependent. Three key factors – namely the sun shape, normal vector error aberrations and astigmatic aberrations – are found to dominate the dispersion of a heliostat beam and they are described analytically. This knowledge presents the principal components required to accurately describe heliostat field performance.

The development and validation of a new analytical method to model flux distribution of a heliostat shows that it is possible to achieve suitable levels of confidence by appropriately accounting for these factors. The accuracy improvements offered by the method is particularly beneficial when used to model higher accuracy heliostats that would typically be used in MGT CSP. The flux distribution error and peak flux error of the proposed method are shown to be up to 60.6 % and 88.2 % lower than that of state of the art methods respectively.

This method is applied in a techno-economic sensitivity study that illustrates that high accuracy optics result in lower levelised cost of energy. Both the cost breakdown and the alternative optical requirements show that MGT CSP does have alternative parameter sensitivities. The collective findings of this thesis suggests that small heliostats offer significant optical performance increases in the context of MGT CSP and potentially leads to cost minimum.

Uittreksel

Mikro gasturbine (MGT) sentrale ontvanger stelsels bied voordele wat die tegno-ekonomiese lewensvatbaarheid van die volgende generasie sonkragkonsentrerende kragstasies kan bevorder. Hierdie relatief nuwe tegnologie word nog nie goed begryp nie, en die optimale konfigurasies moet nog bepaal word. Die hoë termiese vloeddigtheid vereistes en klein modulêre konfigurasie dui daarop dat die heliostaatveld van ′n MGT sonkragkonsentrerende kragstasie moontlik alternatiewe parameter sensitiwiteite as konvensionele stelsels kan hê. Die doel van hierdie tesis is om fundamentele begrip te verwerf van die optika van ′n heliostaat ter ontwikkeling van metodes, modelle en maatstawwe as werktuie om die tegno-ekonomiese lewensvatbaarheid van sentrale ontvanger stelsels mee te verbeter, met bepaalde klem op MGT sonkragkonsentrerende kragopwekking (gekonsentreerde sonkrag – GSK).

Bestudering van die grondbeginsels van heliostaat optika toon dat heliostaatstraal afwykings statisties onderskeidend is afhangende daarvan of dit opeenvolgend voorkom of koers gebonde is. Drie kernfaktore - te wete die son se vorm, normale vektorfoutafwykings en astigmatiese afwykings - is bewese dominante verstrooiers van ′n heliostaatstraal en word analities beskryf. Hierdie kennis behels die hoofkomponente vir die akkurate beskrywing van heliostaatveld prestasie.

Die ontwikkeling en stawing van ′n nuwe analitiese metode om vloeddigtheid verspreiding van ′n heliostaat te modelleer, toon dat dit moontlik is om geskikte vlakke van vertroue te bewerkstellig deur gepaste berekening van hierdie faktore. Die verbeterde akkuraatheid wat hierdie metode bied is veral voordelig by die modelering van hoër akkuraatheid heliostate wat tipies gebruik sou word in MGT GSK. Dit is bewese dat die vloeddigtheid distribusie fout en piek vloeddigtheid dwaling van die voorgestelde metode onderskeidelik 60.6 % en 88.2 % laer is as die van die voorloper metodes.

Hierdie metode word toegepas in ′n tegno-ekonomiese sensitiwiteitstudie wat toon dat hoë akkuraatheid optika tot laer vergelykbare elektrisiteitskoste lei. Beide die koste uiteensetting en die alternatiewe optiese vereistes toon dat MGT GSK wel alternatiewe parameter sensitiwiteite bevat. Die gehele bevinding van hierdie tesis dui daarop dat klein heliostate beduidende optiese prestasiestygings binne die konteks van MGT GSK bied en potensieel tot minimalisering van koste lei.

Acknowledgements

I am extremely grateful for all the people who offered their help and support throughout the duration of this thesis. I would like to acknowledge the following people and organisations:

The Solar Thermal Energy Research Group that made funds available through the solar spoke of the Department of Science and Technology, the National Research Fund and the Stellenbosch University Hope Project.

Special thank you to Dr. Paul Gauché for allowing me freedom in my research, to chase my interests, for allowing me to wander off the path and discover things for myself. The six years I have been under your wing have been some of the most formative and valuable.

Prof. Frank Dinter for taking me on as a his student, the guidance and advice that you are so willing to share and your continued encouragement.

All my colleagues at STERG and Helio100 for making the journey so enjoyable, I have made so many friends. All the people who collaborated with me on this work for sharing their knowledge with me. The staff of the Solar Roof Laboratory for their assistance with my experimentation.

I also want to thank Victor Gouws, one of my close friends, for teaching me to be true to myself and listen to my heart. This would never have happened without you.

My siblings Richter en Mattie who were always there to lovingly lift me up, for the many late nights studying together, the joking and squabbles over who’s turn it is to make coffee. You are my best friends.

I would particularly like to thank both my parents for their belief in me, their encouragement and unwavering support. You have made many sacrifices to give me the opportunities I have had and have pushed me to excel and be the best version of me I can. I am eternally grateful.

Dedications

I dedicate this work to the Lord Jesus Christ in whom I trust.
May the work of my hands be done for the sake of Your glory.

Contents

List of Figures

List of Tables

Nomenclature

Roman symbols

A	area	[m^2]
A	scaling factor	[ ]
C	concentration ratio	[ ]
d	slant range	[m]
D	effective diameter	[m^2]
E	modulus of elasticity	[Nm^2]
f	focal length	[m]
f	factor, function	[ ]
F_r	focal ratio, d/D	[ ]
$\bar{F}_\mathrm{r}$	facet focal ratio	[ ]
h	height	[m]
h	heat transfer coefficient	[ ]
I	irradiance	[$\mathrm{W/m}^2$]
I	moment of Inertia	[m^4]
I_D	direct normal irradiance	[$\mathrm{W/m}^2$]
L	spectral radiance of the solar disc	[$\mathrm{W/rad}^2$]
n	number	[ ]
P	power from the heliostat	[W]
r	radius, radius of curvature	[m]
R	multiple of tower height	[ ]
R	radius of curvature	[ ]
S	distance at which a point image is formed	[ ]
t	thickness	[m]
T	temperature	[K]
w	width	[m]
w	gravitational load per unit length	[N/m]
x	cartesian coordinate, east, sagittal	[m]
y	cartesian coordinate, north, tangential	[m]

z	cartesian coordinate, vertical	[m]

Greek symbols

α	solar absorptance, expansion coefficient	[ ]
α	half angle, fan angle	[mrad]
β	subtending angle	[mrad]
γ	variable	[ ]
δ	variable	[ ]
ϵ	angular deviation	[mrad]
ε	thermal emittance	[ ]
η	efficiency	[%]
θ	Rotation angle	[rad]
θ	toroidal misalignment angle	[rad]
κ	variable	[ ]
ρ	reflectivity	[%]
ρ	ground coverage	[%]
σ	radial standard deviation	[mrad]
σ	Stefan-Boltzmann constant	[W/m^{2}K^4]
τ	optical alignment angle	[rad]
ϕ	incidence angle	[deg]
$\bar{\phi}$	fixed incidence angle	[deg]
ψ	toroid pre-alignment angle	[rad]

Vectors

$\hat{\mathbf{A}}_\mathrm{p}$	position vector of the aim point
$\hat{\mathbf{n}}$	unit normal vector of the surface
$\hat{\mathbf{P}}$	position vector of the reflective element
$\hat{\mathbf{R}}$	position vector of the receiver cell
$\hat{\omega}_\mathrm{i}$	unit normal vector of the incident irradiation
$\hat{\omega}_\mathrm{o}$	unit normal vector of the reflected irradiation

Subscripts and superscripts

A	acceptance
at	atmospheric attenuation
ast	astigmatic aberration
bq	beam quality
Buie	Buie sun shape

conv	convective
CPC	compound parabolic concentrator
CG	circular Gaussian
CG_mod	modified circular Gaussian
disc	solar disc
D	direct
e	electric
EG	elliptical Gaussian
field	heliostat field
g	geometric, glass
H	heliostat
i	count, initial
in	in
int	intercept
j	count
K	Kuiper sun shape
max	maximum
NVE	normal vector error
out	out
Pillbox	Pillbox sun shape
r	ratio
rec	receiver
R	receiver
RT	ray tracer
RMS	root mean square
s	sun, sagittal, steel
sag	sagittal
SU	super Gaussian
sun	sun
spec	specularity
SSE	surface slope error
SSS	standard solar scan sun shape
t	thermal, tracking, tangential
T	temperature
t_pri	tracking error in primary rotation axis
t_sec	tracking error in secondary rotation axis

tan	tangential
tot	total
view	view factor
x	x direction
y	y direction
ϵ	angular deviation
τ	optical alignment angle
0	origin

Abbreviations

AIPWI	Annual incident power weighted intercept
AZ	Azimuth zenith tracking
BCS	Beam characterisation system
BRDF	Bidirectional reflectance distribution function
CDF	Cumulative distribution function
CDF	Centrally defocused
CGD	Circular Gaussian distribution
COA	Coefficient of optical aberration
CMM	Coordinate measuring machine
CPC	Compound parabolic concentrator
CSP	Concentrating solar power
CSR	Circumsolar ratio
DNI	Direct normal irradiance
DSLR	Digital single lens reflex
EFD	Empirical density function
FD	Flux distribution
FDR	Flux density ratio
FHA	Fixed horizontal axis tracking
IRR	Internal rate of return
LCOE	Levelised cost of energy
MGT	Micro gas turbine
ND	Neutral density
OS	Operating strategies
PDF	Probability distribution function
RMS	Root-mean square
ROC	Radius of curvature
SM	Solar multiple

SSE	Surface slope error
SSS	Standard solar scan
STERG	Solar Thermal Energy Research Group
TA	Target aligned tracking
TE	Tracking error
UC	Unconstrained canting

Chapter 1

Introduction

Concentrating solar power (CSP) and the use of Brayton cycles in central receiver systems are introduced as the context of this dissertation, and an investigation into heliostat optics is motivated. The objectives of this work are then stated, and the methodology used to meet these objectives is presented.

1.1 Background

> *The quest for safe, secure and sustainable energy poses one of the most critical challenges of our age.* - Tony Juniper (2008)

The foundations of modern civilisation have been built on mankind's ability to harness energy, but the reliance on fossil fuels as an energy source is thought to be unsustainable. It is recommended that safe, secure, economical and sustainable energy alternatives be developed to sustain our development path.

Renewable energy technologies harness natural phenomena and convert them into useful energy. The irregular nature of most renewable energy sources result in intermittent power production that does not necessarily correlate with power demand. CSP technologies offer a solution to this problem by utilising efficient thermal storage. The ability to store energy at a utility scale and at low cost offers the potential to provide dispatchable solar electricity production [1]. This unique advantage positions CSP as an important renewable technology of the future.

CSP plants concentrate solar irradiance which is then converted to thermal energy. The thermal energy is either transported to storage or used directly in a thermodynamic cycle to generate electricity. For thermodynamic reasons, high temperatures must be achieved to realise high cycle efficiencies. To achieve high temperatures, a high concentration of solar radiation is required.

The central receiver system is regarded as a leading CSP concept [2], allowing the solar irradiance to be highly concentrated at a single point. This concept utilises mirrored structures called heliostats that track the sun and reflect the solar irradiation to a central receiver positioned on a tower.

The high Levelised Cost of Energy (LCOE) typical of technologies which are still early in the technology life-cycle and the large capital expenditure required for market entry have held back large scale deployment of central receiver systems [3]. To ensure economic viability both these factors must be reduced to such a level that that the technology is cost competitive against fossil fuel power generation.

The heliostat field is a substantial cost component of conventional utility scale central receiver systems contributing approximately half the total capital expenditure of the plant [1]. The heliostat field is broadly considered to be the biggest cost reduction opportunity to achieve economic viability. Kolb *et al.* [4] show that both the optical variables and reliability of heliostats have economic value and that an optimum balance between performance and cost must be met to minimise LCOE.

Perceived financing risks of a large central receiver system are substantial and also carry economic value [3]. The debt and equity financing of these capital intensive projects are evaluated based on risk, return on investments and coverage ratios. To mitigate the risks perceived by the investors financing structures typically require a higher interest rate. It is suggested that smaller modular central receiver systems allow initial risk and capital cost to be managed by entering the market in a staggered manner [5].

Brayton cycle systems scale from micro gas turbines (MGT) to utility sized units. MGT CSP thus allow for modular distributed power generation closer to the end user and are mostly independent of water and grid access constraints required for conventional CSP systems. In the context of combined cycles or recuperated gas turbines, Brayton cycles may lead to an overall reduction in the cost of the electricity produced [6; 7; 8].

Brayton cycles require high temperatures, generally above 850 °C [7; 9]. The temperatures obtainable in a solar power plant are directly linked to the flux density from the heliostat field. Flux densities required for cavity air receivers range from $1\,\mathrm{MW/m^2}$ to $10\,\mathrm{MW/m^2}$ [10; 6; 11]. Secondary concentrators [12], accurate heliostat optics and high-precision heliostat control are typically required to achieve these concentrations.

The Solar Thermal Energy Research Group (STERG) at Stellenbosch University is developing a high temperature combined thermodynamic cycle (SUNSPOT cycle) suited to the South African climate [13]. The cycle requires high temperatures in excess of 800 °C. An important aspect of this research is to realise a suitable collector system able to deliver the required flux distribution requirements for such a high temperature air receiver.

The body of work in this dissertation is the first detailed research on heliostat optics within STERG, and it aims to lay a foundation for further research to follow. An in-depth study into the understanding of heliostat performance was identified as the fundamental requirement for the development of a heliostat technology.

Further heliostat development work at STERG led to the Helio100 project [14], which also receives much attention in this thesis. The Helio100 project entailed the development, design and construction of a 200 kW$_t$ pilot facility, pictured in Figure 1.1, to demonstrate an innovative heliostat technology.

Figure 1.1: Aerial view of the Helio100 field during its unveiling at the 2015 SolarPACES conference [14] (arrow indicates the location of the control facet discussed in Section 9.7.4)

It is hypothesised in this work that MGT CSP plants have alternative and distinct heliostat field requirements from those of conventional central receiver systems. A sufficient understanding of both the performance or optical imaging of a heliostat and the techno-economics of a MGT CSP plant are necessary to test this hypothesis, leading to the objective of this study.

1.2 Objectives

The objective is to fundamentally understand heliostat optics to develop appropriate methods, models and figures of merit as tools to improve the techno-economic viability of central receiver systems with particular emphasis on MGT CSP.

To evaluate the hypothesis that MGT CSP plants have alternative heliostat field requirements than conventional central receiver systems, three consecutive objectives were set. The initial objective is to seek and categorise the fundamental principles that determine the optical performance of a heliostat. The second objective is to apply this knowledge to develop relevant methods, models and figures of merit to asses a heliostat's optical performance. The third objective is to apply these tools with the aim to improve the techno-economic viability of central receiver systems with particular emphasis on MGT CSP.

1.3 Intended contribution

The heliostat field is an inherently complex optical system. In order to assess and improve the techno-economic viability of central receiver systems, its definition and performance must be understood. The performance of a heliostat is a result of the spatial irradiance intensity distribution of that heliostat at the receiver aperture. This distribution, also referred to as the heliostat image or flux distribution, forms the primary area of focus in this dissertation. The first intended contribution is a method to analytically describe the flux distribution of a heliostat with sufficient accuracy. The second intended contribution is to identify the heliostat field requirements of a MGT central receiver system and to propose potential improvements.

1.4 Methodology

Some work contained in this dissertation was initially submitted for a Master's degree; however, evidence of contribution resulted in an upgrade to the degree of Doctor of Philosophy. The methodology is carried over from the Master's thesis but includes the expanded objectives and broader scope to further the depth of content.

The methodology includes the study of heliostat optics and the development of an optical performance model, which is then applied in the techno-economic simulation of a MGT CSP system. A high level summary of the methodology is given below:

- The sole purpose of a heliostat is to deliver a flux distribution at the receiver. First, all the components that contribute to the flux distribution of a heliostat are identified and studied until a fundamental understanding can be obtained. A thorough review of the relevant state of the art methods for optical modelling of heliostats is also conducted.
- The flux distribution of a heliostat is considered as a statistical construct, and the aberrations that contribute to heliostat imaging are analytically described. Methods to model the flux distributions are studied, and the state of the art is evaluated.

- The knowledge of the flux distribution components are then reconstructed to provide an accurate analytical description of the flux distribution. An analytical approach is specifically chosen so that the performance can be parametrised, which allows the influence of component errors to be isolated.
- The understanding and methods developed are then further applied to a MGT CSP plant. A techno-economic sensitivity study is completed to determine particular heliostat field requirements that will lead to an economically viable MGT CSP system.

1.5 Delineations and research boundaries

The delineations and research boundaries define the scope of the work. These are implemented to confine the research to a specific area and to avoid straying from the objectives.

- The primary focus of the research is the flux distribution of individual heliostats. The optical performance of the field as a whole, however, is evaluated in the case studies. This study does not aim to contribute to blocking and shading algorithms, although they are used extensively.
- The focus further remains on an analytical description of the flux distribution. Numerical methods are assumed to be accurate and are used to confirm the validity the proposed methods.
- Minimum image size, analogous with high concentration ratios, and the Annual Incident Power Weighted Intercept (AIPWI) are used as the key optical performance indicators.
- Work is limited to optical aspects and does not include workings of the receiver or thermodynamic cycles.
- Existing literature of material properties and atmospheric effects that impact the flux distribution – such as reflectivity, the sun shape and attenuation – are applied, but no attempt is made to further the state of the art in these areas.
- Active manipulation of the reflective surface profile is not considered.
- The practical issues in the implementation of a silvered-glass mirror module are investigated as a complementary task. No attempt is made to develop new reflector techniques.

1.6 Dissertation structure and overview

The work in this thesis does not have a single narrative, rather a compilation of individual work packages and publications are presented in the various chapters. The thesis is divided into three parts, which correspond to the steps in the methodology.

Chapter 1 provided the context of the work contained in this thesis and presented the objectives and methodology.

Part 1 seeks to fundamentally understand heliostat performance, specifically the flux distribution of a heliostat on the receiver aperture, and includes Chapters 2 to 4.

Chapter 2 provides further context specific to the collector subsystem and the heliostat. The principles, limitations, conflicting design parameters and cost drivers that influence heliostat design are discussed.

Chapter 3 presents a literature review of optical modelling of heliostat imaging. Both the fundamental approaches used in the models and the state of the art are included.

Chapter 4 investigates the individual aberrations that contribute to the flux distribution of a heliostat. The principles governing heliostat performance are illustrated parametrically in a simplified model.

Part 2 integrates the knowledge gained in Part 1 and develops methods to accurately determine flux distribution of a heliostat on the receiver aperture; it includes Chapters 5 to 8.

Chapter 5 develops a Monte Carlo ray tracer for applications with complex geometries.

Chapter 6 looks at the performance improvements that can be obtained by the implementation of an optimal canting strategy.

Chapter 7 compares the flux distribution of a commonly used analytical method to that of a ray tracer. A phenomenon in which aberrations in the sagittal plane are reduced at increased incidence angles is observed, and a modification is proposed to account for this effect.

Chapter 8 outlines the development of a novel analytical model for the flux distribution of a heliostat. The model uses a Super Gaussian function to account for sun shape effects and allows aberrations in the tangential and sagittal planes to be treated independently.

Part 3 applies the knowledge gained in Part 1 and the models developed in Part 2 to a MGT CSP system. The findings and conclusions of the thesis are also provided. Part 3 contains Chapters 9 to 11.

Chapter 9 investigates the practical implementation of a silvered-glass mirror module for the Helio100 project. Various different facet concepts are evaluated, and knowledge gained during the several iterations of the chosen concept is described. Various tests evaluate the performance of the final design.

Chapter 10 presents a techno-economic sensitivity study of the heliostat field parameters for a MGT central receiver system. The influence of the operating strategy on the optimum field parameters and economic viability of the system are also investigated.

Chapter 11 summarises the findings of the thesis and states the conclusions. The contributions made and suggestions for further research are also provided.

Part I

Optical principles

Chapter 2

Review of heliostat principles

The collector subsystem of a central receiver system is briefly introduced; after which the heliostat is considered in isolation. This section introduces the context in which a heliostat operates and discusses physical limits and numerous conflicting design parameters that should be considered when evaluating a heliostat design. Some design parameters are also defined for use later in this dissertation.

2.1 The collector subsystem

The basic function of a central receiver system's collector subsystem is to intercept, redirect and concentrate the solar irradiation to the receiver subsystem. Heliostats are the primary collector elements used to track the sun to maintain the focus of energy on the receiver during operation as depicted in Figure 2.1.

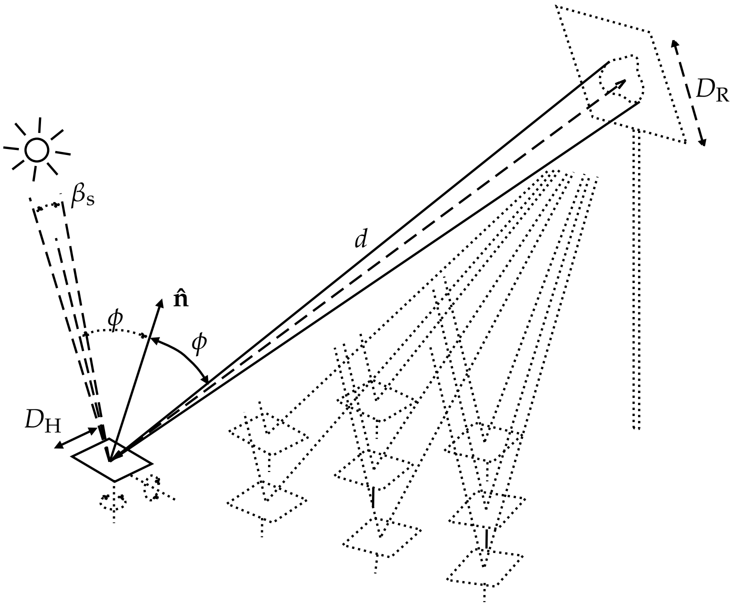

Figure 2.1: The collector subsystem

2.1.1 Flux requirements of the receiver

The reflected beams from the heliostats coalesce at the receiver to achieve the high flux densities required for high temperatures. The receiver absorbs the incident radiation and transfers the energy into the heat transfer fluid. The receiver must be small enough to minimise convection and re-radiation losses, but it must allow sufficient surface area for the heat transfer fluid to remove the thermal energy without inducing a high pressure drop. The receiver materials must also be able to withstand the high temperatures, pressures and thermal stresses.

A receiver design specifies an allowable flux density which should not be exceeded to avoid reducing receiver lifetime. A level of flux uniformity must also be maintained to prevent high thermal gradients and resulting stresses.

Both direct steam and salt receivers are typically omnidirectional (external cylindrical) receivers (Figure 2.2a). Direct steam receivers have allowable flux densities near 0.8 $\mathrm{MW/m^2}$ in the boiling section and 0.3 $\mathrm{MW/m^2}$ for the super-heating section [15]. For conventional utility scale salt receivers, flux limitations are in the order of 1 $\mathrm{MW/m^2}$ [16]. Heliostat fields are generally able to meet and exceed these requirements. If the allowable flux density limitations are not considered in the field layout optimisation, polar fields are favoured typically reaching 2 $\mathrm{MW/m^2}$ to 5 $\mathrm{MW/m^2}$ on the polar side of the receiver [16].

Brayton cycles generally require air receivers and are typically volumetric cavity type receivers (Figure 2.2b). The high temperature volumetric re-

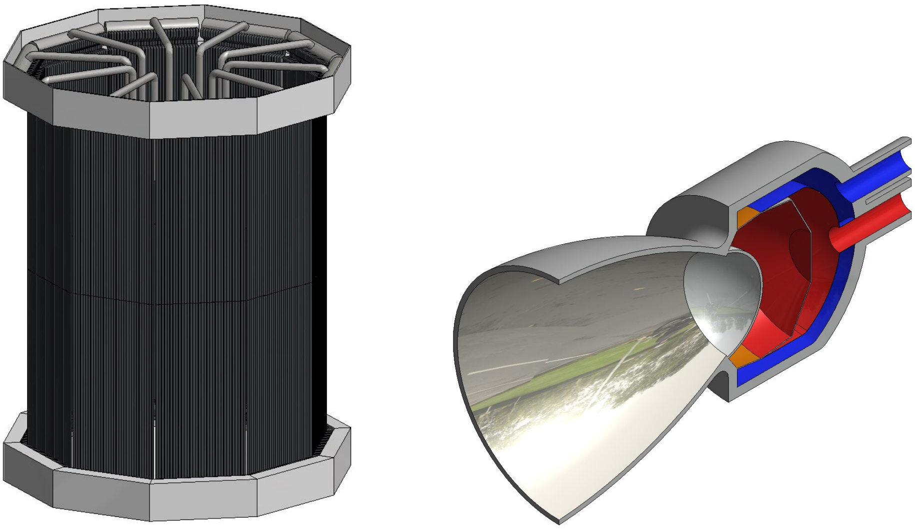

(a) External cylindrical receiver

(b) Pressurised volumetric cavity receiver with a secondary reflector

Figure 2.2: Conceptual representations of (a) an external cylindrical receiver and (b) the Refos pressurised volumetric cavity air receiver with a CPC

ceivers have flux requirements of 0.7 MW/m^2 to 5.3 MW/m^2 [17; 11]. Heliostat fields may require secondary concentrators to reach these flux levels [12].

Ho and Iverson [18] review receiver concepts for high-temperatures above 650 °C. They present the receiver's thermal efficiency, η_t, as a simplified function of the incident radiative power and the radiative and convective heat losses:

$$\eta_t = \alpha - \frac{\varepsilon\sigma F_{\text{view}} T_R^4 + f_{\text{conv}} h \left(T_R - T_{\text{amb}}\right)}{\eta_{\text{field}} I_D C_r} \tag{2.1}$$

where α is the receiver solar absorptance, ε is the receiver thermal emittance, σ is the Stefan-Boltzmann constant (5.67×10^{-8} W/m^{2}K^4), F_{view} is the radiative view factor from the receiver surface to the surroundings, T_R is the receiver surface temperature (K), f_{conv} is a convective heat loss multiplier, h is the convective heat transfer coefficient, T_{amb} is the ambient temperature (K), η_{field} is the heliostat field efficiency, I_D is the direct normal irradiance (W/m^2) and C_r is the concentration ratio.

Considering typical values required for Brayton cycles, Ho and Iverson [18] illustrate that both high concentration ratios on the receiver, $C_r > 900$, and a reduced radiative view cone, $F_{\text{view}} < 1$, are critical to maintain high thermal efficiencies. cavity receivers are used to realise a reduced radiative view cone, while both high accuracy heliostats and secondary concentrators are typically necessary to realise high concentration ratios.

2.1.2 Secondary concentrators

If the desired concentration level cannot be reached by the heliostat field alone, a secondary concentrator is used to concentrate the irradiation further. Secondary concentrators are typically compound parabolic concentrators (CPC) placed in front of the receiver aperture (depicted in Figure 2.2b). The efficiency of light transmission through a CPC varies with the angle of the incident radiation, $\eta_{\text{CPC}} = f(\phi)$ (Figure 2.3). Above a certain angle, known as the acceptance angle, the efficiency drops dramatically, and light is either partly or fully rejected [12]. The higher the geometric concentration ratio, C_g, of the CPC, the lower the acceptance angle, θ_A [19].

$$C_g = \frac{A_{\text{in}}}{A_{\text{out}}} = \frac{1}{\sin^2 \theta_A} \tag{2.2}$$

The acceptance angle results in an effective view cone which restricts the area available for heliostat placement. Depending on the orientation of the CPC, the boundary of this area is elliptic, parabolic or hyperbolic. To warrant the use of a secondary concentrator, the energy gains must outweigh both the optical losses and field limitations which result from its use [9]. Schmitz *et al.* [12] study the use of multiple apertures with secondary concentrators on central receiver systems. The study indicates that multiple apertures are only viable at higher power levels.

2.1.3 Tower configurations

The central receiver system has two tower configurations: the Tower-Top and the Cassegrain, as illustrated in Figure 2.3. The Tower-Top configuration places the receiver at the top of the tower, while the Cassegrain reflects the light down to ground level with a secondary convex mirror.

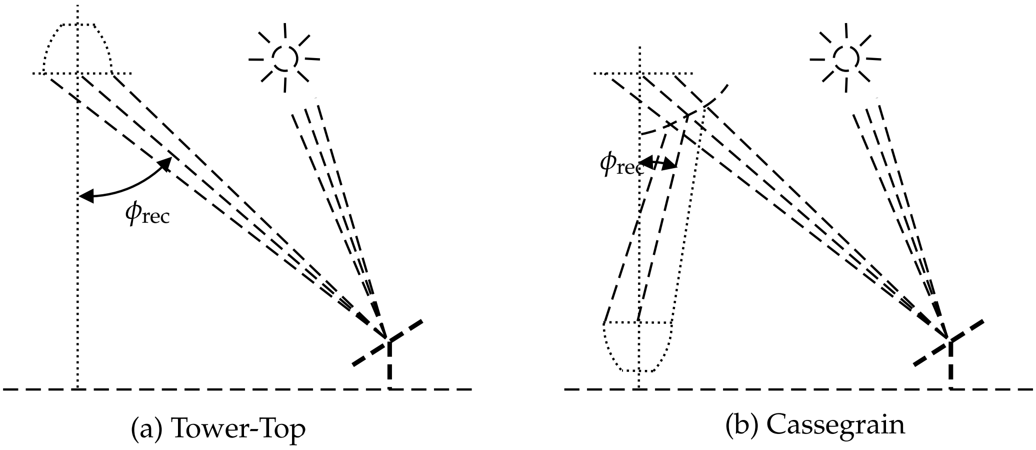

(a) Tower-Top

(b) Cassegrain

Figure 2.3: Tower-Top (a) and Cassegrain (b) concepts (adapted from Kribus *et al.* [2])

The Tower-Top configuration has been utilised in all commercial scale plants due to its simplicity. Schmitz *et al.* [12] show that a multiple-aperture design that allows for a surround field in which several secondary concentrators are placed on a single tower is most cost effective for larger plants from 50 MW_e to 200 MW_e. This configuration in conjunction with a CPC is optically best for high concentrations but places significant restrictions on the heliostat field. Piping the working fluid up to the Tower-Top receiver is also impractical for temperatures above 1000 °C due to the cost of high temperature piping [2]. Placing the heavy receivers, which weigh up to 2500 tons, on top of a tower also requires complex civil construction [20].

Rabl [21] proposes the use of a Cassegrain, also known as the beam down concept, which solves these problems by placing the receiver at ground level. Kribus *et al.* [22] show that the Cassegrain configuration is most attractive in the context of the combined cycle plants as well as for very large scale plants. However, this configuration is a less mature technology than the Tower-Top configuration and incurs additional reflection losses [23].

The power block of a MGT system is small enough to be placed on top of the tower; this avoids the piping problem without incurring additional reflection losses. Both the AORA [24] and CSIRO [8] MGT systems utilise such a configuration.

2.1.4 The heliostat field

The heliostat field consists of a few hundred to several thousand heliostats installed around the tower. The optimum layout of the heliostats is a complex optimisation problem with no clear objective function. The field should meet both the receiver flux requirements throughout the day with minimum investment costs but also ensure that the spillage does not damage the receiver housing or surrounding structures.

The performance of individual heliostats depends on their location relative to the receiver and the placement of the surrounding heliostats. For a given sun position, the heliostat reflects its projected area, which is the product of the aperture and the cosine of the incidence angle. Heliostats placed far away from the receiver have larger images and suffer from atmospheric attenuation. Neighbouring heliostats may also shade or block a portion of the irradiance.

Utility scale plants use surrounding heliostat fields (Figure 2.4a), which have higher annual energy collection compared to polar fields (Figure 2.4b). However, surrounding fields with cylindrical receivers only become economically feasible at scales above 10 $\mathrm{MW_e}$ [25]. Schmitz *et al.* [12] investigate field layouts that utilise secondary concentrators, and they suggest that a single aperture polar field is the most suitable configuration at smaller power levels. They also find that high concentration requirements lead to higher towers to enable tighter packing of heliostats without incurring additional blocking losses.

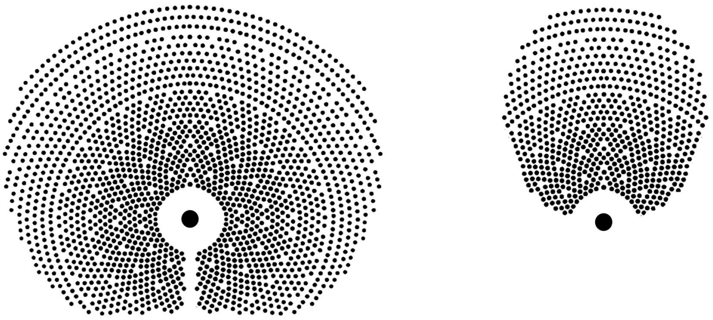

(a) Surround field **(b)** Polar field

Figure 2.4: Two heliostat field layouts utilising radial stagger arrangement

Apart from optical performance, many additional factors need to be accounted for such as heliostat collision, land profile, maintenance access, wiring and water drainage [26]. The layout is typically optimised for a minimum LCOE, and it finds an optimum ratio of field performance to the costs of land, heliostats, receiver, piping, tower, storage, power block and maintenance. Several field layout techniques are available [27; 28; 29], and design methodologies are compared by Mutuberria *et al.* [30].

2.2 The heliostat

In its most abstract form, the heliostat is a mechanically actuated optical reflector. The heliostat must continually track the sun to reflect the irradiation onto the receiver aperture. The ability of the heliostat to optically reflect the irradiation into the aperture with a desirable and predictable flux distribution dictates heliostat performance [31]. In the following sections the components of a heliostat and their performance implications are first discussed after which cost is briefly introduced.

2.2.1 Heliostat components

The components which make up a conventional heliostat are illustrated in Figure 2.5. The reflective surface consists of one or more mirror modules called facets, which are the only optical interface with the solar radiation [32]. Individual facets are mounted on a common backing structure typically consisting of a torque tube and perpendicular trusses [20]. Two drive mechanisms rotate this structure around two axes of rotation [33]. The configuration of these axes of rotation is known as the tracking mechanism. Each

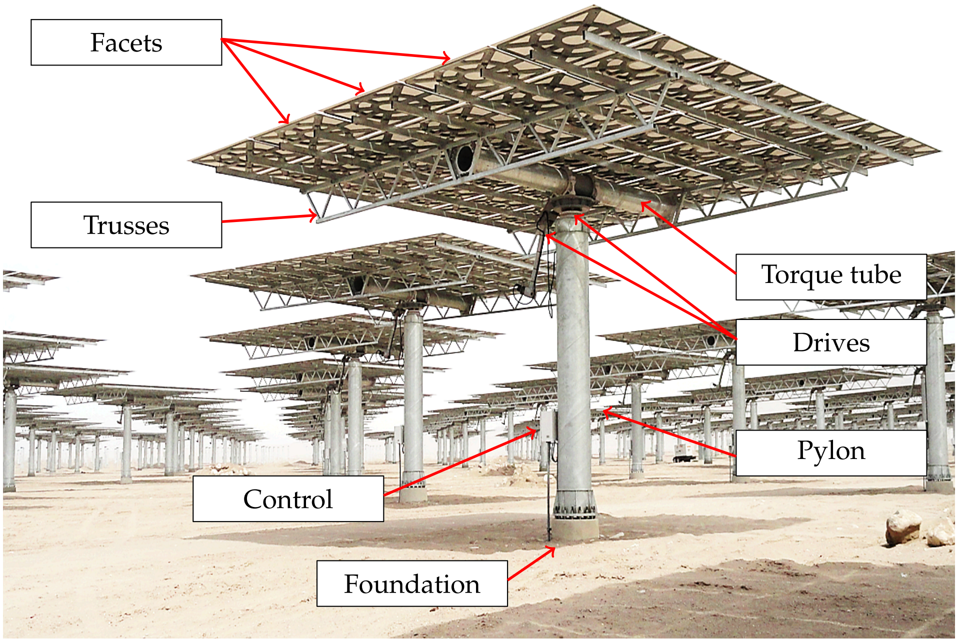

Figure 2.5: Heliostat components [photo taken by author at the Crescent Dunes Solar Energy Project near Tonopah, Nevada]

heliostat has a controller that powers the drives and communicates with a central system controller. The entire assembly is typically mounted on a vertical pylon kept in place by a firm foundation. These components are discussed individually below.

2.2.2 The heliostat surface

Due to the receiver being located a distance from the heliostat, only the directional component of the reflected irradiation intercepts the receiver aperture. It is thus favourable that the reflective surface has the highest specular reflectance over the solar spectrum. Reflection is never fully specular, and a certain percentage of irradiance is lost through absorption and scattering. Reflective surfaces used on heliostats typically have a solar weighted specular reflectance of 90 % to 95 % [34]. The angular dispersion of the irradiation is characterised by the specularity error, σ_{spec}, discussed in Chapter 4. The distribution of the reflected light is generally described using a bidirectional reflectance distribution function.

During operation, the reflective surface material is exposed to climatic stress factors which cause degradation. The surface must withstand these degradation mechanisms, which include exposure to ultraviolet light, dust abrasion, thermal and humidity cycles, cleaning and hail impact. Reflective surfaces that have shown promise for long term outdoor exposure are silvered mirrors, silvered polymer films and anodised sheet aluminium with a protective polymer coating, however, only silver backed glass mirrors have been used in commercial applications [35].

The surface normals over the reflective area are a result of the reflective surface profile. A heliostat with a flat profile casts an image the size of the normal projection increased by 9.3 mrad of sun spread [36]. Such an image is relatively large with a concentration ratio below 1. The concentration ratio can be increased by using a concave surface profile which is able to reduce the image size to the theoretical minimum of 9.3 mrad of sun spread [34].

The deviations of the surface normals from the ideal profile are known as surface slope errors and are specified by an angular standard deviation, σ_{SSE}. Causes of surface slope errors are numerous but include manufacturing imperfections and thermal, gravitational and wind load deformations [37].

The profile is made up of the profiles of individual facets as well as their collective alignment on the common backing structure. The orientation of the facets relative to each other is known as the canting strategy, investigated in detail in Chapter 6.

Both facet profiles and canting strategies typically approximate spherical curvature [38]. The focal length is chosen to equal the slant range, and for a spherical profile the radius of curvature is twice the slant range. A spherically curved profile approximates an aberration free image in the event that the heliostat, target and sun are collinear $\phi = 0°$ [39]. At increased incidence angles, astigmatic aberration is present, which causes image distortion.

2.2.3 Heliostat tracking

To reflect the incident radiation to the desired aim point, the heliostat normal must be oriented in the direction that bisects the unit vectors to the sun and to the aim point. Due to the daily and seasonal movement of the sun, the heliostat requires two degrees of freedom. The specific configuration of these two degrees of freedom is known as the tracking mechanism, and the choice of tracking mechanism has numerous design implications.

The main factor that affects the choice of tracking mechanism is cost. Although the choice of tracking mechanism changes the manufacturing costs, it also affects the optics of the heliostat, the heliostat field layout, the size of the drives, the pylon and the foundations of the heliostat. The unimpeded space volume of the tracking mechanism defines the height of the pivot point above the ground and the proximity at which neighbouring heliostats can be placed [33; 40].

Tracking mechanisms typically use two serial, perpendicular axes of rotation. Two drive mechanisms position the heliostat to sub mrad accuracy. The large reflector area acts like a sail in the wind, and drives should provide adequate force to overcome the resulting wind loads, stiction and the momentum of the structure. During high wind events, the heliostat is taken to a stow position to reduce wind loading. The drives are typically highly geared to ensure that accuracy is maintained, but this results in slow angular velocities.

The heliostat must be able to orientate itself to the range of operational orientations as well as stow and washing positions. The angular ranges required must be met by the range of motion of the drives. The two most common drive types are linear and slew drives. Linear dives can scale down to lower unit sizes but have limited range of motion and require two additional joints per axis of rotation. Slew drives do not have limited range of motion and negate the need for additional joints.

The selection of the tracking mechanism and the position of the heliostat in the field dictate both the angular velocity and the range of motion requirements. The three most commonly used tracking mechanisms are: Azimuth Zenith Tracking (AZ, Figure 2.6a), Fixed Horizontal Axis Tracking (FHA, Figure 2.6b) and Target Aligned Tracking (TA).

AZ has been implemented in almost all large scale plants [4]. AZ is the simplest of configurations, and there is no need for heliostat specific installations. The big advantage of AZ is the shorter pylon, which measures only slightly more than half the surface height and results in reduced wind loads as well as a reduced moment leading to a smaller pylon and foundation.

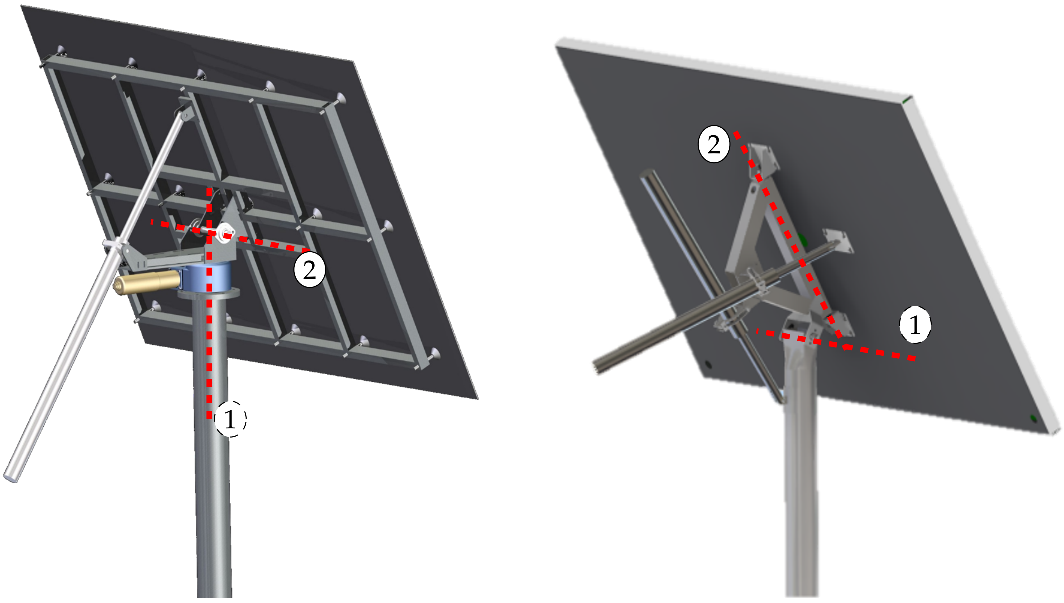

(a) Azimuth-Zenith

(b) Fixed-Horizontal-Axis

Figure 2.6: First and second axes of rotation for an Azimuth-Zenith and a Fixed-Horizontal-Axis type tracking mechanism

TA was developed specifically for correcting first order aberration (see Chapter 4) and is optically superior to other mechanisms [39; 41]. The design, however, is complex to implement, and installation is heliostat location specific.

The unimpeded space volume of FHA results in much denser packing and increased field efficiencies [40; 42]. The maximum ground coverage, ρ_H^{max}, for a rectangular mirror array is increased to 76 % and can theoretically be increased to 100 % using hexagonal arrays [33].

The angular deviation of the image centroid and the intended aim point is known as the tracking error (TE), which can be specified separately in each axis or can be dealt with as a single variable. Deterministic errors can be eliminated using an adaptive control system and heliostat calibration. Indeterminate errors are dominated by backlash in the drives, hinges and structural deformation.

The tracking, communication and parasitic power consumption of the heliostat is an important consideration. Cabling may be a significant cost fraction of the heliostat field. More recently, wireless power and communication have been proposed [42; 43; 44].

2.3 Heliostat cost

As stated previously, the heliostat field contributes ≈50 % of the total plant cost and is considered to provide the greatest potential for cost reduction in central receiver systems [4].

In 2011 the SunShot Initiative was initiated by the U.S. Department of Energy. The aim of the initiative was to make solar energy technologies cost-competitive with other forms of energy by reducing costs by 75 % by 2020 [45]. To achieve this goal, the current projected heliostat cost of \$120/m^2 in 2020 should be reduced to \$75/m^2.

Although heliostat cost is specified in \$/m^2, the optical performance is similarly important. Kolb *et al.* [4] show that more expensive heliostats with improved optics may result in a similar LCOE due to a reduction in the number of heliostats required as well as a reduction in tower height and receiver area. The driving principle behind heliostat design is thus to achieve the optimum balance of cost and performance to minimise the LCOE of the system holistically [46].

Initially pedestal mounted, glass-metal heliostats were considered to be the most cost effective [47]. Reducing heliostat costs was driven through economies of scale by increasing heliostat sizes from 40 m^2 to 150 m^2 [47; 48] as shown in Figure 2.7. In 2011 the ATS150 heliostat [47], developed by Sandia, was considered the low-cost baseline in the United States [4] at \$200/m^2 [1].

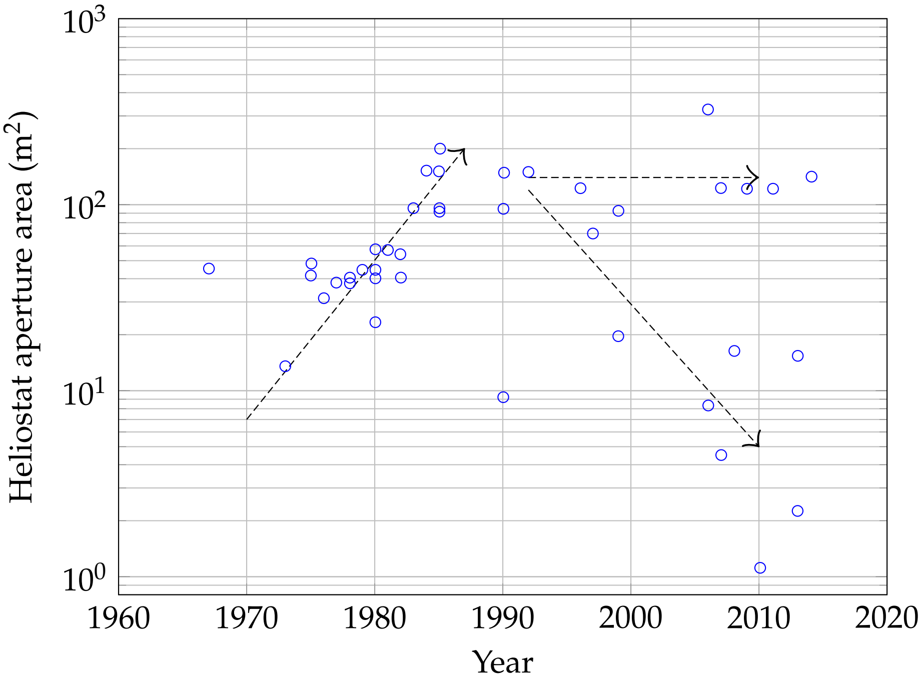

Figure 2.7: Heliostat size trends, (Adapted from Larmuth [49])

More recently, ever smaller heliostats have been implemented in an attempt to reduce costs through increased production volumes [50; 51] as depicted in Figure 2.7. The largest central receiver system to date, built by BrightSource Energy, uses a 15 m^2 design [52]. Smaller heliostats typically have better optical performance and are more suited to ultra-high concentration power tower systems such as the combined cycle plants [22].

Cost reductions through either economies of scale or increased production rates have resulted in a range of heliostat sizes ranging from 1.25 m^2 to 150 m^2. Kolb *et al.* [4] suggests that large heliostats are more cost effective than smaller heliostats, but postulates that an optimum heliostat size may not exist for a minimum LCOE.

Blackmon [53] presents a parametric study of direct heliostat costs per unit area. Heliostat costs are divided into three categories: costs that remain constant on a per unit area basis, costs that scale with imposed loads and fixed costs that are constant irrespective of heliostat area. This generalised model indicates that the asymptote for minimum cost is achieved through reducing fixed costs and utilising small heliostats.

Heliostats are also the least mature technology component of a CSP system and provide the highest learning rate potential [1]. In 2003, Sargent & Lundy [54] find learning rates of collector systems to be ≈92 % with 51 % of the cost improvements coming from increased production volumes, 30 % from technology improvements and 19 % from economies of scale. The recent decline in the cost of electronics, which have reduced heliostat fixed costs, and the potential cost benefit of higher production volumes are driving this trend.

Pfahl [43] suggests that the aggressive cost targets set by the SunShot Initiative do not seem reachable with conventional heliostat designs. Radically new concepts are continuously challenging conventional designs [55; 42; 43] in an attempt to reach these cost targets. Coventry and Pye [44] examine the trends in heliostat design and identify promising cost reduction opportunities.

2.4 Conclusion

Central receiver systems are still in a relatively early stage of the technology life cycle. Optimum configurations are still unknown, and the state of the art is actively being challenged to reduce the LCOE. The flux distribution requirements of MGT CSP indicate the use of a polar type field layout utilising a CPC with a tower-top configuration. Heliostat design is cost driven, but there appears to be no consensus as to which heliostat size would lead to a techno-economic optimum. A parametric approach finds the theoretical asymptote for minimum heliostat cost to result from using small heliostats where fixed costs are minimised.

Chapter 3

Literature review of the optical modelling of a heliostat

The main subject of this thesis is the optical performance of individual heliostats. This chapter outlines the different approaches to optical modelling, and it presents the state of the art in a literature review thereof. This review is focussed on the logic and methodology of different models, specifically for the purposes of understanding and benchmarking the state of the art rather than their implementation or availability.

3.1 Introduction

Being able to determine the performance of the collector subsystem is required in all stages of design, optimisation and operation of central receiver systems. The collector performance can be determined by knowing both the flux distribution over the receiver aperture and the irradiation intercepted by the aperture.

The flux distribution over the aperture plane, represented by $I(x,y)$, is a result of the distribution of the irradiation from the sun, the geometry of the collector subsystem and the numerous aberrations that effect the light along its path from the source to the receiver. Optical models of the heliostat field attempt to account for these phenomena to determine the resulting flux distribution. The power of the intercepted irradiance into the receiver aperture, P_{R}, is simply a result of this distribution and can be determined by solving a double integral of the flux distribution, $I(x,y)$, over the aperture area, A_{R}.

$$P_{\mathrm{R}} = \iint\limits_{A_{\mathrm{R}}} I(x,y)\mathrm{d}x\mathrm{d}y \tag{3.1}$$

Ho [56], Garcia *et al.* [29], Bode and Gauché [57], Yellowhair *et al.* [58] and Li *et al.* [59] review available optical software used in CSP systems and discuss their suitability for different applications. The choice of the model is generally dictated by the highest accuracy obtainable for affordable computational times. Different approaches to the calculation of the flux distribution, with varying accuracy and computational expense, are thus valid for different applications.

3.2 Approaches to calculating the flux distribution

Lipps [60] outlines four different fundamental approaches to the calculation of the flux distribution: shape projection, convolution, cone optics and ray tracing. All flux distribution models typically consist of different implementations or amalgamations of these four approaches.

Shape projection projects the four vertices of a heliostat onto the receiver plane and then enlarges the image based on aberrations. Convolution methods trace only a single ray and describe the flux distribution using a convolution of all the different aberrations. Cone optics is similar but reflects several rays with a very simple flux distribution function. Lastly, ray tracing in its purest form numerically approximates the flux distribution by tracing many rays, which do not carry distribution knowledge themselves.

In the first three approaches, flux distribution knowledge accompanies the reflected rays allowing the flux distribution to be described by an analytical function. In ray tracing, the distribution is computed numerically. The first three approaches will thus be considered analytical models and the latter numerical. In reality some analytical models contain numerical solutions and visa versa. Literature of both analytical and numerical models is discussed in the two subsections that follow.

3.2.1 Analytical models

Lipps [61] first derives an expression for the flux distribution on a plane from a single heliostat. This expression is time consuming to calculate, and Walzel *et al.* [62] suggest the use of a Hermite polynomial expansion to speed up the calculation of the convolution. Though this is faster, its performance is poor at low slant ranges and small tracking errors [63]. Lipps and Walzel [64] suggest a polynomial approximation instead and include sun shape and tracking errors into the model; however, the model is limited to flat heliostats. The analytical calculation remains computationally expensive, and interpolation from a lookup table is used to speed up the calculation.

Lipps and Vant-Hull [65] propose a cell-wise method to simplify simulation of large fields. An array of heliostats is assumed to behave similarly and is represented by a single cell in a large field. This approach is still widely used in high level simulations such as the System Advisory Model [66].

These methods form the DELSOL code [27], which is widely used. The advantage of DELSOL is its ability to use a single heliostat flux calculation and transform it onto any aperture, allowing computationally inexpensive system optimisation to be realised after one initial detailed performance run.

Igel and Hughes [32] investigate geometric optics of spherical surfaces. The astigmatic aberration of edge rays are described in the sagittal and tangential planes for off-axis imaging. This work forms the basis for astigmatism models in HELIOS [67] and HFLCAL [68] codes.

A detailed convolution model is presented by Biggs and Vittitoe [69][67] in the form of the HELIOS code, which derives much of the statistical optics included in later codes. Convolution is solved numerically using Fourier transformations resulting in an accurate and versatile code, but the code is slow and considered to be inappropriate for optimisation [70].

Hennet and Abatut [71] propose an analytical convolution of the principal ray of the heliostat where flux is determined by different intercept conditions of the cone on the receiver aperture. This method does not account for errors which need to be indirectly introduced [70].

Harris and Duff [72] propose that the flux distribution is given by a bivariate normal distribution. This assumption greatly simplifies accounting for errors because it allows variances of different aberrations to be summed. The approach has been widely accepted due to its simplicity. Pettit *et al.* [73] study the computation of the effective error cone for such a model. It is found that approximating the sun shape as a normal distribution holds if the variance of the other errors is greater than twice the sun shape error.

Collado *et al.* [70] present the UNIZAR model, which also treats errors probabilistically but as circular Gaussian distributions. The model is simplistic and computationally inexpensive but is limited to ideally curved surfaces and assumes on-axis imaging. Some limitations are described by Elsayed and Fathalah [74] and Collado [31]. The UNIZAR method is experimentally validated by King [75].

The HFLCAL model also assumes a circular Gaussian distribution but incorporates astigmatic aberration. The model is attractive due to its simplicity. Schwarzbözl *et al.* [68] validate the method for collinear cases but suggest that the method is inappropriate for detailed flux distribution analysis. However, the model has been used in aiming strategy optimization in various studies [6; 76; 77; 78]. Some inaccuracies in the method's prediction of the flux distribution are documented, but the reason for these inaccuracies are apparently not well understood [6; 76; 77; 31].

The UNIZAR and HFLCAL methods are critically compared and again validated experimentally by Collado [31]. The models demonstrate good coherence with errors between 3 % and 10 %. Collado concludes that the newer HFCAL model is simpler and slightly more accurate than the UNIZAR.

Elsayed and Fathalah [74] propose a separation of variables and superposition technique, which creates a convolution between the four intercept points at the vertices of a rectangular mirror simplifying the computation of the double integral.

Huang *et al.* [79] propose Gauss-Legendre integration of an analytical function to calculate the optical efficiency of a heliostat. Results correspond to ray tracing models with a mean absolute error of only 0.76 % and maximum absolute error of 2.4 % for intercept factors.

Apart from trying to find analytical models to describe the flux integral more accurately, there has also been work done in reducing the computational time of simple coarse models. Loomis *et al.* [80] present a diverging polygon-based model that reduces a heliostat to its most fundamental elements. Flux is simply described as the ratio of the area of a series of diverging 3D polygons.

Guo and Wang [81] investigate the correspondence of radial power distribution between elliptical and circular Gaussian distributions. They suggest that the square mean of the elliptical axes is the best conversion method to circular distribution. They also introduce an interpolation reconstruction of elliptical Gaussian distributions from known values on a rectangular boundary, which simplifies the computation of the double integral.

The CRS4-2 code [82] utilise a tessellation technique to account for blocking and shading. The concept of characteristic functions is also introduced which decouples performance from sun position, but the function must be solved for numerically.

Georgiou *et al.* [83] propose the use of caustics surfaces. This method is solved numerically but requires the analytical description of geometric surfaces which include imaging errors. The method is found to be more efficient than Monte Carlo ray tracing but is limited to conic sections.

Belhomme *et al.* [84] suggest that all analytical approaches to calculate flux distribution of a heliostat field are unsuitable for flux distribution calculations based on highly resolved heliostat geometry data since the analytical solution is based on predefined error distributions.

3.2.2 Numerical models

The type of ray tracing generally used to model central receiver systems is path tracing, which is considered the most accurate and unbiased method. Path tracing can go beyond geometrical optics to include radiative and physical optics. The primary challenge of path tracing is to solve the rendering equation defined historically by Kajiya [85]. This integral equation is generally solved numerically by Monte Carlo methods first proposed by Metropolis and Ulam [86] and furthered by Hammersley and Handscomb [87]. This method is preferred above other numerical methods due to its flexibility to include new physical phenomena and the ability to deal with geometrically complex systems [88].

Initially the development of path tracing algorithms focused on minimising computation; best known methods of ray tracer design are well defined [89; 90]. Lafortune [91] propose many refinements to path tracing, including bidirectional path tracing.

More recent research focuses on the implementation of solvers in CPU's and GPU's to speed up image rendering in the computer graphics industry [92; 93; 94]. This area of computer science falls outside the scope of this document and is omitted. The algorithms used in most ray tracers such as TieSOL[92], SolTrace[95], FIAT LUX, Zemax and others remain proprietary.

Daly [96] first used ray tracing to study the effect of performance variables on flux distributions of trough collectors. Rays were traced from the receiver tube backwards to the sun and weighted according to its intercept with the solar disc.

MIRVAL is the first ray tracer dedicated to central receiver systems [97]. Rays are generated on a plane projection of the reflecting surface. Each ray has a direction and an energetic value. The reflected ray is a function of the bidirectional reflectance distribution function which accounts for the emissive, reflective, and absorptive behaviour of the surface. Incident flux on a surface is proportional to the number of impacting rays. MIRVAL has been incorporated into the Fortran based code SPRAY managed by the German Aerospace Centre (DLR) [57].

MIRVAL [97], SolTrace [95] and Tonatiuh [98] ray tracers make use of the collision-based Monte Carlo method where rays are initiated at the light source. Yellowhair *et al.* [58] compare SolTrace [95] and Tonatiuh [98] to DELSOL [27] and HELIOS [67] and find the ray tracing tools to be computationally slower but more flexible for modelling complex receiver geometries, while the analytical models were limited to standard receiver geometries.

De la Torre [99] proposes an integral formulation Monte Carlo method where rays originate from the reflective surface. This eliminates computation of the first intercept point, and ray termination is also reduced. Caliot *et al.* [100] investigate the integral formulation Monte Carlo method and find it to be faster than collision based algorithms.

This same method is realised in the STRAL ray tracer [84] developed at DLR for highly resolved heliostat geometry data. SOLFAST [101] also use the Monte Carlo integral based formulation and accelerate computation by reusing the flux ray paths and using KD-Tree constructions on both CPU and GPU [94].

Currently, Bode [102] is developing an integral based Monte Carlo ray tracer at STERG, which forms a parallel research activity to the work presented in this thesis.

De la Torre *et al.* [88] provide a thorough review of recent advances of Monte Carlo methods applicable to CSP. One key conclusion is that the only approach to accelerate Monte Carlo algorithms for iterative design procedures is to determine a probability density function and derive approximation models. This statement indicates that it is unlikely that Monte Carlo methods will become computationally less expensive in the future and will mainly increase in relevance through increased computational power.

3.3 Conclusion

The accuracy of flux distribution methods appears to be related to computational effort. It is evident that methods are actively being sought to achieve higher accuracies with lower computational effort. Numerical methods are most accurate but are not expected to become computationally less expensive; rather clever and distributed computation may reduce simulation times. Analytical models are used in applications that require computational efficiency but have not been able to achieve suitable accuracies in certain flux distribution applications. This confirms the potential value of a computationally efficient method that can describe the flux distribution of a heliostat with a higher level of confidence.

Chapter 4

Optical aberrations in heliostat imaging

An optical model of a heliostat field has to describe the final distribution of radiation at the receiver and must consider the behaviour of the light on its path from the sun to the receiver. In this chapter, the light source and the behavioural features of light along this path are investigated in detail. Some of the theory discussed is then used to parametrically determine heliostat performance.

A large portion of the work in this chapter has been published in the proceedings of the 2013 SolarPACES Conference in Energy Procedia Journal [103]. The work from this publication has been adapted and condensed.

4.1 Introduction

Optical aberrations are the phenomena in an optical system that cause light to depart from the paraxial image point, resulting in a degradation of the image quality. In this chapter, optical aberrations are interpreted differently as the phenomena in the optical system that cause light to depart from an infinitesimal focal point on the focal plane. This interpretation allows all the factors that contribute to the heliostat image widening to be considered as aberrations.

By classifying the various aberrations and understanding their behaviour in the optical system, analytical expressions can be derived to describe their impact on the image. These expressions can then be used to simplify the description of performance of the system.

Consider a number of photons from the sun which irradiate a heliostat at a given moment. These photons undergo several aberrations or "events" such as reflection, scattering and absorption. Because there are a very large number of photons they may be treated as a continuum rather than discrete phenomenon. The image or flux distribution can thus be defined by the product of the power of the photons, P, and the probability function of the photons as a function of the aberrations, $\mathrm{I}(A_1, A_2, A_3 \ldots A_\mathrm{n})$.

Consider a single photon, intercepting a specific point on the heliostat surface which undergoes several events along its path. These events occur consecutively along the path of the photon and can for practical purposes be considered statistically independent. Probability theory dictates that the joint probability of statistically independent variables is the product of their probabilities [104]. The flux distribution resulting from photons moving along this specific path can thus be described as a product of the probabilities of the events which occur along the path.

$$\mathrm{I}\left(\bigcap_{i=1}^{m} A_\mathrm{i}\right) = \prod_{i=1}^{m} \mathrm{I}(A_\mathrm{i}) \tag{4.1}$$

If the probabilities are given by functions, say $A_\mathrm{i}(x)$ and $A_\mathrm{j}(x)$, the joint probability is then given by their convolution [67]. Convolution is in essence a pointwise multiplication of the functions through a translation.

$$(A_\mathrm{i} * A_\mathrm{j})(x) = \int_{-\infty}^{\infty} A_\mathrm{i}(u) A_\mathrm{j}(x-u) \, \mathrm{d}u \tag{4.2}$$

Now consider that the photon may take another path intercepting a different point on the heliostat surface. The paths that a photon may take are mutually exclusive and collectively exhaustive [104]. Since all the paths have the same probability, the joint probability function can thus be given as the sum of the mean probability of all the paths, where n is the number of paths and m the number of events.

$$\mathrm{I}_R(x,y) = \frac{1}{n} \sum_{i=1}^{n} \left(\prod_{i=1}^{m} \mathrm{I}(A_i) \right) \tag{4.3}$$

This result indicates that two types of aberration exist. The first is a phenomenon that affects the light regardless of its path and includes the sun shape, atmospheric attenuation and specularity of the reflective surface. The second type is path dependent behaviour which is caused by the geometry reflective surface profile of the heliostat.

The distributions of these various aberrations which contribute to the image are investigated individually in the following sections. It is noted here that tracking errors are not included since they result in a translation of the image rather than contribute to the flux distribution itself. If a field with a sufficiently large numbers of heliostats are modelled, the tracking errors should conform to the central limit theorem and may be modelled like surface slope errors.

4.2 The sun

The sun is the source of energy, and knowledge of both the position of the sun and the distribution of the incident irradiation is important for a CSP system. Both of these factors are discussed here.

4.2.1 The position of the sun

For our purpose, the earth travels around the sun once every year in an elliptical orbit, and the earth rotates around its own tilted axis daily. This movement results in both seasonal and hourly position changes of the sun relative to an observer at a specific terrestrial location. Time and location specific knowledge of the sun's position, known as the sun path, is essential for an open-loop control system to determine where each heliostat must point to reflect the light at the desired aim point.

The sun path is generally specified using azimuthal and zenith angles in a spherical coordinate system. Figure 4.1 shows the sun path at Olyfenhoutsdrif, the location where the South African utility, Eskom, is planning on building a 100 $\mathrm{MW_e}$ central receiver system [105]. The resulting cylindrical shape of the collective annual paths of the sun is referred to as the sun band, discussed later in Section 7.5.1.

Several algorithms exist that describe the sun path [106; 107; 108]. The algorithms vary in their precision, computational expense and the time period for which they are valid [109]. This body of work used the algorithm presented by Reda and Andreas [107]. The algorithm is accurate to ± 5 µrad and is the preferred algorithm used by NREL's Measurement and Instrumentation Data Center [110].

4.2.2 Distribution of solar irradiance

When observed from outside the earth's atmosphere, the sun appears as a disc, its size quantified by the angular distance between the centre of the disc and its edge [111]. The solar disc angle, α_{disc}, is dependent on the distance between the sun and the earth, and various formulae for its computation are available [112; 113; 114; 115]. The mean of the solar disc angle is 4.651 mrad, but it varies seasonally between 4.573 mrad and 4.732 mrad [111].

Only the direct component of the solar irradiance or direct normal irradiance (DNI) is typically useful for CSP. DNI is defined as the irradiance on a surface perpendicular to a vector from the observer to the centre of the sun caused by radiation that did not interact with the atmosphere [111]. For solar energy applications, DNI is interpreted practically as the total radiation received from the area subtended by a small half angle centred on the sun's disc, α_{out}. The recommended value for α_{out} is $\approx$40 mrad (solid angle of

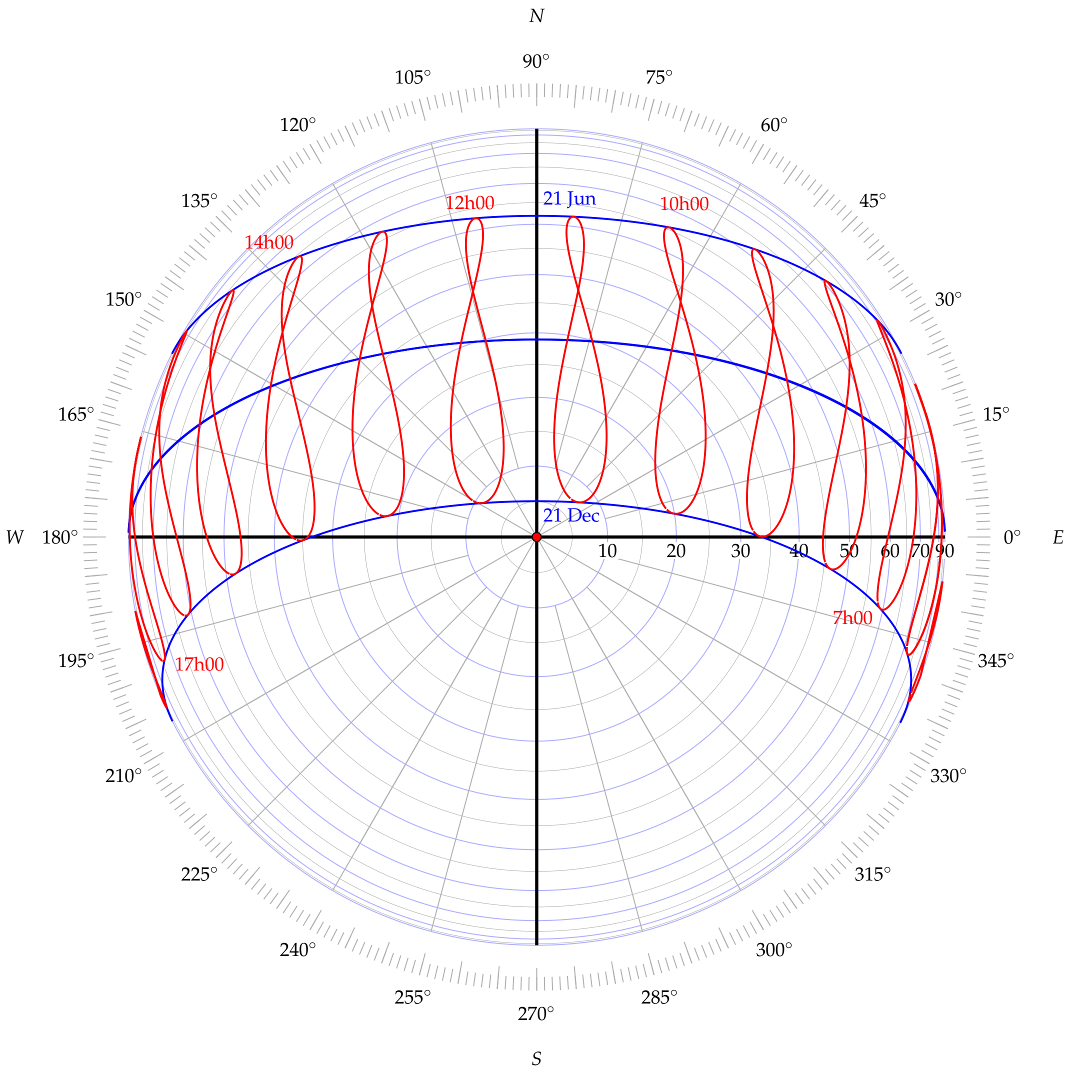

Figure 4.1: Hourly and seasonal positions of the sun at Olyfenhoutsdrif near Upington, South Africa $(28^\circ 28,095'S : 21^\circ 4,291'E)$

5×10^{-3} sr) [116], but it varies according to the measurement instrumentation used.

The distribution of the spectral radiance of the solar disc, L, decreases radially outward as a function of the angular distance α from the centre of the sun. This radiance profile is known as the sun shape.

Kuiper [117] presents a function for an extra-terrestrial sun shape with normalised radiance (see Figure 4.2)

$$\frac{L(\alpha)}{L(\alpha = 0)} = \frac{1 + \beta_K \sqrt{1 - \frac{\tan^2 \alpha}{\tan^2 \alpha_{\text{disc}}}}}{1 + \beta_K} \tag{4.4}$$

where β_K is a wavelength dependent parameter [67]. The Kuiper sun shape

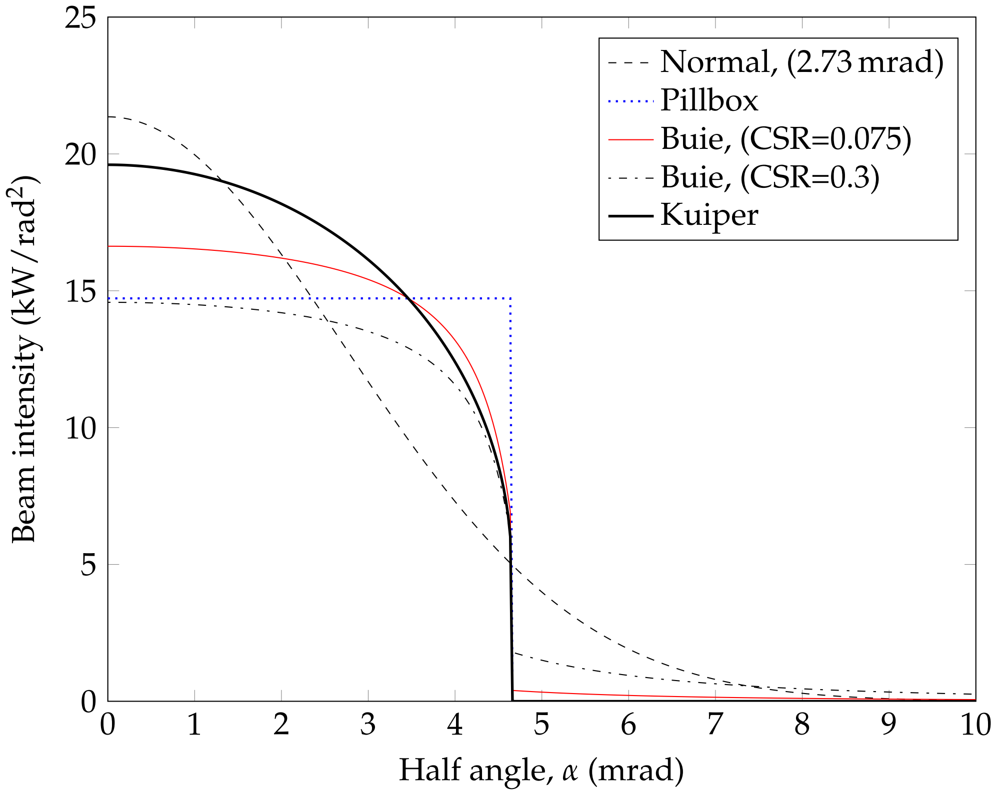

Figure 4.2: Radial intensity of various sun shapes with normalised beam power

is the most commonly used extra-terrestrial sun shape in the field of CSP [111], but other extra-terrestrial sun shapes are also available [118; 119].

As the radiation passes through the atmosphere, its interaction with atmospheric particles result in forward scattering [114], resulting in a widening of the sun shape. The resulting radiance outside the disc ($L(\alpha > \alpha_{\text{disc}})$) is known as the solar aureole. The fraction of the DNI contributed by the aureole is known as the circumsolar ratio (CSR) and can be as low as <0.01 on a very clear sky.

Rabl and Bendt [120] and Neumann *et al.* [121] derive average sun shapes from experimental measurements by Grether and Hunt [122]. These are known as the "standard solar scan" (SSS). Winter *et al.* [123] presents a fit to the relative radiance of the SSS at a CSR(4.653 mrad, 55.85 mrad) of 0.035.

$$L_{\text{SSS}}(\alpha) = \begin{cases} 13.639 \times 10^6 \left(1 - \left(\frac{0.5051\alpha}{\alpha_{\text{disc}}}\right)^2 - \left(\frac{0.9499\alpha}{\alpha_{\text{disc}}}\right)^8\right), & \text{if } \alpha \leq \alpha_{\text{disc}} \\ 72000 \left(\frac{\alpha}{\alpha_{\text{disc}}}\right)^{-2}, & \text{if } \alpha > \alpha_{\text{disc}} \end{cases} \tag{4.5}$$

Buie *et al.* [124] suggest a function of the aureole relative radiance based on the CSR

$$L_{\text{Buie}}(\alpha \mid \gamma, \kappa) = \begin{cases} \frac{\cos(0.326\alpha)}{\cos(0.308\alpha)}, & \text{if } \alpha \leq \alpha_{\text{disc}} \\ e^{\kappa}\alpha^{\gamma}, & \text{if } \alpha > \alpha_{\text{disc}} \end{cases} \tag{4.6}$$

where

$$\gamma = 2.2 \ln(0.52\text{CSR})\,\text{CSR}^{0.43} - 0.1 \tag{4.7}$$

$$\kappa = 0.9 \ln(13.5\text{CSR})\text{CSR}^{-0.3} \tag{4.8}$$

Sun shapes are simplified into simple statistical distributions as well to ease computational expense in certain models. The most simple sun shape assumes that the irradiance is evenly distributed over the solar disc resulting in the pillbox distribution.

$$L_{\text{Pillbox}}(\alpha) = \begin{cases} \frac{1}{\pi\alpha_{\text{disc}}^2}, & \text{if } \alpha \leq \alpha_{\text{disc}} \\ 0, & \text{if } \alpha > \alpha_{\text{disc}} \end{cases} \tag{4.9}$$

The sun shape is also frequently approximated as a circular Gaussian distribution. Pettit *et al.* [73] suggest that root-mean squared (RMS) widths of measured sun shapes should be used to determine an effective σ_{sun}. Based on measurements of Grether and Hunt [122], the narrowest σ_{sun} of 2.73 mrad is determined [73]. This value has been used throughout literature and is the default σ_{sun} of the SOLTRACE ray tracer [95]. Measurements at Plataforma Solar de Almería have resulted in 2.51 mrad [70; 31] using the same method.

$$L_{\text{CG}}(\alpha) = \frac{1}{2\pi\sigma_{\text{sun}}^2} \exp\left(\frac{-(\alpha^2)}{2\sigma_{\text{sun}}^2}\right) \tag{4.10}$$

The influence of the sun shape on the optical efficiency of several concentrators were quantified by different sun shapes in a ray tracing simulation [125; 126; 127; 128]. The results showed large performance deviations of up to 20 % from changes in the sun shape alone.

4.3 Surface errors

In the previous section the direction and distribution of the irradiance from the sun at a given location is discussed. Here, the interaction of this irradiance with a point on a concentrator's reflective surface is considered.

The reflective surface should perform three optical functions: it must reflect as much of the incident radiation as possible, it must reflect the irradiance specularly to maintain its directional properties and the surface normal must be oriented correctly. Real surfaces are imperfect and both the specularity errors and slope errors depicted in Figure 4.3 contribute to image aberration. Specularity errors are a property of the reflector surface, while slope errors are macro deviations of the reflective surface normals from the desired profile.

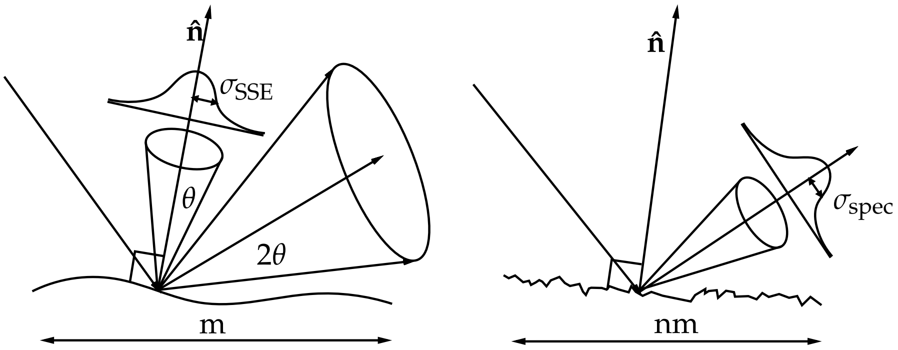

Figure 4.3: Surface errors: left) macro slope errors and right) micro specularity errors

Scattering caused by dust accumulation on the reflector and surface roughness results in non-specular reflection [129]. Dispersion due to non-specularity varies with the wavelength of light; however, specularity error is specified as a solar weighted standard deviation of the resulting angular dispersion, σ_{spec}.

Pettit [130] characterises the scattering of light from solar reflective materials using the sum of the specular and diffuse components. These are represented by the square sum of a high and low amplitude normal distributions. Gee *et al.* [131] then incorporate a weighting factor, K, to describe the specularity error.

$$\sigma_{\text{spec}}^2 = K\sigma_{\text{spec1}}^2 + (1 - K)\,\sigma_{\text{spec2}}^2 \tag{4.11}$$

The macro imperfections in the reflective profile are also present due to manufacturing imperfections and deformations caused by gravitational, wind and thermal loading. This error is known as the surface slope error (SSE). The surface slope error is given by the geometric mean of the standard angular deviation of the surface normals in their components from that of the designed profile. σ_{SSE} is generally in the order of 1.5 mrad [4].

$$\sigma_{\text{SSE}} = \sqrt{\sigma_{\text{SSE,x}} \cdot \sigma_{\text{SSE,y}}} \tag{4.12}$$

These errors are generally dealt with as a single bivariate or radial standard deviation, σ_{bq}, referred to as the beam quality [67].

$$\sigma_{\text{bq}}^2 = \sigma_{\text{spec}}^2 + 4\sigma_{\text{SSE}}^2 \tag{4.13}$$

4.4 Atmospheric attenuation

After the radiation is reflected it must pass a certain distance through the atmosphere to reach the receiver. Aerosols and dust particles in the atmosphere attenuate the radiation.

Transmittance models typically describe a single atmospheric attenuation factor, f_{at}, as a function of the slant range, d, [12; 97; 132; 133]. Different functions are used depending on the levels of aerosol loading. Sengupta and Wagner [134] propose a transmittance model that accounts for aerosol variability and depends only on the DNI.

The extended empirical formula suggested by Schmitz *et al.* [12] is used throughout this thesis and corresponds well to that proposed by Pitman and Vant-Hull [132].

$$f_{\text{at}}(d) = \begin{cases} 0.99321 - 1.176 \times 10^{4} d + 1.97 \times 10^{-8} d^{2}, & \text{if } d \leq 1000 \text{ m} \\ \exp(1.106 \times 10^{4} d), & \text{if } d > 1000 \text{ m} \end{cases} \tag{4.14}$$

4.5 Astigmatic aberrations from profiled surfaces

Up to this point, only path independent aberrations have been considered. Here, geometric aberrations resulting from the profile of the reflective surface are investigated. Astigmatic aberrations are the dispersions which result from the foci of the reflective surface occurring either before or beyond the focal plane as illustrated in Figure 4.4.

Igel and Hughes [32] propose an analytical approach to describe the boundaries of the resulting image; this approach is applied throughout this section. For the purpose of simplicity, terminology used in this document is sourced from Igel and Hughes [32]. The model assumes a circular heliostat aperture, and the boundaries of the flux image are created by the edges of the circular reflective profile. This implies that the remainder of the flux will fall within these boundaries. These assumptions reduce the problem to only four points to be analysed; these are the opposing points on the tangential and sagittal planes which result in the height, h_{tan}, and width, w_{sag}, of the image as depicted in Figure 4.4.

The astigmatic dispersion can be determined using the Coddington equations [135]. Although fairly elementary, the proofs of these equations are reproduced in Appendix A.3 (p. 153) since it forms the basis for further analysis later on in this section. These equations give the astigmatic dispersion of the edge rays in the tangential, h_{tan}, and sagittal planes, w_{sag}, based on the radius of curvature of the surface in these planes, r_{tan} and r_{sag}, the slant range, d, and the incidence angle, ϕ. To non-dimensionalise the equation, the focal ratio, F_{r}, is defined as the slant range, d, divided by the reflector

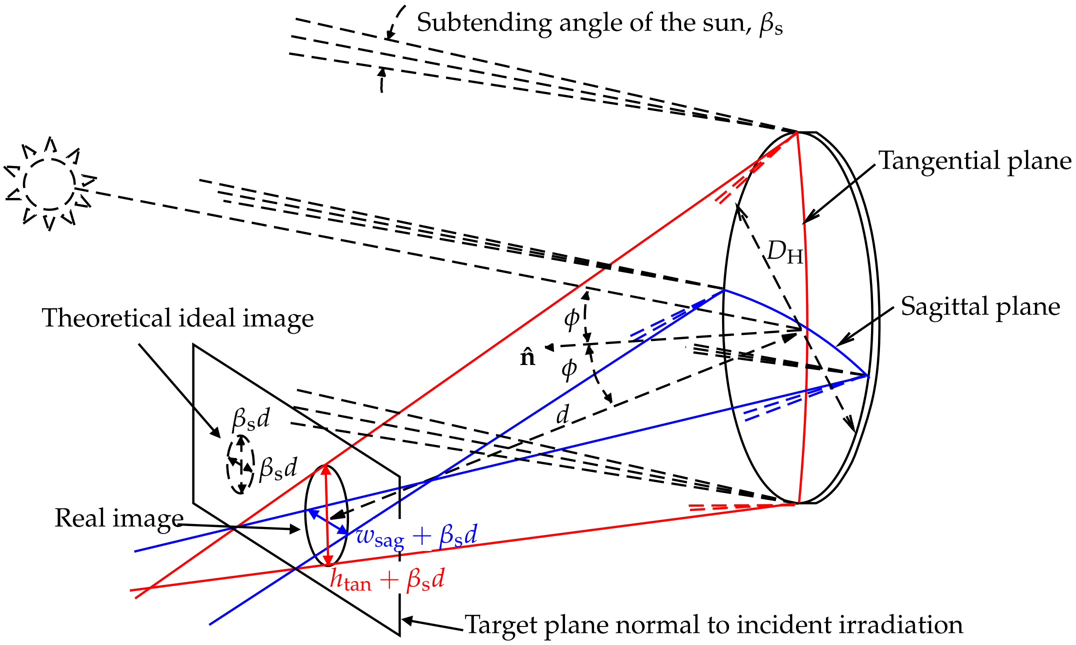

Figure 4.4: Image height and width in tangential and sagittal planes

diameter or chord length, D_H.

$$h_{tan} = \frac{d}{F_r} \left| \frac{2d}{r_{tan}} - \cos\phi \right| \qquad \text{and} \qquad w_{sag} = \frac{d}{F_r} \left| 1 - \frac{2d\cos\phi}{r_{sag}} \right| \tag{4.15}$$

4.5.1 Objective measure for astigmatic aberration

To assess the implications of the astigmatic aberration, an objective measure is required. Literature does not appear to expose good non-dimensional objective measures of astigmatic aberrations to compare distributions. To address this need and allow for comparative measures, this study proposes two new measures; the Coefficient of Optical Aberration (COA) and the Flux Density Ratio (FDR). Both measures compare image dimensions and flux to the theoretical ideal image and can be applied to any single aberration or combination of aberrations. In this section they are used to evaluate astigmatic aberrations.

The theoretical minimum image dimension is limited by the subtending angle of the sun, β_s. At a slant range, d, the minimum height and width of an image is given by $\beta_s d$. The COA is defined as the ratio of the ideal image diameter to the real image diameter. This measure compares a single dimension in either the tangential or sagittal plane and is useful to observe image distortion.

$$\text{COA}_{tan} := \frac{h_{tan} + \beta_s d}{\beta_s d} \qquad \text{and} \qquad \text{COA}_{sag} := \frac{w_{sag} + \beta_s d}{\beta_s d} \tag{4.16}$$

Furthermore, the FDR is defined as the ideal flux relative to the average flux density of the image. This measure compares flux density or image area and is useful to compare performance.

$$\mathrm{FDR} := \frac{1}{\mathrm{COA}_{\mathrm{tan}}\mathrm{COA}_{\mathrm{sag}}} = \frac{\beta_s^2 d^2}{(h_{\mathrm{tan}} + \beta_s d)(w_{\mathrm{sag}} + \beta_s d)} \tag{4.17}$$

4.5.2 Flat profile

A flat profile has an infinite radius of curvature. By substituting $r_{\mathrm{tan}} = r_{\mathrm{sag}} = \infty$ into Equation 4.15, the astigmatic dispersion from a flat profile can be determined.

$$h_{\mathrm{tan}} = \frac{d\cos\phi}{F_r} \quad \text{and} \quad w_{\mathrm{sag}} = \frac{d}{F_r} \tag{4.18}$$

This result correlates to the findings of Parrott [136] which states that a flat heliostat facet creates an image size equal to the normal projection of the surface increased by 9.3 mrad of sun spread.

Since a small image is desirable, a large F_r is required to maintain a reasonable COA in both planes. The range of F_r's that can be expected is dependent on the field layout and heliostat dimensions. Typical focal ratios are given in Table 4.1 for the H16 and ATS150 heliostats [137] in two plant configurations calculated from field size estimations by Battleson [138].

Table 4.1: Typical focal ratio ranges for heliostats and heliostat facets

Field Type		**Focal Ratio, F_r**	
		H16 (16 m^2)	ATS150 (148 m^2)
Large Surround Field	Heliostat:	62-304	20-97
(500 $\mathrm{MW_t}$)	Facet:	250-1216	41-199
Small North Field	Heliostat:	47-263	15-84
(100 $\mathrm{MW_t}$)	Facet:	188-1061	31-178

The ranges of F_r for both field sizes are similar for a specific heliostat, and the smallest F_r occurs nearest the tower. For large area heliostats, the heliostat F_r remains below 100, although smaller heliostats allow higher F_r's up to 300.

To place these numbers in perspective, the product of the cosine factor and the FDR was calculated for various F_r's and is plotted in Figure 4.5. The cosine factor is taken into account to illustrate that the reflected power decreases with the cosine of the incidence angle, ϕ. The top curve represents the ideal profile without astigmatic aberration. The image size is reduced and flux density increased as this curve is approached, illustrating the desire for high F_r's.

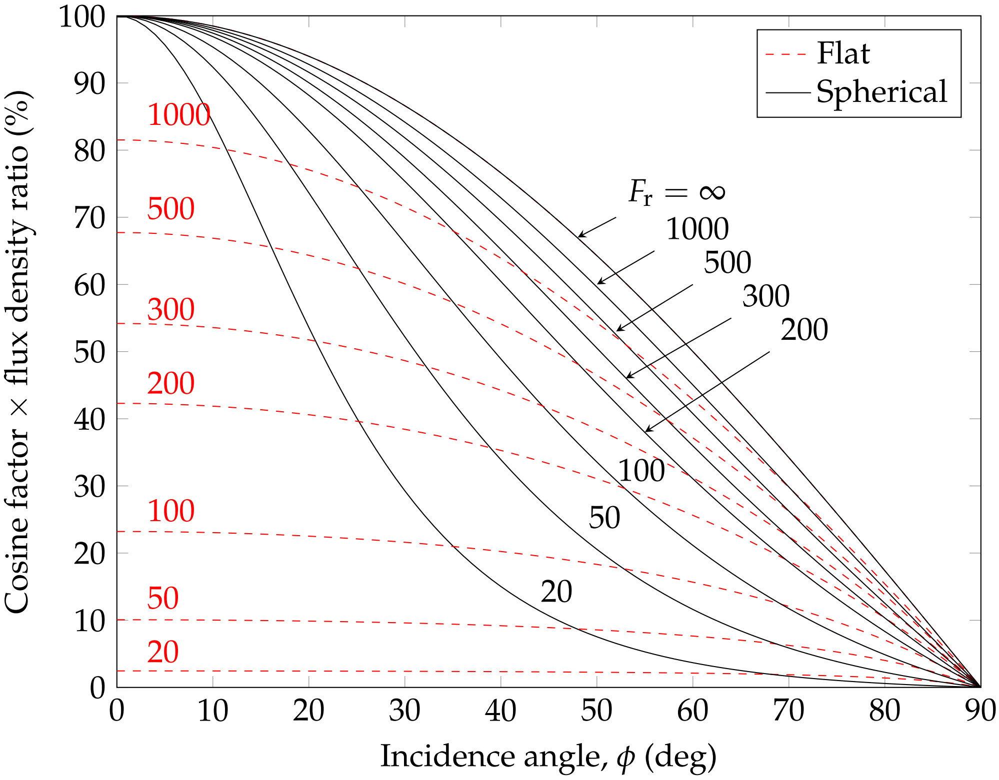

Figure 4.5: Flux density as a function of incidence angle for flat and spherical profiles of various focal ratios

It is immediately obvious that flat profiles at low F_r's cast very large images, significantly reducing the FDR. Only at very high F_r's will flat facet profiles be acceptable for high flux requirements. This also motivates the use of curved profiles or small heliostats.

4.5.3 Spherical profile

The concave shape that is generally utilised in optical concentration is the paraboloid [20]. A paraboloid has the property that light parallel to the axis of symmetry can be specularly reflected to a single focal point from any point on the parabola. The curved profiles discussed here are discussed with reference to the paraboloidal surface. The vertex of a paraboloid approximates a sphere at high F_r's as proven in Appendix A.1 (p. 151). The desirable property of a spherical profile is that it reflects all rays to a single point at zero ϕ. The radii of curvature of a spherical profile is simply twice the focal length, $r_{tan} = r_{sag} = 2f$. Substituting these radii into Equation 4.15, the astigmatic dispersion is obtained.

$$h_{\text{tan}} = \frac{d}{F_{\text{r}}} \left| \frac{d}{f} - \cos\phi \right| \qquad \text{and} \qquad w_{\text{sag}} = \frac{d}{F_{\text{r}}} \left| 1 - \frac{d \cos\phi}{f} \right| \tag{4.19}$$

Assuming the ideal on-axis case where the focal length, f, is equal to the slant range, d, the product of the FDR and the cosine factor for a spherical profile was calculated and is also plotted in Figure 4.5.

A significant improvement from the flat profile is observed for low incidence angels, and as expected, no astigmatic effects are present at zero incidence angle. At increased ϕ the spherical profile distorts the image resulting in reduced FDR's. Astigmatic aberration is responsible for the increased image area and reduced flux densities [39].

It is important to grasp that a heliostat experiences a range of incidence angles throughout the day. In practice, zero incidence angles are not of interest since the heliostat will be shaded by the target, and very high incidence angles are only approached by certain heliostats at dawn or dusk. The range of practical incidence angles is dependent on the position of the heliostat in the field and the sun position.

The average yearly incidence angles at Olyfenhoutsdrif were calculated assuming a 150 m tower; these are plotted in Figure 4.6. The average ϕ ranges from approximately 25° upwards to as high as 50° for a surround field, indicating that increasing the FDR at non-zero incidence angles would be advantageous.

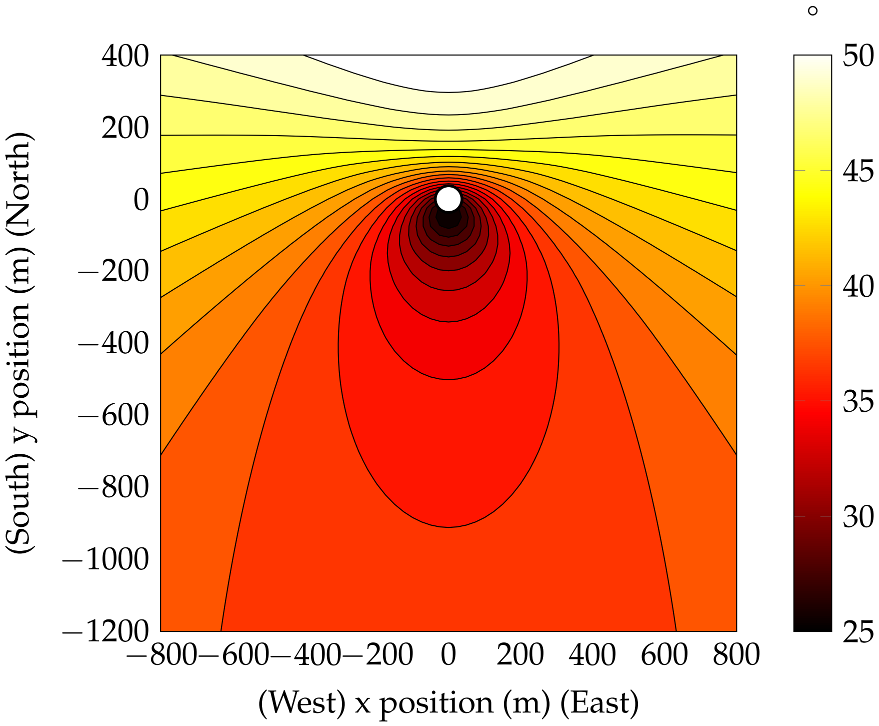

Figure 4.6: Linear average of hourly incidence angles for 2012 at Olyfenhoutsdrif

4.5.4 Toroidal profile

For a heliostat to obtain the ideal image at non-zero incidence angle, the heliostat profile must again form part of a paraboloidal surface. However, the profile cannot lie at the vertex of the paraboloid; rather it must be situated on the side wall of the paraboloid at an angle twice the incidence angle from the focal point as depicted in Figure 4.7.

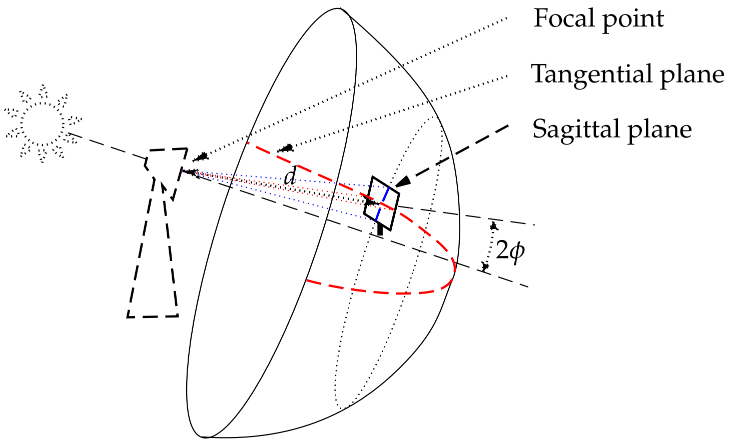

Figure 4.7: Heliostat profile as a section of a paraboloid side wall

The radii of curvature in the tangential and sagittal planes at a point on a paraboloid side wall is solved for in Appendix A.2 (p. 152), which corresponds to that proposed by Brueggemann [139].

$$r_{\text{tan}} = 2d \sec \phi \qquad \text{and} \qquad r_{\text{sag}} = 2d \cos \phi \tag{4.20}$$

An ideal astigmatism free profile can thus be approximated by an elliptical paraboloid with the specified radii of curvature. This shape is also known as a toroid, and an example of such a profile is given in Figure 4.8.

The radii of curvature of the toroid vary according to the incidence angle, ϕ. Since the profile of the heliostat is fixed, a certain incidence angle must be chosen at which the profile performs optimally, represented here as $\bar{\phi}$. Assuming the axis of the toroid remains in the tangential and sagittal planes, the image dimensions can be calculated from Equation 4.15.

$$h_{\text{tan}} = \frac{d}{F_{\text{r}}} \left|\cos \bar{\phi} - \cos \phi\right| \qquad \text{and} \qquad w_{\text{sag}} = \frac{d}{F_{\text{r}}} \left|1 - \frac{\cos \phi}{\cos \bar{\phi}}\right| \tag{4.21}$$

The product of the FDR and the cosine factor is plotted in Figure 4.9 for various focal ratios with $\bar{\phi}$ set to 30°. The toroidal profile shows a performance improvement above that of the spherical profile over a large range of more practical incidence angles, with the exception of poorer performance at very low incidence angels.

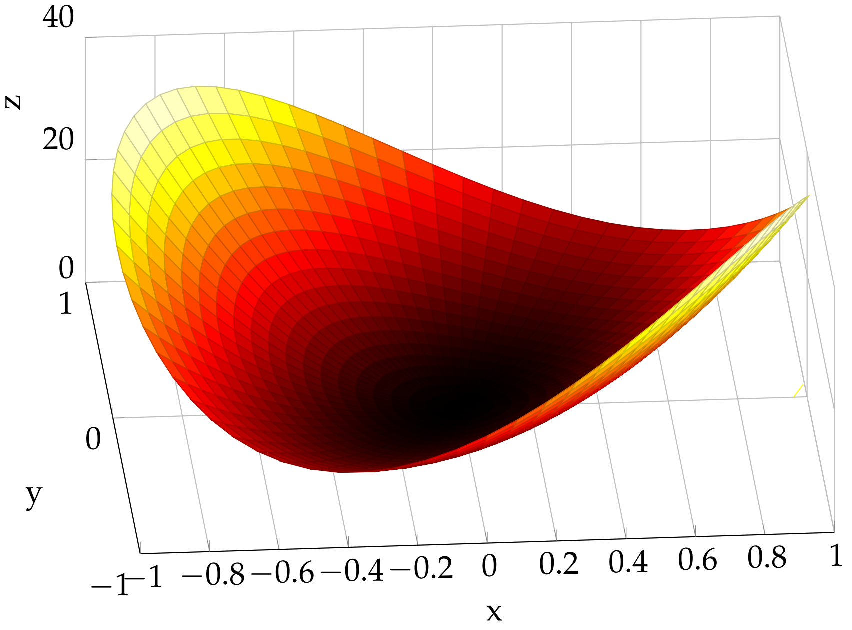

Figure 4.8: Exaggeration of a toroidal profile

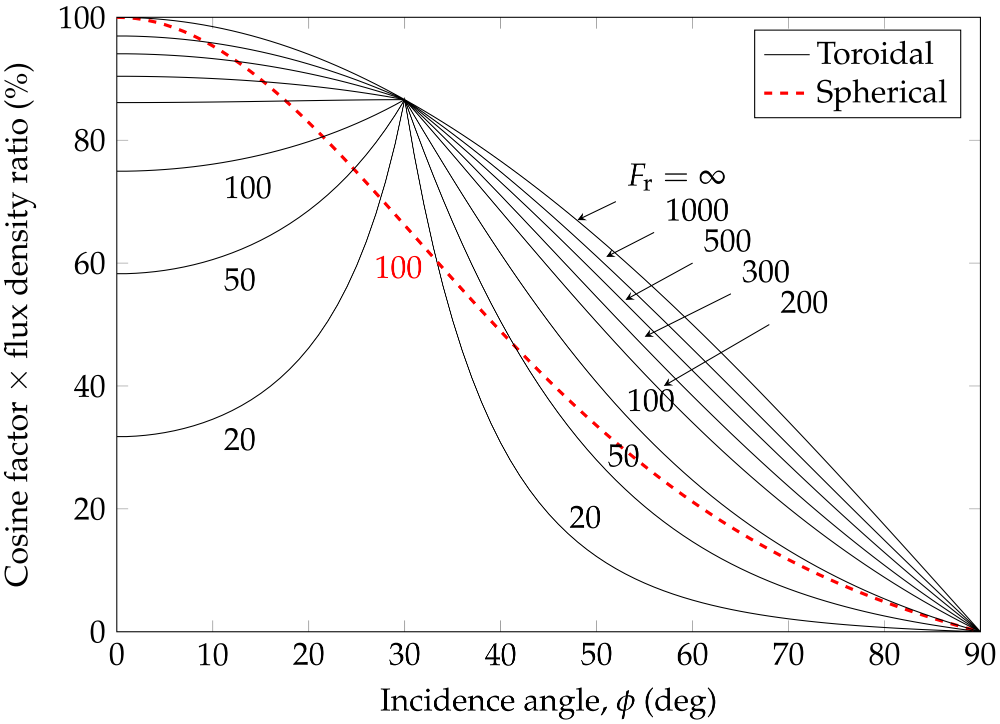

Figure 4.9: Flux density as a function of incidence angle for an aligned toroidal profile at various focal ratios ($\bar{\phi} = 30$) and for a spherical profile ($F_r = 100$) as reference

The toroidal nature of the profile dictates that the profile is no longer axisymmetric, and the orientation of the profile relative to the operational plane must be taken into account. The optical alignment angle, τ, can be defined as the angle between the axis of the heliostat and the operational plane as depicted in Figure 4.10. Similarly the toroid pre-alignment angle, ψ, is defined as the angle between the major axis of symmetry of the toroidal profile and the heliostat axis.

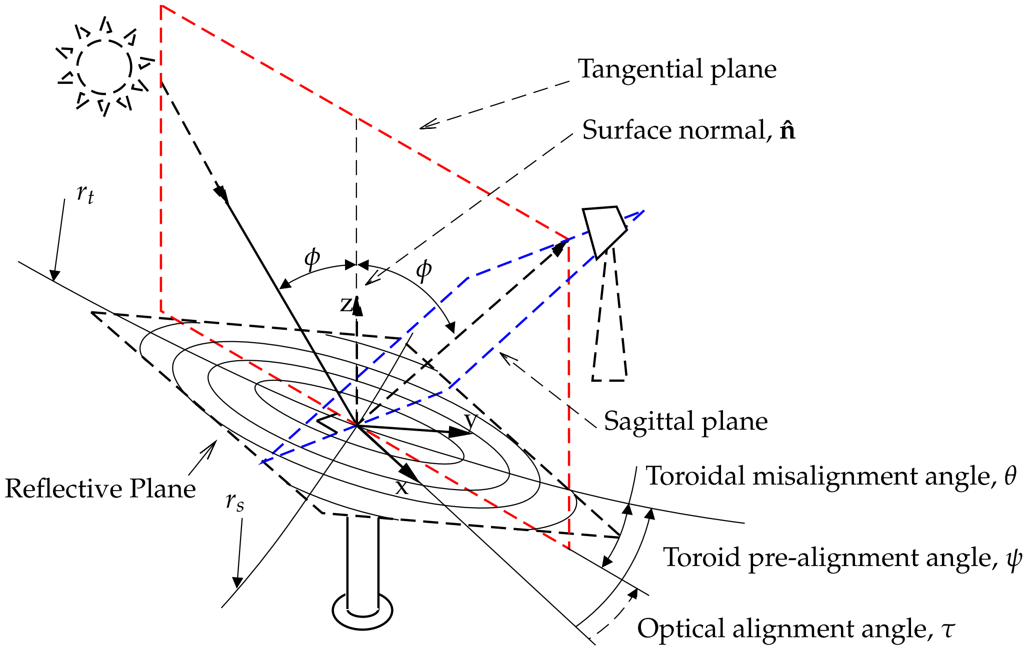

Figure 4.10: Diagram describing the geometric parameters

The variation of τ is dependent on the tracking mechanism chosen. TA orients the reflective surface to ensure that τ remains zero, and setting ψ equal to zero ensures the toroid is always aligned as assumed in Figure 4.9. This is, however, not the case for AZ and FHA tracking where τ varies during the day. The absolute misalignment between τ and ψ is given by the toroidal misalignment angle, $\theta = |\psi - \tau|$.

The operational radii of curvature in the tangential and sagittal planes were solved for at a specified misalignment angle, θ (Proof included in Appendix A.4, p. 154).

$$r_\theta(\bar{\phi}, \theta) = \left| \frac{2d}{\cos^2(\theta)\cos\bar{\phi} + \sin^2(\theta)\sec\bar{\phi}} \right| \tag{4.22}$$

$$r_{\theta+90}(\bar{\phi}, \theta) = \left| \frac{2d}{\sin^2(\theta)\cos\bar{\phi} + \cos^2(\theta)\sec\bar{\phi}} \right| \tag{4.23}$$

The radii of curvature vary from the ideal, causing some defocussing to occur at misalignment. Since the toroidal pre-alignment angle, ψ, is constant, the variation of the optical alignment angle, τ, is of interest to quantify the defocussing. The standard deviation, σ_τ, of τ for AZ and FHA tracking fields at Olyfenhoutsdrif are plotted in Figure 4.11.

The toroidal profile is symmetrical about the toroid axis. Assuming ψ is equal to the average of τ distributed normally, then by definition the profile will be aligned to within the standard deviation 68.2 % of the time. The standard deviation, σ_τ, is below 20° for a substantial section of the southern

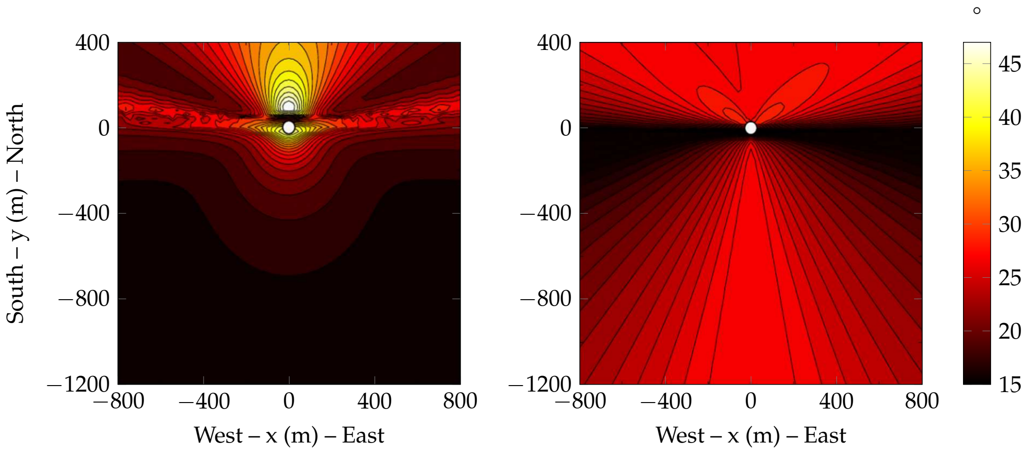

(a) AZ **(b)** FHA

Figure 4.11: The standard deviation, σ_τ (deg), of τ, for a AZ tracking (left) and a FHA tracking (right) heliostat field (80 m tower)

section of the AZ tracking field and only increases above 25° in the easterly and westerly fans as well as the northern section. The FHA tracking field remains below 27° and reduces in the eastern and western sections. This finding suggests that to reduce astigmatism utilising toroidal profiles, AZ tracking is best suited in the northern section of the field and FHA tracking in the eastern and western sections.

To quantify the optical influence of the misalignment, the product of the FDR and the cosine factor are plotted for various misalignment angles in Figure 4.12.

At 0° misalignment, the facet was aligned and resulted in the same shape as that of an aligned toroid given in Figure 4.9. As the toroid is misaligned, the ideal focal ratios are shortened in the tangential and lengthened in the sagittal planes, resulting in image spread. The change in radii of curvature causes the optimum performance to shift to a lower incidence angle. For small angles, this effect is not pronounced, as seen for 10° and 20°, indicating that a toroid is insensitive to misalignment up to 20°. At 45° the performance is reduced to that of a spherical profile and continues to decrease to a minimum at 90°.

Since the standard deviation of the misalignment (Figure 4.11) is relatively low, below 20° for a substantial part of the field, the toroidal profiles perform as expected, and misalignment does not significantly affect optical performance.

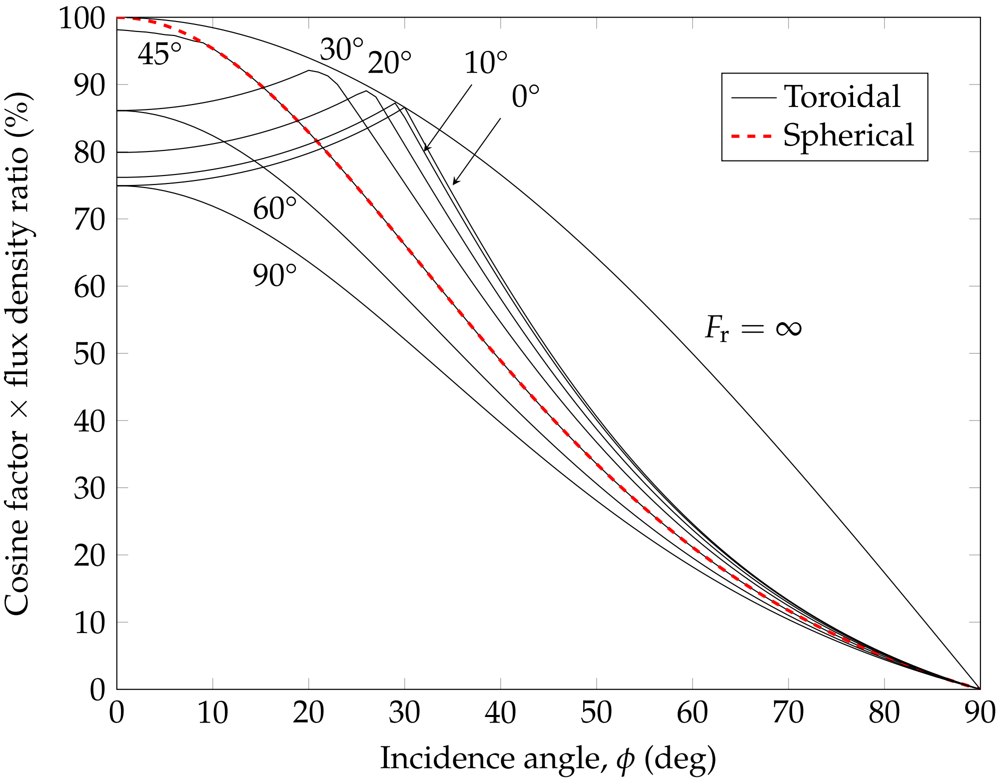

Figure 4.12: Flux density as a function of incidence angle for a toroidal profile at various misalignment angles ($F_r = 100$, $\bar{\phi} = 30$) and for a spherical profile ($F_r = 100$) as reference

4.5.5 Analysis of a multi-faceted heliostat

As previously discussed, it is impractical to use a single facet on a large heliostat; thus, large heliostats are multi-faceted. These facets are canted to a desired profile. The canting strategy is responsible for the orientation of the two edge facets, and the radius of curvature of the edge facets additionally contribute to the curvature of the edge of the heliostat. On this basis, the astigmatic dispersion of a multi-spherically-faceted but toroidally canted heliostat can be solved for, where $\bar{F}_r$ is the focal ratio of the facet.

$$h_{\tan} = \left(\frac{d}{F_r} - \frac{d}{\bar{F}_r}\right) \left|1 - \cos\phi(\cos\bar{\phi}\cos^2\theta + \sec\bar{\phi}\sin^2\theta)\right| + \frac{d}{\bar{F}_r}\left|\frac{d}{f} - \cos\phi\right| \tag{4.24}$$

$$w_{\text{sag}} = \left(\frac{d}{F_r} - \frac{d}{\bar{F}_r}\right) \left|\cos\bar{\phi}\cos^2\theta + \sec\bar{\phi}\sin^2\theta - \cos\phi\right| + \frac{d}{\bar{F}_r}\left|1 - \frac{d\cos\phi}{f}\right| \tag{4.25}$$

The first term accounts for the canting strategy and the second for the spherical facet profile. This finding indicates that both the facet profile and focal ratio still play a role in the dimensionless ratios for a multi-faceted profile.

4.5.6 Influence of profile choice on field flux distribution

Having solved for the astigmatic aberrations of flat, spherical and toroidal profiles analytically, it is of value to test the validity of the equations and to illustrate the implications thereof in the context of a heliostat field. To achieve this, a simple method to determine the flux distribution of a heliostat is required.

The HFLCAL method, briefly introduced in Chapter 3, allows the flux distribution to be approximated as a circular Gaussian distribution (transition from a pillbox beam to a Gaussian beam is discussed in Appendix A.5). Schwarzbözl *et al.* [68] suggest that the statistical approach used in this method is not appropriate for detailed flux distribution analysis; nevertheless, this method is able to provide a fast and reliable indication of the optical performance of the field.

The main interest in the HFLCAL method is that it utilises the image dimensions in the tangential and sagittal planes, which are already known for the discussed profiles. Thus, with some modification, the HFLCAL method allows for profile variation to be incorporated in the analysis. A detailed review of the structure and calculations of the method are provided in Appendix B. By substituting h_{tan} and w_{sag} from the various profiles into the astigmatism term (Equation B.8, p. 158) the performance of the discussed profiles can be evaluated.

To illustrate the performance effect of the reflective profile and as a validation case, a result of two previous studies is reproduced. The profiles considered use an off-axis canting strategy to produce a perfect image at a specific date and time. The Annual Incident Power Weighted Intercept (AIPWI, see Section 6.2.2, p. 67) of a heliostat (discussed by Buck and Teufel [137]) at varying canting times is shown in Figure 4.13. AIPWI is shown to vary from 80 % to 97 %, depending on the time of day the heliostat was canted. The analytical method is able to reproduce the performance trend of a toroidally canted multi-faceted heliostat with a maximum error of 6 %.

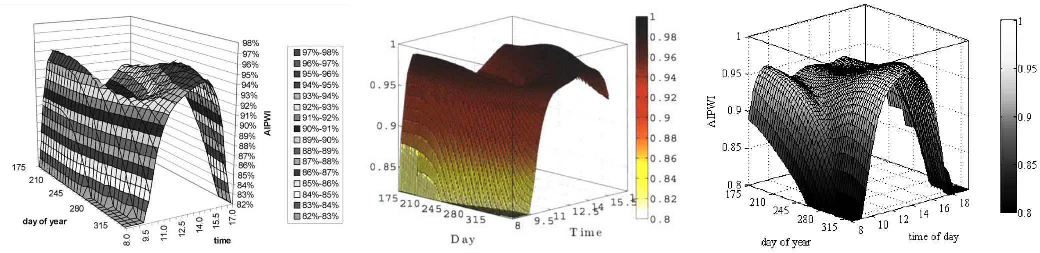

(a) **(b)** **(c)**

Figure 4.13: AIPWI using various off-axis canting times (a) Buck and Teufel [137] (b) Noone [140] (c) HFLCAL method modified to account for profile variation

To illustrate the effect of profile choice in the context of a field, a simple polar field of 1089 ATS150 heliostats [4] is considered. The effect of different profiles on the hourly average flux distribution at solar equinox is plotted in Figure 4.14a, assuming a single point aiming strategy. The shape obtained is a result of the summation of the various image sizes of the heliostats at different slant ranges. Close heliostats concentrate all their power in a smaller radial distance, whilst the heliostats at larger slant ranges have larger images. The sum of the images is normally distributed. The most prominent feature of the results is the significantly higher flux densities obtained by the curved profiles. The spherical profile produces a slightly lower peak flux due to the additional astigmatism. The flux non-uniformity in Figure 4.14 illustrates the need for aim point strategies.

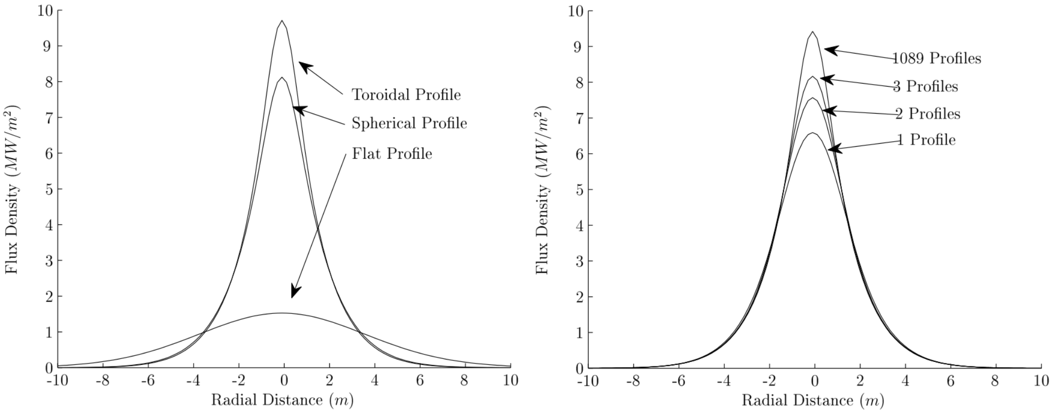

(a) **(b)**

Figure 4.14: a) Radial flux distribution profile for toroidal, spherical and flat profiles. b) Radial flux distribution profile for an off-axis canted (toroidal) multi-spherical-faceted heliostat field using a given number of profiled facets

A single faceted heliostat is impractical as it results in the use of multiple facets for large heliostats. For manufacturing purposes, customised facets also are not practical; rather, fewer mass manufactured profiles would reduce costs. Since canting is merely the orientation of the facets relative to each other, canting is required to be completed individually for each heliostat. This allows the macro heliostat profile to be customised for the heliostat while the individual facets are mass produced. Utilising various numbers of spherically profiled facets in the heliostat field with an off-axis canting strategy, the flux distribution of the field is plotted in Figure 4.14b. As expected, increasing the number of facet profiles used in the field reduces astigmatism and increasingly approximates the toroidal profile.

4.6 Parametric description of heliostat intercept efficiency

Having described the various aberrations analytically, these functions can be combined to parametrically describe a heliostat's optical performance. This application aims to illustrate how the aberrations relate to each other and influence the optical performance. To achieve this, the relationships between the primary performance variables need to be simplified to a manageable yet descriptive level. In this section, numerous simplifying assumptions are made to enable a unified description of the intercept efficiency of a heliostat.

Assuming the same circular Gaussian flux distribution used in the HFLCAL method, and a round receiver normal to the incident beam with a representative diameter, D_R, the intercept efficiency, η_int, can be calculated by integrating image radially outward to the edge of the receiver.

$$\begin{aligned}\eta_\mathrm{int}(D_\mathrm{R},\sigma_\mathrm{tot},d) &= \frac{1}{2\pi d^2\sigma_\mathrm{tot}^2}\int_0^{2\pi}\int_0^{\frac{D_\mathrm{R}}{2}} r\exp\left(\frac{r^2}{2d^2\sigma_\mathrm{tot}^2}\right)dr\,d\theta \\ &= 1-\exp\left(-\frac{D_\mathrm{R}^2}{8d^2\sigma_\mathrm{tot}^2}\right)\end{aligned} \tag{4.26}$$

To simplify the mathematics, all aberrations that cause errors in the normal vector of the surface are combined into a single term (σ_NVE).

$$2\sigma_\mathrm{NVE}^2\left(1+\cos^2\phi\right) = \left(2\sigma_\mathrm{SSE}^2+2\sigma_\mathrm{t\_pri}\sigma_\mathrm{t\_sec}\right)\left(1+\cos^2\phi\right) \tag{4.27}$$

For a spherical profile with the focal length, f, equal to the slant range, d, the astigmatism term can also be further reduced, as detailed in Appendix A.5. This assumption is often made but represents the ideal case and should not be used when an accurate result is required.

$$\sigma_{\text{ast}}^2 = \frac{D_{\text{H}}^2(1-\cos\phi)^2}{16d^2} \tag{4.28}$$

Combining the three equations above allows the intercept efficiency to be reduced into a single equation.

$$\eta_{\text{int}}\left(D_{\text{R}}, D_{\text{H}}, \sigma_{\text{sun}}, \sigma_{\text{NVE}}, d, \phi\right) = \\ 1 - \exp\left(-\left(\frac{D_{\text{R}}^2}{d^2}\right) / \left(8\sigma_{\text{sun}}^2 + 16\sigma_{\text{NVE}}^2(1+\cos^2\phi) + \frac{1}{2F_{\text{r}}^2}(1-\cos\phi)^2\right)\right) \tag{4.29}$$

The three angular terms which contribute to the spillage are isolated for the purpose of understanding the implications of this result. First the commonality between the terms is considered. Each term represents a ratio of two solid angles or steradians. Knowing that the angle can be defined as the length of an arc divided by the radius of the arc, the solid angle, which contains the receiver, is given by $(D_{\text{R}}/d)^2$ in the numerator. The denominator contains the sum of the various aberrations.

Figure 4.15 plots the intercept efficiency, η_{int}, as a function of the inverse of the ratios, illustrating the effect of the solid angle of the beam on performance. Note that the Y-axis of the curve is logarithmic and thus as the sum of these three terms increases, the η_{int} decreases with an increasing rate.

As expected the aberration terms must be minimised or the receiver enlarged to minimise spillage losses. For several practical reasons, such as the high flux requirements to reach the temperatures required by the cycle, economic implications of a large receiver and the re-radiation and convection losses, the area of the receiver is typically limited.

The first term represents the contribution of the sun shape. The sun shape, σ_{sun}, varies with atmospheric conditions but is "near constant" error, typically in the order of 2.73 mrad if normally distributed [73], and cannot be reduced or avoided. The slant range, d, varies from heliostat to heliostat based on the field layout and may be slightly reduced by increasing the field density, but this generally leads to additional blocking and shading losses. This also indicates that closer heliostats will inherently have a higher intercept efficiency than heliostats further away from the tower.

The second term accounts for heliostat errors, which include both the surface and tracking errors. This term can be thought as being indicative of the build quality of the heliostat and can be improved through using more material, higher tolerances, more accurate control or higher accuracy drives. These improvements do, however increase the heliostat cost in $\$/\text{m}^2$. As shown in the next chapter, the second term also lessens as incidence angles increases, ϕ. This effect is not accounted for in the HFLCAL method [68].

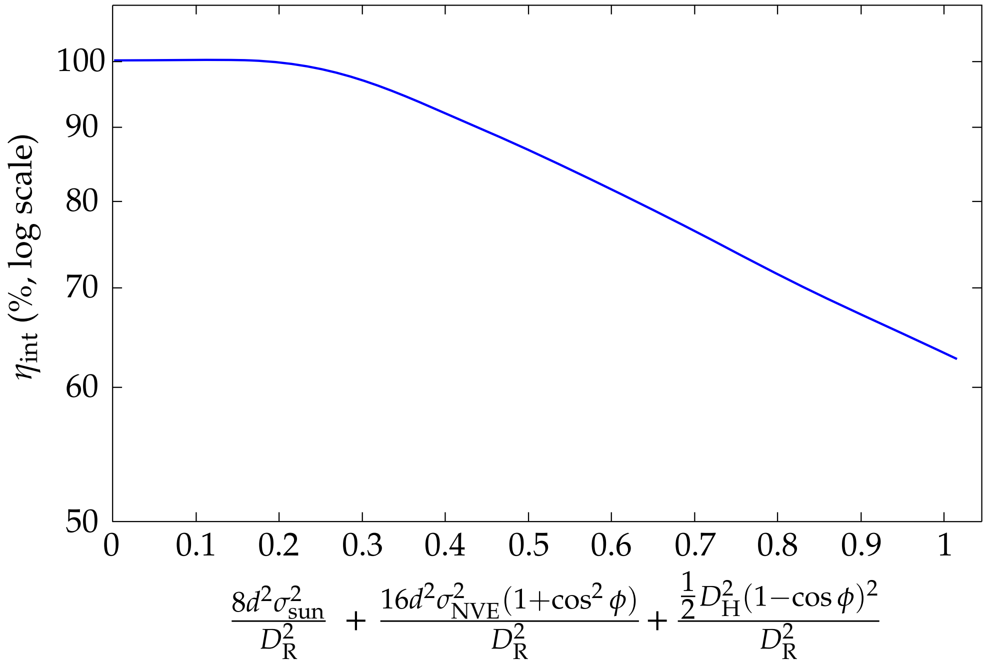

Figure 4.15: Components contributing to heliostat intercept efficiency

The third term represents the astigmatic aberration, which is the geometric dispersion due to the shape of the surface. What is interesting is that, if simplified, the term is independent of the slant range, d, as shown in Figure 4.15. Rather the term is a ratio of the heliostat's effective diameter, D_{H}, and the receiver's effective diameter, D_{R}. This implies that the astigmatism term affects all heliostats in the field equally, regardless of the distance from the tower. This means that reducing heliostat area benefits all heliostats, not only those with low focal ratios.

Astigmatism is also dependent on the range of incidence angles experienced at a certain position in the field. This term is zero for a zero degree incidence angle but increases with increasing incidence angles. The range of incidence angles cannot be manipulated, so the only way to improve the astigmatic aberration is to reduce the effective diameter of the heliostat, D_{H}. Although there are theoretical performance benefits of reducing the D_{H}, the practical and economical implications are complex.

The basic parametric function highlights the fundamentals of heliostat optics and can be used to guide heliostat field layout design. It indicates that heliostats should be close to the tower, they should be accurate, small and avoid high incidence angles.

4.7 Conclusion

The fundamental approach used in this study showed that aberrations are either path dependent or occur within a consecutive series. This finding implies that the common assumption made by convolution methods, that aberrations are statistically independent, is not strictly correct, although the practical implications of this may not be statistically significant for a large number of heliostats.

Widening of the radiance distribution appears to be dominated by three sources: the sun shape, NVE aberrations and astigmatic aberrations. Due to lack of a non-dimensional objective measure for the flux distribution, two related coefficients are proposed in this study. The COA and FDR, which relate the real image to the ideal image, offer elegant measures to illustrate and compare flux distributions and are used to show the effects of astigmatic aberrations.

The use of spherical and toroidal concave profiles reduces the image size, but they are largely dependent on incidence angle. It is shown that by increasing focal ratios, astigmatism is reduced at all incidence angles. This suggests that smaller heliostats will optically outperform larger heliostats.

Considering both the validation case and the parametric description of intercept efficiency, an analytical description of the optical aberrations proves to be valuable to understand and model heliostat optics. Further applying this knowledge in other areas, such as plant performance and economic models, could lead to additional benefit.

Part II

Integration

Chapter 5

Development of a numerical model

Previously astigmatic aberrations have only been studied analytically and the results are limited to their effects in the sagittal and tangential planes. To address these limitations, a more comprehensive method was required to investigate additional effects. This chapter outlines a Monte Carlo type ray tracer that was developed for this purpose and applies it to further study effects of the reflective surface profile.

Portions of the work in this chapter were published in the proceedings of the 2012 SolarPACES Conference [36] and have been abbreviated here.

5.1 Introduction

The ability to analyse the behaviour of increasingly complex optical systems is not typically viable with analytical analysis. Numerical methods such as ray tracing use stochastic modelling to enable highly complex systems to be evaluated. Several ray tracing codes do exist commercially [57], but it was decided that the development of an in-house Monte Carlo ray tracer would be advantageous. In-house development enabled the ray tracer to be adapted to suit different and unique applications, and its development gave further insight into heliostat optics itself. One example of this, discussed in Chapter 6, is that the ray tracer could be de-constructed, and some of source code could be utilised in optimisation algorithms to generate reflective geometries. This application, which essentially reverses conventional use of ray tracers by using a desired flux distribution to determine a suitable reflective surface, was not viable with ray tracers with proprietary source code.

This chapter does not attempt to provide new ray tracing algorithms but merely showcases an implementation of current best known methods. Because the ray tracer was written for the purposes of this thesis only, some functionality of a more general purpose CSP ray tracer has been negated.

Limitations include modelling the effects of different wavelengths of light and light refraction.

5.2 Monte Carlo ray tracing

This section introduces Monte Carlo techniques and ray tracing methods used in the ray tracer. Details of the methods are not provided since ray tracing is not a core focus area of this thesis.

A ray is a theoretical construct that represents the path of a single photon of light. Ray tracing recreates an optical condition by means of tracing individual photons of light in a simulated environment and observing the behaviour of the photons (depicted in Figure 5.1). The purpose of this ray tracer is to numerically replicate the optical interactions of light with the heliostats and to predict the resulting distribution of flux at the target aperture.

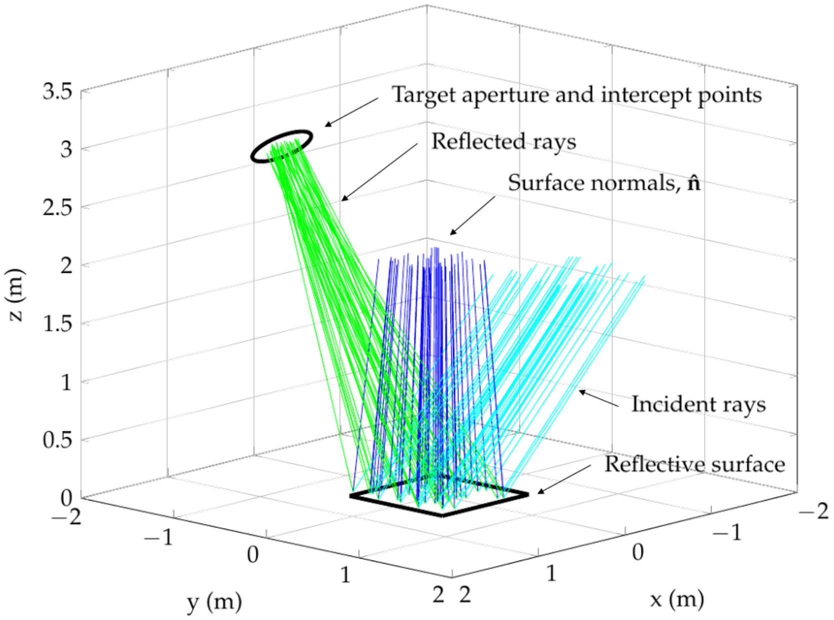

Figure 5.1: Illustrative example of the ray path and target intercept in the heliostat coordinate system

The Monte Carlo technique generates random numbers according to a given integral known as the probability density function (PDF), which describes the relative likelihood of a random variable taking a certain value [141]. By accurately defining the statistical behaviour of light with a surface, the Monte Carlo technique uses a PDF to determine the energetic and directional properties of the reflected photon. A highly realistic model can thus be generated by tracking simulated photons until they are absorbed at a final location of termination.

The collision-based Monte Carlo method is used to reduce the number of missed rays in the model. Rays originate from hit points generated on the reflective profile, and surface normals are calculated at these hit points. Errors are accounted for by manipulating the incidence ray and the surface normal vectors using PDFs. Once the surface normals and incident rays are representative, the reflected rays are determined. The incident and reflected rays are then tested for blocking and shading from nearby heliostats and the target.

Differentiation of transformed surfaces in the Euclidean space is mathematically challenging. To avoid this problem, surfaces are always dealt with in a local coordinate system using a bounding-box approach. Rays passing into or out of a bounding-box are transformed between a local and global coordinate system. Ray intercepts and surface differentiation is then simply done within the bounding-box.

5.3 Ray tracer validation

There are no standard test cases that are used to validate or compare solar ray tracers; however, recent ray tracer validations have been published: SolTrace [142], SolFast [101] and Tonatiuh [98]. SolTrace is a widely used and publicly available ray tracer developed by NREL for CSP applications.

The developed ray tracer was validated against SolTrace software [95] using several different geometries. Model results of a 16 m^2 spherically profiled heliostat at 60° incidence and slant range of 125 m are shown in Figure 5.2. After 20 000 rays, the mean power of the focal spots correlated to within 0.18 %, which is negligible considering that flux variances of 0.79 % and 0.67 % were present over consecutive iterations for the developed ray tracer and SolTrace respectively. The one area where the ray tracer underperformed was computational time. The model was approximately seven times slower than SolTrace, which can be explained by inefficient coding, the use of MatLab, which is a high-level programming language, and not making use of parallel computing.

The ray tracer was also validated experimentally and results are compared in Figure 5.3. For the validation case, a mirror was purposefully deformed to achieve a highly irregular flux distribution. The reflective surface profile was characterised using a coordinate measuring machine (CMM, see 9.4.1, p. 115), and the flux distribution was analysed using a beam characterisation system (BCS, see Section 9.4.3, p. 116). The ray tracer replicated the general shape of the image well, but it did overestimate total power by 6.0 % and peak flux by 6.2 %. This deviation can be accounted for by the 3.8 % measurement uncertainty of the BCS and the inability of the CMM to cap-

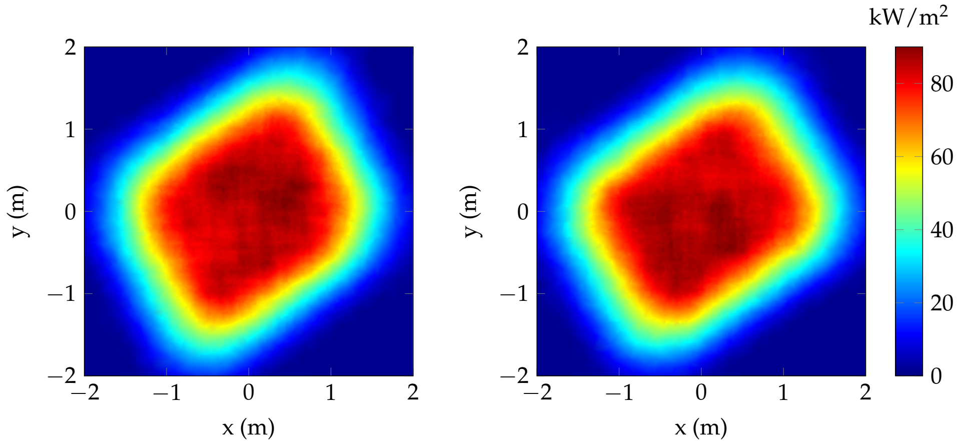

(a) Ray tracer **(b)** SolTrace

Figure 5.2: Validation of the ray tracer (a) against SolTrace (b)

ture certain surface errors given its volumetric and discretised measurement technique.

5.4 Ray interpretation

Once the ray intercept data on the target has been obtained, the data must be processed to determine the flux distribution. Each ray intercept point is specified with an x and y coordinate, and each ray has a power value. A binning process is used to determine the flux at a point on the target. Image parameters can also be fitted to the data or the flux distribution as quantifiable measures of the image.

5.4.1 The binning process

Flux by definition is power per unit area. To compute the flux at a given point, it is necessary to determine the power of the rays within a localised area or 'bin' as depicted in Figure 5.4. Consider a number of ray intercept points obtained from the ray tracer (Figure 5.4a). Bins of appropriate sizes are then allocated to the points where the flux needs to be determined (Figure 5.4b). By summing the power of the rays that fall within each bin and dividing by the corresponding area, the flux can be determined (Figure 5.4c).

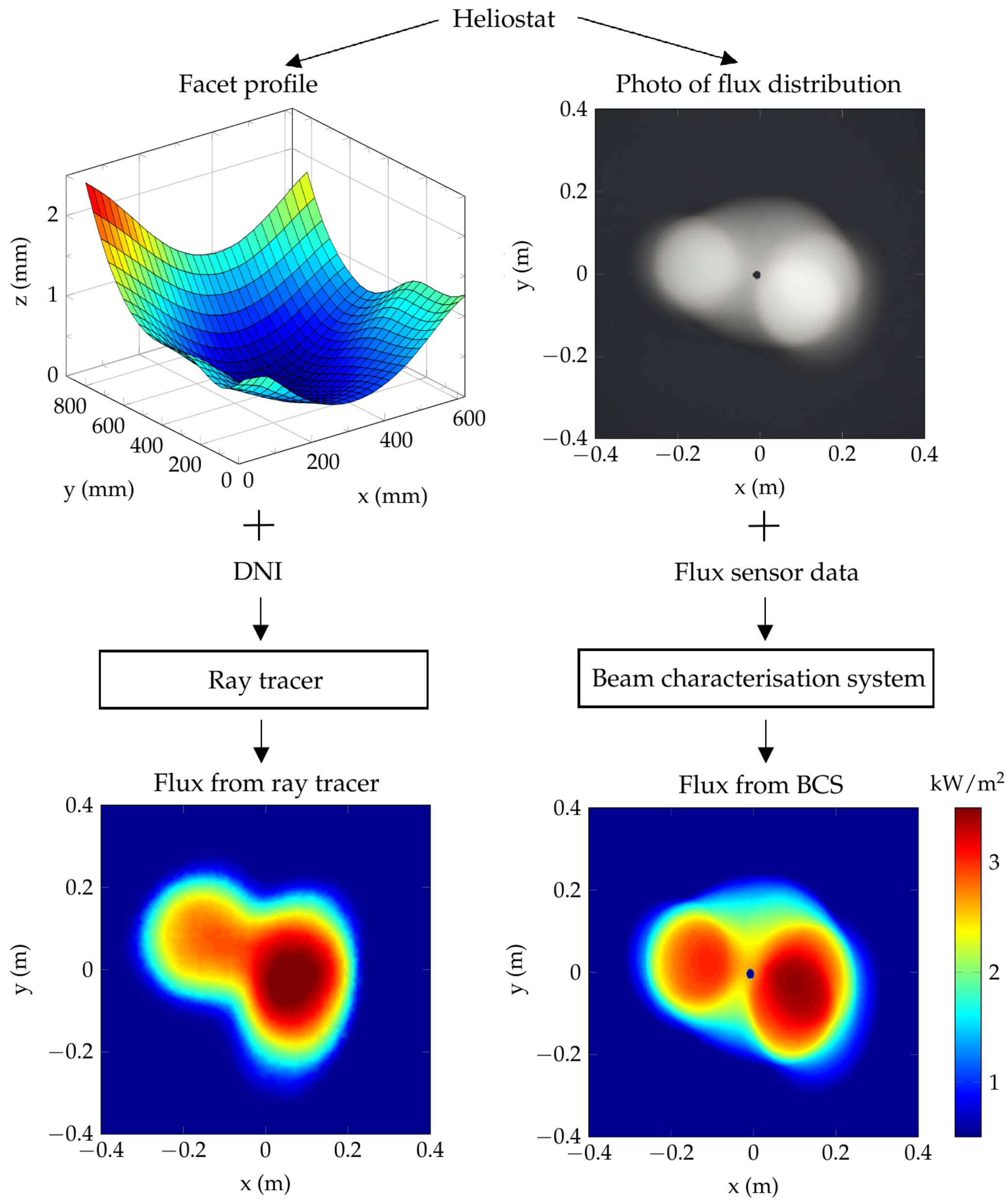

Figure 5.3: Experimental validation of the ray tracer

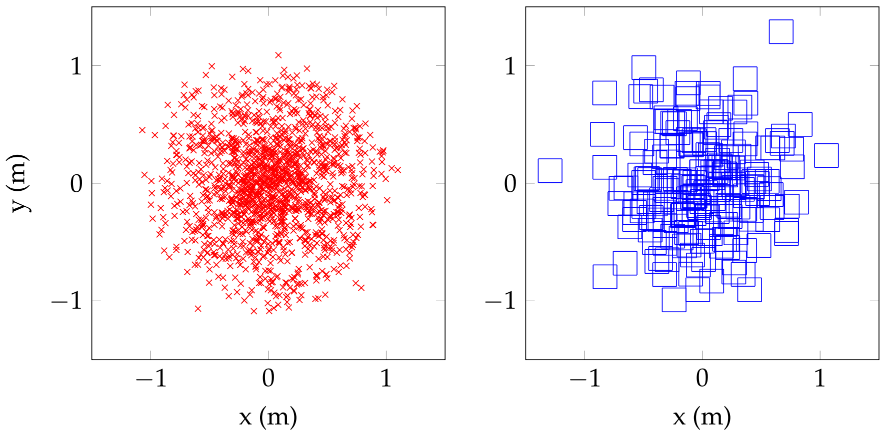

(a) Ray intercepts **(b)** Bins

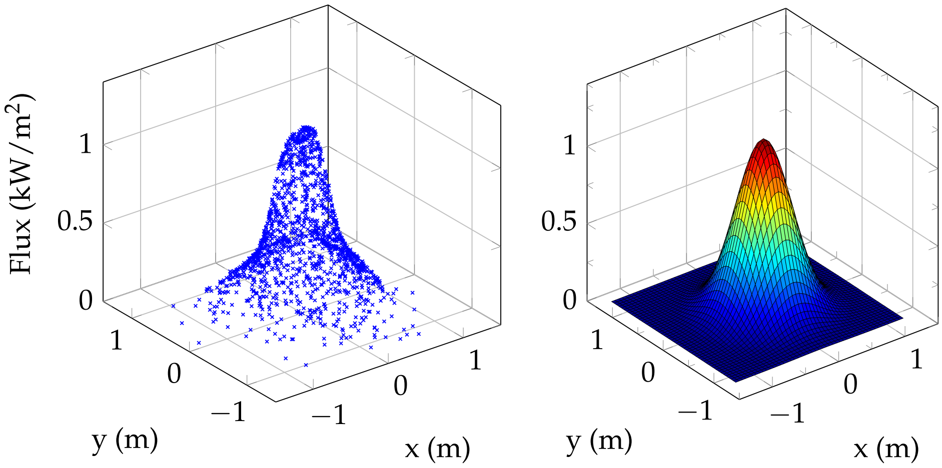

(c) Flux at each bin **(d)** Fit of a bivariate Gaussian function

Figure 5.4: An illustrative example to explain the binning process: a) ray intercept data, b) distributed bins, c) flux values of each bin position and d) a surface fit of the flux

If a bin is too small for a certain density of rays, it may give an inaccurate or null flux reading. Alternatively, if the bin is too large, some features of the flux distribution may be averaged out. This relatively simple binning process should thus also consider the resolution of the flux computation.

A grid based set of bins is typically used to cover the target area; however, user inputs are essential to ensure that appropriate resolution is maintained in the areas of interest. For the purposes of this study, the ray tracer needed to identify image trends. This in turn required that the binning process be automated without creating bias toward certain distributions.

One way to achieve adequate resolution is to use a very large number of rays. This approach is computationally expensive, and an alternative is to appropriately distribute and size the bins based on the estimated distribution of the rays. This is known as 'sampling' theory and is typically used in Monte Carlo integration to improve computational efficiency.

A statistical binning strategy is proposed where the number of bins is specified as a fraction of the number of ray intercept points. Bins are positioned and sized using the 'importance sampling' [90] technique, enabling high resolution at the centroid of the image without creating data noise in low flux areas.

5.4.2 Characterization of facet images using optical performance parameters

To evaluate the effect of a given variable on the flux distribution, a measure is required that allows two distributions to be quantitatively compared. One such measure often used is the 90 % intercept radius [31], which is indicative of the radial dimension of the image. Chapter 4, however, suggests that the image is anisotropic; thus, a set of parameters which have a correlation to the image shape is desirable. To achieve this, it is proposed that a representative flux distribution function be fitted to the data.

It is generally accepted that the flux distribution of a heliostat can be approximated using a Gaussian distribution [68; 70; 79]. To account for directional properties, a multivariate Gaussian function is further proposed as a more generalised form. The two dimensional Gaussian function is given by:

$$f(x,y) = Ae^{-(a(x-x_0)^2+2b(x-x_0)(y-y_0)+c(y-y_0)^2)} \tag{5.1}$$

where

$$a = \frac{\cos^2\theta}{2\sigma_x^2} + \frac{\sin^2\theta}{2\sigma_y^2} \tag{5.2}$$

$$b = \frac{\sin 2\theta}{2\sigma_x^2} + \frac{\cos 2\theta}{2\sigma_y^2} \tag{5.3}$$

$$c = \frac{\sin^2\theta}{2\sigma_x^2} + \frac{\cos^2\theta}{2\sigma_y^2} \tag{5.4}$$

The most noteworthy characteristic of the function is that it can be described using parameters that have direct correlation to the image dimensions. Parameters are described below and depicted in Figure 5.5b.

- x_0 and y_0, specify the location of the image centroid
- A is a flux density scaling factor
- θ accounts for the axis alignment
- σ_x and σ_y are the standard deviations of the flux density values along the new axes, which indicate the ellipticity of the image

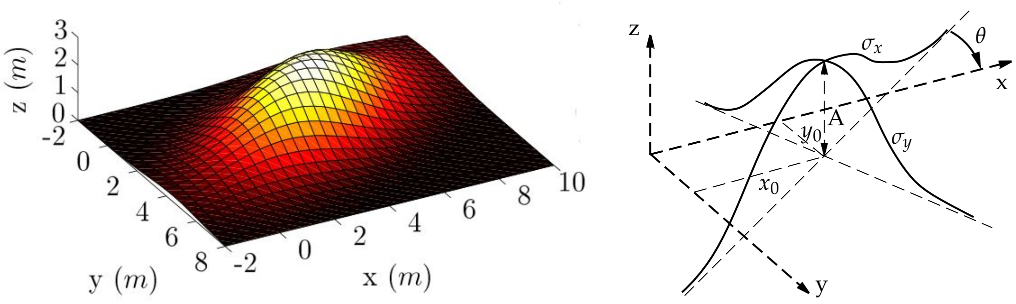

(a)

(b)

Figure 5.5: The Gaussian function and descriptive parameters

The Trust-Region curve fitting algorithm was used to fit the multivariate Gaussian function to the flux points (Figures 5.4d and 5.5a). After the Gaussian function was fitted to the data, the six fitting parameters, which are indicative of the flux distribution, were recorded as the results. It is reiterated that this function was not intended to accurately reproduce or mathematically represent the image but rather used to reduce the image to six parameters that can be compared for trend identification.

5.4.3 Characterisation anomalies

The use of the proposed statistical binning strategy resulted in a larger concentration of flux data near the centroid of the image (red dots in Figure 5.6), thereby biasing the curve fitting toward the image centroid. In the event that the image had a sharp edge, resembling a step function, the standard deviation of the function was overestimated (Figure 5.6a). This anomaly was only prevalent for low focal ratios below 5 and can thus be ignored for more general cases (Figures 5.6b and 5.6c).

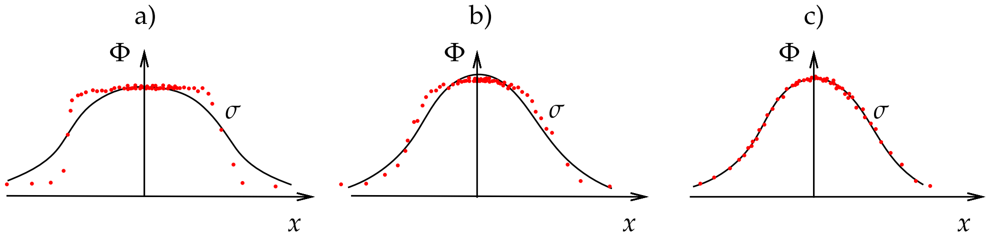

Figure 5.6: Overestimation of σ for sharp images at low focal ratios

5.5 Parameter sensitivity on flux distribution

As discussed in Chapter 4, the flux distribution of a heliostat is dependent on various optical parameters. This section further explores the sensitivity of these parameters using the ray tracer. All results presented in this section assume a single faceted ATS150 heliostat [4] at a slant range of 124 m. A low F_r of 10 was purposefully selected to showcase the combined effects of astigmatism and the relevant variable.

5.5.1 Heliostat position and orientation

The effect of the heliostat position and orientation on the image was first investigated. The image behaved as expected, and the findings are discussed below.

The slant range is found to be linearly proportional to the image size, provided that the focal length is maintained. The slant range also dictates the attenuation losses, which result in a power loss. The power of the reflected image is dependent on the cosine of the incidence angle, ϕ, and the image area is proportional to the cosine of the receiver incidence angle, ϕ_{rec}, which is in turn dependent on the field placement and receiver orientation.

The tracking mechanism defines the variation of τ. This has minimal effect for flat and spherical profiles and merely results in image rotation around the incident vector onto the receiver. The optical alignment angle does, however, influence image size if a toroidal profile is used since it influences the mismatch angle, θ, as was discussed in Section 4.5.4 (p. 38). For the remainder of this section the effects in the tangential plane are presented.

5.5.2 Tracking and surface slope errors

The influence of NVE on image was also investigated. Tracking errors simply result in a linear translation of the image on the aperture in a direction perpendicular to the axis of rotation. The accuracy of the heliostat installation has a time dependent effect on the tracking error, which can be reduced by corrective software and regular calibration [143].

SSE is dependent on both the specularity of the surface as well as the slope errors. Since the SSE defines the angular deviation of the surface normal, SSE is expected to be linearly proportional to the image dimension. SSE typically ranges from 0.3 mrad to 4 mrad.

Using the directional standard deviations a COA can be determined. Figure 5.7 depicts the COA_{tan} of a spherical facet profile as a function of SSE. Initially at low SSE values, the COA_{tan} was constant up to 0.7 mrad. After 0.7 mrad, COA_{tan} increased linearly as expected with a gradient of 0.56 COA_{tan}/mrad. This effect can be explained by SSE's initially being dominated by the astigmatic aberration of the spherical profile. This suggests that improving SSE below a certain case specific threshold may have a negligible effect on optical performance. This threshold for SSE varies according to the profile and its orientation.

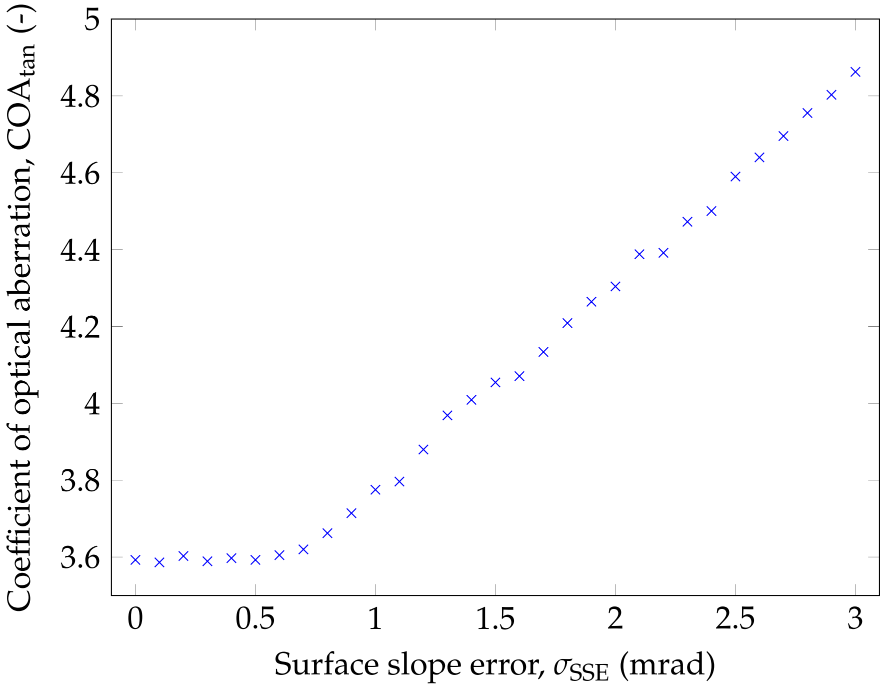

Figure 5.7: Coefficient of optical aberration for varying surface slope errors (Spherical profile with $F_r = 10$ and $\phi = 45$)

This effect was not immediately apparent, and documentation regarding this phenomenon could not be found in literature. This finding is significant in that it further confirms that the generally accepted assumption, that is that the components of beam dispersion error are statistically independent (Equations B.3), does not hold true in cases where the image is dominated by astigmatic effects.

5.5.3 Structural deformation resulting from gravity

Gravitational loading, temperature changes and wind loading cause deformation of the heliostat structure. Only the deformation of the heliostat structure due to gravitational forces (wilt) is considered here. Modelling details of the gravitational deformation are provided in Appendix E.5.3 (p. 169).

Heliostat canting is done at a specific orientation which can be considered as the no load case, and variations from this case result in either positive or negative wilt. For a more vertical orientation of the mirror rack plane, the component of the gravitational loading decreases below that of the alignment point resulting in negative wilt. Inversely, at a more horizontal orientation, the gravitational component increases above that of the alignment point resulting in positive wilt.

The effect of the gravitational loading will also be linked to the incidence angle, which is in turn directly dependent on the field position. Figure 5.8 shows a case for a heliostat that was canted off-axis at 35° and currently oriented at $\phi = 45°$. Here the ratio of structure loading to stiffness varied. For a negative loading, indicating a more vertical orientation, a minimum is reached at the point where the structure decreases its radius of curvature to match that of the current ϕ. A positive loading has the effect of increased radii of curvature creating a further image aberration. Structural deformation is again case specific and can increase or decrease optical performance depending on the heliostat orientation for the range of incidence angles.

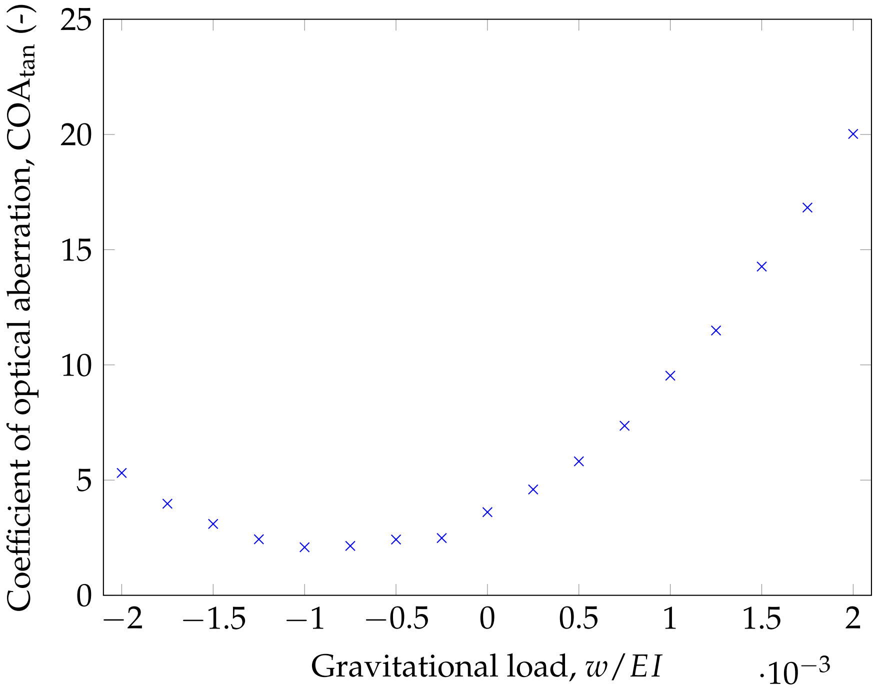

Figure 5.8: Coefficient of optical aberration for varying gravitational loading (Spherical profile with $F_r = 10$ and $\phi = 45$)

5.5.4 Profile selection

As discussed in Chapter 4, image size and concentration is largely dependent on the incidence angle, ϕ, for concave profiles. Figure 5.9 compares the COA_{tan} variation to ϕ for six facet profiles.

To obtain the theoretical ideal, a dynamic facet profile that changes shape depending on the sun position was used to obtain an aberration free image,

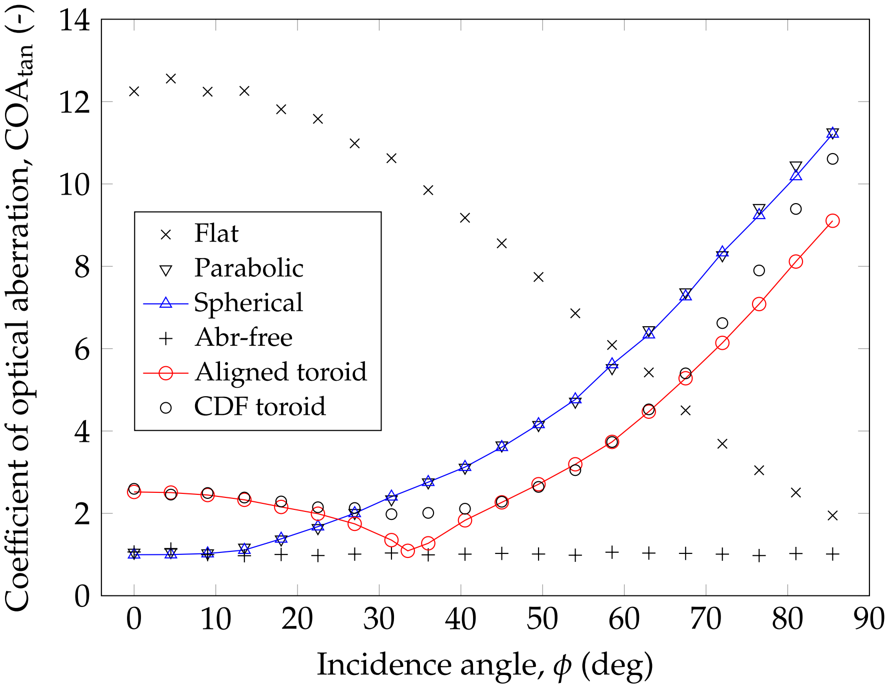

Figure 5.9: Coefficient of optical aberration as a function of the incidence angle for selected profiles ($F_r = 10$)

as specified by Landman and Gauché [144]. As expected, the aberration free facet profile maintained the ideal COA$_{tan}$ of 1.

For a flat profile, the image was largest at a zero ϕ and decreased as ϕ increased due to the cosine effect. Inversely, the spherical and parabolic profiles produce a perfect image at a zero ϕ but were susceptible to astigmatic aberration for increased ϕ as predicted in Figure 4.5.

The performances of the spherical and parabolic profiles were equal. This result confirmed the presumption that a paraboloid can be approximated as a spherical profile and validated the proof given in Appendix A.1 (p. 151).

The toroidal profile was tangentially aligned with a radius of curvature for alignment at 35°. COA was, as expected, lowest at ϕ of 35° and degraded in both directions as predicted in Figure 4.9 (p. 40). From Figure 5.9 it is clear that a toroidal facet profile of correct curvatures that remain aligned (TA tracking) performs best for the required ϕ range.

Since the outer facets of the heliostat largely define the image size, the focal length of facets closer to the heliostat centre can be varied or defocused within a certain range without affecting the overall image size. Such an adjustment would maintain the image size at increased ϕ but would increase image size at the alignment point. A centrally defocused (CDF) toroidal facet profile is proposed that gives a more constant COA over the ϕ range.

5.6 Conclusion

The implementation and validation of a ray tracer method illustrates the ability to successfully describe the flux distribution of a heliostat. This numerical method enables the analysis of complex optical phenomenon, which is beyond the limitations of the analytical methods.

Best known methods for the post processing of the ray intercept data does not seem to be well defined for CSP applications. It appears that the utilisation appropriate for post processing methods may reduce the number of rays required, which could potentially enhance computational efficiency of ray tracing methods. An automated post processing method is thus proposed that maintains adequate resolution of the flux distribution data and is able to determine descriptive image parameters used to identify flux distribution trends.

Applying this method to a parameter sensitivity study shows that improving NVE beyond a certain threshold may not provide any benefits since image is dominated by astigmatic effects. This finding implies that optical parameter improvements should be balanced, and improving individual parameters in isolation may be unproductive. This further suggests that heliostat design should address both NVE and astigmatism in high accuracy applications.

A comparison of surface profiles validates previous findings but also suggests that alternative profiles, not necessarily limited to bi-directional curvature, may provide some benefit. Such profiles are investigated further in Chapter 6.

Chapter 6

Performance benefits of unconstrained heliostat surface profiles

The components of the heliostat image resulting from astigmatic aberration of spherical and toroidal profiles are described analytically in Chapter 4. Chapter 5 suggests that some performance benefits may also result from the use of alternative surface profiles. In this chapter the ray tracer is used to determine the performance benefits of such alternative surface profiles.

6.1 Introduction

Reducing heliostat image area is non-trivial, and Chapter 4 discussed the numerous optical aberrations that result in image enlargement. Astigmatism is the dominant aberration [32], and it is known to have a major influence on the optical efficiency of a heliostat field [36; 137]. Chapter 4 showed that astigmatic aberration is dependent on the geometric profile of the reflective surface and varies with the incidence angle and the alignment angle. By realising an improved reflective surface profile, the astigmatic aberration can be minimised, resulting in improved heliostat imaging performance.

The reflective surface profile of a heliostat is made up of both the profile of the individual facets as well as the canting strategy. Since facets have to be aligned accurately regardless of the choice of canting strategy, selecting an optimum canting strategy may potentially be a cost free improvement to the optical performance [137].

Several studies have investigated different canting strategies [32; 145; 137; 146; 4; 140]. The four known canting strategies are on-axis (ON), off-axis (OFF), parabolic (PAR) and target aligned (TA) canting, and these are defined below [137].

ON - facets are aligned to produce the minimum image area when the sun, target and heliostat are collinear (spherical profile).

OFF - facets are aligned to produce the minimum image area for a specific sun position specified by canting time and date (toroidal profile).

PAR - facets are aligned to form a paraboloid stretched in the x and y axis (toroidal profile).

TA - facets are aligned to produce the minimum image area for a specific sun position on a target aligned tracking heliostat specified by canting time and date (toroidal profile).

Jones *et al.* [145] suggest that on-axis canting generally performs better on an annual basis, while off-axis canting shows superior performance only at certain field locations. They further propose the AIPWI as a figure of merit to determine the performance of canting strategies.

Kolb *et al.* [4] investigate the economic value of optical variables in the context of a 700 $\mathrm{MW_t}$ molten salt plant and conclude that canting has a significant reduction on the LCOE but that facet focussing has little impact.

Buck and Teufel [137] optimise and critically compare the four canting strategies. Their results contradict previous findings and show that off-axis canting produces a more favourable AIPWI. Furthermore, improvements are case dependent. TA was superior in all considered cases. The optimisation results of off-axis canting time are repeated in a separate study [140].

The above mentioned canting strategies all conform to a predefined profile according to ideal optics at a certain heliostat orientation or sun position. Literature has not considered alternative canting strategies, and profiles with alternative shapes may result in favourable performance characteristics.

Without limiting the profile to a predefined geometry, a method to generate an unconstrained profile is desired. Such a method is presented here. An optimisation algorithm optimises the profile gradients discretely; after which a photoclinometry technique is used to create a profile without any predefined structure. Results are then compared to the on-axis canting strategy.

6.2 Methodology

An optimisation study is performed on the heliostat reflective surface profile to obtain improved performance characteristics. The ray tracer described in Chapter 5 was used for this study. The optimisation requires both a set of input parameters as well as an objective function to reach and quantify an optimum. These are introduced here.

6.2.1 Defining the input variables

The input variables to the optimisation model are in essence very basic, and the single variable is the surface profile. Still, this very simple problem is complicated in that the surface profile must be described mathematically.

Since the surface profile exists in the Euclidean space, the intuitive solution would be to define the surface by a parametric equation with two space parameters, $z(x, y)$ as suggested by Landman and Gauché [144]. The optimum profile at the start of the optimisation is, however, unknown. Since a parametric equation relates variables through its predefined structure, such an equation would limit the surface to the structure of the parametric equation. Instead, a method is needed to describe an unconstrained surface mathematically, which itself requires an infinite number of variables to be introduced into the equation.

It is reiterated here that increasing the number of variables results in an exponential growth in computation time. Such a problem may easily become unsolvable due to this impracticality.

Frankot and Chellappa [147] propose a photoclinometry technique that eliminates the presumption that a surface is defined by an equation, thus providing a solution that minimises the number of variables. Previously, the approach was to alter the surface as the variable vector and then analyse the effect on the optics iteratively. The Frankot and Chellappa algorithm allows the process to be reversed so that the surface can be generated using the surface normals. This is possible by describing the surface as an integrable derivative of the surface itself.

The approach, illustrated in Figure 6.1, allows the analysis of only the surface normals per iteration. After the optimisation process is complete, a surface is generated from the surface normals. At this point a parametric equation can easily be fitted to the surface. The process is illustrated in Figure 6.1.

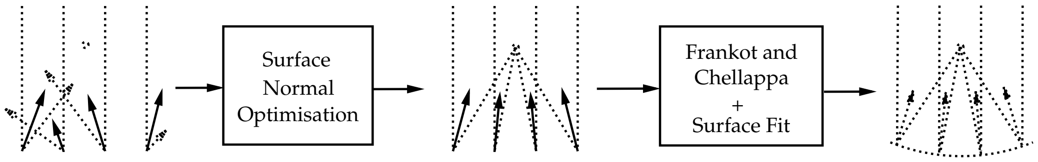

Figure 6.1: Vectors are generated on a planar surface. Each surface normal vector is then optimised individually accoridng to an objective function. Based on these normals a surface can be generated.

The advantage of this approach is that the surface derivative, which defines the surface normals and optical performance of the profile, remains the primary area of focus, leaving the profile as merely a secondary result of the optics. This approach also allows the opportunity to optimise individual points or areas on the heliostat for certain objective functions through discretization without the loss of smoothness or continuity.

The process no longer requires variables to define the surface; rather surface unit normals, requiring only two variables, can be dealt with individually at discretized points. The unit normal can be defined simply by the displacement of the x and y components of the unit vector. Because fewer unknown variables have to be defined, the optimisation method becomes less computationally expensive.

Vectors are generated on the reflective xy plane using regular sampling. One concern was that the planar generation of the normals may not be representative. Since the focal length is much larger than the profile elevation, $d \gg z$, it was assumed that the profile elevation has negligible effect on the optics of an infinitesimal point. To validate this assumption, the surface normals to be optimised were generated on both the reflective plane and a sphere of correct focal length. No discrepancies in the results were observed.

6.2.2 Defining the objective function

The objective function serves the purpose of evaluating the variable vector in question and provides a performance measure in the form of a single number. The choice of objective functions is limitless, and any desired effect can be incorporated into the objective function. However, since the surface is generated discretely, the objective function must be able to evaluate the performance of an infinitesimal point on a heliostat. This performance measure will be minimised through the optimisation process. In addition, the objective function must be computationally efficient and will be evaluated many times during the optimisation process.

Literature on facet canting methods have considered the AIPWI as the most appropriate figure of merit because of the direct tie to plant performance and economics [137; 148]. AIPWI is defined as the annual amount of solar radiation that intercepts the receiver aperture divided by the annual amount of radiation that arrives at the receiver and is thus solely a percentage measure of annual spillage losses. AIPWI considers only intercept effects, and although a high AIPWI is a requirement for efficient heliostat performance, other effects such as cosine effects can result in a heliostat with high AIPWI to perform poorly [137].

Using an annual performance measure such as AIPWI as the objective function will require a ray tracer to be incorporated into the objective function evaluation. This approach was used by Buck and Teufel [137] but required the use of ten million (10^7) rays per iteration. This approach is not practical for an unconstrained profile which will require numerous iterations.

A computationally inexpensive solution was to rather evaluate performance by considering the axis of the reflected cone from the infinitesimal point on the heliostat. By computing the radial distance from the ray intercept to the target centre, d_i, an objective function could be defined according to the ray distribution on the aperture. Objective functions are discussed with each resulting profile in Section 6.4.

The constraint penalties are also specified to ensure that the normals do not drift from the feasible region, avoiding unnecessary computation and indirectly reducing computation. The initial value of the normal was given as the equivalent normal of a spherical profile. Constraints were specified as an angular deviation from the initial value.

6.3 Validation

To validate the method proposed in this chapter, results were compared to the study by Buck and Teufel [137] (MIRVAL) in Figure 6.2. Although the geometry could be replicated, the DNI data for the results were unknown and sourced from the Plataforma Solar de Almería (PSA). The model shows good correlation even though different solar data inputs were used. Root mean square variations of 1.5 % and 2.1 % were obtained for positions 30° and 90° north of east at distances of various tower multiples, R.

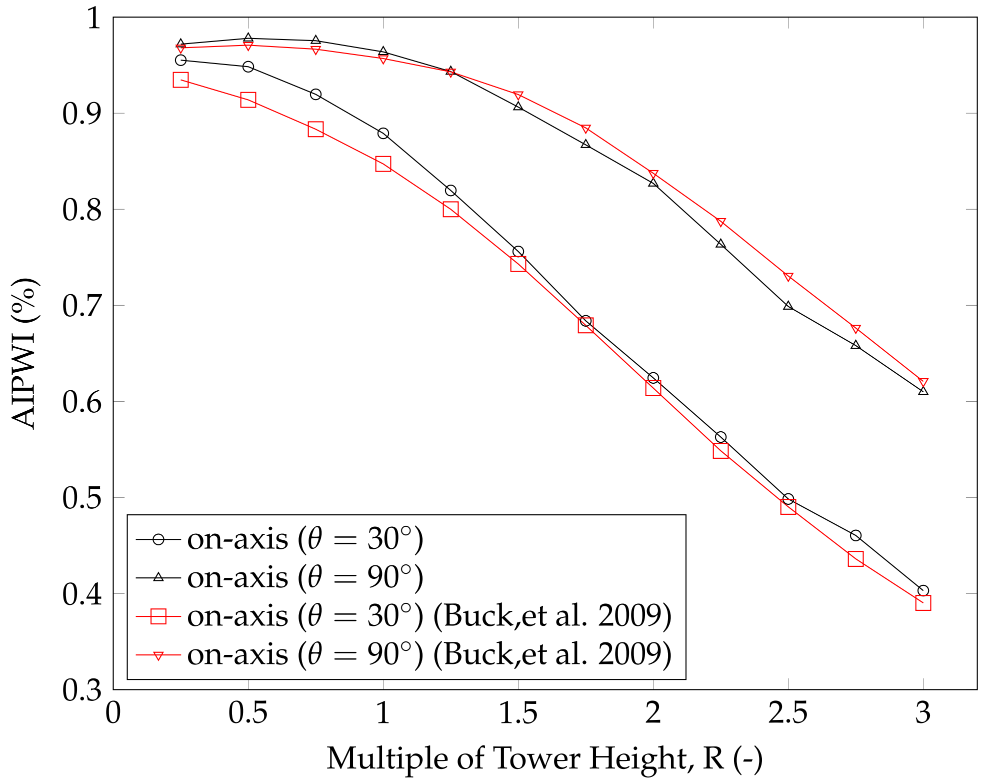

Figure 6.2: Variation of flux density from the ideal for various focal ratios of flat profiles

6.4 Results

For the sake of comparative purposes, the plant specifications, heliostats and heliostat placements were the same as those used by Buck and Teufel [137]. The results considered the H16 and ATS150 heliostats in both a 100 kW_e and 100 MW_e plants. The heliostats were placed at a given angle, θ, north of east and at a distance equal to a multiple of the tower height, R, from the tower base.

6.4.1 Effect of profile variation on annual imaging

The first optimisation case considered the H16 heliostat, with a single profiled facet, at 60° and R of 3 for the 100 kW_e plant. A least squares approach was taken where the objective function was penalised by the annual sum of d_i^2 and additionally penalised at high DNI and low incidence angles.

$$f(d) = \sqrt{\frac{\sum_n^i d_i^2 I_i \cos\phi_i}{\sum_n^i I_i \cos\phi_i}} \tag{6.1}$$

The resulting surface was toroidal, however, the toroid did not conform to the curvatures of the paraboloid side wall as given in Equations 4.22 and 4.23 (p. 41) and thus could not be obtained by off-axis or parabolic canting strategies.

The annual flux distribution on the receiver aperture was compared to that of a spherically profiled heliostat. As seen in Figure 6.3, the peak annual flux was increased by 10.6 %, resulting in an AIPWI increase of 2.1 %. The increase in both annual flux distribution and AIPWI confirmed that the optimisation algorithm creates a desired profile according to the objective function.

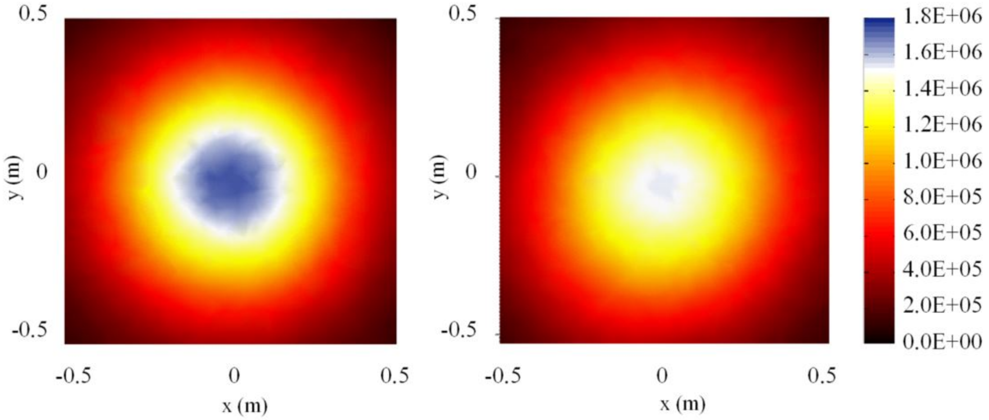

Figure 6.3: Sum of hourly flux distribution on the receiver aperture for 2012 (a) optimised profile and (b) spherical profile

6.4.2 Optimisation for AIPWI

AIPWI is considered the figure of merit for heliostat performance. Using the least squares approach, AIPWI values were again found for the H16 heliostat canted according to the optimised profiles; hereafter referred to as unconstrained canting (UC). UC showed AIPWI improvements of up to 3.5 % for the same configuration above that of on-axis canting, as shown in Figure 6.4.

UC shows significant improvements above the optimisations of Buck and Teufel [137] for $R > 1$, which can be accounted for by the fact that the canting strategy used by Buck and Teufel [137] is limited to a predefined profile. UC does, however, result in a decrease of AIPWI for heliostats closer than one tower length.

The results showed higher improvements in the northern part of the field ($\theta = 90°$), while in the more eastern location ($\theta = 30°$), lower improvements could be achieved. This was found to be due to the higher variance of τ in the eastern and western sections of the field. τ dictates the alignment of

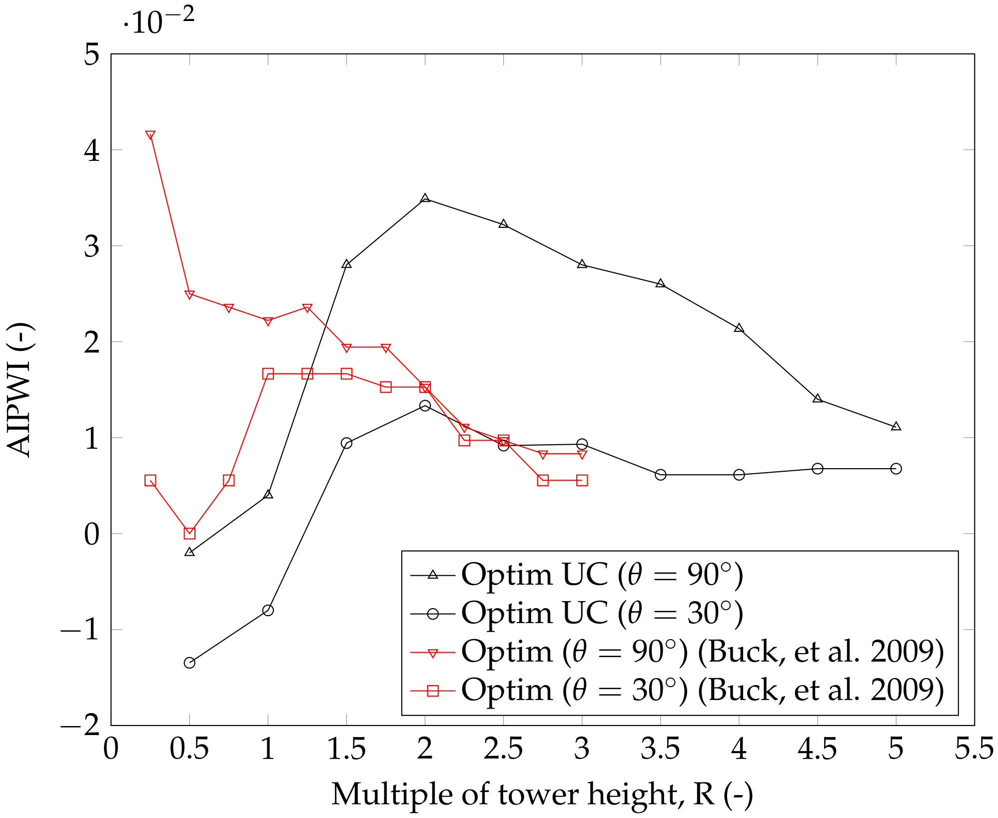

Figure 6.4: Improvement in AIPWI of UC above on-axis canting

the toroid as discussed previously in Section 4.5.4 (p. 41). If a high variance is present, the profile tends towards a spherical profile. However, if τ has a lower variance, the profile is able to create a toroid with the optimum curvatures for the range of τ and incidence angles. For TA tracking, τ is constant; this resulted in an absolute increase in average AIPWI of 7.6 % and 6.5 % for 90° and 30° with a range of R respectively.

At high R, improvement is also reduced. Increased R results in increased focal ratios, F_r, of nearly the same magnitude. FDR was previously shown to tend toward the ideal as F_r is increased. This thereby reduces the astigmatic aberration and capacity for improvement.

6.4.3 Profile flexibility

Up to this point, only the 100 kW$_e$ plant with a small cavity receiver has been considered. The 100 MW$_e$ plant with a large external receiver and ATS150 heliostats show significantly different behaviour. Here the receiver is relatively large resulting in an AIPWI of 1 for $R < 4$, as shown in Figure 6.5. Optimisation for this scenario resulted in AIPWI increases of <0.3 %.

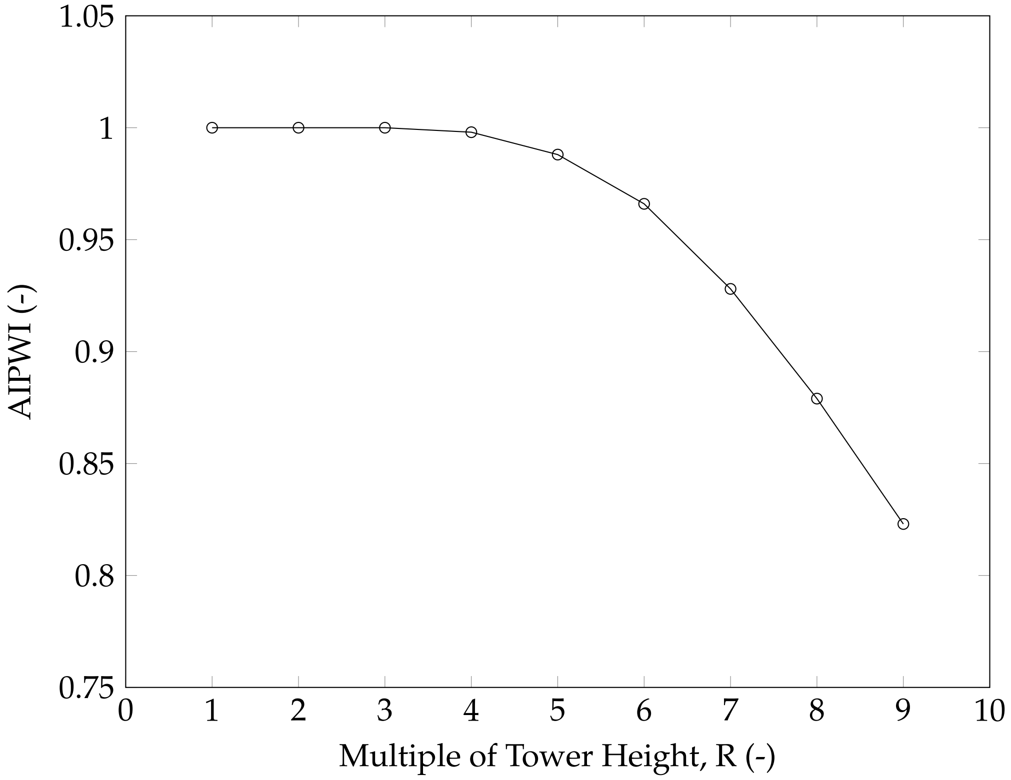

Figure 6.5: AIPWI for a ATS150 heliostat in a large system

Since all heliostats, for the $100\,\mathrm{MW_e}$ plant, located within $R < 4$ will have no annual spillage losses, the question can be raised as to whether the profile of these heliostats can be altered to a certain degree whilst not affecting the AIPWI. By defining an objective function where a large penalty is given for missing the aperture but that simultaneously favours the edges of the receiver aperture, the 'worst case' profile can be obtained, as shown in Figure 6.6.

$$f(d) = \sum_{n}^{i} \begin{cases} -d_i^2 I_r & d_i \leq r_{aperture} \\ d_i^2 I_i & d_i > r_{aperture} \end{cases} \tag{6.2}$$

In Chapter 4 it was shown that the image size is dependent on the F_r, and increasing the F_r decreased the COA. An indirect conclusion can thus be drawn that the outer edge of the profile results in the edges of the image. Since the image generally experiences aberration and assuming that the flux distribution within the limits of the heliostat image is irrelevant, SSE can be relaxed nearer to the centre of the heliostat without affecting image size. This affect is observed here.

The central section of the resulting profile is insensitive to spillage caused by astigmatic effects and, therefore, does not conform to a toroidal pro-

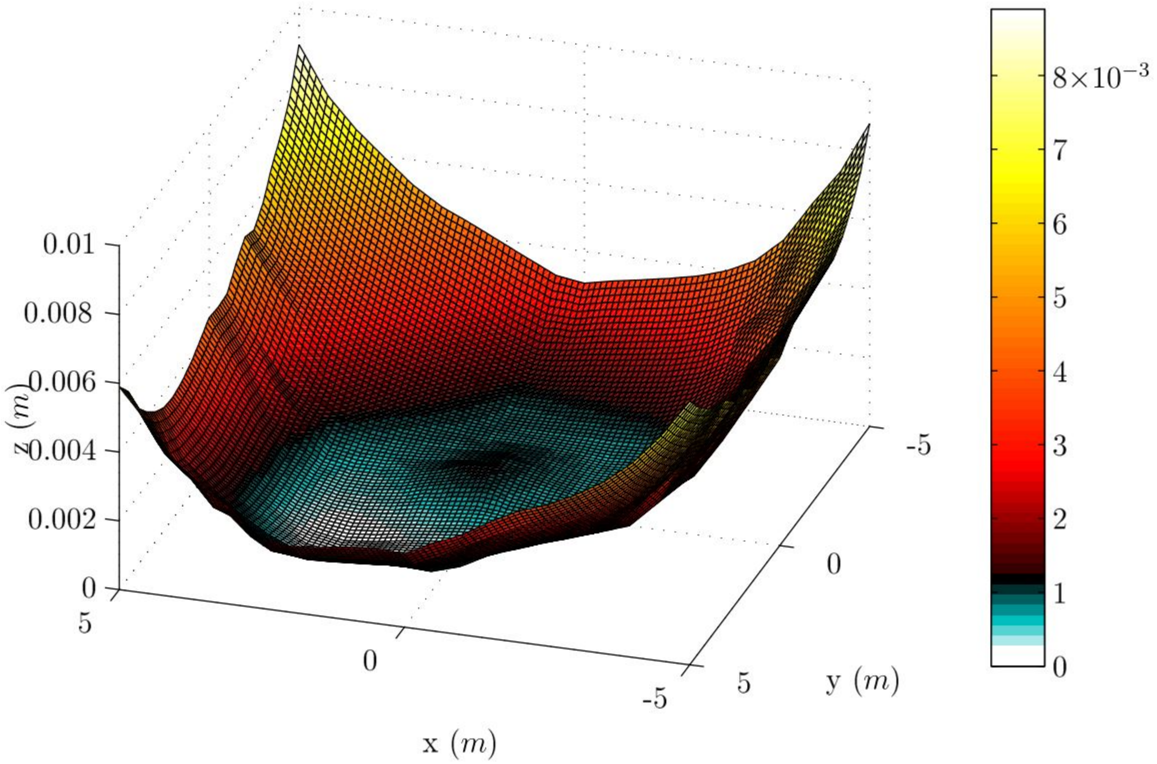

Figure 6.6: 'Worst-case' profile which maintains an AIPWI of 1

file. The edges of the profile do, however, still conform in order to reduce astigmatic aberration to within the required aperture.

6.5 Conclusion

A novel method using ray tracing methods and an objective function to generate reflective surface profiles is implemented. Canting strategies obtained using this method is shown generally to outperform the state of the art (constrained to a predefined bidirectional curvature) by achieving increases in AIPWI of up to 3.5 %. The largest improvements were for TA tracking type heliostats where average AIPWI increases of 6.5 % and 7.6 % are found. The findings suggest that performance improvements using optimised canting strategies are limited and typically only significant in cases with low F_r, low variation in τ and small receiver apertures.

The study also illustrates how astigmatic affects increase with the radial distance from the heliostat pivot point. The edges of a heliostat are shown to be more prone to spillage than the centre, and the centre of the heliostat is shown to be less sensitive to NVE losses than the edges. This implies that smaller heliostats may have less stringent NVE requirements than larger heliostats with the same optical performance requirements.

Chapter 7

Incidence angle effects on circular Gaussian flux density distributions for heliostat imaging

Chapter 3 highlighted the need for an accurate and computationally efficient method to determine the flux distribution of a heliostat. Analytical methods which assume a circular Gaussian flux distribution are used for this purpose and can be considered to be the state of the art. Inaccuracies of these methods are documented and apparently are not well understood.

In this chapter, methods that assume the circular Gaussian flux density distribution assumption are evaluated. An incidence angle phenomenon is identified as a reason for these inaccuracies, and a modification to the method is proposed.

This work has been published in the Solar Energy Journal in 2016 and is presented here as an article. This chapter is substantially a reproduction of the publication [149], and only minor changes have been made. This chapter contains some repetition, but it has intentionally not been removed to maintain the coherence of the argument.

7.1 Abstract

Circular Gaussian distribution methods are used in certain applications to determine the flux distribution of central receiver systems. Although the method is computationally inexpensive, some assumptions bring the accuracy of the results into question. This paper addresses the confines in which acceptable accuracies are maintained. Flux distributions of an implemented HFLCAL-type model and a ray tracer were compared, and deviations of up to 20 % were found in cases where both high incidence angles and high normal vector errors are present. The deviations resulted from the circular Gaussian distribution method not accounting for the shortening of the minor axis of the elliptical image. A modification is proposed that incorporates the effect of the incidence angle into the beam quality and tracking error terms. The modification corrects for the deviation, has negligible computational expense and is shown to be robust. In a case study of a commercial central receiver system, accuracy of the flux distribution was improved by up to 16 %.

7.2 Introduction

Flux distribution (FD) models of varying accuracy and efficiency are used in the design, optimisation and operation of central receiver systems. The accuracy of a FD model improves as more variables are taken into account, but as the model complexities increase, the model becomes more computationally expensive. Computationally efficient models make assumptions that simplify the computation of the FD. Although these assumptions attempt to represent realistic scenarios, they introduce uncertainty. Several analytical models, such as UNIZAR [70] and HFLCAL [68], rely on the assumption that the FD from a heliostat is normally distributed and that beam dispersion errors are statistically independent [81]. Full use of these models can be made by pushing the boundaries of their applications, but the confines of acceptable accuracies must be quantitatively known beforehand.

Numerous models that determine the FD are reviewed by Garcia *et al.* [29]. Convolution methods (also known as cone optics) use the convolutions of Gaussian distributions corresponding to various error sources to calculate an error cone. In reality, the FD over a planar image will be closer to an elliptical Gaussian distribution [81; 150]; although the image is commonly modelled as a circular Gaussian distribution (CGD) to further reduce the computational expense [29].

Typical applications for convolution methods are field layout optimizations and plant performance estimations. As Garcia *et al.* [29] point out, "the greatest errors observed on annual performance of a central receiver system do not come from the optical model but from the other component models (turbine, storage...)". For this reason the inaccuracy of convolution methods has not been much of a concern in the past. Recent applications, specifically looking at obtaining an instantaneous FD, require more from convolution models. These applications, such as aiming strategy optimisation, require higher accuracies and inexpensive computational times. One such model, a software tool for Heliostat Field Layout CALculations (HFLCAL), has been used in aiming strategy optimization in various publications [6; 76; 77] and was chosen as the representative convolution method for the purposes of this paper.

Some inaccuracies in the CGD method's prediction of the FD have been documented, but the reason for these inaccuracies apparently is not well understood [6; 76; 77; 31]. Schwarzbözl *et al.* [68] validate the method for collinear cases and suggest that the method is inappropriate for detailed FD analysis. This raises the question, whether its increasing use for the analysis of FD is in fact appropriate. It is essential to know the confines in which acceptable accuracies are maintained to ensure validity of the method's results. This study aimed to investigate the validity of the CGD method.

In this paper, an interpretation of the HFLCAL method was implemented, and the resulting FD was compared to that of a ray tracer with common input parameters. Substantial deviations were observed in cases where both high incidence angles and normal vector errors are present. This paper investigated the reasons for these deviations and found there to be a non-astigmatic aberration of the image that result from surface normal vectors at increased incidence angles. The deviations were due to the CGD method not accounting for the shortening of the minor axis of the elliptical image with increasing incidence angles. An alteration to the computation of the beam quality term and tracking error term are proposed to correct for the deviations. The correction factor in the proposed modification has been used previously [70], but it does not appear in HFLCAL [6; 76; 77; 31], and to the authors' knowledge, an understanding of the implications of the term is not in the public domain. The meaning and sensitivities of the proposed alteration are provided in sections 7.4 and 7.5.

7.3 Evaluation method

The interpretation of the CGD method used in this paper (HFLCAL) is described in detail in Appendix B. Readers unfamiliar with HFLCAL are encouraged to read Appendix B first to ease the understanding of the terms and variables referred to in the remainder of this paper.

The inaccuracies of the CGD method were quantified by comparing it to the SolTrace ray tracer [142], which is able to determine the FD on the receiver aperture in detail [29]. The modelled system was simplified as much as possible to isolate the elementary deviations between the CGD and the ray tracer. A general case was intentionally chosen to allow the results to be extrapolated to larger and more complex systems.

An objective measure was required to compare the CGD method to the ray tracer. The CGD is defined by a single standard deviation, σ_{CG}. A logical choice then is to calculate a comparative standard deviation value, σ_{RT}, from the distribution of the ray tracer's final ray intercept points.

The FD of the ray tracer is generally elliptical [81; 150]. Guo and Wang [81] show that the square mean of the major and minor axes of an ellipse is the most appropriate way to reduce an elliptical FD to a single radial dimension. To obtain σ_{RT}, the bivariate distribution of the ray intercept data is calculated. First the covariance matrix of the intercept data is determined on the intercept plane. The diagonal values of a covariance matrix contain the variances of the intercept data in both the x- and y-axes, and the square mean of the variances result in a radial standard deviation (Equation 7.1). Since the square mean is computed the rotation of the ellipse has no effect, and the resulting radial standard deviation is constant for any orientation of the ellipse.

$$\sigma_{\mathrm{RT}} = \sqrt{\frac{\sigma_{\mathrm{x}}^2 + \sigma_{\mathrm{y}}^2}{2}} \tag{7.1}$$

Both the σ_{CG} and σ_{RT} form comparable objective measures representing the radial FD of the images of the CGD method and ray tracer respectively. Now that the CGD method can be evaluated against the ray tracer, individual error sources must be varied to observe in which cases the CGD method would deviate from the realistic scenario, which is represented by the more accurate ray tracer.

7.4 Evaluation and improvement of method

There are numerous parameters that influence the FD of a heliostat. Key parameters were selected and varied to look for instances where the results from the CGD method deviated from that of the ray tracer. The most significant deviation occurred when both high normal vector errors and high incidence angles were present. Section 7.4 presents and discusses the results obtained and proposes a modification to take this discrepancy into account. Section 7.5 discusses determining factors for when the deviations will occur as well as what the implications are as a result of the deviations. Finally, an explanation of how the proposed modification was implemented and tested in a case study is presented in section 7.6.

7.4.1 Initial assumptions

The parameters that best illustrate the deviation discussed in this section were initially assumed and are provided in Table 7.1. The generalised analytical method was used to describe the results, and values were adapted to represent more realistic cases in sections 7.5 and 7.6.

A single AZ tracking heliostat with no blocking or shading was considered. To eliminate the effect of the aspect ratio, a circular heliostat aperture was assumed. The heliostat was placed at the origin and the target was situated vertically above it at a slant range, d, of 100 m. The focal length of the heliostat, f, was assumed to be equal to the given slant range, and a focal ratio, F_{r}, of 100 was initially assumed. The plane of the target aperture was then set to face the heliostat. Apart from the translation of the image, tracking errors have no influence on the FD of a single heliostat and, therefore, were ignored. The sun's position could be varied to achieve the desired incidence angle, ϕ. Adequate convergence of the ray tracer model was achieved with 100 000 rays.

Table 7.1: Initial assumptions

Item	**Value**
Focal ratio	100
Heliostat aperture	circular
Pylon height	0 m
Reflectivity	100 %
Tracking method	Azimuth Zenith tracking
Focal length	Slant range
Heliostat location	[0, 0, 0]
Target centre	[0, 0, 100]
Target orientation	[0, 0, -1]
Sun shape	Kuiper ($\beta_K = 2.2$, $\alpha_{disc} = 4.65\,\text{mrad}$)

7.4.2 Incidence angle and normal vector error

Before considering the results in detail, the two variables responsible for the observed deviation are defined and discussed here.

The first variable is the incidence angle, ϕ, which is simply the angle between the incident ray and the surface normal at the point of reflection (depicted in Figure 7.3a). The two major implications of increased incidence angles are cosine losses due to the projected area of heliostat decreasing (Equation B.2) and the increased image spread resulting from astigmatic aberrations (discussed in Sec. 7.5.2).

The second variable is the normal vector error, that is, the error by which the surface normal vector deviates from the intended ideal. Normal vector errors fall into one of two categories: Surface Slope Errors (SSE) and Tracking Errors (TE).

SSE include local imperfections in the reflector surface, deformations or sag of the surface, canting of the heliostat, etc. TE are the pointing errors of the drives, backlash and structural deformations. Both are normally distributed, but the two errors have very different implications. For SSE, each point on the reflective surface deviates independently; while for TE, the entire reflective surface deviates around the two tracking axes. In large fields with numerous heliostats, TE behave the same as SSE because of the central limit theorem. For the purposes of this paper, only SSE are considered.

SSE are more accurately defined as the isotropic Gaussian distribution of the angular deviations of the surface normal vectors from their ideal locations with the angular standard deviation given by σ_{SSE}. The effect of SSE on the image for a collinear case ($\phi = 0$) is plotted in the published validation case of HFLCAL [68]. Linear agreement is seen at a larger SSE where the effect dominates the sun shape. This finding agrees with that of Pettit *et al.* [73] who show that agreement of the images will occur for cases where $\sigma_{\text{tot}} \geq 2\sigma_{\text{sun}}$.

7.4.3 Initial results

Up to this point only collinear geometries have been considered, but in reality a perfect collinear situation ($\phi = 0$) will practically never exist since the heliostat will be shaded by the receiver. Here, the results were evaluated for SSE at realistic incidence angles. For the general case provided in Table 7.1, which utilises the Kuiper sun shape [69] and a σ_{SSE} of 2.24 mrad, the incidence angle was varied. These results are shown in Figure 7.1. Although the CGD model correlates with the ray tracer at low incidence angles, results show large deviations of up to 20 % for the case at increased incidence angles.

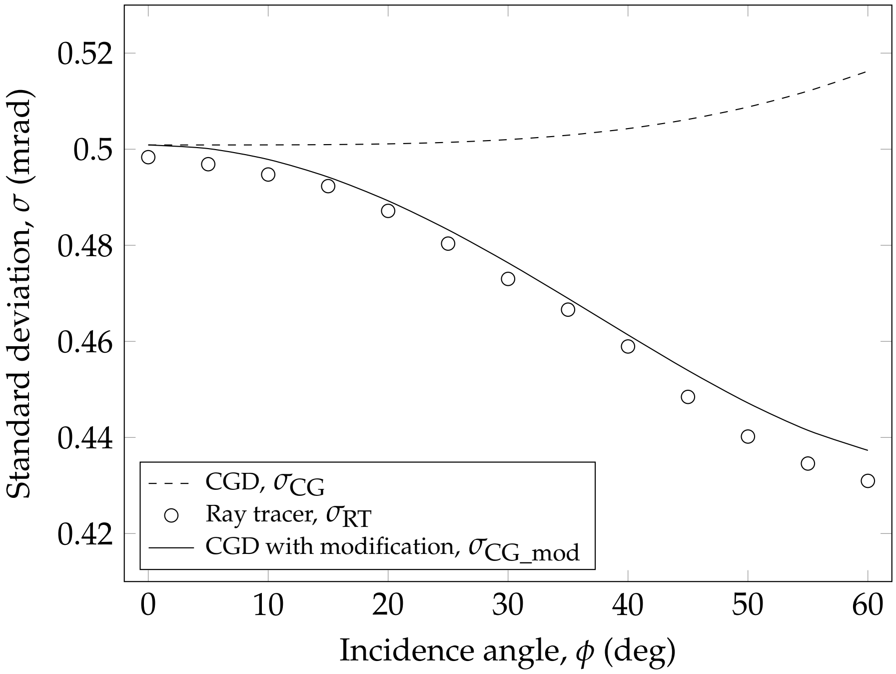

Figure 7.1: Standard deviation of the flux distribution for various incidence angles (σ_{SSE} = 2.24 mrad)

For a spherically curved heliostat where the focal distance equals the slant range, the width and height of the image increase at the same rate [32]. Thus, at increased incidence angles it is expected that the astigmatic aberration increases the image area and, therefore, the standard deviation. This increase due to astigmatic aberrations is observed for the CGD method in Figure 7.1. The contrary, however, is observed in the ray tracer, which shows a reduction in the standard deviation for increased incidence angles. The overestimation of the beam dispersion error results in conservative predictions for the power entering the receiver, but this also implies underestimating the FD, which is particularly important for applications such as aiming strategy optimisation. This deviation may be the cause of the inaccuracies reported in the FD of the CGD models [6; 76; 77; 31].

Upon investigation, it was found that the deviation was not caused by astigmatic effects but rather by the bidirectional reflectance distribution function resulting from the presence of SSE's. Figure 7.2 shows the image variation for both increasing incidence angles, resulting in increased astigmatism, and increased SSE. Initially, at low incidence angles, the images are circular as expected. For a SSE of 0 mrad the image size increases radially with increasing incidence angles due to astigmatic aberrations, also as expected. However, at the higher SSE of 5 mrad the image becomes elliptical as the incidence angle is increased. The ellipticity of the image results in a lower radial FD and explains the decrease in standard deviation as seen in the ray tracer results. Since this phenomenon is SSE dependent, it can be concluded that astigmatism does not cause the ellipticity of the image. It should be noted that the specific case has minimal astigmatic aberration and was chosen to illustrate the phenomenon. Astigmatism is discussed further in Section 7.5.2.

To explain the ellipticity of the image, the reflected rays have to be evaluated in the sagittal and tangential planes, as depicted in Figure 7.3a. First the tangential plane is considered; this includes the sun, incident ray, point of reflection, surface normal, reflected ray and target. Since the surface normal is situated in the tangential plane, the angular deviation, σ_{SSE}, causes the reflected ray to deviate twice this angle, $2\sigma_{\text{SSE}}$ (Figure 7.3b). The dimension of the image in the tangential plane, h_{tan}, can be determined by the product of the angular deviation and the length of the reflected ray, d.

$$h_{\text{tan}} = 4\sigma_{\text{SSE}} \cdot d \tag{7.2}$$

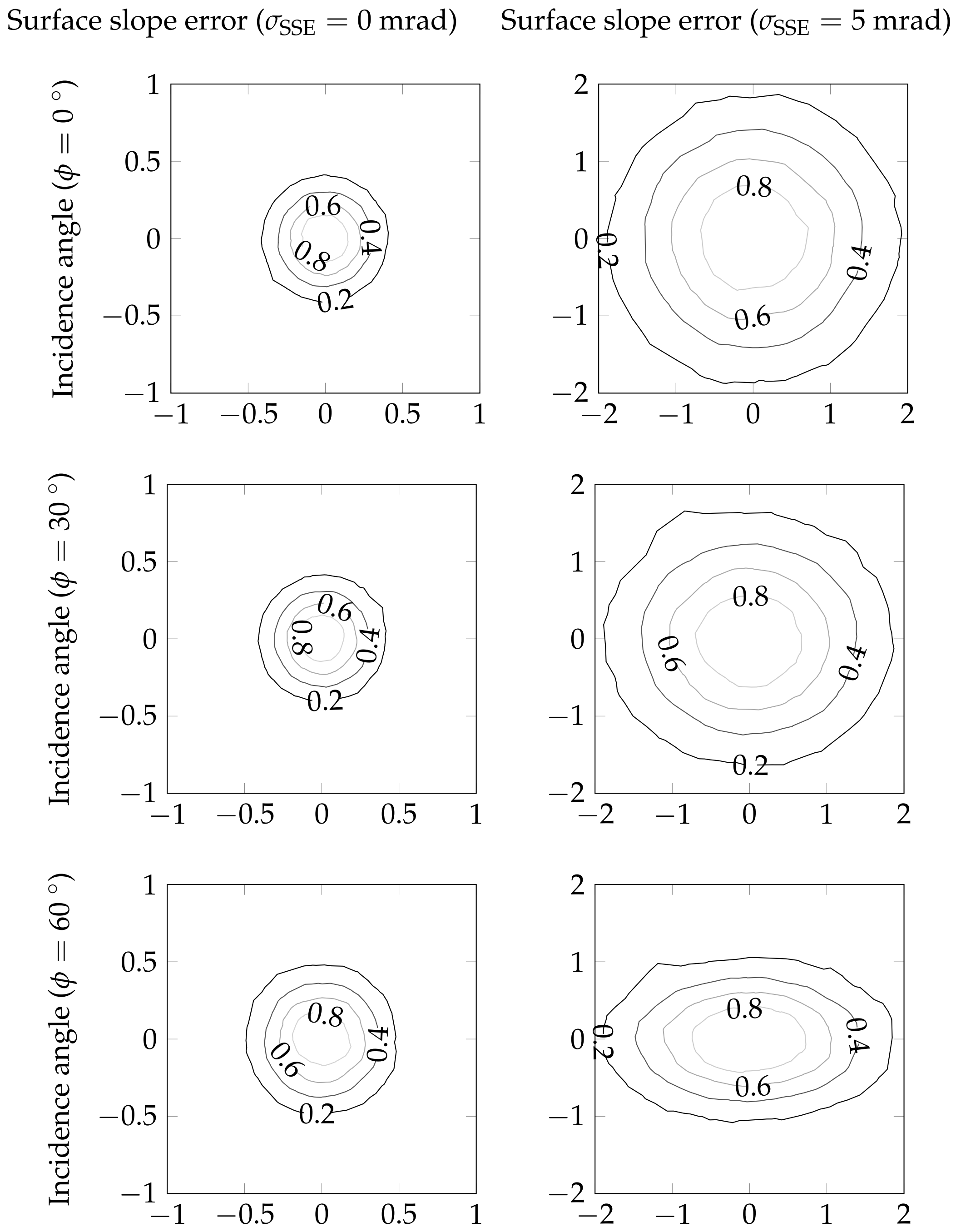

Figure 7.2: Normalised FD from the ray tracer for incidence angles of 0°, 30° and 60° with surface slope errors of 0 mrad and 5 mrad (where the tangential plane corresponds to the x-axis and the sagittal plane to the y-axis). Note: The contour lines are fractions of the maximum flux of the image, and the x- and y-axes of the two cases also differ

Consider the sagittal plane which is perpendicular to the tangential plane and contains only the point of reflection and the reflected ray (Figure 7.3a). Here the reflected ray travels the same distance, d, but contrary to the tangential plane, the sagittal plane does not contain the surface normal. The implication is that only the component of the reflected ray, in the direction of the surface normal, will experience angular deviation (Figure 7.3c). The dimension of the image in the sagittal plane, w_{sag}, can thus be determined by the product of the angular deviation and the component of the reflected ray in the direction of the surface normal, given by the cosine of the incidence angle, $d\cos(\phi)$.

$$w_{\text{sag}} = 4\sigma_{\text{SSE}} \cdot d\cos(\phi) \tag{7.3}$$

Consequently, at low incidence angles ($\phi \approx 0$) the projected distances in both the sagittal and tangential planes are similar and result in a circular image. At high incidence angles ($\phi \gg 0$), the projected distance in the tangential plane remains the same, but the distance in the sagittal plane decreases with the cosine of the incidence angle, resulting in a smaller diameter in the minor axis of the elliptical image. Note that this decrease occurs only for the SSE component of the image spread. Thus, the effect will be negligible at very low SSE and pronounced in cases where the SSE dominate the FD.

In the CGD model, the image dimension is not directly computed; rather a representative angular deviation is specified in the form of the beam dispersion error, σ_{tot}. The σ_{bq} is the component of the σ_{tot} that accounts for SSE. The image dimensions in both the tangential and sagittal planes (h_{tan} and w_{sag}) can be converted into an angular form by dividing by the common slant range, d. By substituting these values into Equation B.4, a new σ_{bq} that accounts for the effect of the incidence angle on the FD is determined, as given in Equation 7.4. The addition of the $1 + \cos^2\phi$ term had a negligible effect on computational time. This proposed modification improves the correlation of the CGD model to that of the ray tracer from deviations as high as 19.8 % to within 1.8 % at 60° incidence angle for the case provided, as shown earlier in Figure 7.1 (p. 79).

$$\sigma_{\text{bq}}^2 = 2\sigma_{\text{SSE}}^2\left(1 + \cos^2\phi\right) \tag{7.4}$$

As mentioned, TE is also a normal vector error and behaves the same as SSE with an increased number of heliostats. The TE term, σ_{t}, is thus also affected.

$$\sigma_{\text{t}}^2 = 2\sigma_{\text{t\_pri}}\sigma_{\text{t\_sec}}\left(1 + \cos^2\phi\right) \tag{7.5}$$

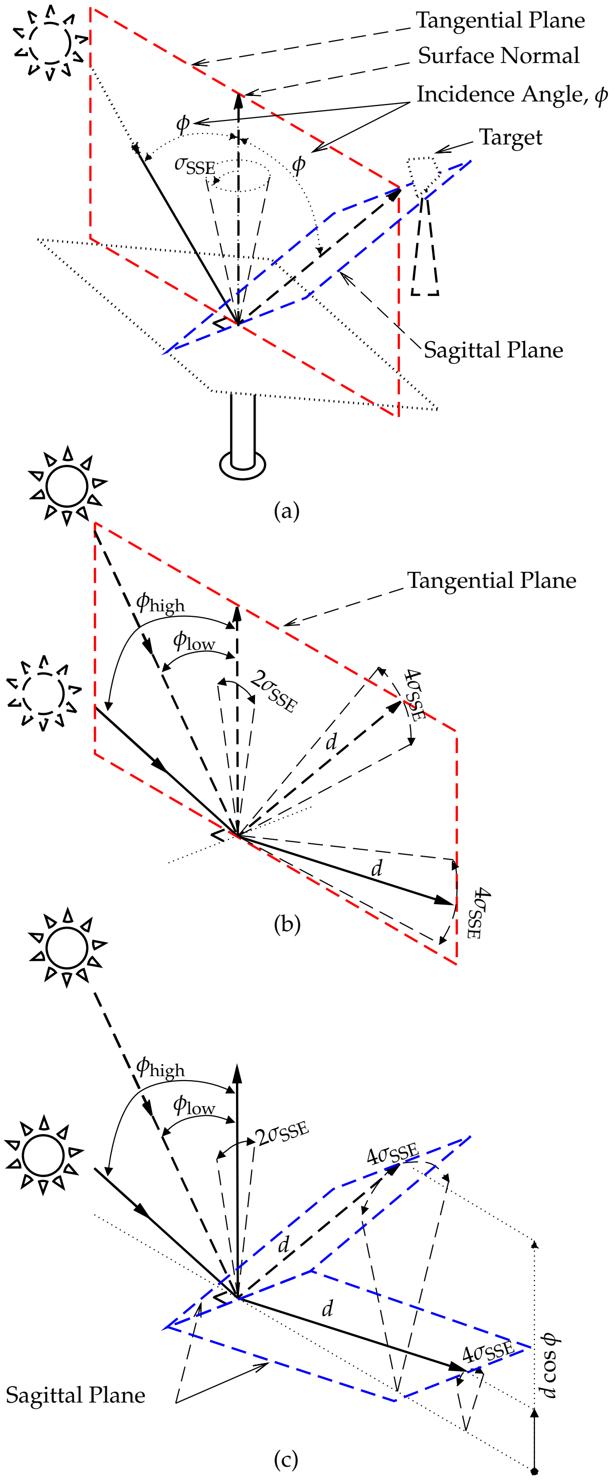

(a)

(b)

(c)

Figure 7.3: (a) The tangential and sagittal planes. Aberrations due to surface slope errors in (b) the tangential plane and (c) the sagittal plane, for both low and high incidence angles

This factor was derived by Biggs and Vittitoe when mapping elliptic-normal distributions from the concentrator plane to the reflected ray reference plane [67]. Pettit *et al.* [73] briefly mentions "a slight improvement in accuracy results when both σ_{SSE} and σ_{t} are multiplied by $\sqrt{1+\cos^2\phi/2}$". To my knowledge, the only CGD method where this is implemented is that of Collado *et al.* [70], which later is shown to be more complex and less accurate than the HFLCAL method used here [31].

7.5 The effect of the phenomenon on a heliostat field

Although this effect shows large variations of the final σ_{tot} term at higher incidence angles, it is useful to consider the effect in the context of a heliostat field to evaluate whether the effect is in fact significant. Here, the typical incidence angles in a heliostat field were determined, and the extent of the effect in comparison to other error sources of image spread, specifically astigmatic aberrations, was investigated (see Section 7.5.2). The robustness of the proposed modification was also demonstrated using a Monte Carlo simulation with representative input parameters.

7.5.1 Incidence angles in a heliostat field

The proposed modification varies solely with the incidence angle. The $\cos^2\phi$ term remains close to one at small incidence angles, but it then decreases strongly until it reaches 0 at 90°. The resulting effect is that larger deviations are present at increased incidence angles. The incidence angle is dependent on the position of the sun and the position of the receiver relative to the heliostat. The vector from the heliostat to the receiver is defined here as the target vector.

The sun can be thought of as moving around the edge of a circular disc. The disc is centred on the polar axis, which is inclined to the horizon by the latitude angle. The position of the disc moves along the polar axis seasonally with its minimum and maximum positions occurring at winter and summer solstices, as previously plotted in Figure 4.1 (p. 29). The resulting cylindrical shape representative of all the potential sun positions throughout the year is referred to here as the sun band. The position of the sun band is solely dependent on the site latitude and is thus constant for all heliostats in the field.

The DNI weighted average incidence angle for a field located at Plataforma Solar de Almeria is shown in Figure 7.4. The tower is at the origin, and the axes are defined as multiples of the tower height, R. The average incidence angles are found to vary between 20° and 50°, depending on the location of

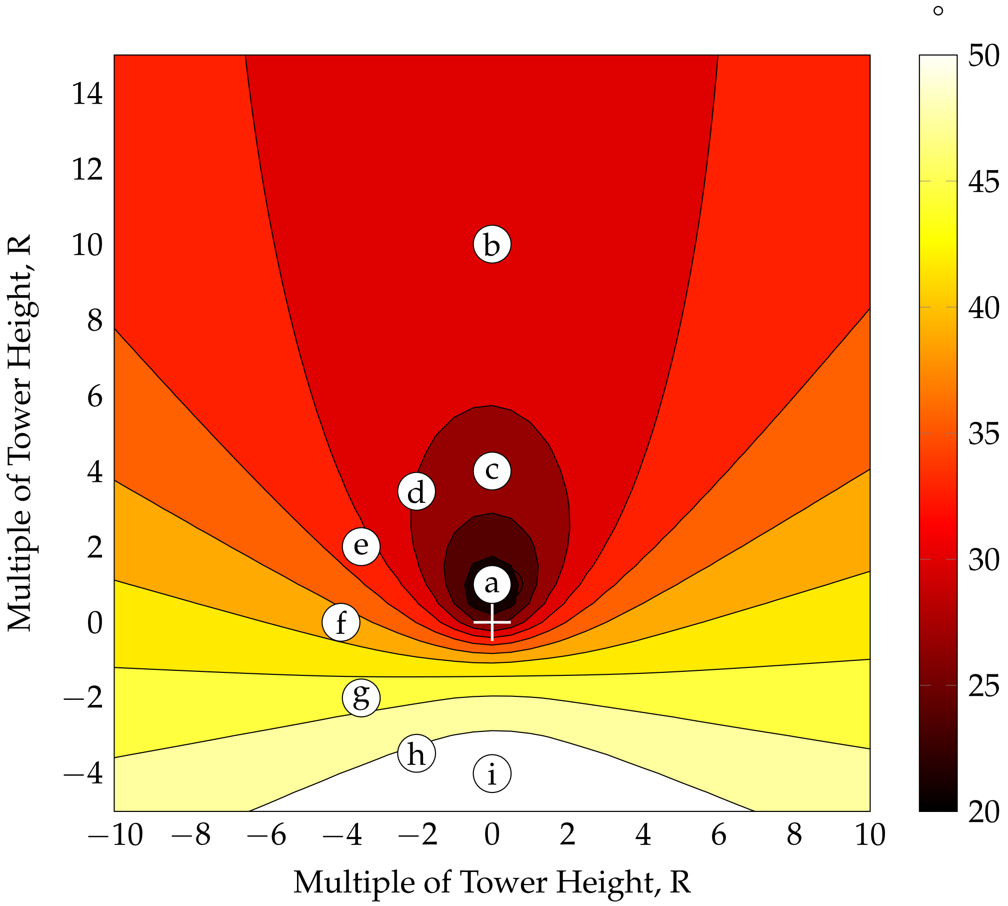

Figure 7.4: The DNI weighted average incidence angle for a heliostat field located at Plataforma Solar de Almeria (GPS: 37.094400, -2.358200). Solar data for 1994 obtained from GeoModel Solar [151]. Tower is located at origin, and *R* is multiple of tower height

the heliostat in the field. Incidence angles are observed to be particularly high in early morning, late afternoon and on the equatorial side of the field (south for a field in the Northern Hemisphere).

To gain a better understanding, the incidence angle distribution of several heliostats was determined. The heliostats are positioned directly north of the tower (Northern Hemisphere) at increasingly greater distances – at 0.7R (a), 3R (c) and 10R (b) – and anticlockwise around the tower at 30° increments at a constant distance of 3R (c-i). Only one side was considered due to the symmetry of the sun's movement about the north-south axis. The distributions are shown in Figure 7.5.

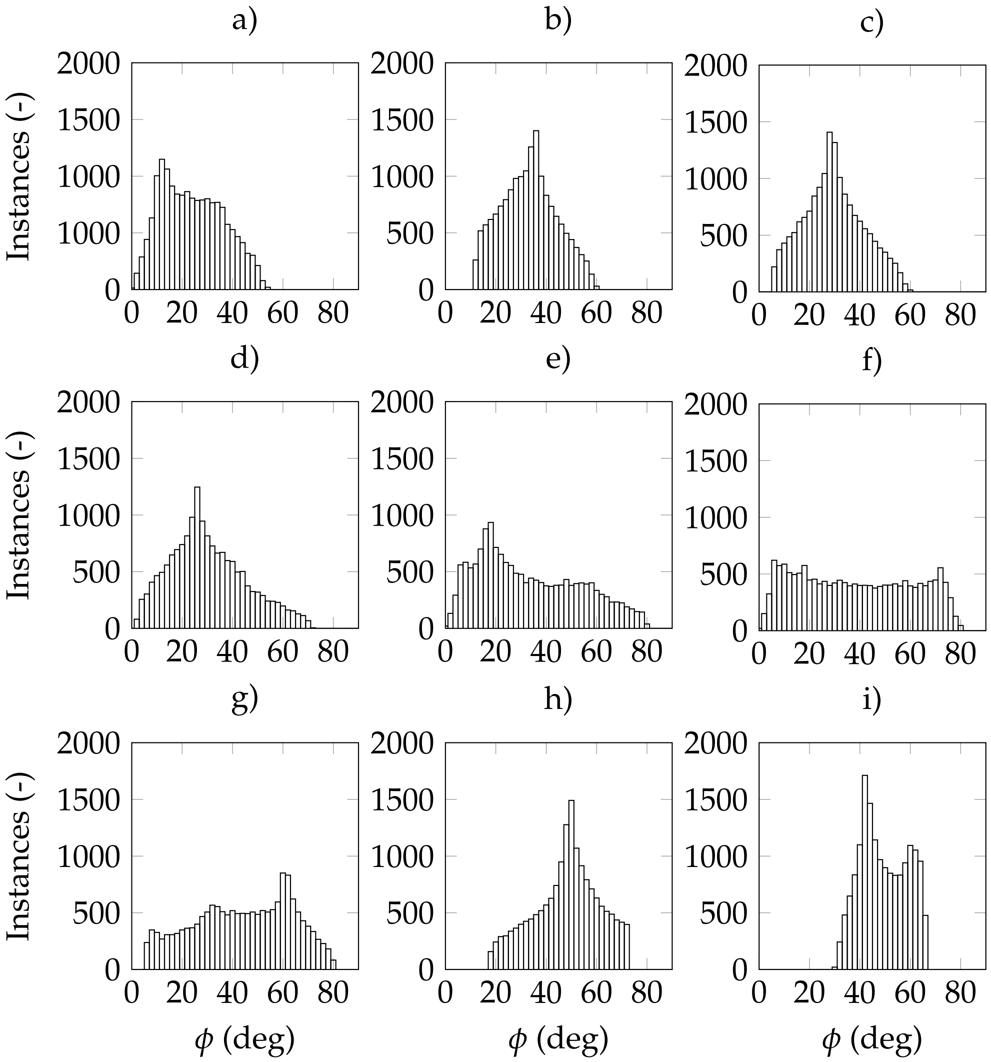

Figure 7.5: Distribution of incidence angle of heliostats (positioned as indicated in Figure 7.4)

First, the results show that the closest heliostat to the tower (i.e., directly in front of the tower) (a) has relatively low incidence angles due to the sun passing behind the target, which results in incidence angles of just above 45° in early morning and late evening. Heliostats positioned further from the tower (c and b) have target vectors that are progressively more acute to the polar axis, resulting in higher incidence angles, that are now up to 60°. The minimum incidence angle is no longer 0° but rather the half-angle between the top edge of the sun band and the target vector. High peaks also form that correspond to the longest path in the sun band.

The most striking changes to the distributions are seen moving around the tower. Here the target vector pans horizontally, closer to the edge of the sun band. As this occurs, the distributions flatten out until the receiver lies within the sun band (d-e), resulting in a near even distribution. Incidence angles of near 0° are obtained in the morning or afternoon (f). Continuing anticlockwise toward the south of the tower (g-i), the distributions are similar to the corresponding northern points, with the distinct difference that the peak distributions now occur at much higher incidence angles. The reason for the difference is that the angle between the target vector and the polar axis decreases.

The main conclusions from the distributions are that incidence angles higher than 45° will occur everywhere in the field. Low and even distributions will occur in positions corresponding to the target vector being inside the sun band. The probability of higher incidence angles increases as the target vector moves away from the band, resulting in peaks at low incidence angles in the northern part of the field and peaks at higher incidence angles in the southern parts.

An additional point to note is that heliostats suffer from 'cosine losses' where the power from the heliostat decreases with incidence angle. Thus, the effect of the phenomenon on the field performance diminishes by an additional factor.

7.5.2 Astigmatic aberrations

The convolution method allows errors to be treated as statistically independent, enabling the direct comparison of individual errors. Here the phenomenon is compared to astigmatic aberration, which is another dispersion error that increases with the incidence angle. Astigmatic aberration is a distortion of the heliostat image due to the physical geometry and curvature of the heliostat surface and is considered a major component of beam dispersion error [32].

Astigmatic aberration is dependent on the incidence angle, ϕ, the focal ratio, F_r, and the focal length, f, of the heliostat. Detailed computation of the astigmatism term, σ_ast, is provided in Appendix B.

To ensure a fair comparison, realistic values for the SSE, focal ratio and focal length should be selected. The SSE of heliostats are generally in the order of 1.5 mrad [4] but can range from 0.7 mrad to 3 mrad [109; 152; 153].

The ranges of focal ratios of several commercial power tower projects are provided in Table 7.2. Satellite imagery from the Google Earth software was used to measure the distances from the heliostats to the tower base. Tower heights were obtained from NREL [52], and heliostat dimensions were obtained from various sources [109; 154; 52]. Focal ratios were then determined by dividing the heliostat slant ranges by the heliostat chord length.

Focal ratios at the 20 MW Gemasolar plant are relatively low, 15-80, due to the lower slant ranges and large 115 m^2 heliostats. The range is much

Table 7.2: Estimated focal ratios, surface slope errors and tracking errors of commercial central receiver systems (estimated with data from [109; 154; 52])

Project	**Focal Ratio**		**SSE**	**TE**
	min	max	(mrad)	(mrad)
Crecent Dunes	26	204	-	-
Gemasolar	15	80	2.6 [109]	2.1 [109]
Ivanpah	36	552	-	-
Khi Solar 1	22	99	-	-
Sierra Sun Tower	40	174	-	1.4 ± 0.1 [51]

higher at the 377 MW Ivanpah project, 36-552, because of the smaller 14.4 m^2 heliostats and increased slant ranges.

The focal length of a heliostat does not necessarily correlate with its slant range. Facets are typically produced with only a few discrete focal lengths. These facets are then canted so that they collectively approximate the ideal focal length. Three cases in which the focal length is equal to 90 %, 100 % and 110 % of the slant range were considered here.

The contribution of the beam quality, σ_{bq}, and astigmatism, σ_{ast}, to the total error, σ_{tot}, for various values of SSE, focal ratios and focal lengths are shown in Figure 7.6. Assuming a typical value for SSE of 1.5 mrad, the modifier decreases the contribution of the σ_{bq} term by 0.258 mrad at 35° and 0.628 mrad at 60°. Comparing this to the σ_{ast} term, which has an ideal focal length and typical focal ratio of 50 for a Gemasolar type plant, the contributions by astigmatism are much higher: 0.904 mrad at 35° and 2.5 mrad at 60°. Considering, however, a typical F_{r} of 200 for an Ivanpah type plant, contributions are comparable at 0.226 mrad at 35° and 0.625 mrad at 60°.

If we consider cases where the focal length is 10% longer or shorter than the slant range, the astigmatism is significantly higher at low incidence angles (0.455 mrad and 0.556 mrad respectively at F_{r} of 50 and incidence angle of zero). At higher incidence angles, the effect is similar to that observed at the ideal slant range (2.41 mrad and 2.67 mrad respectively at F_{r} of 50 and incidence angle of 60°).

It was concluded that the phenomenon may play a small part in a field with low focal ratios but would be comparable to astigmatism in a field with large focal ratios.

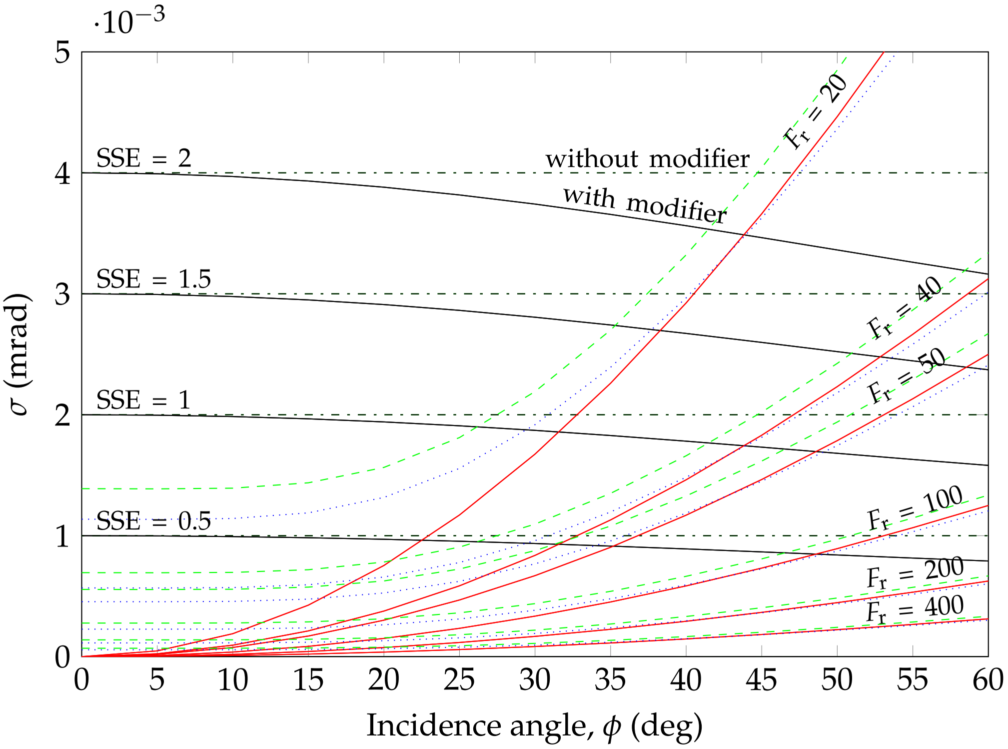

Figure 7.6: The error contribution to the beam quality term with (black, solid) and without (black, dashed) the proposed modification for a range of surface slope errors. Also plotted is the astigmatic error contribution to the beam quality term for various focal ratios at focal lengths equal to the slant range (red, solid), 90 % of the slant range (green, dashed) and 110 % of the slant range (blue, dotted)

7.5.3 Test for robustness

To determine the robustness of the proposed modification, a Monte Carlo simulation was performed for 500 cases. Input parameters were sampled from the following ranges assuming uniform distributions: $F_r = 20$ to 500, $\sigma_{SSE} = 1$ mrad to 5 mrad, $\phi = 0°$ to $60°$. Results for the CGD method, σ_{CG}, as well as the CGD method with the proposed modification, σ_{CG_mod}, are plotted against that of the ray tracer, σ_{RT}, to illustrate correlation in Figure 7.7. The fact that the data points fall below the line indicate that the CGD method is conservative by overestimating the σ_{CG} (Figure 7.7a). The improvement in the correlation is evident from the linear relationship (Figure 7.7b), and Pearson's correlation coefficient is improved from 0.9815 to 1.0000, indicating a robust model with a strong linear correlation.

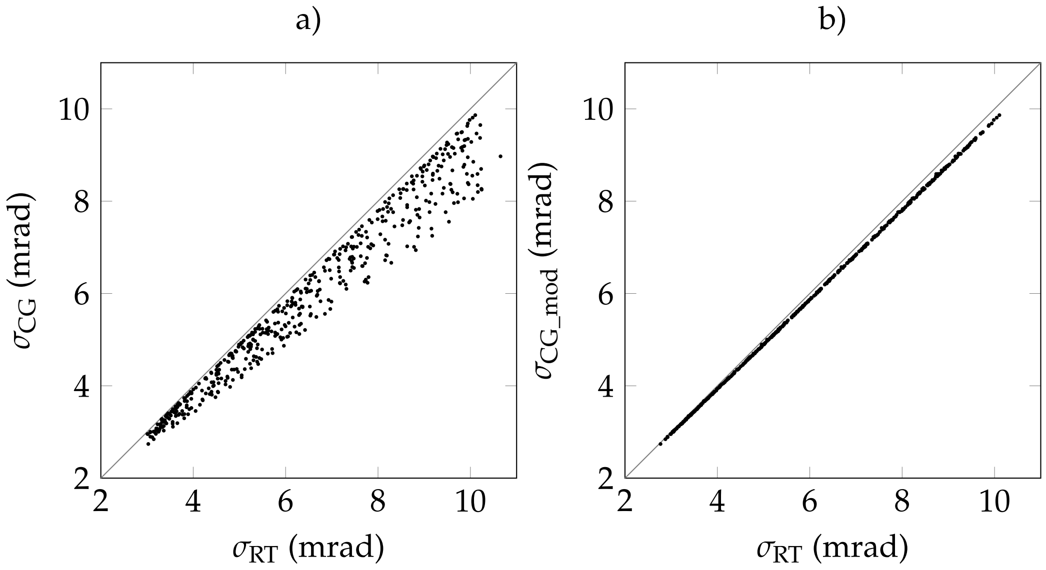

Figure 7.7: Scatter plot of Monte Carlo simulation to show correlation between the ray tracer, σ_{RT}, and a) the CGD method, σ_{CG}, as well as b) the CGD method with proposed modification, σ_{CG_mod} (input parameters were uniformly distributed between the following ranges: $F_r = 20$ to 500, $\sigma_{SSE} = 1\,$mrad to 5 mrad, $\phi = 0°$ to 60°)

7.6 Case study

This section describes the testing and implementation of the proposed modification in a case study.

A heliostat field representation of Torresol Energy's Gemasolar central receiver plant was generated using the methods described by Siala and Elayeb [155] and using the input values provided by Augsburger [109]. The field layout contains 2244 heliostats and is depicted in Figure 7.8. A surround field was specifically chosen to include the effects of heliostats on the equatorial side of the tower. For the purposes of the simulation, the plant was located at Plataforma Solar de Almeria (GPS: 37.094400, -2.358200).

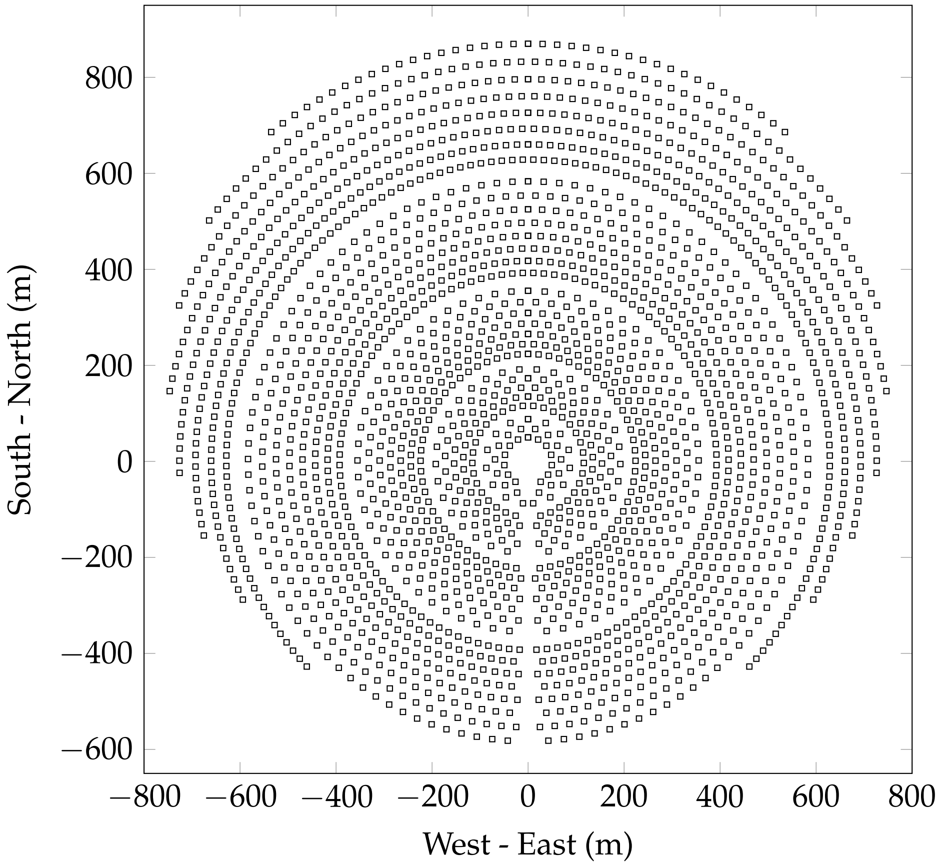

Figure 7.8: Simulated field layout, generated by estimated values from Augsburger [109], approximating the heliostat field layout of the Gemasolar central receiver system

A cylindrical receiver oriented vertically and with a height of 10 m and radius of 5 m was assumed. The geometric centre of the cylinder was placed at [0, 0, 120]. A simple aiming strategy was adopted where the aim points are located on a belt around the centre of the cylindrical receiver (at a height of 120 m). Each heliostat aims at the point on the belt closest to that heliostat.

The results provided here are for 8h00 on the morning of the solar equinox (20th of March 2015) with an assumed DNI of 1000 W/m^2. The simulation specifically negated blocking and shading to avoid effects that inaccuracies from a blocking and shading algorithm would have on the FD.

The flux was computed at 952 points on the receiver surface and arranged in a grid pattern. 10×10^6 rays were used for the ray traced simulation. The results are summarised in Table 7.3. The percentage deviation of the flux distribution of CGD and the modified CGD methods from that of the ray tracer, are given in Figures 7.9a and 7.9b respectively. The impact of the proposed modification was evaluated by comparing the two figures.

Table 7.3: Results of the flux distribution on the cylindrical receiver for the ray tracer and the CGD model with and without the proposed modification

	Ray tracer	**CGD model without modification**	**CGD model with modification**
Mean flux (MW/m^2)	0.354	0.328 (-7.5%)	0.355 (0.1%)
Max flux (MW/m^2)	0.673	0.678 (0.6%)	0.712 (5.8%)
Min flux (MW/m^2)	0.087	0.092 (5.9%)	0.094 (8.2%)
Total power (MW)	111.3	102.9 (-7.5%)	111.4 (0.1%)
RMS error (kW/m^2)	-	38.2	27.8

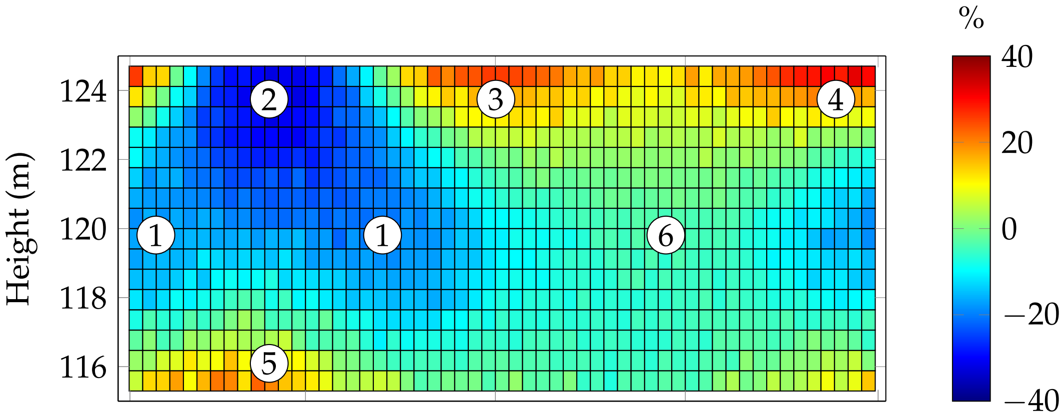

(a) CGD method

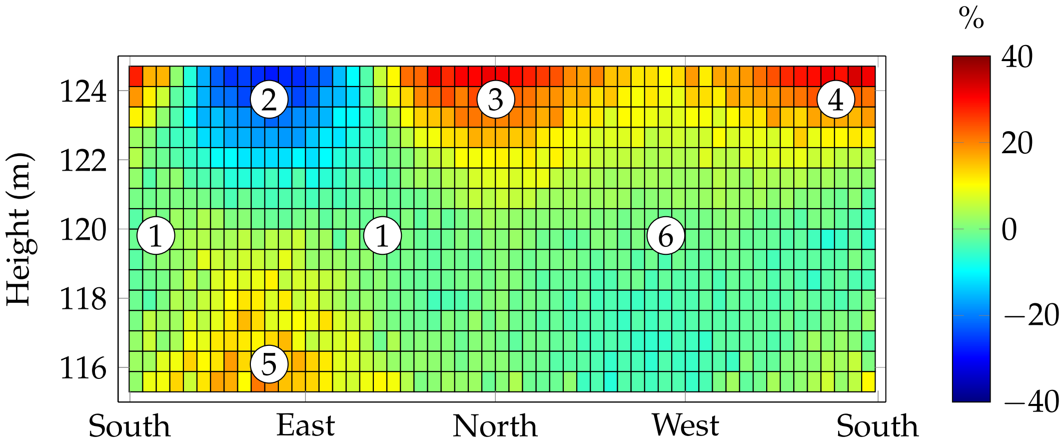

(b) CGD method with the proposed modification

Figure 7.9: Percentage deviation of the flux distribution from that of the ray tracer

For the conventional CGD method (Figure 7.9a), the most striking feature is the underestimation of the flux in the eastern side of the tower by roughly

30 % (1). Flux is overestimated at the top of the receiver in the north and south sides by 25 % (3-4) and at the bottom of the receiver in the southeast by 20 % (5). For the remainder of the receiver, flux is predicted within 10 % (6). The modified CGD method shows very similar results with the exception of correcting the underestimation on the East side (1).

These results can be explained by considering the optics of the field at the moment considered. Since the sun was located low in the sky in an east-southeasterly direction the heliostats in the east experienced high incidence angles. For this reason, the conservative CGD method underestimated flux in the east, which was corrected by up to 16 % by the modified CGD method (1). Almost no change is seen in the western side due to the low incidence angles of the heliostats in that area (6).

The overestimation of flux in the north and south (3-4) is present in both methods but is a result of the CGD assumption. The tangential plane of the heliostats in the north and south are tilted diagonally across the receiver, resulting in diagonal elliptical images. This in turn results in lower flux at points 3, 4 and 5 and higher flux at 2. The assumption of the CGD does not take this into account and thus overestimates the flux at 3, 4 and 5 and underestimates flux at 2.

It is interesting to note that the total power on the receiver aperture also varied from the 111.3 MW given by the ray tracer. The CGD method resulted in a conservative 102.9 MW, while the modified CGD method gave a very accurate 111.4 MW. Both CGD methods calculate the power in the same manner, and the difference is solely due to spillage. On the other hand, the CGD method predicted the peak flux to within 0.6 %, while the modified CGD method over-predicted flux by 5.8 %.

The distribution of the percentage flux deviation (Figure 7.10) shows that the proposed modification only affected areas where the flux was underestimated, demonstrating again the improvement in high incidence angle areas where the CGD method has been shown to be conservative.

In the case considered, the large number of heliostats (2244) masks the FD deviations of individual heliostats due to the central limit theorem. In the event of a field with fewer heliostats, the FD deviations are expected to be larger and more pronounced. The benefit of this modification in flux distribution applications is illustrated by the 27.2 % reduction in the RMS error of the flux distribution on the receiver aperture.

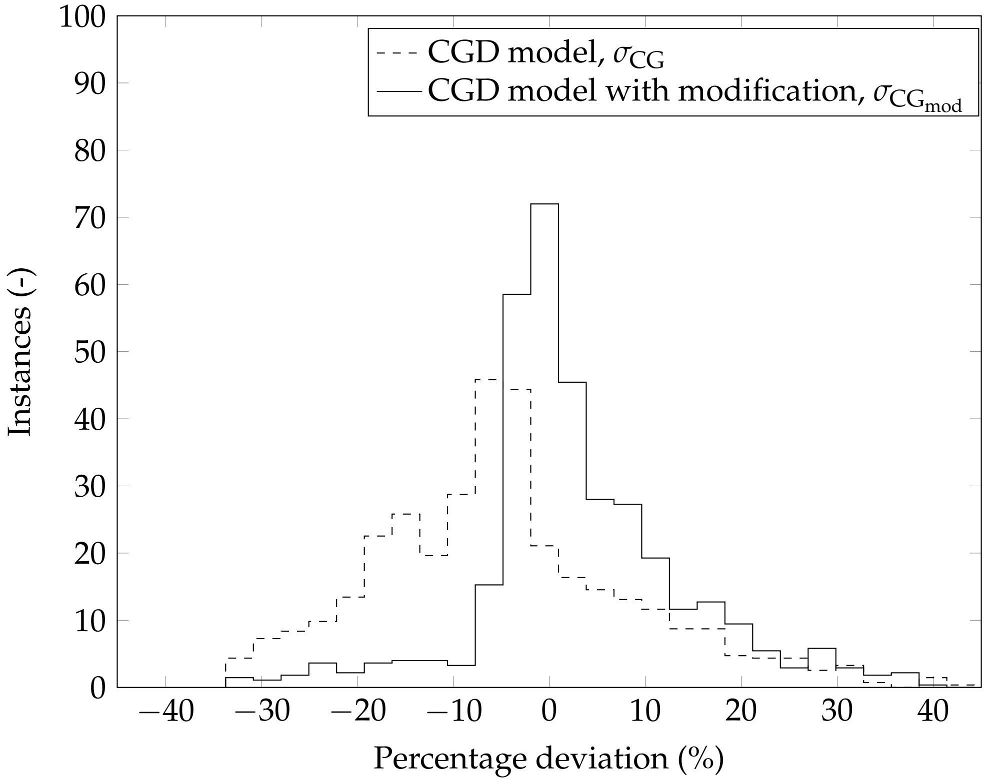

Figure 7.10: Histogram showing the error distribution of the percentage deviation of the flux for the CGD method and the CGD method with the proposed modification from that of the ray tracer

7.7 Conclusion

The most significant deviations between the implemented CGD method (HFLCAL) and the ray tracer occurred at high incidence angles where normal vector errors were present. The deviations are due to the CGD method not accounting for the shortening of the minor axis of the elliptical image with increasing incidence angles. This shortening occurs with a decrease of the light path component in the sagittal plane. The effect is negligible for low normal vector errors and pronounced in cases where the normal vector errors dominate the beam dispersion error. For typical surface slope error values, the effect is small for low focal ratios but comparable to astigmatism at higher focal ratios.

A modification to the CGD method is proposed that incorporates the effect of the incidence angle into the beam quality and tracking error terms. This modification results in much smaller deviations at high incidence angles, which predominantly occur in early mornings, late afternoons and for heliostats at the equatorial side of the tower. The proposed modification has an insignificant effect on the models computational time and has been shown to be robust. Improvements in the accuracy of the flux distribution do, however, reduce the conservative margin of the power on the receiver aperture.

Although this modification improved the accuracy of the flux distribution by 27.2 % for the case study, it's ability to describe the flux distribution is limited by the Circular Gaussian assumption. This indicates that this method is, however, not well suited to describe realistic flux distributions accurately.

Since the proposed modification demonstrates sufficiently significant improvements at negligible computational cost, it is suggested that it be implemented into the HFLCAL method for flux distribution applications such as aiming strategy optimisation. So doing will offer plant designers and operators greater accuracy during the simulation of the flux distribution on their receiver with a fast analytical method.

Chapter 8

Development of an analytical model for heliostat flux distribution

In this chapter a novel analytical model for flux distribution applications is proposed. This chapter presents the reasoning for the model's approach, provides an overview of the flux distribution function, showcases a validation case and discusses the shortcomings. Detailed calculations of the model are provided in Appendix C.

8.1 Introduction

Chapter 3 found that applications, such as aim point optimisation and real-time flux prediction, require an accurate and computationally inexpensive method to determine the flux distribution, and suggests that this need is not yet satisfied. Chapter 7 reinforced this finding by showing that state-of-the-art circular Gaussian methods are not well suited to describe realistic flux distributions. This chapter attempts to develop a method to address this need and is specifically aimed at these applications. All the previous learnings are collectively applied here to analytically describe the flux distribution as accurately as possible without incurring excessive complexity or computational expense.

8.2 The approach of the method

The fundamental analysis of heliostat optics (Chapter 4) found that optical aberrations can be statistically differentiated according to whether they occur in a set of consecutive optical events or whether they are path dependent. It is shown that the flux distribution of a heliostat is predominantly defined by collective effects of three aberration components: the sun shape, NVE aberrations, and astigmatic aberrations. The optical effect of these three aberrations on the beam radiance is distinct, and it is proposed that they be considered individually.

The first component is the sun shape. Section 4.2.2 presents the state of the art sun shape models, which show that the sun shape is not normally distributed or a pillbox distribution but rather represents a flat-top beam with reduced intensity at the beam edge. It is further indicated that variations in the sun shape alone may lead to large performance deviations.

NVE's appear to be normally distributed (Section4.3) (also confirmed experimentally in Appendix D), however, Section 7.4.3 demonstrates that the angular aberration of the NVE's vary in the tangential and sagittal planes based on incidence angle and results in an elliptical beam.

Chapters 4, 5 and 6 consider astigmatic aberrations that consist of both the surface profile and aperture shape. The surface profile effects can be shown to vary in the tangential and sagittal planes based on the curvature of the profile, the incidence angle and the aperture dimensions; however, effects such as the aspect ratio and canting strategies are not well represented analytically and should be accounted for explicitly.

To analytically describe the flux distribution accurately, all these effects must be considered in the method. Of the four fundamental approaches to calculate the flux distribution [60], only convolution methods and cone optics provide flux distribution knowledge non-numerically. Convolution methods are computationally the most efficient, but they are limited to a predefined distribution. Cone optics enable additional flexibility by discretising the surface and then using multiple beams to describe the flux distribution.

This method combines convolution and cone optics to account for the statistical behaviour of the two types of aberrations. Consecutive aberrations can be incorporated into a two dimensional convolution function, and path dependent aberrations can be accounted for explicitly by discretising the reflective surface, as depicted in Figure 8.1.

Although the combined approach enables some astigmatic effects to be accounted for explicitly, the convolution function must still account for the sun shape, the anisotropic NVE aberrations and the anisotropic astigmatic aberration of the disctretised cell in question. The biggest obstacle for this approach is thus finding a function capable of describing the resulting distribution with sufficient accuracy. This is known to be a non-trivial problem (Section 3.2.1).

To reduce the complexity of the convolution function some simplifications can be made by considering the effects of the components. The first simplification is to consider the tangential and sagittal components of the two anisotropic aberrations separately as depicted in Figure 8.2. These effects are well described in Chapters 4 and 7.

The generally accepted assumption that aberrations are normally distributed and statistically independent [156; 81; 67; 68] also allows convolu-

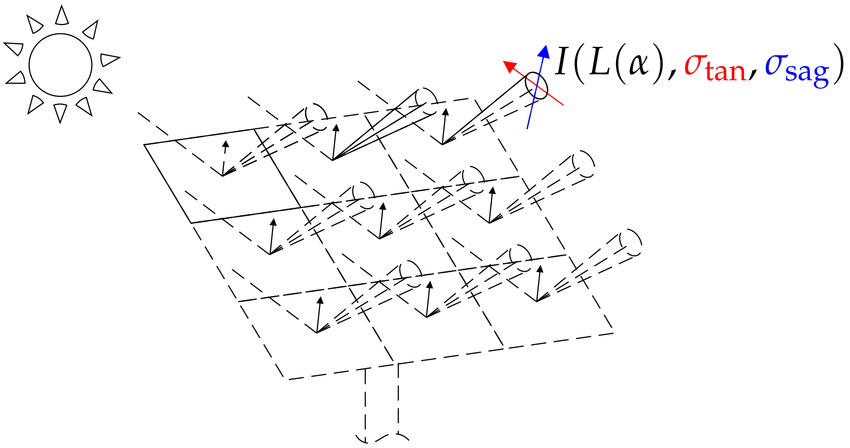

Figure 8.1: Convolution of individual reflective elements ($I(L(\alpha), \sigma_{\text{tan}}, \sigma_{\text{sag}})$) repeated for nine discretised cells over a heliostat surface

tions to be simplified. To leverage this advantage the NVE aberrations and astigmatic aberrations of individual cells are assumed to be normal and are combined separately in the two planes. Although this assumption has previously been shown to not hold true (Sections 4.7 and 5.5.2), because NVE are normally distributed and the astigmatic aberrations are predominantly dealt with explicitly, the inaccuracy resulting from this assumption is expected to be minimal.

$$\sigma_{\text{tan}}^2 = \sigma_{\text{NVE}_{\text{tan}}}^2 + \sigma_{\text{ast}_{\text{tan}}}^2 \qquad \text{and} \qquad \sigma_{\text{sag}}^2 = \sigma_{\text{NVE}_{\text{sag}}}^2 + \sigma_{\text{ast}_{\text{sag}}}^2 \tag{8.1}$$

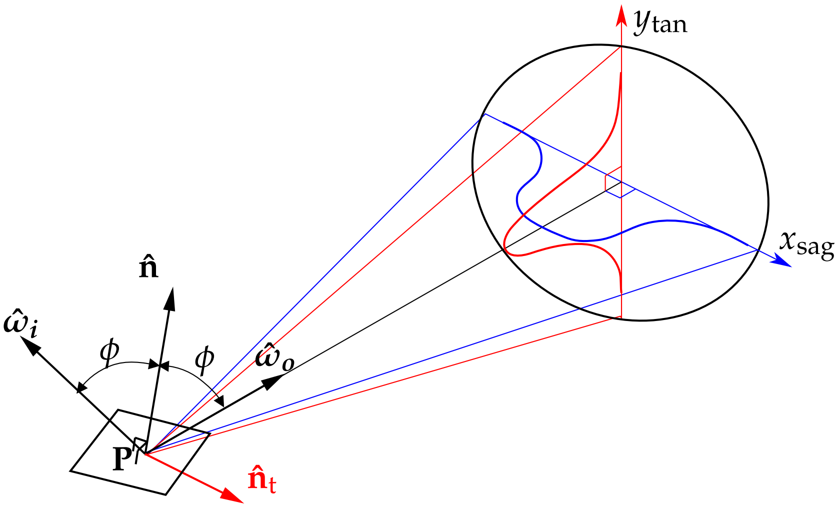

Figure 8.2: The radiance distribution of the reflected beam from a single cell

With these assumptions made, the convolution function, I, only has to account for the sun shape, $L(\alpha)$, and the anisotropic aberrations, σ_{sag} and σ_{tan}. The convolution function which represents the radiance distribution of the beam can be represented by $I(x_{\mathrm{sag}}, y_{\mathrm{tan}} \mid L(\alpha), \sigma_{\mathrm{sag}}, \sigma_{\mathrm{tan}})$ where x_{sag} and y_{tan} are angular coordinates in the two planes.

With the inputs and variables of I understood, the formula to describe their relationship is still required. Numerous attempts were made to solve the convolution integrals with realistic sun shapes; however, an analytical solution could not be obtained. An alternative approach is to propose a function that can approximate the distribution.

8.3 Evaluating the accuracy of convolution functions

Evaluating the accuracy of a proposed convolution function requires a basis to compare against and an objective measure. The functions were compared against the SolTrace ray tracer [95], and based on the envisaged application of the model, both the RMS error over the flux distribution and the maximum or 'peak' flux error are considered as important accuracy measures.

The function must also be compared over the entire range of input parameters to ensure an unbiased comparison. Assuming that the sun shape remains constant, the accuracy of $I(x_{\mathrm{sag}}, y_{\mathrm{tan}} \mid L(\alpha), \sigma_{\mathrm{sag}}, \sigma_{\mathrm{tan}})$ only needs to be determined for the expected range of σ_{sag} and σ_{tan}. This allows for a two dimensional representation of the function's accuracy as depicted later in Figures 8.4 and 8.5. Each individual pixel in these plots represents a comparison of the function with a ray traced image. Comparisons were made in 0.1 mrad increments ranging from 0 mrad to 10 mrad for both axes.

By manipulating ϕ and σ_{SSE} for a circular heliostat aperture, representative images at all these points could be generated in the ray tracer. A F_{r} of 1000 was used to ensure that astigmatic effects did not dominate the results. All the results presented here use a pillbox sun shape. Once these images were obtained any proposed function could be evaluated against them.

To further ensure an unbiased comparison, the functions should be compared given realistic input parameters. Figure 8.3 shows σ_{sag} and σ_{tan} values for randomly selected heliostats, at random dates and times, at three known heliostat fields with estimated performance parameters. The main objective of this graph is to define typical σ_{sag} and σ_{tan} values, which should be considered when evaluating proposed functions.

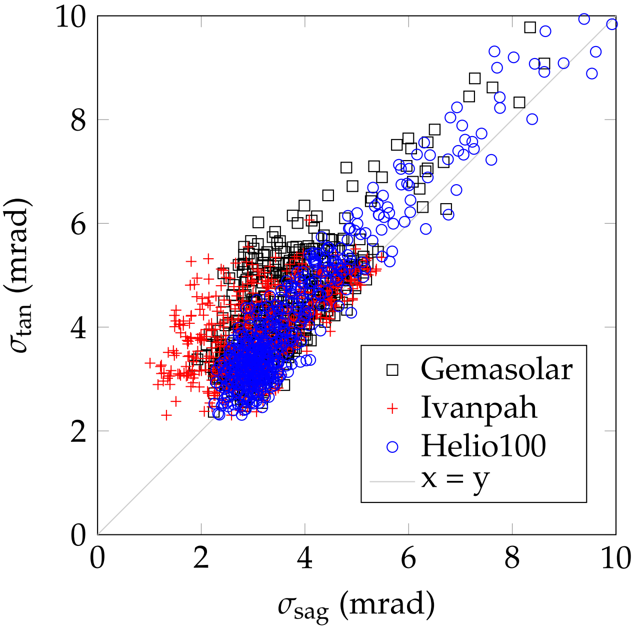

Figure 8.3: Beam spread in the tangential and sagittal planes

One apparent feature is that σ_{sag} and σ_{tan} appear to be linearly related, so large deviations in either plane do not typically occur. The higher errors of both Helio100 and Gemasolar heliostats are a result of the low focal ratios, which are not present in the Ivanpah field. These can be avoided by discretising the surface. σ_{tan} is typically larger than σ_{sag} due to incidence angle effects, but σ_{sag} may also dominate in cases where the focal length of the heliostat is shorter than the slant range. Since it is unlikely that σ_{SSE} will drop below 0.5 mrad, low deviations may for practical purposes be neglected.

8.4 Results

Figures 8.4 and 8.5 show the RMS error over the flux distribution and the peak flux error respectively for various functions. To best depict the results, the absolute value of the error is plotted on a logarithmic scale. This enables the large range of quantities to be represented and maintains some resolution at lower orders of magnitude. In Figure 8.5a and 8.5b, a zero error line (dark blue) is observed, which represents the point where the peak flux of the convolution function crosses from below to above that of the ray traced image.

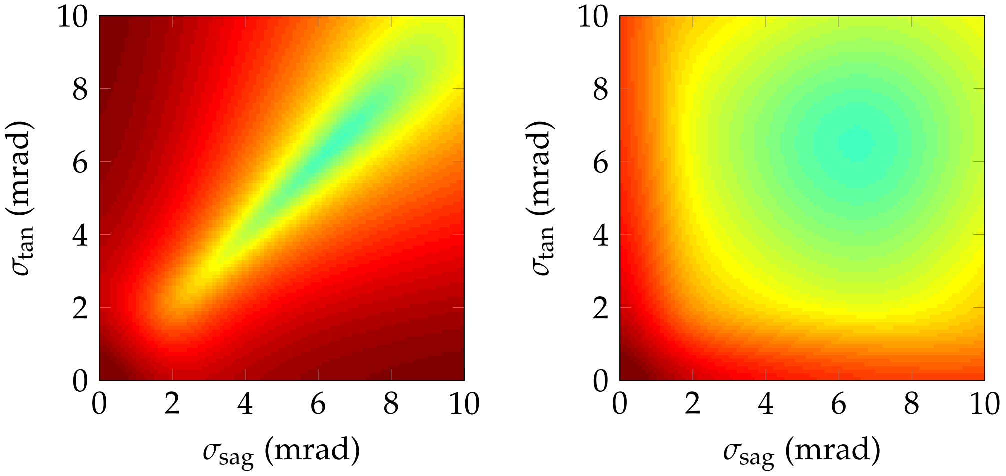

(a) Circular Gaussian **(b)** Elliptical Gaussian

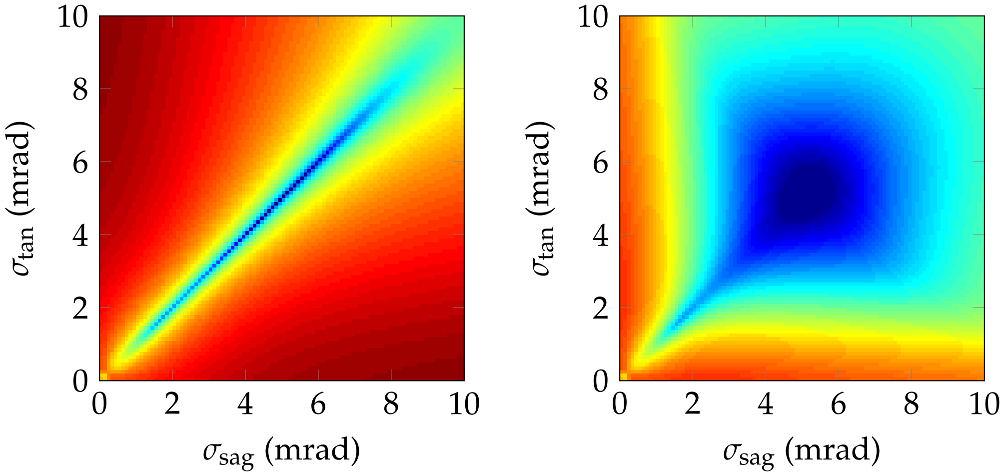

(c) Circular Super-Gaussian **(d)** Elliptical Super-Gaussian (fit)

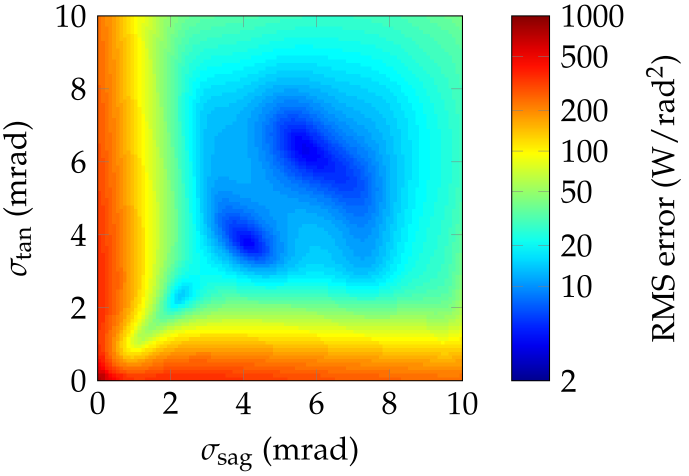

(e) Elliptical Super-Gaussian (function)

Figure 8.4: The Root Mean Squared deviation of the intensity of various functions from ray traced images: (a) Circular Gaussian, (b) Elliptical Gaussian, (c) Circular Super-Gaussian with best fit parameters, (d) Elliptical Super-Gaussian with best fit parameters, (e) Elliptical Super-Gaussian with function parameters (Note the logarithmic scale of the colour-bar, all plots use the same scale)

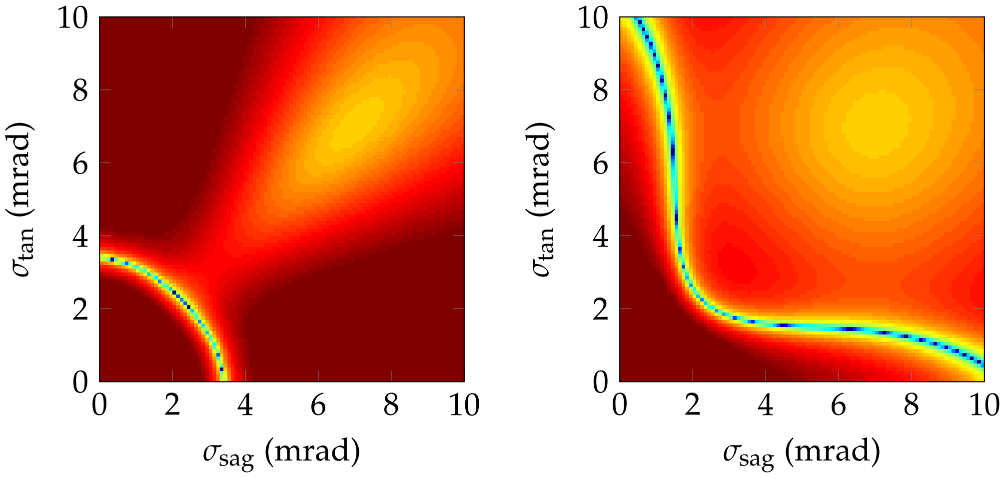

(a) Circular Gaussian **(b)** Elliptical Gaussian

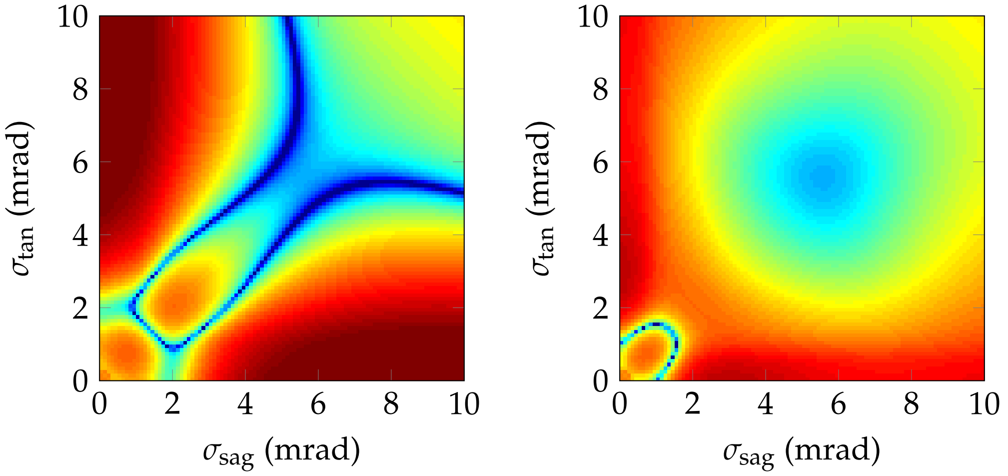

(c) Circular Super-Gaussian **(d)** Elliptical Super-Gaussian (fit)

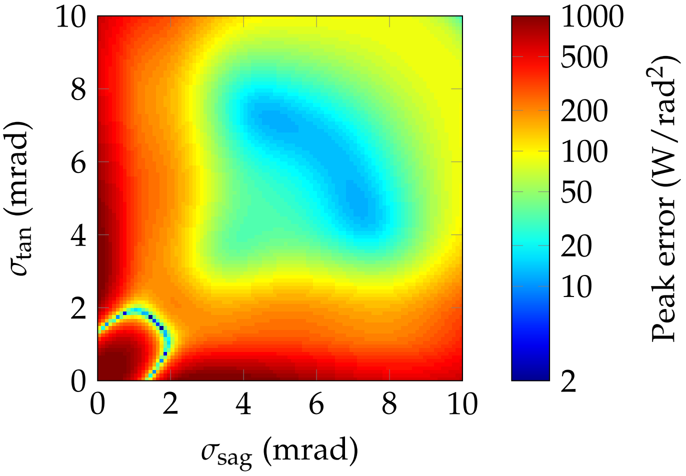

(e) Elliptical Super-Gaussian (function)

Figure 8.5: The deviation of the maximum flux of various functions from ray traced images: (a) Circular Gaussian, (b) Elliptical Gaussian, (c) Circular Super-Gaussian with best fit parameters, (d) Elliptical Super-Gaussian with best fit parameters, (e) Elliptical Super-Gaussian with function parameters (Note the logarithmic scale of the colour-bar, all plots use the same scale)

The first function evaluated is the Circular Gaussian function, presented previously in Chapter 7. As expected, the Circular Gaussian approximates the real distribution best when σ_{sag} and σ_{tan} are both relatively high and equal ($4\,\text{mrad} < \sigma_{\text{tan}} = \sigma_{\text{sag}}$). For $\sigma_{\text{tan}} \neq \sigma_{\text{sag}}$, the distribution is elliptical and the circular assumption no longer holds. At low beam spread ($\sigma_{\text{tan}}, \sigma_{\text{sag}} < 4\,\text{mrad}$), the assumption of a Gaussian sun shape breaks down resulting in high deviations. The maximum flux also does not correlate well. Maximum flux is over-predicted at low beam spread ($\sigma_{\text{sag}} < 3.4\,\text{mrad}$) and under-predicted above this value. The over-prediction at low spread is caused by the incorrect assumption of a normal sun shape as observed previously in Figure 4.2 on pg. 30.

Chapter 4 and Chapter 7 highlight the importance of accounting for the elliptical nature of the reflected cones caused by both the bidirectional reflectance distribution function (BRDF) at the point of reflection as well as the astigmatic effects of the surface. The elliptical cone is symmetrical about both the tangential and sagittal planes for the BRDF component and for the astigmatic aberration if the alignment angle is zero. Since facets are generally spherically curved, this assumption generally holds true.

Elliptical distributions can be accounted for by dealing with the probability distribution functions of each plane separately exceeding the limitations of a single radial distribution. This is achieved by computing flux distribution in a reference plane perpendicular to both the tangential and sagittal planes.

To accommodate for the variation between the tangential and sagittal spread, a bivariate or elliptical Gaussian function is considered.

$$I_{\text{EG}}(x_{\text{sag}}, y_{\text{tan}} \mid \sigma_{\text{tan}}, \sigma_{\text{sag}}) = \frac{P_{\text{h}}}{2\pi\sigma_{\text{sag}}\sigma_{\text{tan}}} \exp\left(\frac{-x_{\text{sag}}^2}{2\sigma_{\text{sag}}^2} + \frac{-y_{\text{tan}}^2}{2\sigma_{\text{tan}}^2}\right) \tag{8.2}$$

Figures 8.4b and 8.5b show an improved performance for larger ($4\,\text{mrad} < \sigma_{\text{tan}}, \sigma_{\text{sag}}$)) and unequal $\sigma_{\text{tan}} \neq \sigma_{\text{sag}}$ spread for both RMS and maximum flux errors; however, at low spread the error remains large.

To correct for the error at low beam spread, a function is required that can approximate the sun shape at lower errors and the Gaussian function at higher beam spread. Shealy and Hoffnagle [157] compare four different flattened irradiance distributions for laser beam profiling. The Super-Gaussian is such a function, which can approximate both a pillbox sun shape and the normal distribution.

Equation 8.3 defines the normalised Super Gaussian function in a radial form. R_{SG} is the radius at which the output irradiance falls to e^{-2} of its axial value, and P is a dimensionless shape parameter.

$$I_{\text{CSG}}(r \mid P, R_{\text{SG}}) = \frac{4^{1/P} P}{2\pi R_{\text{SG}}^2 \Gamma(2/P)} \exp\left(-2\left(\frac{r}{R_{\text{SG}}}\right)^P\right) \tag{8.3}$$

Γ is the Gamma function which can be approximated using a function proposed by [158]:

$$\Gamma(z) \approx \sqrt{\frac{2\pi}{z}} \left(\frac{1}{e} \left(z + \frac{1}{12z - \frac{1}{10z}} \right) \right)^{z} \tag{8.4}$$

Figure 8.6 illustrates the variability of the function. For $P = 2$, the function simplifies to the Circular Gaussian function, while as $P \to \infty$, the function approximates a pillbox distribution. One complexity that exists is that two secondary functions are now required to relate P and R_{SG} variables with the beam spread: $P(\sigma_{\tan}, \sigma_{\text{sag}})$ and $R_{SG}(\sigma_{\tan}, \sigma_{\text{sag}})$.

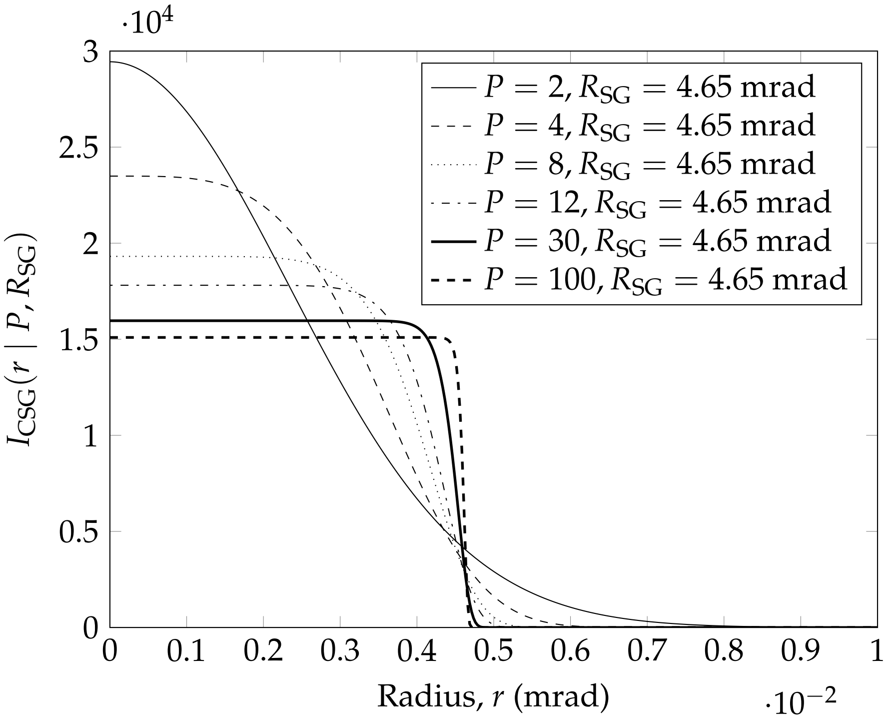

Figure 8.6: Radial intensity of the normalised circular Super-Gaussian function for various values of the shape parameter, P

For an initial assessment of the viability of this function, the circular Super-Gaussian function was fitted to the ray tracer data, and the results are provided in Figures 8.4c and 8.5c. The RMS errors are significantly improved at low beam spread, while the circular nature of the function still results in high errors where $\sigma_{\tan} \neq \sigma_{\text{sag}}$. The maximum flux error was also significantly improved over a much wider range of beam spread.

By introducing an additional stretch factor, f_{sag}, the function can be adapted to accommodate distributions where $\sigma_{\tan} \neq \sigma_{\text{sag}}$. The "Elliptical" Super Gaussian function is defined in Equation 8.5. It is reiterated that the function parameters must be described using the beam spread in the sagittal and tangential planes: $P(\sigma_{\text{sag}}, \sigma_{\tan})$, $R_{\text{SG}}(\sigma_{\text{sag}}, \sigma_{\tan})$ and $f_{\text{s}}(\sigma_{\text{sag}}, \sigma_{\tan})$.

$$I_{\text{ESG}}(x, y \mid P, R_{\text{SG}}, f_{\text{s}}) = \frac{4^{1/P} P}{2\pi R_{\text{SG}}^2 \Gamma(2/P)} \exp\left(-2\left(\frac{\sqrt{(x/f_{\text{s}})^2 + (f_{\text{s}} \cdot y)^2}}{R_{\text{SG}}}\right)^P\right) \tag{8.5}$$

Again the function is fitted to the ray tracer data and the results are provided in Figures 8.4d and 8.5d.

RMS errors are reduced to $< 20\,\text{W}/\text{rad}^2$ for the practical range of beam spread. This indicates a 50 % to 75 % reduction in the RMS error of the circular and elliptical Gaussian functions. The maximum flux error is also an order of magnitude smaller. This result indicates a significant improvement in the approximation of heliostat flux distribution.

To practically implement this function in an analytical model, the three function parameters need to be related to the beam spread: $P(\sigma_{\text{sag}}, \sigma_{\tan})$, $R_{\text{SG}}(\sigma_{\text{sag}}, \sigma_{\tan})$ and $f_{\text{s}}(\sigma_{\text{sag}}, \sigma_{\tan})$. These three functions are critical to the accuracy of the model and must thus consider both the choice of sun shape and achieve adequate accuracy over the practical range of beam spread.

A crude but effective solution is to use the parameter values obtained for the fitted function considered above (Figures 8.4d and 8.5d). A five point polynomial fit is used to describe the parameters over the range of beam spread. The resulting RMS and maximum flux errors are shown in Figures 8.4e and 8.5e, which can be compared to the previous fitted function. The five point polynomial fit appears to adequately describe the function parameters and no significant increase in errors is observed. These fitted functions are used for the remainder of this chapter. Further detail of the calculations is provided in Appendix C.

8.5 Model validation

A single case has been selected for this section, which showcases both the advantages and shortcomings of the proposed method. The Helio100 field layout is modelled on the afternoon on the summer solstice. A time is chosen where the sun is high enough so that there is no blocking or shading but low enough so that incidence angles are still high. The heliostats are assumed to have a slope error of 1 mrad with no tracking errors. In a case such as this, where the errors are low, the Circular or Elliptical Gaussian methods typically fail to describe the flux distribution appropriately. For the case considered here, the average σ_{sag} and $\sigma_{\tan}$ are 2.8 mrad and 3.1 mrad respectively, and each heliostat is discretised into 24 cells.

Figure 8.7 shows the deviation of the model from the ray tracer as a percentage of the maximum flux error and the results are summarised in

Table 8.1. The Elliptical Gaussian model (Figure 8.7a) over-predicts the maximum flux by 6.8 % with an RMS error of 22.6 kW/m^2. Around the centre of the image, the flux is underestimated, resulting from the inability of the Elliptical Gaussian to accommodate for the shoulder of the sun shape. On the contrary, the proposed Elliptical Super-Gaussian model (Figure 8.7b) is able to account for both the sun shape and correct the maximum flux. Maximum flux is determined to within 0.8 % and RMS error is reduced by 61 % to 8.9 kW/m^2.

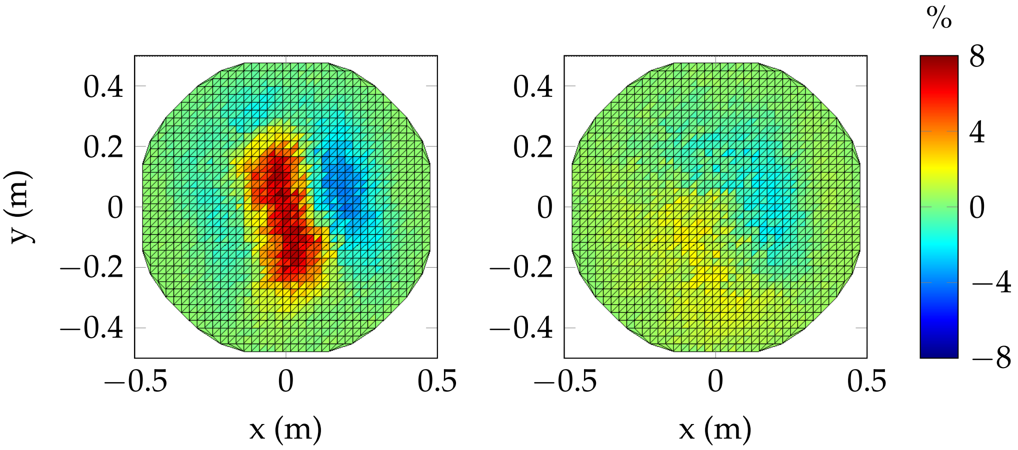

(a) Elliptical Gaussian, SSE = 1 mrad **(b)** Elliptical Super-Gaussian, SSE = 1 mrad

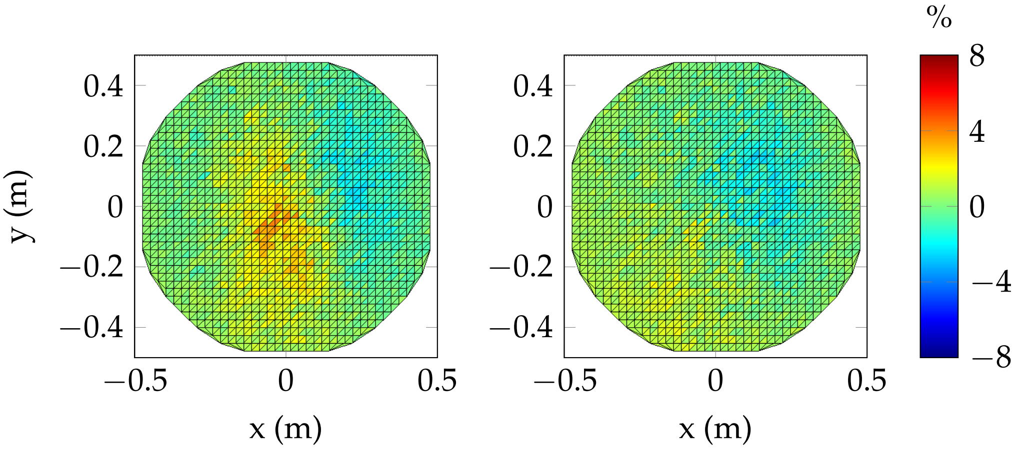

(c) Elliptical Gaussian, SSE = 3 mrad **(d)** Elliptical Super-Gaussian, SSE = 3 mrad

Figure 8.7: Model error as a percentage of maximum flux for a) elliptical Gaussian model and b) the elliptical super-Gaussian model

Table 8.1: Summary of the results of the flux distribution

	Ray tracer	**EG model**	**ESG model**
Helio100 Field, SSE = 1 mrad			
Mean flux ($\mathrm{kW/m^2}$)	250.6	252.7 (0.8 %)	252.5 (0.7 %)
Max flux ($\mathrm{MW/m^2}$)	1.131	1.207 (6.8 %)	1.139 (0.8 %)
Total intercepted power (kW)	196.9	198.5 (0.8 %)	198.3 (0.7 %)
RMS error ($\mathrm{kW/m^2}$)	-	22.6	8.9
Helio100 Field, SSE = 3 mrad			
Mean flux ($\mathrm{kW/m^2}$)	218.5	219.1 (0.3 %)	217.7 (-0.3 %)
Max flux ($\mathrm{MW/m^2}$)	0.546	0.555 (1.6 %)	0.540 (-1.15 %)
Total intercepted power (kW)	171.6	172.1 (0.3 %)	171.0 (-0.3 %)
RMS error ($\mathrm{kW/m^2}$)	-	6.1	5.1

In a case where the errors are much larger (SSE = 3 mrad), the advantage of the proposed method is less pronounced. Here the sun shape no longer plays a significant role and starts to approximate an Elliptical Gaussian distribution as shown in Figure 8.7c. In this case the RMS advantage of the Elliptical Super-Gaussian is only 16.4 % reducing the error from 6.1 $\mathrm{kW/m^2}$ to 5.1 $\mathrm{kW/m^2}$. Here both methods are able to predict maximum flux to within 1.6 %. This result indicates that the proposed method only provides an substantial advantages in cases where beam spread is low, and for higher beam spread cases elliptical Gaussian function may be used.

Up to this point blocking and shading have been omitted, and the results represented have been analogous with the summation of flux distribution of single heliostats. In the context of a heliostat field where blocking and shading do occur, certain complexities are introduced that reduce the accuracy of the model. The model has been structured in such a way that the flux distributions of each heliostat are determined without accounting for either blocking or shading. Using the method of Sassi [159], a blocking and shading factor is determined, $\eta_{\mathrm{B+S}}$, with which the distribution is then scaled.

This method works well for large, irregular and radially spaced fields with distributed aim-point strategies. However, in cases where field layouts are regularly spaced, such as the Helio100 or eSolar fields, and at low sun elevation angles, the majority of heliostats are shaded in the same way. The same portion of the reflective surfaces of these heliostats are shaded at the same time, as shown in Figure 8.8a. In this case the same portion of all the images is omitted resulting in an over-prediction in the flux distribution at this point. Figure 8.8b shows the over-prediction of light at a point for the case shown in Figure 8.8a. This issue is not unique to the proposed method but is rather an inherent limitation of the convolution type methods and highlights the need for blocking and shading to be discretised as well.

Here, flux errors of up to 100 % have been encountered, and total intercepted power varies as much as 10 %.

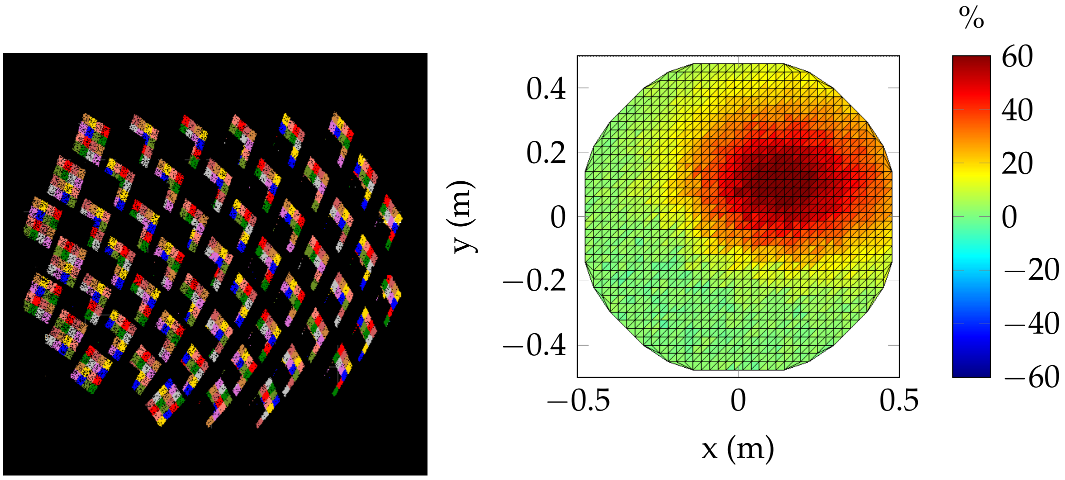

(a) Repetitive shading

(b) Error

Figure 8.8: a) The heliostat field as viewed from receiver showing consistent shading of lower right corner of most heliostats and b) Model error as a percentage of maximum flux

An additional factor that needs consideration is how the number of discretisations affects the resulting image. Figure 8.9 shows the maximum flux error, the RMS error and total intercepted power error for varying number of heliostat discretisations for the initial low beam spread case. Results of both the EG and ESG cases appear to converge with more than eight discretisations. Here again the advantage of the proposed model for flux distribution applications are clear, significantly reducing both maximum flux and RMS Error; however, for total intercepted flux, both methods produce similar results.

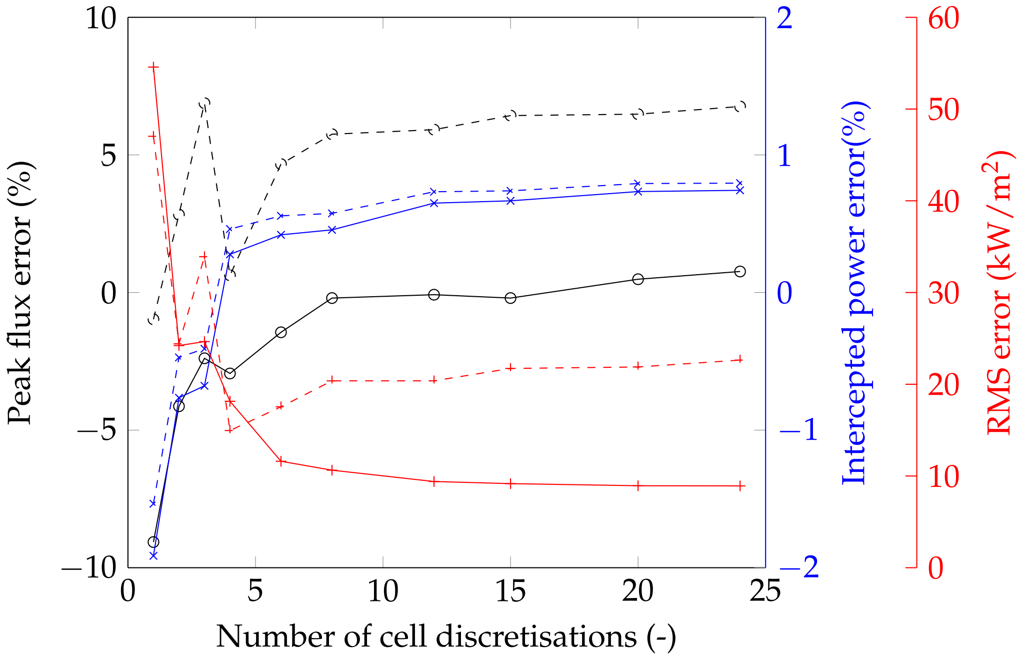

Figure 8.9: Maximum flux error, RMS error and total intercepted power error for varying number of heliostat discretisations for both Elliptical Super-Gaussian (solid) and Elliptical Gaussian (dashed) (SSE = 1 mrad)

8.6 Conclusion

A novel analytical method to model heliostat flux distribution is proposed based on an Elliptical Super-Gaussian function. This method demonstrates the ability to incorporate the behaviour of the three main aberrations, namely the sun shape, NVE aberrations and astigmatic aberrations. The method is shown to improve flux distribution accuracies beyond the state of the art circular Gaussian methods, and the most substantial improvement is found to be in cases where beam spread is low. RMS errors were reduced by up to 61 %, and the maximum flux was determined to within 1.6 % for the validation case. By improving the level of confidence of an analytical flux distribution model, it appears that this method effectively addresses the need identified in Chapter 3 for a computationally efficient analytical method to model flux distribution.

Erroneous over-prediction of areas in the flux distribution were found to occur for regularly spaced fields at low sun angles where the same area of the reflective surface of several heliostats are blocked or shaded. This error results from the use of convolution methods, and it is suggested that the method can mitigate this problem by incorporating blocking and shading effects into the cone optics discretisation.

Part III

Application, findings and conclusion

Chapter 9

Development of a facet for the Helio100 project

Up to this point the focus has been the theoretical analysis of heliostat optics. In this chapter the development and practical implementation of a heliostat facet for the Helio100 project is discussed. This work is a complementary activity to the main focus of this dissertation and is not intended to contribute directly in context of theoretical framework presented.

The facet presented here represents the culmination of numerous generations of facet designs over the last 6 years. Analytical and experimental studies, cost analysis, fabrication process, transport and installation have all been considered in this holistic design. All the variables, in both the design and fabrication procedure, contribute to the performance of the facet. Many of these variables and their effects are not intuitive and have been learned through trial and error process. Due to the complexity and numerous aspects of the work, only selected concepts, critical findings and the facet design most pertinent to the Helio100 project are presented here.

9.1 Introduction

The heliostat facets are among the highest cost components of a heliostat [153]. The reflective surface alone represents about 30 % of the heliostat cost, and due to the implications on the structure, the cost impact of facet design are as high as 50 % [35]. The Sandia Power Tower Technology Roadmap and Cost Reduction Plan highlighted heliostat facet optimization as one of twelve technology improvement opportunities regarding the heliostat field [1]. Sandia aims to reduce costs by >25 % while maintaining surface slope errors of <1 mrad by investigating low cost materials and alternative manufacturing methods [160].

The facet design not only has large cost implications but the heliostat performance is directly dependent on the facet's ability to achieve and maintain the desired profile and reflective properties. The facet is thus a critical component for the techno-economic viability of the collector system.

In April of 2014, the Helio100 flagship project, funded by the Technology Innovation Agency, was initiated to develop a novel low cost collector system for small scale modular gas-turbine based central receiver systems. This section outlines the facet development work that led up to this point and discusses the Helio100 facet design. Further detail of the project and the technology are discussed by Landman *et al.* [161].

9.2 Requirements and constraints

The requirements for the facet need to be considered in context of both the project requirements and constraints as well as the design philosophy and value proposition of the heliostat technology. The various requirements are in direct contention with each other, and the design sought to find an appropriate consensus in terms of the collector system as a whole. A summary of the minimum requirements which the design had to meet and the desired values are provided in Table 9.1.

Table 9.1: Requirements of the facet and backing structure

Requirements	**Minimum**	**Outstanding**	**Units**
Cost (@ 46 000 m^2 p.a.)	45	35	$\$/\mathrm{m}^2$
Reflectivity, ρ	90	95	%
Specularity, σ_{spec}	< 0.2	0.1	mrad
Surface slope error, σ_{SSE}	< 1.2	0.7	mrad
Profile	Spherical	-	m
Radius of curvature	≥ 56	≥ 70	m
Δ Radius of curvature	± 10 %	± 5 %	m
Facet life	≥ 5	≥ 30	yr
Mounting	3 points only	-	-
Installation time	10	3	min
Handling and installation	2 persons with hand tools only	-	-
Weight	< 15	10	kg/m^2

9.3 Initial investigation

In this section, deductive reasoning is used to select a reflective surface and propose a hypothesis of the stress distribution in a spherically curved glass pane.

9.3.1 Selecting a reflective surface

Specular reflectivity is of paramount importance when selecting a reflective surface. The percentage of light absorbed or scattered from the reflective surface results in the collector subsystem having to be larger. The percentage increase in field size is higher than the percentage of lost reflectivity because the additional heliostats are placed at increasingly suboptimal locations. Thus, selecting a high specular reflectivity has significant techno-economic advantages.

Specularly reflective surfaces that have shown promise for long term outdoor exposure are silvered mirrors, silvered polymer films and anodised sheet aluminium with a protective polymer coating [35]. Silvered glass mirrors are predominantly used in CSP applications due to its optical and degradation advantages above existing alternatives. Polymer films, however, show potential for replacing glass in CSP applications [162; 163].

Traditionally only silvered glass mirrors, in which the glass acts as a protective layer, have been able to withstand severe mirror degradation and maintain specularity [35]. Based on the wide spread use and availability of silvered glass, it was identified as the reflective surface with the lowest risk. Glass' disadvantages include its high fragility and the small potential for cost reduction since glass is already a commodity item [4; 164; 49].

9.3.2 Mechanical deformation of a glass pane

The short focal length requirements of 28 m meant that the glass panes needed to be curved to a radius of 56 m. The cost of thermal slumping and tempering were found to be infeasible and are not discussed further. To evaluate whether this relatively high curvature is obtainable with annealed float glass, the fracture point during three-dimensional curvature was tested. To curve the annealed glass, a vacuum was applied behind a 300 mm diameter circular glass sample supported uniformly on the edge. Curvature was measured in the centre of the sample using a spherometer.

Applying the vacuum resulted in the glass taking on a parabolic shape, and as expected the glass fractured at the centre of the sample coinciding with the fulcrum of the paraboloid with the highest curvature. Results are shown in Figure 9.1. The radius of curvature at the fracture point was an order of magnitude lower than that required, initially indicating that mechanical deformation of annealed float glass would not be an issue. Results also show that thinner glass can achieve higher curvatures.

The Australian building standard (AS1288-1994) specifies a maximum deflection of a glass pane a 60th of the structural span [165; 166], which translates to a radius of curvature of 9.2 m for the design size. Although both test results and literature suggest that float glass may be deformed

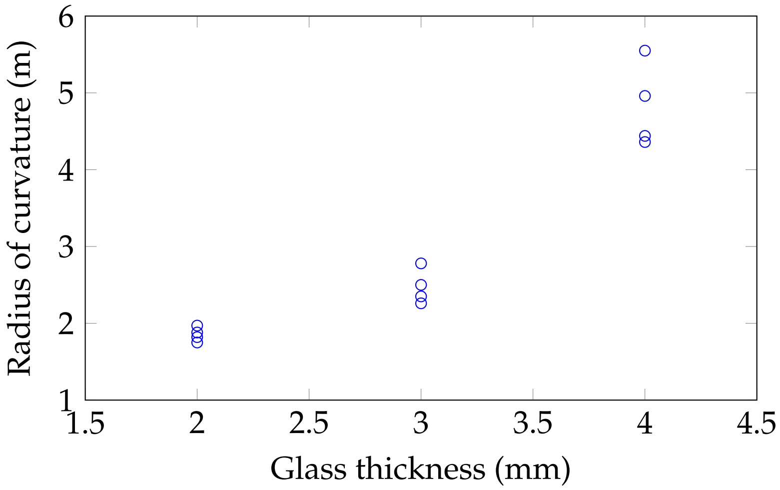

Figure 9.1: The radius of curvature at which float glass samples of different thickness fractured during three-dimensional bending

to the required curvatures, several practical limitations were found during implementation which led to additional investigations.

Kirchoff's plate theory calculates the stress distribution of a section of glass pane based on the curvature and assumes an infinite plane of glass. Because the curvature is constant for a spherically curved facet, results indicate a uniformly tensioned surface. Although this is inaccurate because the facet has a finite area, it is indicative of the stress distribution in the central area of the facet. Although not implemented here, large plate deflection theory [167] applied in finite element methods is the preferred method to evaluate stresses in large glass panes. Logic dictates that if the central area of the facet is tensioned, a compressive ring is required around this section to maintain the tension; this is shown in an illustrative example in Figure 9.2.

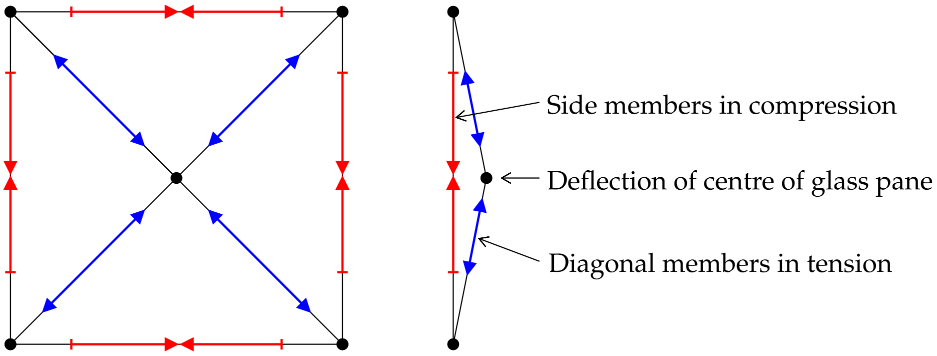

Figure 9.2: Eight-bar truss model illustrating stress distribution during deflection of the centre of the glass pane (Adapted from [167])

Through qualitative observations, this hypothesis appears to be true. During prototyping of high curvature facets, edges of the glass produced waves, also termed in the industry as "bottle topping". For larger facets or thin glass, the slenderness ratio of the compressive spans is higher, resulting in bowing and sideways buckling that causes these waves. This also explains the observations of Strachan and Houser [168] who suggested that poor mirror quality results from a large percentage of the mirror surface lying outside the stud support pattern (see Figure 9.5). This effect is found to be negligible at high focal lengths but intensifies with increased curvature.

9.4 Tools and techniques

The ability to assess the accuracy of the reflective surface of a facet is necessary to quantitatively evaluate performance and track quality control. Tools and techniques to assess the optical quality of prototypes and facet designs were developed in-house because budget constraints did not allow commercial systems to be purchased. These tools and techniques were used throughout this section and are briefly introduced here.

9.4.1 Coordinate measuring machine

Initial investigations of the mirror profile were done using an existing CMM. A CMM uses a touch probe that touches the mirror surface and records the touch point with a volumetric accuracy of 6.1 µm. This method allows a grid of discrete points to be evaluated on initial prototypes but the method had several limitations for this investigation. The CMM could only accommodate a mirror smaller than 650 mm by 950 mm and the force of the touch probe was found to affect the surface profile. Measurements were also time intensive and could last several hours. An example of profile evaluated using this method is shown in Figure 9.5 (p. 118).

9.4.2 The Zebra deflectometry system

An in-house deflectometry system, nicknamed Zebra, was developed in the Helio100 project to assists in the development process and production. Space constraints required the system to operate on a shared workshop floor, and novel use of Moiré patterns allowed the system to be uniquely robust against environmental lighting conditions.

The deflectometry system provides the user with a normal vector data of the reflective surface as shown later in Figure 9.8 (p. 124). A summary of the post processing of the normal vector data in the deflectometry system is given in Appendix D. Accuracy of the deflectometry system has not been validated and has only been evaluated on a qualitative manner and is estimated to be 0.5 mrad. Repetitive measurements resulted in a standard deviation of 0.047 mrad for the σ_{SSE} term indicative of system precision.

Throughout the project, the deflectometry system underwent several iterations to fix bugs and improve accuracy. Zebra was the only quantitative measure available to assess surface errors and deviations from desired curvature.

9.4.3 Beam characterisation system

The BCS used an optical system to determine the flux distribution of a heliostat image and was based on the BCS at Sandia's National Solar Thermal Test Facility [168]. A DSLR camera fitted with a neutral density filter was used to capture the flux distribution of a heliostat on a lambertian target. An actively cooled circular foil heat flux gauge was used to scale the pixel values to obtain flux distribution data. The method corrected for external light sources on the target, and included calibration of the camera and flux sensor and perspective correction, resulting in a measurement uncertainty of 3.8 %. The components, and setup of the BCS are depicted in Figure 9.3, and an example of a flux distribution obtained using this method was shown earlier in Figure 5.3 (p. 55).

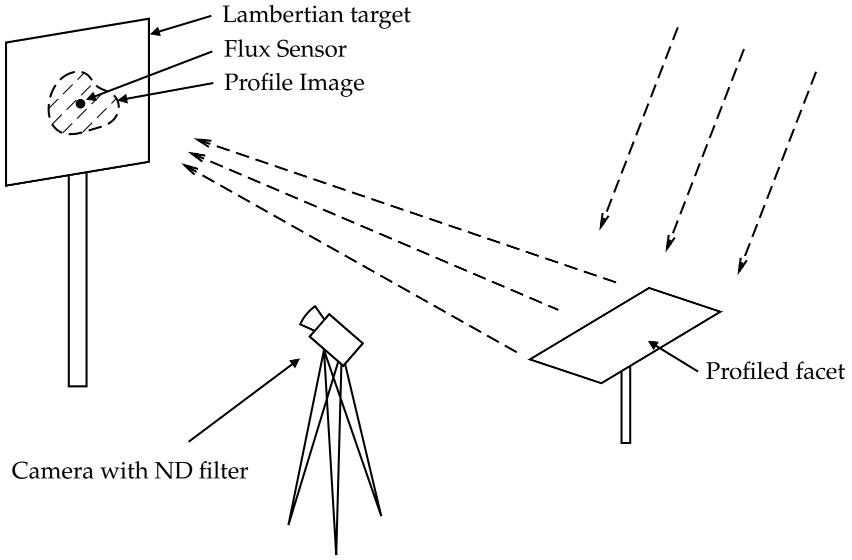

Figure 9.3: A depiction of the beam characterisation system (BCS)

9.5 Concept evaluation

To achieve the desired profile, the reflective surface must be allowed to deform to the desired profile, but then it requires a support structure to maintain this profile and minimise undesirable effects such as "bottle topping". Depending on the stiffness of the glass pane, the support design must also consider deformations caused by gravitational and wind loads. Yellowhair and Andraka [153] suggest that no facet design has achieved an optimal balance between low cost and good optical performance.

Several prototypes were constructed to investigate advantages of different design elements and identify issues. The three most feasible concepts are briefly discussed here after which a final concept is proposed.

9.5.1 Point supported facet

Since a glass pane has some rigidity of its own, it is possible to support the glass pane discretely and allow the glass to support itself in the areas between support points. Such an approach essentially minimises the support structure to only specific points, which reduces cost but at the expense of optical performance [153]. Discrete support has the advantage that individual support points can be adjusted independently, allowing the profile to be manipulated. The long stud supports also provide good thermal stability (see Section 9.7.3).

The point supported facet is widely adopted due to its simplicity. The mounting points support the glass in both radial (in plane) and axial (normal to plane) directions. The studs used in the prototype allowed three degrees of rotational freedom through a ball joint, which is thought to alleviate bending moments at the supports.

Radial forces should ideally act in the surface plane; however, the ball joints were located in the stud, resulting in localised moments depicted in Figure 9.4. This effect was more pronounced with fewer support points as the load per stud increased. Axial forces also created bending moments in the pane in the form of a network of "fold lines". In the areas where the folds intercept, pinch points were created resulting in irregular local deformations.

Figure 9.5 shows the spatial deviation of the reflective surface of a prototype facet from the desired spherical shape. Data was obtained using the CMM. Here the undesirable deformations outside the stud pattern are visible.

Figure 9.4: Bending moment and deformation at stud connection.

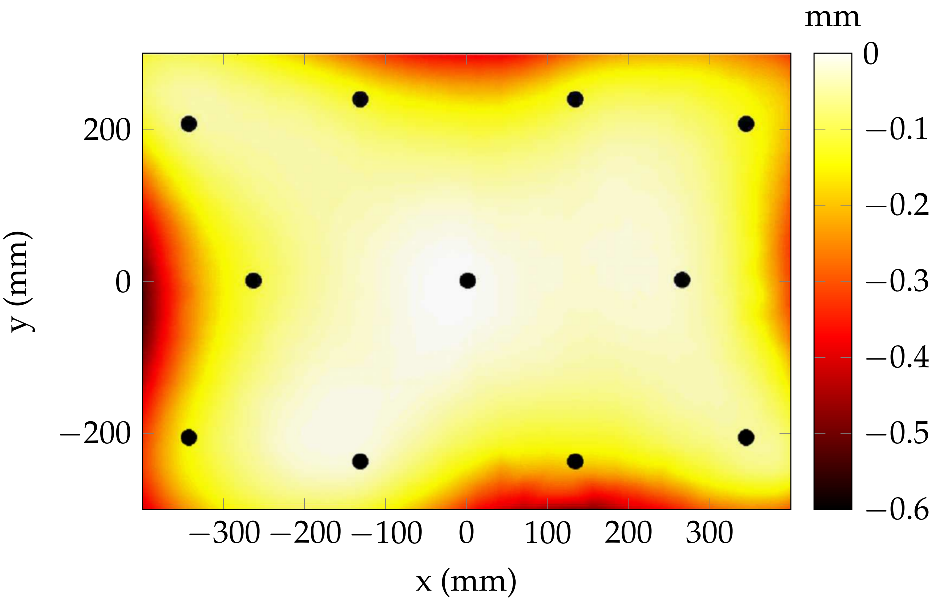

Figure 9.5: Spatial deviation of a facet from ideal profile (dots indicate stud placements) obtained using the CMM

Glass pane deflections under point and ring support for telescope applications have been studied by Nelson *et al.* [169] who conclude that deviations can significantly be reduced by increasing the number of support points and minimising the unsupported area. A triangular grid is also shown to be the most efficient layout of support points.

9.5.2 Stamped plate facet

A stretch-formed or stamped steel sheet can be bonded to the glass pane to increase the support area and improve the facet's moment of inertia. Similar to the construction of a car's bonnet, this concept is well suited to high volume manufacturing, which could lead to lower manufacturing costs. The design is lighter than conventional steel frame facets, and the greater contact area allows the use of thinner mirrors than point supported facet. Yellowhair and Andraka [153] suggest that the cost reductions achieved using this concept come at the expense of optical performance.

The formed steel sheet needs to be flexible enough to ensure that it can drape over the glass to the desired curvature. The design stiffness of the facet is only reached after bonding the sheet to the glass.

Initially, a concept where numerous replicated steel indentations in the steel sheet, similar to a muffin pan, was used to increase the moment of inertia. This concept worked well for small facets, but as the span between indentations increased, deformations occurred along lines of weakness. This finding reiterates that the moment of inertia must be maintained along all cross-sections of the facet.

An elementary prototype was constructed with folded sheet metal, and it was found that three-dimensional inertia is essential. This was achieved using radial arms and compressive edge channels. "Spring-back" in the steel resulted in local deformations, and the "print through" effect, where the supporting members can be observed from the front of the glass sheet, was prominent.

A stamped facet for Stirling dish technology has achieved σ_{SSE} of $<0.6\,\text{mrad}$ using 0.7 mm glass at radii of curvature of 14.9 m [170]. σ_{SSE} were not affected by cracks in the glass, and the design showed no degradation over an eight year period.

This design has been adapted to heliostats and has successfully been implemented in the both the Gemasolar and Tonopah central receiver systems (Figure 9.6). The patented design manufactured by BATZ Energy [171] uses sheeting thinner than 1 mm and claims repeatability and high tolerances. The sheet extends beyond the edge of the glass to avoid breakages and aids in perimeter rigidity. The sheet is also punched using a press in non-critical areas to reduce weight, and the design accounts for water drainage from the cavities.

9.5.3 Sandwich type facet

Previously the moment of inertia and support of the reflective surface were highlighted as important factors to reduce slope errors. Both of these factors are addressed by the sandwich type concept.

The moment of inertia of a panel can be maximised with minimum material by placing the material as far away from the bending axis. This results in the sandwich concept where the stressed material is placed above and below a core material. The outer skins carry compressive and tensile stresses, while the core must withstand relatively low compressive and shear stresses. The reduction in material use results in high strength to

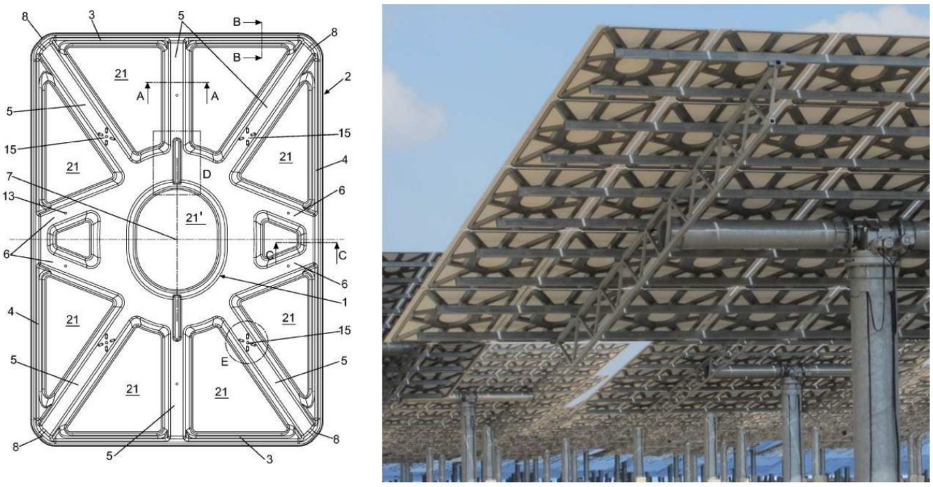

Figure 9.6: Formed sheet facet used at Gemasolar and Tonopah central receiver systems [171]

weight ratios. The structural rigidity allows the facet to be incorporated as a structural member of the backing structure.

The sandwich construction also offers support over the entire surface of the mirror, essentially creating the ideal load distribution. The greater contact area also allows the use of very thin glass and is considered to be well suited for good optics [160]. Diver and Grossman [37] suggest that sandwich designs provide structural stability and superior optical performance but are more expensive than other designs.

Sandwich construction has been experimented with since the 1970's but was initially abandoned due to high costs and moisture problems. More recently, companies such as Tough Trough [172] and Rio Glass [173] have reintroduced this technology into the market.

Diver and Grossman [37] conduct optical performance, environmental durability and cost prediction studies of sandwich type facets. All sandwich constructions are shown to be very accurate. All foam cores are found to result in long term degradation due to creep, but honeycomb cores are both accurate and durable.

The use of moulds and composites require higher production volumes to become economical. Sandwich constructions are known to suffer from thermal deformation, and thermal cycling [37]. Although the stiffness of the core material itself will not play a significant role in the overall structure stiffness [174], delamination may occur due to high shear loads at the bonding surface. These effects can be avoided through correct material selection and manufacturing methods [175].

Sandwich facet prototypes resulted in better optical performance than the other concepts, but the composite construction introduced various complexities. Initially fibreglass was used as the outer skin, but fibreglass was discovered to be an unstable material [176], and deformation occurred after three months. A galvanised steel backing was found to be stable, but adequate adhesion to the galvanising was problematic.

9.5.4 Concept selection

The sandwich concept was found to be most suitable for the Helio100 heliostat design. Various factors were considered for the selection. The continuous support offered by the sandwich concept gave the best probability of achieving the high accuracy requirements and allowed the use of thin glass, which maximises reflectivity. Cost goals could be met with this concept, and by using only a single facet with a sandwich construction, the need for a backing structure was negated, further reducing cost (see Figure 9.7). The panel construction was inherently more rugged than alternative concepts due to the continuous glass support and the incorporation of a protective edge. The panel construction also allowed for easy handling, transport and installation; all could be done by hand. The primary risks associated with this concept were surface degradation and de-lamination of the skins. Mitigating these risks was one of the main challenges during the facet development.

Figure 9.7: Sandwich type facets installed at the Helio100 field

9.6 Design iterations and learnings

The components that make up the sandwich panel include a core with two outer skins. Although many high performance products are available for sandwich type panels, most of these products were rejected based on cost. The design was strictly limited to the use of cost effective materials.

The initial facet design was constructed using a "cast in place" foam core with the glass pane and a galvanised steel sheet as the two outer skins. The glass was used as a structural element to reduce cost, and the use of liquid foam eliminated the need for adhesives. The fabrication process consisted of injecting the liquid foam into an artificial cavity. The pressure of the expanding foam forced the glass pane onto a mandrel, creating the correct profile.

Although this design could meet the requirements, the fabrication method contained numerous variables which could not all be controlled. Additionally, the quality of the facets produced was inconsistent, ranging between 1.2 mrad and 2 mrad. Variability of factors that affected the exothermic reaction such as temperatures of the skins and the foam components, their mixing and pouring, and the reaction pressure and flow characteristics of the foam in the cavity could not be eliminated.

The suboptimal foam reactions resulted in uneven core densities. One specific problem resulted from flow patterns during foam expansion in the cavity. Foam cells were found to elongate in the flow direction, resulting in elliptical cell structures. These elliptical cells resulted in anisotropic material properties, and cells collapsed in certain areas, leading to local surface deformations and facet degradation.

To achieve a more repeatable process, liquid foam was replaced with a precast foam core that was bonded to the skins with an adhesive. The selection of a precast foam core and the adhesives was done experimentally. Numerous types of affordable cores were purchased and tested for their material properties. Effects resulting from moisture on the foam were also considered. Bonding of the adhesives to the galvanised sheeting was prone to peeling but was resolved with a polyurethane adhesive.

The fabrication process clamped a memory foam sheet with the layup to achieve an even and repeatable pressure distribution on the panel. The repeatable results allowed determinate errors to be identified. A software algorithm was developed to determine 30 µm shim profiles that could be cut and placed on the mandrel to correct the determinate errors, resulting in σ_{SSE} of 0.7 mrad to 1 mrad.

The initial "cast in place" facet was implemented for the majority of the heliostats in the Helio100 field, pictured in Figure 1.1. The precast design was implemented on the second generation heliostats which make up a smaller portion of the field.

9.7 Facet performance

Here the optical performance, the structural properties, the thermal stability and degradation of precast facet design are discussed.

9.7.1 Optical performance properties

As discussed throughout this work, reflective surface profile is an important aspect of heliostat performance. Using the in-house deflectometry system, the optical performance of a facet was evaluated based on two main parameters: the surface slope error and the facet focal length. The σ_{SSE} of the design ranged from 0.5 mrad to 0.85 mrad. The design radius of curvature of the mandrel was 77.6 m. The facets ranged from 75.3 m to 81.4 m. Figure 9.8 shows the normal vector errors of a facet selected to showcase the typical errors present in the facet design.

The fabrication of the facets was done by hand, making it difficult to achieve repeatability. Several indeterminate errors resulted from the process itself. The adhesive was applied by hand, and its consistency and setting time varied according to the temperature and the mixing and application process. Depending on the room temperature and the order and force with which the clamps were applied, the composite mandrel deformed differently under pressure. These are just some examples of the issues that can be resolved with automation.

The most prominent errors were edge errors as can be seen on the left edge of Figure 9.8a. This type of error resulted from four different sources. In the case where the pressure applied to the sandwich structure did not extend over the edge of the facet layup, the edge would not properly contact the mandrel. Friction between the pre-cast foam and the bath walls also caused an uneven pressure. A taping procedure before gluing to seal the bath, if done incorrectly, also caused an unsupported edge. Lastly, the steel backing sometimes drifted during clamping resulting in a reduction of moment of inertia on an edge, which also resulted in an error along that edge.

A print through of the three mount locations is also observed. At these points, the tensioning of the mounting plates result in concave dimples. The points that carry the weight of the facet (bottom centre) give the highest errors.

Some of the errors are inherent to the glass pane itself. The glass panes had visible waves parallel to either the x or the y direction. These waves are referred to as "streaks" [130] and appeared at intervals of roughly 40 mm. It was also common to find a wave along one of the four edges. Yellowhair [160] suggests that this is a common error in float glass. This wave caused a deformation roughly 40 mm to 80 mm from the edge, as observed on the top edge of Figure 9.8b. Errors inherent to the glass pane could not be eliminated during facet fabrication; this presents a limitation of what surface slope errors can be achieved.

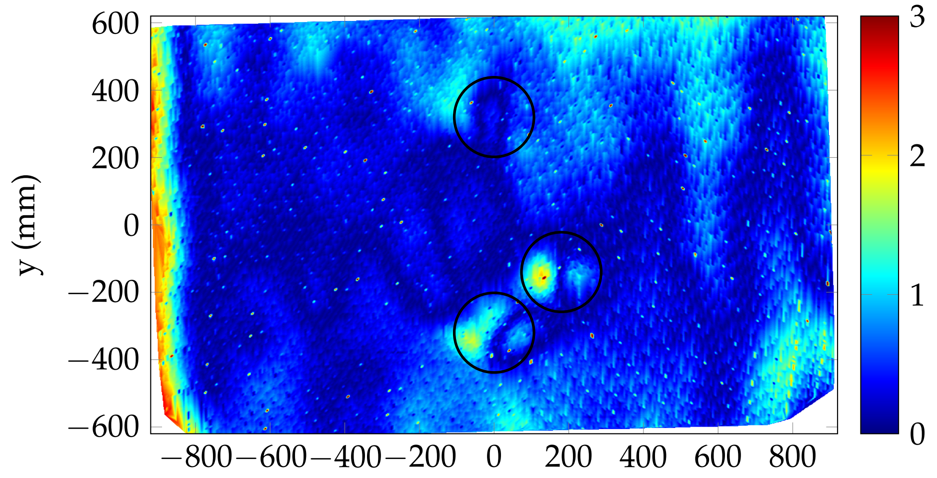

(a) x component of the normal vector error, ϵ_x (mrad) ($\sigma_\text{x} = 0.612\,\text{mrad}$)

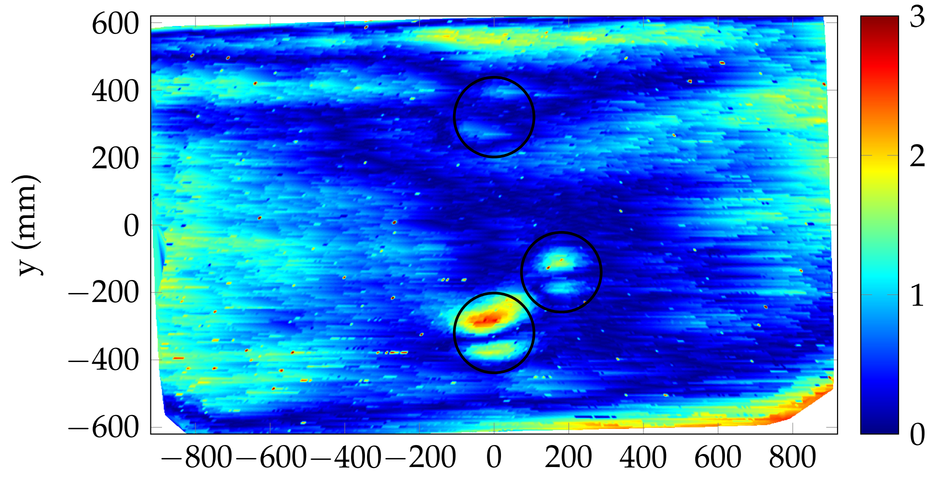

(b) y component of the normal vector error, ϵ_y (mrad) ($\sigma_\text{y} = 0.788\,\text{mrad}$)

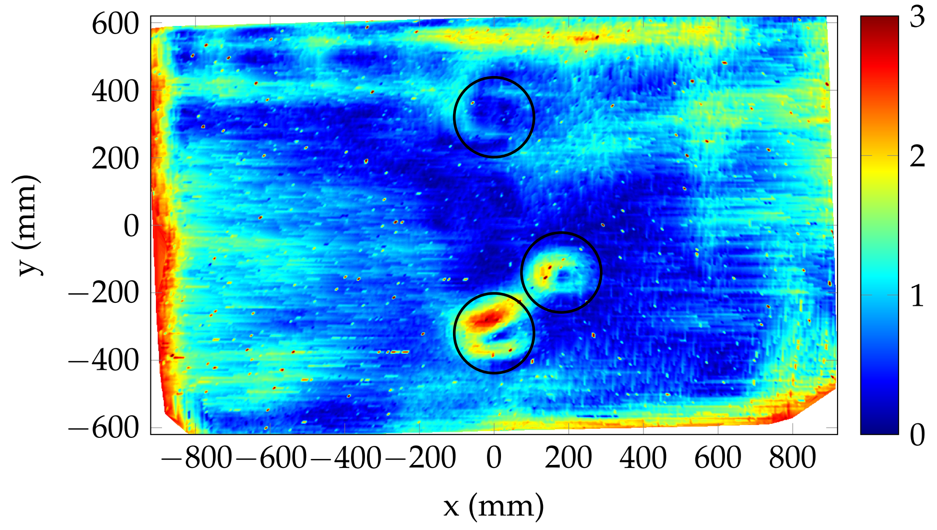

(c) Normal vector error, ϵ (mrad) ($\sigma_\text{SSE} = 0.695\,\text{mrad}$)

Figure 9.8: Normal vector error of a facet in the x and y components as well as total error; the three circles indicate facet mounting positions

9.7.2 Facet stiffness and deformation

During operation, the facet experiences both gravitational and wind loading, which can alter the profile of the facet, as depicted in Figure 9.9a. The facet should have adequate stiffness to maintain its profile during loading.

The unique three central mounting point configuration of the facet requires an additional consideration of pointing accuracy. During non-uniform wind loading, local deformations normal to the mirror plane at the support points cause a global change in facet normal directions as illustrated in Figure 9.9b.

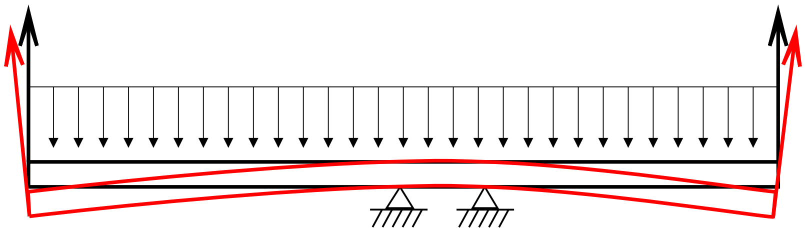

(a) Wilt from gravitational and wind loading

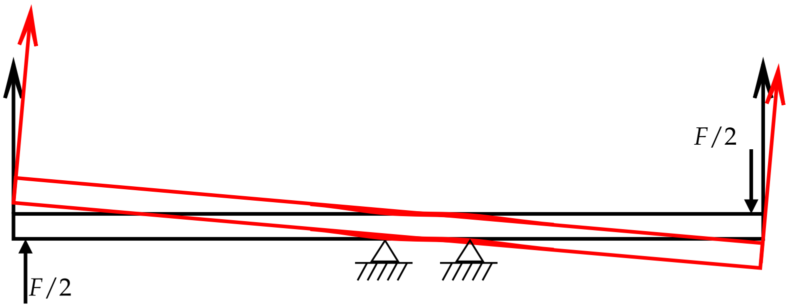

(b) Pointing error from local deformations at mounting points

Figure 9.9: The two loading cases illustrating wilt and pointing error

Worst case quasi-static wind loading on the facet, assuming an isolated heliostat, is detailed by Larmuth [49] based on the method of Peterka and Derickson [177] using corrections for both the aspect ratio and revised load coefficients proposed by Pfahl *et al.* [178] and Pfahl *et al.* [179]. This method is considered to be conservative [49]. Different requirements needed to be met in three wind speed categories outlined in Table 9.2.

Table 9.2: Wind load cases

Wind speed	Orientation	Requirement
≤20 km/h	All	Must meet normal tracking requirements
≤50 km/h	All	Must meet reduced tracking requirements and survive in an operational state
≤135 km/h	Stow	Survive in an operational state

For the first two load cases, the moment around the secondary axis (see Figures 2.6b and 9.9b) was the dominant load, with moments of 20.6 N m and 128.6 N m at wind speeds of 20 km/h and 50 km/h respectively. At 135 km/h, a normal force of 499 N dominated.

The survival loads testing showed no damage for normal forces of up to 530 N and moments up to 588.6 N m. Instead the focus was on achieving the stiffness to meet the tracking and slope error requirements for the 20 km/h corresponding to a moment of 20.6 N m.

The stiffness of composite beams is typically given as an equivalent flexural rigidity, EI, which is the combined elastic modulus and moment of inertia of a composite beam. The minimum flexural rigidity in the plane normal to the longest edge was experimentally determined to be 0.215 MPa.

Figure 9.10 shows the pointing error and slope error variation with an increasing moment as depicted in Figure 9.9b. The loads were applied using a whiffle tree arrangement to avoid point loads. The most prevalent error is the pointing error, which increases linearly at 17 µrad/(N m). As stated previously, this error occurs due to local deformations at the mounting points normal to the mirror plane. This error presents the most potential for improvement in the design.

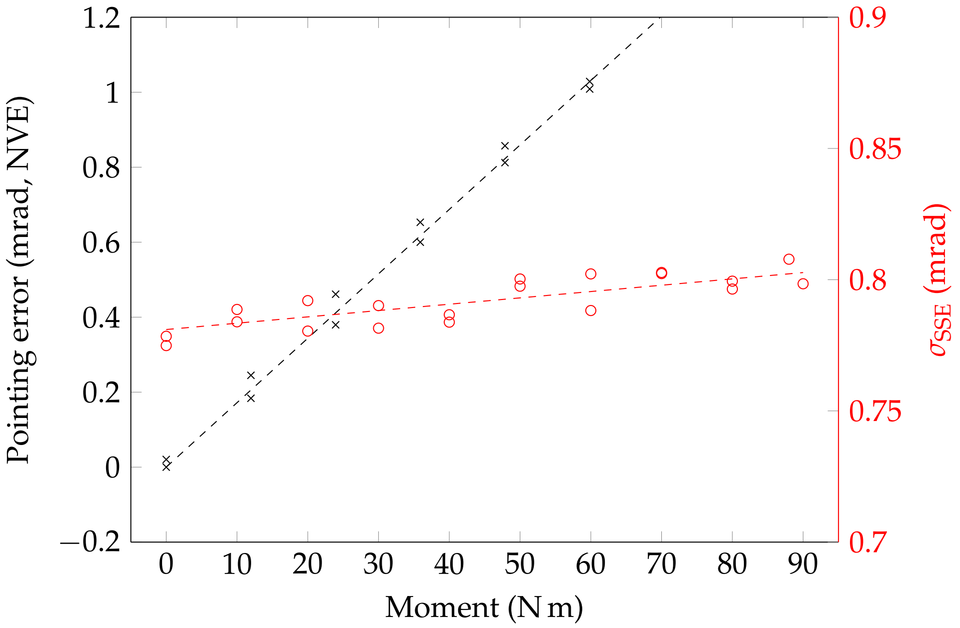

Figure 9.10: Pointing error and surface slope error variation with applied moment on the facet

The slope error increase of 0.24 µrad/(N m) is predominantly from the increased local deformations at the three mounting points during loading.

The noise in the σ_{SSE} data is a result of the precision of the deflectometry system.

The facet weight of 27 kg results in gravitational loading, or wilt. Figure 9.11 shows the decrease in the radius of curvature as the facet normal moves away from the gravitational vector, from a maximum loading in a horizontal stow position (0°), to zero normal load in a vertical position (90°). This effect causes a variation in the focal length of 0.3 m over the range of facet orientations.

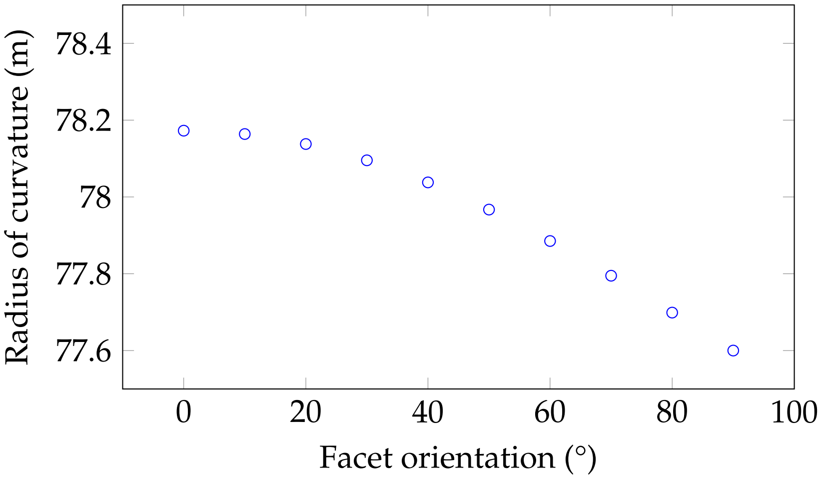

Figure 9.11: Radius of curvature of the facet relative to the gravitational vector. Facet is horizontal at 0° and vertical at 90°

The resonant frequencies of the facet were also considered. Wind excitation was estimated to be below 4.4 Hz. During testing the facet showed a resonant frequency as low as 6.7 Hz about the excitation axes, which should be increased in a future iteration.

A resonant frequency of 1.7 Hz was measured axially around the facet surface normal. Although the facet is not expected to experience any loading in this mode, the low resonant frequency could result in excitation at wind speeds of approximately 60 km/h.

9.7.3 Thermal performance

There exists several cases where the surface temperatures of the facet may exceed typical operational temperatures. Consider a heliostat tracking in the field that is blocking a second heliostat. This facet receives radiation from both the front and the back. Assuming the backing sheet is an electro galvanised steel sheet, the sheet will have a high specular reflectance redirecting light back to the blocked heliostat, which in turn may reflect the radiation back to the blocking heliostat. Such an event, or permutations thereof, may result in a facet exposed to large amounts of radiation, resulting in elevated temperatures. The specular reflectance of the galvanised backing sheet reduces with oxidation.

A degree of thermal stability must be maintained within a specified temperature range to ensure optical performance [37]. To test the behaviour of a facet at elevated temperatures, a facet fitted with thermocouples was placed in a heated room and allowed to reach thermal equilibrium at a temperature of 34 °C. The facet was then moved to a room at 15.3 °C and allowed to cool under natural convection. During cooling a deflectometry system was used to take readings at 3 min increments. The deflectometry system estimated the radius of curvature of the facet by finding the radius at which the RMS error was a minimum in increments of 0.37 m.

Figure 9.12 shows the average core and surface temperatures of the facet as well as the increase in the curvature of the facet during cooling. The first observation is that surface skins cool faster than the core of the facet; this was as expected. The thermal expansion coefficient of glass is 8.5×10^{-6}/°C [165] while that of steel is 12×10^{-6}/°C. As expected, the steel contracted more than the glass, resulting in an increase of the radius of curvature of 11 % during the 14 °C temperature drop.

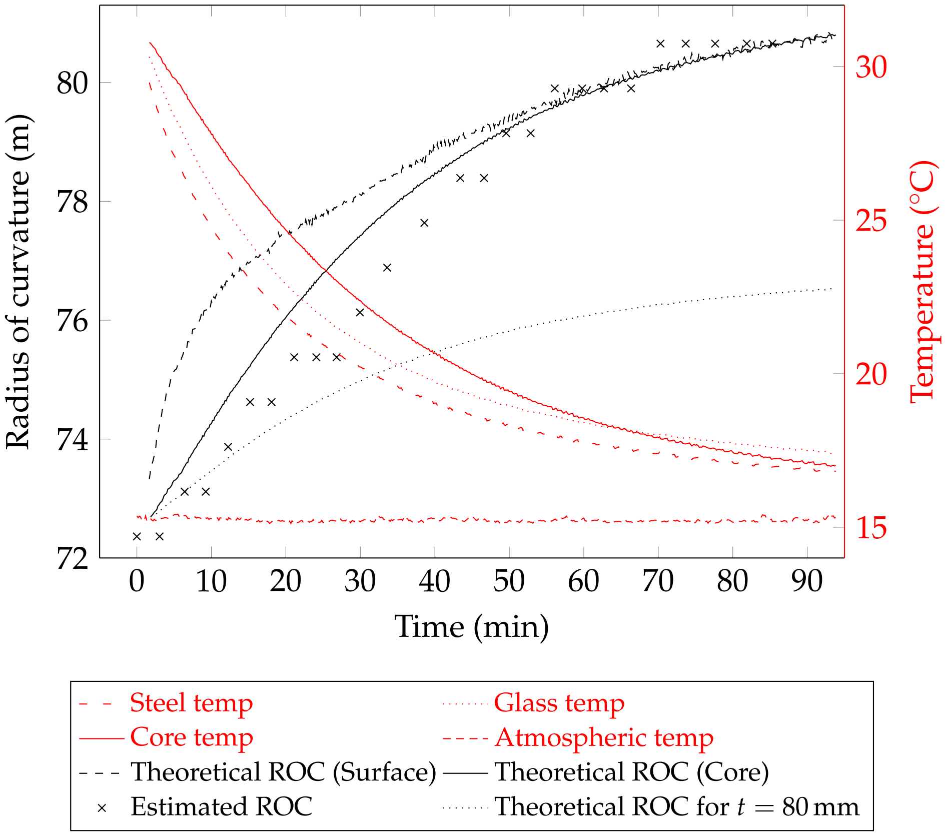

Figure 9.12: Effect of temperature variation on facet focal length

A theoretical function for the radius of curvature can be derived by considering the expansion coefficients, α, and temperature changes, ΔT, in both the glass pane and the steel sheet, where r_i is the initial radius of curvature and t is the distance between the mid-planes of the upper and bottom skins. The function is able to describe the variation of the radius of curvature using the core temperature of the facet. The surface temperatures, which cool significantly faster than the core, may be misleading. It appears that the average glass and steel temperatures are similar to that of the core.

$$r_\mathrm{T}(\Delta T_\mathrm{g}, \Delta T_\mathrm{s} \mid \alpha_\mathrm{g}, \alpha_\mathrm{s}, t, r_\mathrm{i}) = \frac{t}{\frac{\left(\frac{t}{r_\mathrm{i}}+1\right)(1-\alpha_\mathrm{s}\Delta T_\mathrm{s})}{\left(1-\alpha_\mathrm{g}\Delta T_\mathrm{g}\right)} - 1} \tag{9.1}$$

By increasing the core thickness, the sensitivity of the panel to temperature changes can be reduced. In the case where the core thickness is doubled from 40 mm to 80 mm the change in the radius of curvature is halved (Figure 9.12). Alternatively, steel sheets used in both the top and bottom skins may completely eliminate this effect, but it would increase the facet weight and cost.

9.7.4 Degradation

A control facet pictured in Figure 1.1 was installed in the field and used to monitor facet degradation. At each evaluation, the facet was disassembled from the heliostat and transported by road to be tested by the deflectometry system. Figure 9.13 plots the surface slope error of the facet over a twelve month period. During this time the facet underwent typical operations and was exposed to atmospheric conditions, including wind speeds of up to $47\,\mathrm{km\,h^{-1}}$.

Initially, the facet appears to be stable and no degradation is observed for the first four months. In the fifth month both σ_x and σ_y degrade by 0.2 mrad. Deflectometry results indicate that degradation occurred predominantly at the three mounting points. It is speculated that this degradation resulted from creep in the polyurethane foam; however, an unknown loading event may also have caused this abrupt increase in surface deformation. After this point no additional degradation was observed. Remaining features of the surface profile appear to be stable although some edge effects appear marginally amplified.

During this time period the deflectometry system underwent several software and hardware iterations, and it is unclear what influence this may have had on the results. Although no definitive degradation mechanisms or de-lamination could be identified during this period, the time that facet had been exposed was relatively short. A definitive conclusion on the future degradation cannot be made using a single sample and a further 12 facets are currently undergoing a similar tests.

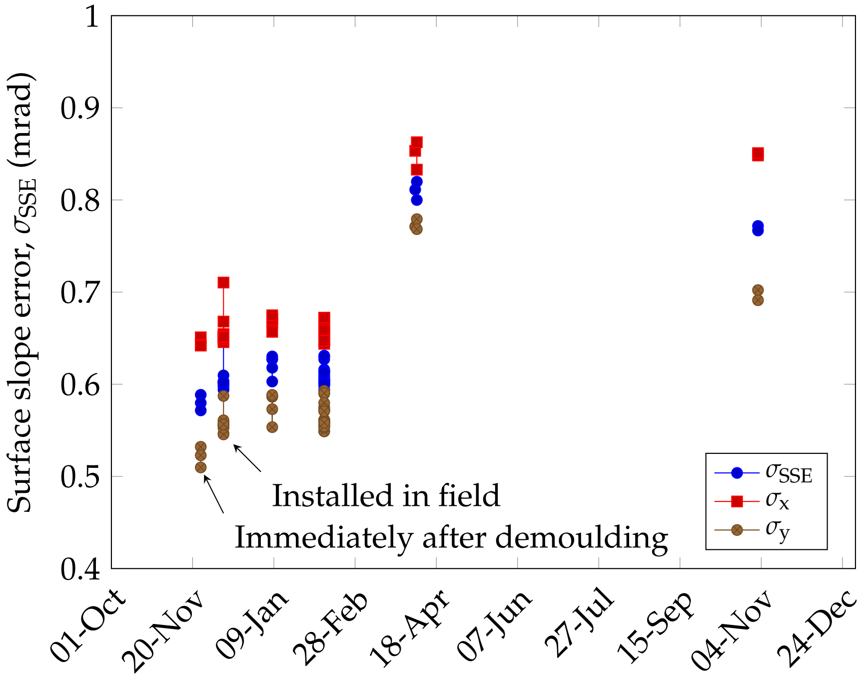

Figure 9.13: Degradation of the control facet pictured in Figure 1.1 (p. 3)

9.8 Conclusion

This qualitative investigation of a glass based facet design indicates that implementation of an optically accurate, stable and cost effective facet is non-trivial. This finding supports the literature, which suggests that no single facet concept provides an optimal balance between low cost and good optical performance [153].

The study focused primarily on achieving optical accuracy. It shows that the reflective surface profile is sensitive to numerous variables of both the design and the fabrication process. This suggests that a fabrication process that can ensure repeatability is important to enable determinate errors to be identified and corrected. SSE's are found to be most prevalent in cases where the facet either has a short focal length, is large, uses thin glass or supports the glass pane discretely. The edges of the facet seem to be particularly susceptible to SSE due to a buckling effect from the compressive stresses present during three-dimensional curvature.

The implementation of a sandwich type facet provides evidence that optically accurate, short focal length facets with SSE as low as 0.7 mrad is achievable. It appears that the main challenge of the sandwich type facet is not optical accuracy but rather the development of a sandwich panel that is both economical and able to withstand atmospheric degradation.

Chapter 10

Techno-economic sensitivity study of heliostat field parameters for MGT CSP

In this chapter the knowledge gained in Part 1 and the methods developed in Part 2 are applied to a MGT central receiver system, and a techno-economic sensitivity study of heliostat field parameters is presented.

The content and format of this chapter is substantially a reproduction of a paper submitted to the 2016 SolarPACES conference and only slight amendments have been made.

10.1 Abstract

Concentrating solar power systems based on MGT potentially offer numerous benefits should they become commercially viable. Heliostat fields for such systems have unique requirements in that the number of heliostats and the focal ratios are typically much lower than conventional central receiver systems. This paper presents a techno-economic sensitivity study of heliostat field parameters for a MGT central receiver system. A 100 $\mathrm{kW_e}$ minitower system is considered for the base case and a one-at-a-time (OAT) strategy is used to investigate parameter sensitivities. Increasing heliostat focal ratios are found to have significant optical performance benefits due to both a reduction in astigmatic aberrations and a reduction in the number of facet focal lengths required; this confirms the hypothesis that smaller heliostats offer a techno-economic advantage. A FHA tracking mechanism is shown to outperform the conventional AZ tracking mechanism in high density heliostat fields. Although several improvements to heliostat field performance are discussed, the capex fraction of the heliostat field for such a system is shown to be almost half that of a conventional central receiver system. Furthermore, optimum utilization of the higher capex components, namely the receiver

and turbine subsystems, are more rewarding than that of the heliostat field.

10.2 Introduction

CSP systems based on MGT potentially offer numerous benefits should they become commercially viable. Higher temperature power cycles, such as the Brayton cycle, are generally more efficient. In the context of combined cycles or recuperated gas turbines, they may lead to an overall reduction in the cost of the electricity produced [7; 8]. These cycles are scalable from large grid-connected modular power stations to small distributed modular power generation closer to the end user. Additional advantages of gas turbine systems include their independence of water required for conventional CSP systems and decentralized generation reduce grid access constraints.

Brayton cycles require temperatures above 850 °C [7]. The temperatures obtainable in a solar power plant is linked to the flux density from the heliostat field. Flux densities required for cavity air receivers range from $1\,\mathrm{MW/m^2}$ to $10\,\mathrm{MW/m^2}$ [11], necessitating the need for secondary concentrators [12], high-precision optics and accurate heliostat control.

Heliostat fields for MGT CSP have unique requirements in that both the number of heliostats and the focal ratios are typically much lower than conventional CSP plants. This paper presents a techno-economic sensitivity study of field parameters for an MGT CSP plant to identify sensitivities and highlight important field variables with the hypothesis that the small low cost Helio100 [180; 161] heliostat system offers a significant techno-economic advantage.

10.3 System assumptions

The primary focus of this paper is the techno-economic sensitivity of the heliostat field parameters in the context of a MGT CSP system. These parameters are investigated in detail while additional parts of the system such as receiver performance, thermodynamic cycle, operating strategy and financing mechanisms make some simplifying assumptions. The case study is representative of a small scale MGT central receiver system. However, since neither the system configuration nor the field layout is optimized, performances documented here may be lower and costs higher than what can be expected in the implementation of an optimized system configuration.

The case study investigated here assumes the $100\,\mathrm{kW_e}$ minitower configuration with the $16\,\mathrm{m^2}$ heliostat as detailed by Buck and Teufel [137]. The system includes no storage and has a solar multiple (SM) of 1.8 to ensure that the turbine can achieve maximum power output for a large portion of the day. The option of supplementing energy production by the combustion of a fossil fuel is not included in the base case, but is discussed later in this paper.

Due to the small size of MGT's, economies-of-scale typically do not apply; thus, design simplification and production economics are of higher importance [181]. The Turbec T-100 is a simple 100 $\mathrm{kW_e}$ recuperated MGT system with a nominal electrical efficiency of 30 %. Turbine performance under varying load cases are deduced from the efficiency curves provided by the supplier [182] and assume atmospheric pressure of 101.325 kPa. Although not considered in this study, the elevation and atmospheric temperature has a significant influence on turbine efficiency. The system assumes the DIAPR receiver is capable of reaching 1200 °C and can handle flux densities of up to 10 $\mathrm{MW/m^2}$ [11]. Kribus *et al.* [183] suggest receiver efficiencies between 85 % and 90 % excluding CPC are viable for flux densities of 5 $\mathrm{MW/m^2}$ on a receiver aperture. Set receiver efficiency of 87.5 % was assumed.

An untruncated CPC as described by Welford and Winston [184] was used to obtain the required flux densities. The CPC performance is deduced from interpolating transmission efficiencies obtained from ray tracing in SolTrace [95]. The heliostat field is sized to provide a SM of 1.8 at a summer solstice with a DNI of 800 $\mathrm{W/m^2}$. The field layout assumes a regular spacing, which consists of a tessellation of equilateral triangles such as employed by Helio100 [180; 161] and eSolar [51]. The spacing or sides of the triangles are a function of a specified field density. Further field assumptions are given in Table 1 below.

The capital expenditure (capex) is financed through a single loan with a payback period of 10 years at an interest rate of 10 %. The discount rate is also assumed at 10 % and plant life is 30 years. Operation and maintenance cost is assumed to be 1.5 % of the total capex, and fuel costs rise annually by 8 %. Costs assume construction of 100 modular units, resulting in a total nominal power of 10 $\mathrm{MW_e}$. In the case where heliostat sizes are varied the $\$/\mathrm{m^2}$ cost was assumed to remain constant.

10.4 Methodology

A convolution based analytical model described by Landman *et al.* [149] was used for the optical modelling of the heliostat field. The model is based on the HFLCAL methodology [68] but additionally accounts for incidence angle effects. Each heliostat can be modelled with a varied number of beams as done in cone optics, and most heliostat performance parameters are accounted for. Blocking and shading is done using the method described by [159].

The optical model is validated by Landman *et al.* [149] but is again validated here against the SolTrace ray tracer [95]. Figure 10.1 shows the power into the receiver aperture throughout a clear summer day. It is noted that a

Table 10.1: Initial assumptions

Heliostat parameters	**Parameter values**
Facet dimensions	1 m x 1 m
Facet configuration	4 x 4 =16 m^2
Reflectivity	87 %
Specularity error	0.8 std dev (Gaussian distribution)
Surface slope error	1.2 std dev (Gaussian distribution)
Tracking error (Primary Axis)	0.65 std dev (Gaussian distribution)
Tracking error (Secondary Axis)	0.225 std dev (Gaussian distribution)
Canting strategy	On-Axis
Pylon height	2.25 m
Number of facet focal lengths	8 evenly distributed between shortest and longest slant range
Tracking mechanism	Fixed Horizontal Axis
Field parameters	**Parameter values**
Tower height (center of aperture)	29.2 m
Field layout	Regular, (Tessellation of equilateral triangles)
CPC aperture	Circular, 1.02 m diameter
CPC acceptance angle	30°
CPC orientation	North facing, tilted 43° downwards
Aim-point strategy	Single aim point at centre of CPC entrance aperture

maximum deviation of 7.2 % occurs at 17h00. The discrepancies are predominantly caused by the simplifying assumptions made in the blocking and shading algorithm and are most severe at low sun elevations when blocking and shading losses are high. The analytical method provides a significant computational advantage with a computational time of 0.57 seconds while the ray tracer took 66.12 seconds for 100 000 rays still not providing a fully converged distribution.

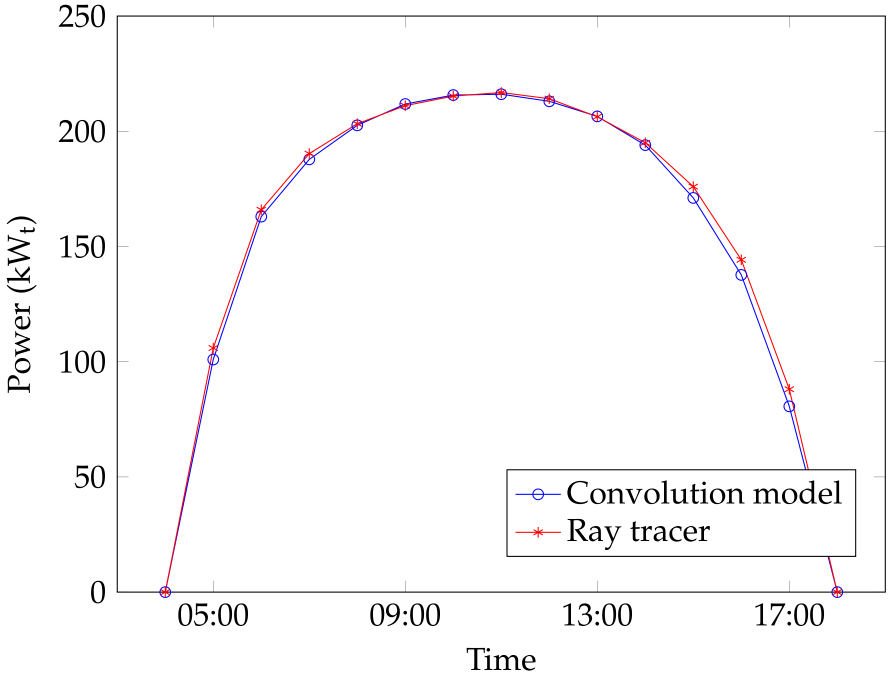

Figure 10.1: Optical power intercepted by the receiver over a single day for both the analytical model and the ray tracer

For annual simulations, heliostat field efficiencies are computed in a grid of 5-degree intervals for both azimuth and zenith of the sun. The field efficiency is then interpolated from this grid, allowing the field performance at any sun position to be determined in a computationally efficiently manner. The system is then run hourly for 30 years using TMY3 weather data.

10.5 Sensitivity analysis

The sensitivity analysis determines how the variability of several input parameters will impact specific dependent variables. The most basic method for assessing sensitivities is the OAT strategy where a correlation is determined between input and output variables over a specific range. Here, the techno-economic effects of heliostat design parameters, field parameters and the chosen operational strategy of the MGT plant are investigated using the OAT method. Each of these subsections is dealt with individually below. Although a large number of parameter variations are important in the context of the system, only a few sensitivities of interest are highlighted here.

10.5.1 Heliostat parameter sensitivities

Four heliostat parameters, including aperture area, aspect ratio, tracking mechanism and the number of facet focal lengths used in the field, are considered. The most useful parameter to observe the effects of heliostat parameters is the AIPWI [137]. AIPWI indicates the fraction of the annual reflected energy leaving the heliostats that is intercepted by the receiver. Jones [148] suggests that AIPWI is directly tied to the plant economics because it is an indicator of the heliostat cost to performance ratio. AIPWI, however, does not indicate system performance and does not account for field parameters such as layout and blocking and shading.

The first apparent observation in the study was that although AIPWI and LCOE are related, the LCOE minimum does not necessarily correlate with the maximum AIPWI (see Figure 10.6 and 10.7). In conventional power tower systems the heliostat field contributes a very large fraction of the plant capex (Figure 10.2), resulting in the LCOE being very sensitive to AIPWI. In contrast, for a small scale MGT system, the receiver and turbine dominate the capex, resulting in LCOE that is less sensitive to AIPWI. This implies that the commoditization of MGT's and receivers are important for cost reduction and that optimum utilization of the receiver and turbine subsystems may be more rewarding than the heliostat field. Furthermore, the optimal configuration is very sensitive to the financial assumptions made.

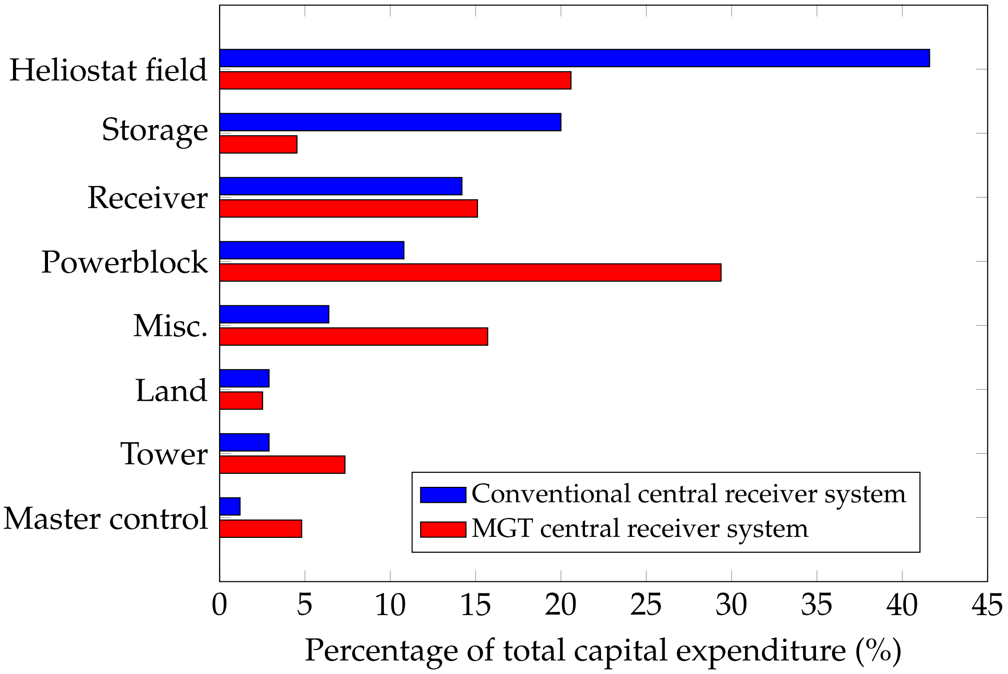

Figure 10.2: Breakdown of the capital expenditures of both a conventional central receiver system and a MGT central receiver system

The first sensitivity considered is the heliostat aperture shown in Figure 10.3. To compare the performance implications of different size heliostats, the different field layouts required should ideally be unbiased; however, this is difficult to achieve since field layout inherently affects the performance. The chosen approach populated an elliptical area with different heliostat sizes using a regular tessellation pattern while maintaining a common field density and total field aperture. For the simulation, the heliostat cost per area and pylon height also remained constant. It is noted here that an additional advantage of slight reduction in tower height is achieved using smaller heliostats for the same relative receiver position because smaller heliostats are closer to the ground. This effect is not included in the simulation.

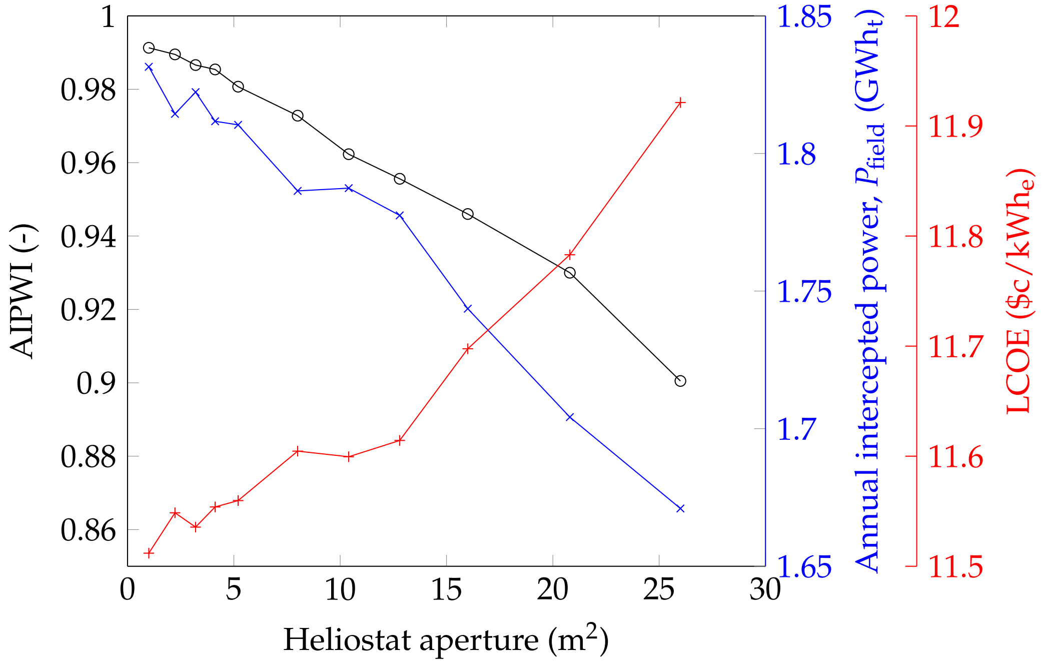

Figure 10.3: Sensitivity of the heliostat aperture on cost and optical performance measures

The AIPWI is found to decrease with increasing heliostat aperture as expected due to the lower focal ratios increasing astigmatic aberrations. The near linear correlation shows that heliostat optical performance is directly related to the heliostat aperture. The reduced performance also reduces the annual incident power on the CPC aperture (P_{field}) and increases the LCOE. The "noise" in both the LCOE and the Pfield data is a result of the suboptimal field layouts considered in which effects such as blocking and shading vary. A minimum LCOE is expected for smaller heliostat apertures given the assumption of a constant heliostat cost per area. This confirms the hypothesis that increasing the focal ratio by using smaller heliostats, such as the Helio100 heliostat system [180; 161], offers a techno-economic advantage. For the base case, reducing the aperture area by a factor of four reduces LCOE by 1.3 % and improves P_{field} by 4 %.

Figure 10.4 shows the effect of varying the number of facet focal lengths for the base case. The manufacturing of heliostat facets generally require a mandrel to shape the glass pane to a desired focal length. The mandrel is typically a large, expensive piece of equipment with high tolerances, and its production is limited to a single focal length. By reducing the number of facet focal lengths, the part variations are reduced, which in turn increase production volumes of a given focal length facet, and fewer capital intensive mandrels are required. Here, facet costs are assumed constant regardless of the number of focal lengths.

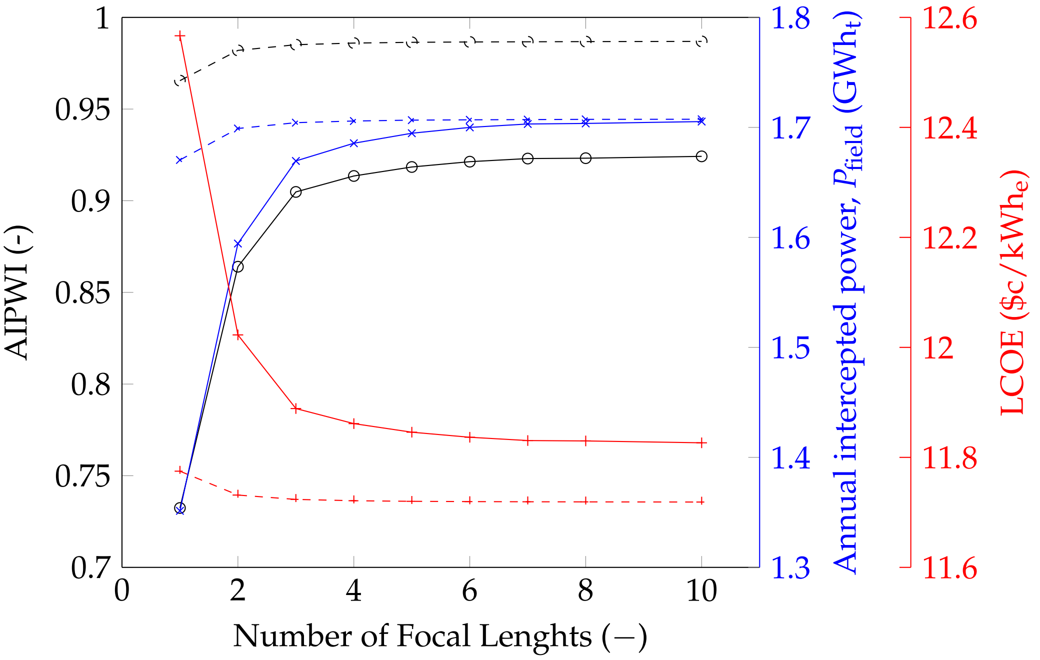

Figure 10.4: Sensitivity of the number of facet focal lengths on cost and optical performance measures. Solid lines are for the 16 m^2 base case heliostat; the dashed lines are for a 4 m^2 heliostat

The optical performance represented by AIPWI and related, P_{field}, increases and LCOE decreases with number of focal lengths. No cost penalty was included for increased number of focal lengths, resulting in a continued decrease of LCOE as the number of focal lengths increased. However in reality, reducing the number of facet focal lengths will reduce cost as well, and LCOE is expected to increase with the number of focal lengths. Initially the benefit of additional focal lengths is significant but increasingly deteriorates until the effect is negligible above 8 focal lengths. If the facet focal length is shorter or longer than the slant range, an astigmatic effect enlarges the image at the target plane. This effect is dramatically reduced the nearer the focal length is to the slant range, which explains the performance improvement.

The dashed lines in Figure 10.4 show a more constant performance for a smaller 4 m^2 heliostat. Since astigmatism is inversely proportional to the focal ratio, it is less pronounced at higher focal ratios. An advantage of smaller heliostat apertures would thus be a reduction in sensitivity to the number of focal lengths in the field.

The aspect ratio of the heliostat is another important parameter for regularly spaced fields and influences the tower height and field layout. Because the spacing of heliostat rows are set for specific sections of the field, a balance must be found between shading near the tower and blocking further from the tower. Figure 10.5 shows the effect of aspect ratio on the field for both a FHA type tracking mechanism and an AZ type tracking mechanism. As expected, an optimum aspect ratio is near one, representing a square heliostat. For low aspect ratios below one, where the heliostat is taller than it is wide, heliostats at the rear of the field experience high blocking, resulting in a sharp drop in P_{field}. At higher aspect ratios, blocking remains relatively low. AIPWI is found to be symmetrical at about one and drops gradually as astigmatism increases due to the decreasing focal ratio.

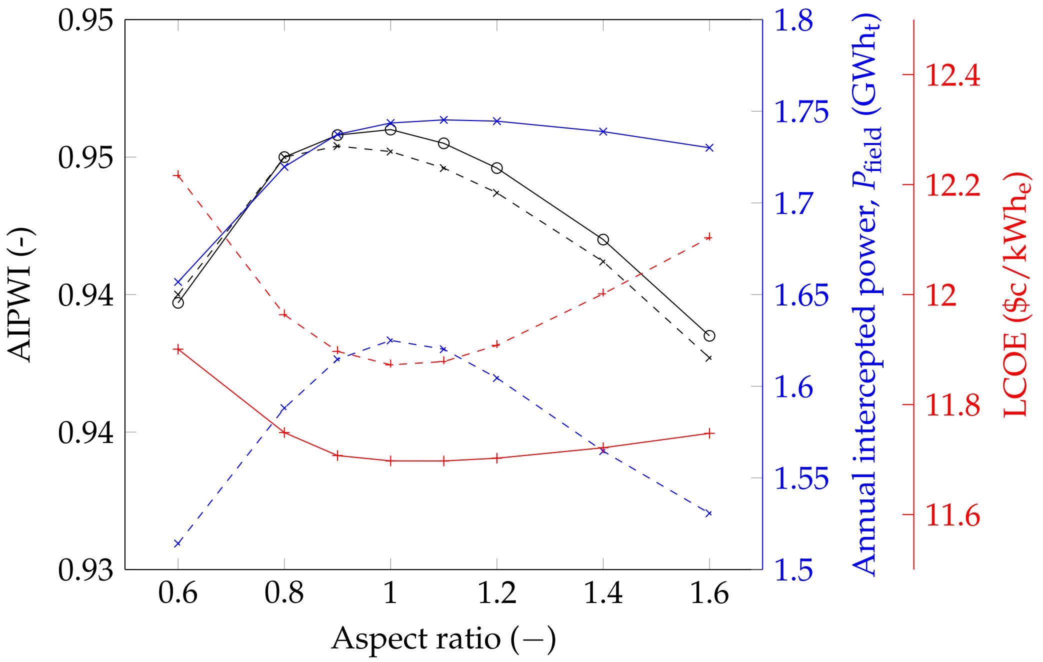

Figure 10.5: Sensitivity of the heliostat aspect ratio (w/h) on cost and optical performance measures for both FHA tracking (solid lines) and AZ tracking (dashed lines)

FHA tracking mechanisms are found to perform optically better than AZ tracking mechanisms in dense packed field configurations as considered in the base case. The reduction in blocking can be accounted for by the nature of the rotational envelope of FHA type tracking mechanisms as described by Schramek and Mills [33]. This implies that different tracking mechanisms will have different optimum field layouts, and the advantage of FHA may be a result of the regularly spaced field configuration chosen.

10.5.2 Layout and system optical sensitivities

The first system parameter considered is the tower height, as plotted in Figure 10.6. As the tower height increases, the receiver moves into the sun band (see Section 7.5.1, p. 84), reducing the range of incidence angles experienced by the heliostats and increasing performance. However, as the receiver moves further away from the field, the size of the heliostat images also increase, incurring spillage as is shown by the drop in AIPWI at 34 m. Power into the receiver continues to increase with tower height due to a reduction in blocking losses. Interestingly, the minimum LCOE is for a much lower tower near 22 m, again illustrating the capex sensitivity of MGT CSP.

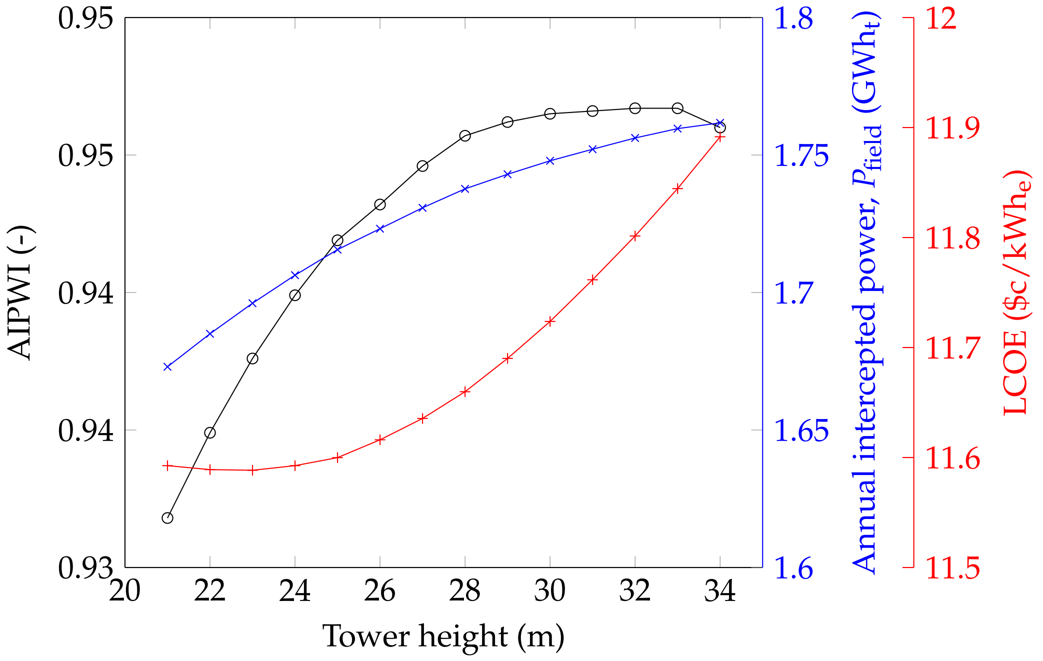

Figure 10.6: Sensitivity of tower height on cost and optical performance measures

The receiver size is also very sensitive due to its large percentage of the capex (Figure 10.7). A minimum LCOE results from balancing the improved intercept performance of a large receiver with the increasing capex.

Observations regarding the CPC acceptance angle confirmed the findings of Schmitz *et al.* [12] who showed that for smaller fields where the tower costs are still low the field layout is similar regardless of the use of secondary

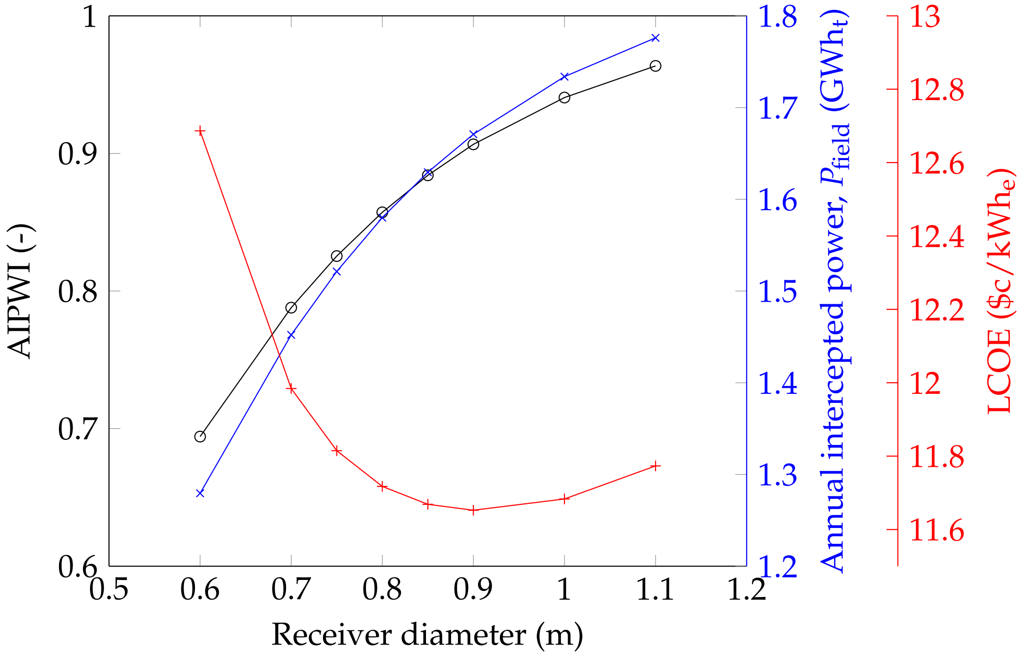

Figure 10.7: Sensitivity of receiver diameter on cost and optical performance measures

concentrators. For very small acceptance angles, the heliostat field becomes stretched out, resulting in heliostats being further away from the tower but also increasing flux density at the receiver aperture. Alternatively, larger acceptance angles allow heliostats to be placed in more optimum locations nearer the tower while still meeting the flux requirements. Pitz-Paal *et al.* [185] highlight that the higher flux density requirements lead to increased blocking and shading in high density heliostat fields, as well as higher spillage losses at the CPC aperture.

The heliostat field size was also varied and the effects of increasing field aperture are shown in Figure 10.8. Fields with different apertures were generated using the method described earlier for both 16 m^2 (solid lines) and 2 m^2 (dashed lines) heliostats using pod structures, as proposed by both Helio100 and eSolar.

Initially, as the field increases from 400 m^2 the LCOE drops sharply due to the increase of the turbine's capacity factor. The annual power delivered by the field increases almost linearly with the field aperture; however, due to the limited capacity of the turbine, the increase in the capacity factor slows with the increasing oversupply. This results in a limited performance advantage of a very large field and explains the reduced improvements in LCOE from 800 m^2 with a SM of 1.8 to 944 m^2 with a SM of 2.1.

The low cost fraction of the heliostat field does not seem to have a significant influence on the LCOE over the range considered, which suggests that the small increase in capacity factor still outweighs the cost of additional

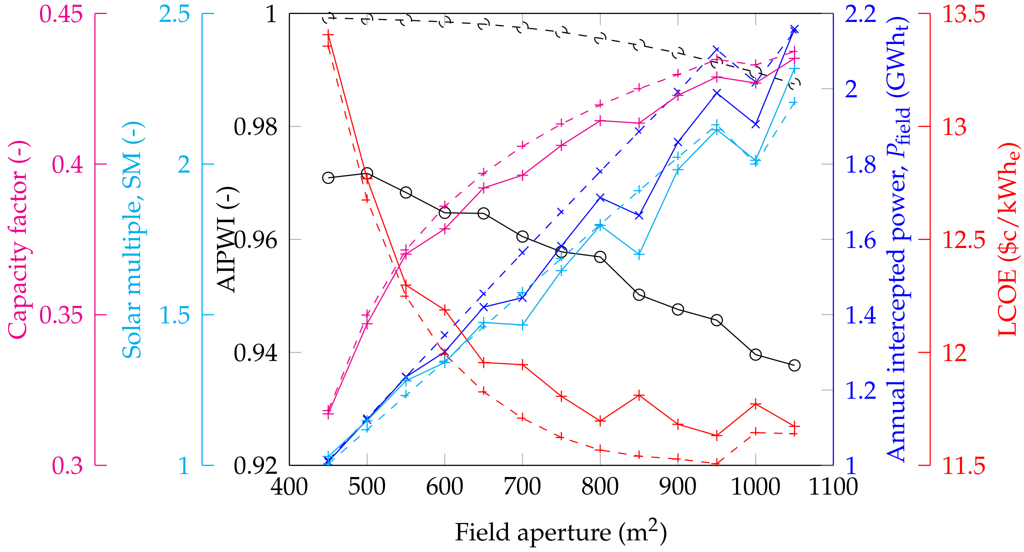

Figure 10.8: Sensitivity of the heliostat field aperture on cost and optical performance parameters using both 16 m^2 (solid lines) and 2 m^2 (dashed lines) heliostats

heliostats. The fact that the AIPWI remains high and the P_{field} behaves linearly suggests that the heliostats in the larger field still perform well optically. At an aperture of 1008 m^2 the field starts to exceed the limits of the CPC acceptance angle, which limits the P_{field} resulting in an increase in LCOE.

Comparing the two heliostat sizes further validates previous findings, which suggest that smaller heliostats optical performance benefit and the $\approx \$c2\,/\mathrm{kWh_e}$ drop in LCOE confirms that smaller heliostats have a higher marginal value. The smoother curves of smaller heliostats is indicative of the higher number of heliostats in the field, which behave in a more analogue fashion eliminating the digital "noise" of the field layout effects found with fewer large heliostats.

10.5.3 Operational strategy sensitivities

One advantage of MGT systems is that they can be hybridized. The solar heat input into the turbine can be supplemented or boosted by the combustion of a fossil fuel. This supplementation allows the turbine to be operated at peak efficiency or maximum power output during the day, and if required, the plant can produce electricity after dark.

Five different operating strategies (OS) were compared here:

1. System operates on solar heat only.
2. Fuel only supplements the solar heat during the day to maximize turbine efficiency.

3. Fuel supplements the solar energy to maximize turbine efficiency during the day and covers the peak demand time. Earnings assume the two-tariff system used in South Africa from round 3 onwards (REIPPP).

4. Fuel supplements the solar energy and maintains maximize turbine output for 24 hours a day.

5. Fuel supplements the solar energy to maximize turbine efficiency during the day, produces at peak demand time and runs at 60 % load at night. Earnings assume the two-tariff system used in South Africa from round 3 onwards (REIPPP).

Figure 10.9 compares the Internal Rate of Return (IRR) for each of the five strategies for a SM of 1.2 (dotted lines) and 1.8 (solid lines). A base tariff of \$0.15 /kWh$_e$ is assumed.

Strategies which use little fuel (OS 1 and OS 2) result in low gradients indicating insensitivity to fuel cost; however, as the use of fuel increases (OS 3, OS 4 and OS 5), sensitivity to fuel costs increase dramatically. At low fuel costs the higher use OS have lower cost of energy resulting in high returns, and on the contrary, high fuel costs result in a low or negative return. To achieve maximum returns one should implement a high fuel use strategy when the cost fuel is low and minimize fuel use when fuel costs are high.

OS 2 was expected to boost returns by ensuring that the turbine runs at maximum efficiency. However, this strategy did not result in an increase in IRR above a fuel cost of \$0.07 /kWh$_t$, and an increase in the SM (see Figure 10.8) is more rewarding, indicating that the capex invested into the heliostat field is more worthwhile than paying the fuel cost over the life of the plant.

For OS 3 the increase in the earnings during peak periods results in a significant increase in the IRR, indicating that this peak period is a high income generator and should be maximized. If such a peak tariff structure is not available, a high SM field is most attractive. The feasibility of high SM's illustrate the advantage of thermal storage.

Another interesting feature of the plot is the intersection point at \$0.05 /kWh$_t$ of OS 3-5 for both SM's; this is the cost at which the cost of burning additional fuel is cost "neutral". For any cost above this point, selling additional fuel actually reduces the return on investment, and a peak only strategy such as OS 3 should be used.

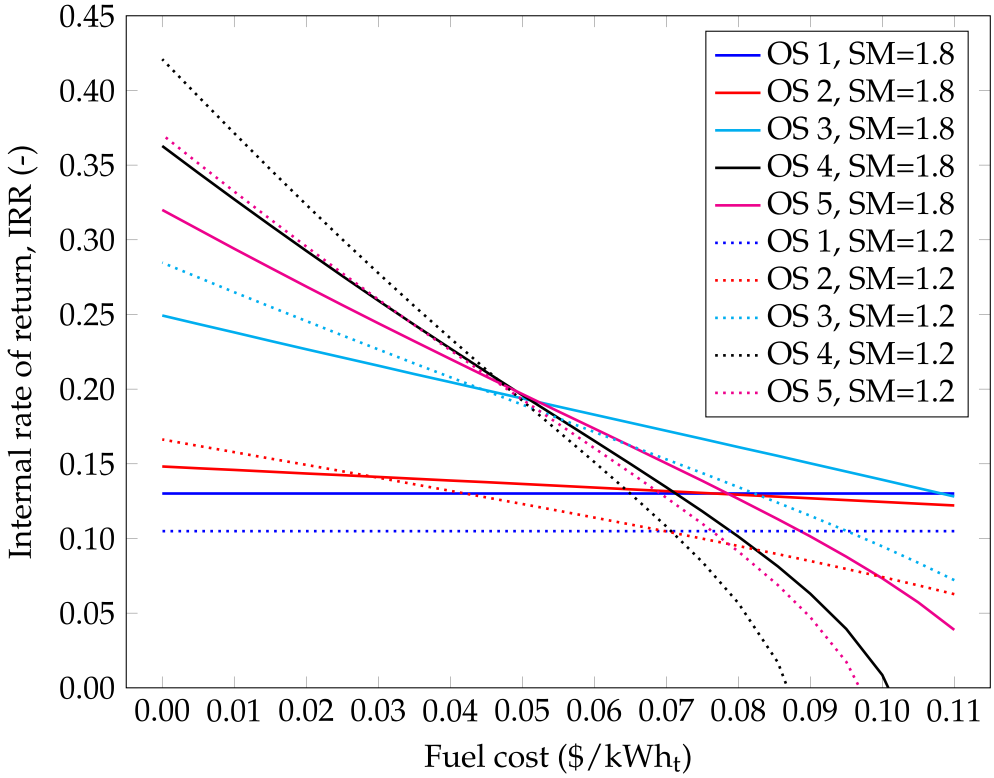

Figure 10.9: The internal rate of return of five operating strategies for a field with a solar multiple of 1.2 (dotted lines) and 1.8 (solid lines)

10.6 Conclusions

The proportionally high cost of the MGT power unit relative to that of a conventional central receiver system indicates that MGT technology is still in its infancy. Larger acceptance of this technology is expected to lead to changes in the cost breakdown due to the different learning curves and maturity of the various cost components.

The high capital expenditure and the high fuel costs used in this model result in the minimum LCOE occurring at high SMs. Such a configuration represents an oversized heliostat field with excess thermal capacity. Capturing this un-utilised energy in a small scale thermal storage system may be an opportunity to improve the techno-economics of MGT CSP.

The study validated previous findings, which show that, all things equal, smaller heliostats do provide higher optical performance. A 4 % increase in the annual intercepted power and a 1.3 % reduction in LCOE was achieved for the base case by reducing the effective heliostat area by a factor of four.

The variations of both the cost breakdown and the optimum optical field configurations suggest that MGT CSP does have different heliostat field parameter sensitivities than conventional central receiver systems.

Chapter 11

Conclusion

MGT central receiver systems can arguably be considered as a viable technology contender for future generations of CSP plants. The small modular configuration and the high flux requirements of the Brayton cycle suggest that heliostat fields have alternative parameter sensitivities. The objectives of this study were to fundamentally understand heliostat optics and develop tools and methods to investigate the techno-economics of MGT CSP. Here the findings and the conclusions of this dissertation are stated.

11.1 Summary of findings

Literature indicates that the methods used for optical modelling of heliostats typically fall into one of two categories. The methods either numerically describe the flux distribution, achieving high accuracies but at high computational cost, or alternatively, methods analytically describe the flux distribution using simplifying assumptions which reduces accuracy but provides a computational advantage. Literature also suggests that state of the art analytical methods that are used in flux distribution applications and require computational efficiency are unable to meet the accuracy requirements. This indicates that a computationally efficient analytical model with improved levels of confidence of the flux distribution of a heliostat would be a valuable contribution.

The flux distribution at the receiver target, which this study considers to be a key performance indicator, can be determined from the radiance distribution of individual heliostat beams. Two non-dimensional performance measures were introduced that prove to be valuable tools for the analysis and parametrisation of the reflected beam. The dispersion of the beam was found to be dominated by three fundamental factors; the sun shape, NVE aberrations and astigmatic aberrations. Minimising these factors would lead to optical performance improvements. The sun shape is an inherent property of the incident irradiation and is not directly influenced by the heliostat design. NVE aberrations are indicative of the build quality of the heliostat and appear to be related to the cost of the heliostat. Cost implications of reducing NVE may restrict the techno-economic benefit. Astigmatic aberrations were shown to be dependent on the profile of the reflective surface and the dimensions of the heliostat aperture. Performance improvements of concave profiles were explored, but the benefit of further optimisation was found to be limited. Dynamic canting, which actively manipulates the reflective profile to reduce astigmatism, was not investigated and is out of the scope of this work. The utilisation of reduced heliostat aperture areas appears to be the most feasible way to reduce astigmatism and improve optical performance. This implies that, all other things equal, smaller heliostats have an inherent performance benefit over larger heliostats.

An adequate understanding of the fundamentals of heliostat optics enabled the shortcomings of state of the art analytical methods to be evaluated. The study confirmed the flux distribution inaccuracies of a circular Gaussian distribution method as documented in literature. An optical phenomenon which causes a shortening of the minor axis of the elliptical image at increased incidence angles was identified as an error source, and a modification to account for this phenomenon was proposed. Although the modification improves the accuracy of the total intercepted power from 7.5 % to 0.1 % for the case considered, the flux distribution error over the receiver surface is reduced by 27.2 %. This result is indicative of the inherent limitation of circular Gaussian distribution methods to accurately describe realistic flux distributions.

The realistic beam of a heliostat has a more complex radiance distribution. The fundamental analysis of heliostat optics found that optical aberrations can be statistically differentiated according to whether they occur in a set of consecutive optical events or whether they are path dependent. This finding implies that astigmatic aberrations should be dealt with explicitly to account for factors such as the aspect ratio, the canting strategy and the reflective profile, all of which influence the astigmatic projection of the aperture. This finding also implies that the sun shape and NVE aberrations can be combined by convolution. Evidence of real flux distributions further highlights that this convolution should ideally account for the anisotropic widening of NVE aberrations and for distribution of real sun shapes. Development of a new method to model flux distribution showed that it is possible to achieve suitable levels of confidence analytically by accounting for these factors. The accuracy improvements offered by the method is particularly beneficial when used to model higher accuracy heliostats that would typically be used in MGT CSP. In such a case the method reduced the peak flux error from 6.8 % to 0.8 % and reduced flux distribution error by 60.6 %.

As a complementary activity, the development and practical implementation of a glass based heliostat facet was outlined. The sheer number of variables that affect the performance of the facet suggests that this is not an exact science, and (in particular for this study) learnings are predominantly based on a trial and error process. The design of a repeatable fabrication process in which these variables can be controlled is key to eliminate determinate errors and is considered to be as important as the facet design itself. Experimentation suggests that the use of thinner glass, higher curvatures, larger glass panes and discrete support of the glass pane will increase the susceptibility of local surface deformations and in turn increase the SSE. A sandwich structure type facet which provides continuous supports enables SSE between 0.5 mrad and 0.85 mrad to be realised. Although this design meets the accuracy requirements, thermal instabilities and long term degradation have not yet been adequately addressed.

The flux distribution method developed proved to be a useful tool in a techno-economic analysis of a MGT CSP system. The analysis provides sufficient evidence that the optimum optical configuration of a MGT CSP system differs from conventional central receiver systems, which implies variation in the optical parameter sensitivities. Higher accuracy heliostats than that used in conventional salt based central receiver systems were shown to yield lower LCOE. The case study also validated the finding that smaller heliostats produce performance benefits. The cost breakdown of MGT CSP was found to differ from that of a conventional central receiver system. A particularly high cost is allocated to the power block, which is indicative of the immaturity of MGT technology. The cost breakdown is expected to change as MGT CSP is implemented in the market according to the different learning rates and maturities of the cost components.

11.2 Conclusions

The central receiver system is a CSP technology that is still in a relatively early stage of the technology life cycle. MGT CSP is a small modular configuration that appears to be a strong technology contender for the next-generation of central receiver systems. Although this emerging technology is not yet well defined, it has sparked significant interest and has become an emerging research field. One specific aspect that is not yet understood is the heliostat field, which is itself an inherently complex and multivariate system. Numerical methods that use a stochastic analysis approach are able to accurately describe the optical performance of the field but do not on their own provide a component level understanding. This work attempts to address the need for a more fundamental understanding of the system by developing an analytical method that is able to parametrically describe the optical performance with suitable levels of confidence. Three key factors – the sun shape, NVE aberrations and astigmatic aberrations – are found to dominate the dispersion of a heliostat beam, and if appropriately accounted for, enable the accurate description of the heliostat image. This knowledge presents the principal component to describe heliostat field performance.

To obtain the optimum optical performance, each of these three factors should be addressed; however, they present technological and cost limitations. Of the three contributing factors only the NVE aberrations and astigmatic aberrations are influenced by the heliostat design. The cost implications of reducing NVE may restrict the techno-economic benefit, but astigmatism is not necessarily cost related and may provide some techno-economic value. The study showed that performance benefits from surface profile optimisation are limited, and it indicated that higher focal ratios, obtained by using smaller heliostats, do improve performance and results in lower LCOE. Smaller heliostats do not necessarily lead to higher cost, and complementary work by Blackmon [53] suggests that the ultimate cost minimum will be achieved using smaller heliostats driven by the reduction of fixed costs. This implies that reducing fixed costs is a key enabler to improve optical performance and reduce LCOE.

The modular approach of MGT CSP systems results in smaller heliostat fields; this implies lower focal ratios and in turn indicates that such systems will have high astigmatic aberrations. The MGT CSP case study confirms this and suggests that lower LCOE can be achieved with smaller heliostats.

The outcomes of this work suggest that the objectives were met. Noting that objectives were restricted to the optics of a single heliostat, supplementing the proposed flux distribution method with complementary methods would extend its application and allow issues such as life cycle design to be addressed.

11.3 Summary of contributions

The fundamentals of heliostat optics have been described analytically, and two new performance measures have been proposed, which are valuable tools enabling a quantifiable analysis and parametrisation of the optical aberrations. A parametric description of the intercept efficiency generalises heliostat performance. Astigmatic aberration was identified as a major contributing factor to beam spread and was further investigated. The use of optimised reflective surface profiles to reduce astigmatic aberrations was shown to have a limited effect; however, increased focal ratios were demonstrated to be effective. This provides evidence that smaller heliostats have optical performance benefits.

Literature suggests that state of the art analytical methods are unable to meet the accuracy requirements for certain flux distribution applications. An evaluation of the state of the art analytical method confirmed that this need was not met and a modification to the method has been proposed to account for the shortening of the minor axis of the elliptical image with increasing incidence angles. A unique analytical flux distribution method, aimed specifically at these applications, was developed. This contribution enables the flux distribution to be determined with computational efficiency, and with an improved level of confidence above the state of the art.

This work is predominantly based on several peer reviewed publications which have been cited within this dissertation. This study initiated research in the field of heliostat optics at STERG and has laid the groundwork for further research to follow.

11.4 Suggestions for further research

The following recommendations highlight key research questions that were raised during this work and are expected to add value to CSP in general. These recommendations include and extend beyond the natural progression of this work.

- To leverage the advantages of the proposed flux distribution method, it is recommended that this method be used in conjunction with complementary methods to further its applications. To optimally utilise the computational advantages offered by this method, the method should also be coded in a more efficient software environment.

- A second area of research that follows from this work is to complete a techno-economic optimisation of a MGT CSP system to investigate the current economic viability of the technology and identify the cost limitations. This work has already identified MGT's as a critical cost component, and a cost reduction study has been initiated at STERG.

- The cumulative findings of this research suggest that smaller heliostats have significant optical performance benefits, especially for MGT applications. The parametric cost studies by Blackmon [53] further suggest that the ultimate heliostat cost minimum will be achieved by smaller heliostats if fixed costs can be reduced. This implies that significant cost and performance benefits could be achieved by reducing fixed costs.

- To meet the high accuracy optical requirements of MGT CSP, a sandwich type facet was developed in Chapter 9. The results provide evidence that optically accurate, short focal length facets, with SSE as low as 0.7 mrad are achievable with sandwich type facet. The main challenge of this concept appears to be engineering an economical core material that is stable and able to withstand atmospheric degradation. Realising such a material may enable a reliable low cost facet with high optical performance.

Appendices

Appendix A

Geometric optics

The goal of geometrically shaping the reflective surface is to reduce the heliostat image size. Geometric optics are used to derive the equations used in Section 4.5 which describe astigmatic aberrations. Supportive mathematics are also provided.

A.1 Large focal ratio approximation

In Figure 5.9 (p. 62) the paraboloidal and spherical facet profiles behave similarly. The reason for this is that for large focal ratios ($x \ll r$) a spherical profile approximates a paraboloid. This implies that the optical behaviour of a surface can be described by its radius of curvature. A two-dimensional proof is provided here.

A circle with focal point $r/2$, as shown in Figure A.1, is given by

$$y = r - \sqrt{r^2 - x^2} \tag{A.1}$$

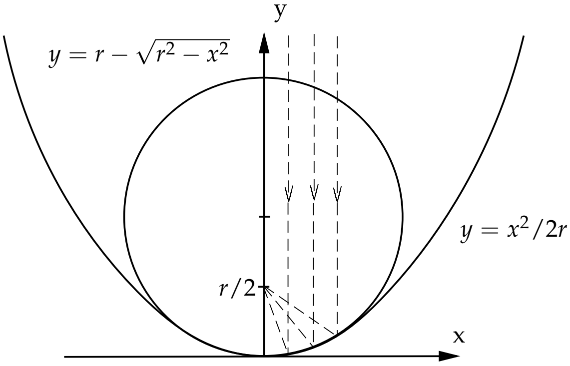

Figure A.1: Approximation of a circle as a parabola for $x \ll r$

Using the Taylor expansion, this can be rewritten as

$$y = r\left(1 - \left(1 - \frac{x^2}{2r^2} + \frac{x^4}{8r^4} - \frac{x^6}{16r^6} + \dots\right)\right) \tag{A.2}$$

Large focal ratios, $x \ll r$, allow the following simplification, which describes a parabola with focal length, f, of $r/2$.

$$y = \frac{x^2}{2r} = \frac{x^2}{4f} \tag{A.3}$$

A.2 Ideal surface profile

One fundamental question is what the ideal surface profile must be to create a perfect point image, or an aberration free surface, at any given moment.

Consider a parabola, with focal length, f, which is known to have this property (Equation A.3). If the receiver is placed at the focal point, and the heliostat at the fulcrum of the parabola, the heliostat will be shaded by the receiver, suggesting that an on-axis configuration never practically exists. In reality the heliostat should take the profile of an off-axis point on the parabola to obtain a point image as depicted in Figure 4.7 (p. 38).

Landman and Gauché [144] describe such a surface in the Cartesian coordinate system; however, a more elegant solution relates the incidence angle, ϕ and radius of curvature to the distance at which the light will converge. Here the radius of curvatures in the sagittal and tangential planes are solved for separately.

A.2.1 Ideal radius of curvature in the sagittal plane

By projecting the geometry onto the sagittal plane the problem is reduced to an on-axis reflection case where the projected focal length is given by $d\cos\phi$, resulting in a radius of curvature of

$$r_{\text{sag}} = 2d\cos\phi \tag{A.4}$$

A.2.2 Ideal radius of curvature in the tangential plane

Radius of curvature at any point on a function is given by

$$r = \frac{(1 + (y\prime)^2)^{\frac{3}{2}}}{y\prime\prime} \tag{A.5}$$

When combined with Equation A.3 the radius of curvature in the tangential plane can is given by

$$r_{\tan} = \frac{(1 + \frac{x^2}{4f^2})^{\frac{3}{2}}}{\frac{1}{2f}} \tag{A.6}$$

A parabola has the property that the distance of any point to the focal point, d, is equal to the height of the point plus the height of the focal point

$$d = f + y \tag{A.7}$$

which can be written as

$$\frac{d}{f} = 1 + \frac{x^2}{4f^2} \tag{A.8}$$

The gradient at any point on the parabola can be given by the first derivative or by the tangent of the incidence angle

$$y\prime = \frac{x}{2f} = \tan\phi \tag{A.9}$$

Substituting Equations A.8 and A.9 into Equation A.6 simplifies the radius of curvature in the tangential plane down to

$$r_{\text{tan}} = 2d\sec\phi \tag{A.10}$$

A.3 Image dimensions at the slant range

Section A.2 described the relationship between: the incidence angle, the radius of curvature and distance at which a point image is formed. Here these equations are applied to determine the image dimensions at the slant range.

Consider a heliostat with fixed radii of curvatures, r_{tan} and r_{sag}, with an incidence angle, ϕ and the target placed at the slant range, d. Equations A.4 and A.10 can be rewritten in terms of the distance at which the point image is formed, S_{sag} and S_{tan}.

$$S_{\text{tan}} = r_{\text{tan}}\cos(\phi)/2 \qquad \text{and} \qquad S_{\text{sag}} = r_{\text{sag}}\sec(\phi)/2 \tag{A.11}$$

By dividing the arc length by heliostat dimensions by S_{sag} and S_{tan}, the fan angles is determined.

$$\alpha_{\text{tan}} = D\cos(\phi)/S_{\text{tan}} = 2D/r_{\text{tan}} \tag{A.12}$$

$$\alpha_{\text{sag}} = D/S_{\text{sag}} = 2D\cos(\phi)/r_{\text{sag}} \tag{A.13}$$

Using the law of similar triangles the image height and width a the slant range is given by

$$h = \alpha_{\text{tan}}|d - S_{\text{tan}}| \qquad \text{and} \qquad w = \alpha_{\text{sag}}|S_{\text{sag}} - d| \tag{A.14}$$

Assuming that r_{tan} and r_{sag} are twice the focal length, f, results in the image dimensions for a spherical profile given by Equation 4.19 (p. 37).

A.4 Radii of curvature for a misaligned toroid

Assuming a toroidal surface with known radii of curvature, an axes aligned elliptical paraboloid is given by

$$z = f(x, y) = \frac{x^2}{2r_{\text{tan}}} + \frac{y^2}{2r_{\text{sag}}} \tag{A.15}$$

For a misaligned toroid the radii of curvature in the direction θ and $\theta + 90^\circ$ are desired. Equation A.15 can be rewritten to allow the elliptical paraboloid a rotation of θ.

$$z = f(x, y, \theta) = \frac{(x \cos\theta - y \sin\theta)^2}{2r_{\text{tan}}} + \frac{(x \sin\theta + y \cos\theta)^2}{2r_{\text{sag}}} \tag{A.16}$$

The directional curvatures of a surface are given by

$$k_x = \frac{\frac{\partial^2 f}{\partial x^2}}{\left(1 + \frac{\partial f}{\partial x}^2\right)^{3/2}} \quad \text{and} \quad k_y = \frac{\frac{\partial^2 f}{\partial y^2}}{\left(1 + \frac{\partial f}{\partial y}^2\right)^{3/2}} \tag{A.17}$$

Assuming the surface gives an aberration free image at slant range, d, and fixed incidence angle $\bar{\phi}$, Equations A.4, A.10 and A.16 can be combined and the directional curvatures determined. The reciprocal of the curvatures give the radii of curvature in the θ and $\theta + 90^\circ$ directions.

$$r_\theta(\bar{\phi}, \theta) = \left| \frac{2d}{\cos^2(\theta) \cos\bar{\phi} + \sin^2(\theta) \sec\bar{\phi}} \right| \tag{A.18}$$

$$r_{\theta+90^\circ}(\bar{\phi}, \theta) = \left| \frac{2d}{\sin^2(\theta) \cos\bar{\phi} + \cos^2(\theta) \sec\bar{\phi}} \right| \tag{A.19}$$

A.5 Describing astigmatism as a radial standard deviation

Section 4.5 used edge rays of a circular reflective profile to determine the height and the width of the astigmatic dispersion in the tangential and sagittal planes respectively. Astigmatism must, however, be accounted for in conjunction with other aberrations to effectively describe the flux distribution. Aberrations can conveniently be amalgamated into a single standard deviation term by assuming they are statistically independent and normally distributed (see Equation B.3).

The statistical independence assumption enables astigmatism to be treated as a path independent aberration and can thus be modelled as a beam with an irradiance distribution. Consider the astigmatic dispersion of a spherical profile, where h_{tan} and w_{sag} are given in Equation 4.19. The linear dependence of both terms on the heliostat diameter suggests that the irradiance distribution is uniform between the edge rays, resulting in a pillbox type distribution. However, an equivalent circular Gaussian beam is required.

The field of laser beam characterisation, use several different methods to determine beam equivalence. The second moment method, (also known as the D4σ or $1/\text{e}^2$ method) has the advantage that the equivalence holds throughout the beams propagation and is described in the ISO standard, ISO 11146-1 [186]. This method sets the radial standard deviation of the circular Gaussian beam equal to a quarter of the pillbox beam diameter, as depicted in Figure A.2.

$$\sigma_{\text{tan}} = \frac{h_{\text{tan}}}{4} \qquad \text{and} \qquad \sigma_{\text{sag}} = \frac{w_{\text{sag}}}{4} \tag{A.20}$$

These terms can be divided by the slant range, d, to obtain them in an angular form. The square mean of the resulting terms provide a representative standard deviation of astigmatic dispersion as a circular Gaussian beam, as used in the HFLCAL method (see Equation B.8).

$$\sigma_{\text{ast}}^2 = \frac{h_{\text{tan}}^2 + w_{\text{sag}}^2}{32d^2} \tag{A.21}$$

Further expanding the equation with the assumption that the focal length and slant range are equal, results in the term used in Section 4.6 (see Equation 4.28).

$$\sigma_{\text{ast}}^2 = \frac{D_{\text{H}}^2(1-\cos\phi)^2}{16d^2} \tag{A.22}$$

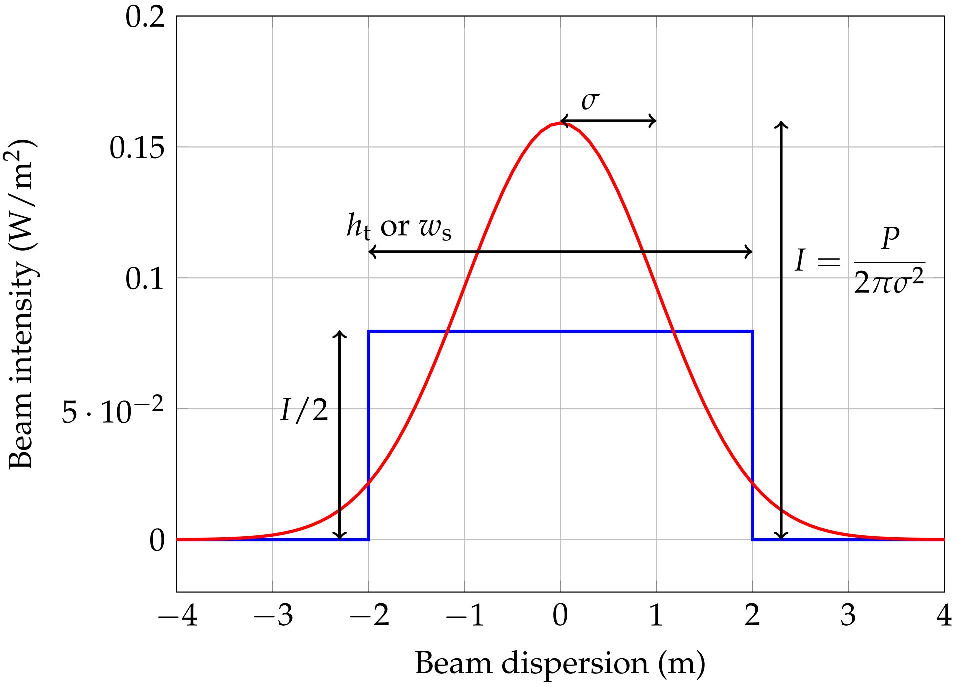

Figure A.2: Equivalent and normalised circular Gaussian and pillbox beams according to the second moment method (ISO 11146-1) ($\sigma = 1$)

Appendix B

The HFLCAL method

The HFLCAL method assumes that the image cast by a heliostat will be a single CGD and that the heliostat is round and spherically curved. These assumptions allow the model to be extremely simple. Details of the method are widely published [68; 76; 77; 31], although there are some variations in how certain variables are dealt with. For the sake of completeness and for readers' convenience, the model is described here as implemented in this thesis. The method was implemented according to the descriptions by Schwarzbözl et al. [68] and Collado [31]. The notations used in the various sources are not common; the notation used by Collado [31] and Igel and Hughes [32] are adopted here.

The FD of a single heliostat is described using the reflected power from the given heliostat onto the receiver plane, P_{H}, (Equation B.2) and the angular dispersion, thereof, given by the beam dispersion error, σ_{tot}.

$$FD(x,y) = \frac{P_{\mathrm{H}}}{2\pi\sigma_{\mathrm{tot}}^2} \exp\left(\frac{-(x^2+y^2)}{2\sigma_{\mathrm{tot}}^2}\right) \tag{B.1}$$

P_{H} is dependent on the direct normal irradiance, I_{D}, reflective area, A_{H}, incidence angle, ϕ, attenuation factor, f_{at}, and reflectivity, ρ.

$$P_{\mathrm{H}} = I_{\mathrm{D}} A_{\mathrm{H}} \cos\phi f_{\mathrm{at}} \rho \tag{B.2}$$

The advantage of assuming a CGD is that the problem is reduced to a single dimension. This allows the component errors to be isolated and quantified [67] and then amalgamated into a single standard deviation, σ_{tot} [73], (Equation B.3). The four errors that are taken into account in the HFLCAL method are the sun shape (σ_{sun}), astigmatic aberration (σ_{ast}), surface slope error (σ_{bq}) and tracking error (σ_{t}) [68]. Each term is dealt with individually below. The σ_{tot} may be further increased by deviding sum of squares by the cosine of the receiver incidence angle, $\cos\phi_{\mathrm{rec}}$.

$$\sigma_{\mathrm{tot}}^2 = \sigma_{\mathrm{sun}}^2 + \sigma_{\mathrm{bq}}^2 + \sigma_{\mathrm{ast}}^2 + \sigma_{\mathrm{t}}^2 \tag{B.3}$$

The σ_{sun} is specified as the standard deviation of the incident radial flux distribution from the sun and varies depending on location and atmospheric conditions. A σ_{sun} value of 2.73 mrad is typically used [73], but the sun shape should be chosen depending on conditions and application.

The σ_{bq} term and the σ_{t} are both errors defined according to the surface normal vector and are thus doubled in the reflected ray. The surface slope error (σ_{SSE}) as well as the positioning errors of the drives around the axes of rotation ($\sigma_{\text{t\_pri}}$ and $\sigma_{\text{t\_sec}}$) are isotropic Gaussian distributions of the angular deviations of the normal vectors from their ideal directions. As governed in Snell's Law, the deviation of the reflected ray is twice the deviation of the surface normal about which it is reflected. The CGD method takes this into account when calculating the beam quality (σ_{bq}) and tracking error (σ_{t}) terms by doubling the component errors and computing a geometric mean (Equation B.4 and Equation B.5).

$$\sigma_{\text{bq}}^2 = 4\sigma_{\text{SSE}}^2 \tag{B.4}$$

$$\sigma_{\text{t}}^2 = 4\sigma_{\text{t\_pri}}\sigma_{\text{t\_sec}} \tag{B.5}$$

The modification of the σ_{bq} and σ_{t} terms proposed in this thesis is given in Equation B.6 and B.7 below, as well as previously in Equation 7.4 and 7.5.

$$\sigma_{\text{bq}}^2 = 2\sigma_{\text{SSE}}^2 \left(1 + \cos^2 \phi\right) \tag{B.6}$$

$$\sigma_{\text{t}}^2 = 2\sigma_{\text{t\_pri}}\sigma_{\text{t\_sec}} \left(1 + \cos^2 \phi\right) \tag{B.7}$$

The standard deviation resulting from astigmatism, σ_{ast}, is the square mean of the aberration in the tangential and sagittal planes, (h_{tan} and w_{sag}).

$$\sigma_{\text{ast}}^2 = \frac{h_{\text{tan}}^2 + w_{\text{sag}}^2}{32d^2} \tag{B.8}$$

$$h_{\text{tan}} = D\left|\frac{d}{f} - \cos\phi\right| \qquad \text{and} \qquad w_{\text{sag}} = D\left|\frac{d}{f}\cos\phi - 1\right| \tag{B.9}$$

Assuming the ideal case where the focal length, f, is equal to that of the slant range, d (see Table 7.1), then Equations B.8 and B.9 reduce down to simply

$$\sigma_{\text{ast}}^2 = \frac{(1-\cos\phi)^2}{16F_{\text{r}}^2} = \frac{\sin^4\left(\frac{\phi}{2}\right)}{4F_{\text{r}}^2} \tag{B.10}$$

Appendix C

Analytical model

Chapter 8 presents an analytical model for calculating the flux distribution of a heliostat. Appendix C provides supporting calculations of this model and additional detail.

C.1 Model inputs

The analytical model computes flux distribution using known information of the surface profile, the receiver cell and the incident radiation. The initial calculations to define the profile are not given explicitly, rather, the procedure is described in general terms. All terms are defined in a common global coordinate system. Both Figures 8.2 (p. 98) and C.1 depict the physical meaning of the variables.

The position, $\mathbf{P}$, and surface normal, $\hat{\mathbf{n}}$, of each discretised cell of the collective profile is required. Based on the chosen canting strategy or the specified profile, the cell positions and surface normals can be defined in the heliostat coordinate system and then then multiplied by a transformation matrix to determine $\mathbf{P}$ and $\hat{\mathbf{n}}$ in a global coordinate system. The generalised method proposed by Chen *et al.* [187] is used to compute transformation matrices for a tracking mechanism with arbitrarily oriented axes. This calculation is dependant on the direction of the incident irradiation, $\hat{\omega}_{\mathrm{i}}$, and the intended direction of the reflected light, $\hat{\omega}_{\mathrm{o}}$.

Similarly the position, $\mathbf{R}$, and normal vector, $\hat{\mathbf{n}}_{\mathrm{R}}$, of a given receiver cell at which the flux will be computed is also defined in the same coordinate system.

C.2 Computing the power on a receiver cell

The power on a receiver cell, P_{R}, is dependent on the product of the projected cell area, $A_{\mathrm{R}} \cos \phi_{\mathrm{rec}}$, the slant range, d, and the angular radiance distribution of the beam, $I(x_s, y_t \mid L(\alpha), \sigma_{\mathrm{sag}}, \sigma_{\mathrm{tan}})$ evaluated at the relative angular

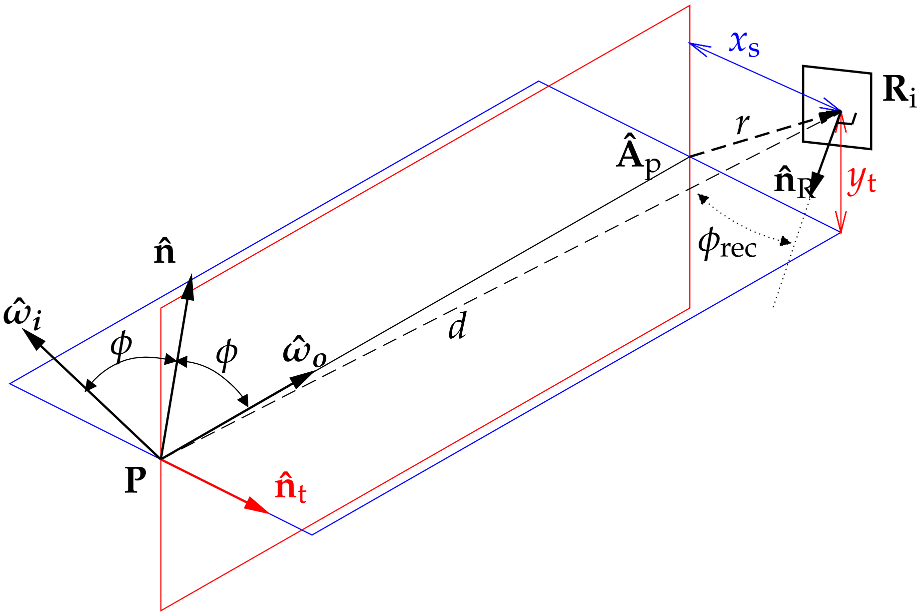

Figure C.1: Planes of symmetry of the reflected beam and the receiver cell

receiver position (x_s, y_t). If $\cos \phi_\mathrm{rec}$ is negative, the angles are obtuse, indicating that the cell faces away from the incident radiation and $P(x_s, y_t)$ is set to zero. The computation of each of these terms are briefly discussed here.

$$P_\mathrm{R}(x_s, y_t) = \begin{cases} A_\mathrm{j} \cos()\phi_{\mathrm{rec}_\mathrm{i}}) dI(x_s, y_t \mid L(\alpha), \sigma_\mathrm{sag}, \sigma_\mathrm{tan}), & \cos \phi_{\mathrm{rec}_\mathrm{i}} > 0 \\ 0, & \cos \phi_{\mathrm{rec}_\mathrm{i}} \leq 0 \end{cases} \tag{C.1}$$

The cosine, $\cos \phi_\mathrm{rec}$, results from the dot product of the normal vector and light path away from the cell:

$$\cos \phi_{\mathrm{rec}_\mathrm{i}} = \frac{\hat{\mathbf{n}}_\mathrm{R} \cdot (\mathbf{P} - \mathbf{R})}{\|\mathbf{P} - \mathbf{R}\|} \tag{C.2}$$

Similarly, the slant range of the cone, d, is given by:

$$d = \hat{\omega}_\mathrm{o} \cdot (\mathbf{R} - \mathbf{P}) \tag{C.3}$$

Several different methods to determine $I(x_s, y_t \mid L(\alpha), \sigma_\mathrm{sag}, \sigma_\mathrm{tan})$ are discussed in Chapter 8; however, the relative position of the receiver cell is still required. If a circular radiance distribution of the beam is assumed the beam is axis symmetric and only the radial distance of the receiver cell from the beam axis is required.

$$r^2 = (\mathbf{R}_\mathrm{i} - \mathbf{P} - d_\mathrm{i}\hat{\omega}_\mathrm{o}) \cdot (\mathbf{R}_\mathrm{i} - \mathbf{P} - d_\mathrm{i}\hat{\omega}_\mathrm{o}) \tag{C.4}$$

If the cone is not axially symmetric the components of r in the tangential and sagittal planes is determined. A vector normal to one of the planes and perpedicular to the axis is required to define either the sagittal or tangential planes. In this case it is easiest to define the tangential plane by using the cross product of $\hat{\boldsymbol{\omega}}_{\boldsymbol{o}}$ and $\hat{\mathbf{n}}$.

$$\hat{\mathbf{n}}_{\mathrm{t}} = \hat{\boldsymbol{\omega}}_{\boldsymbol{o}} \times \hat{\mathbf{n}} \tag{C.5}$$

$$x_{\mathrm{s}}^2 = \hat{\mathbf{n}}_{\mathrm{t}} \cdot (\mathbf{R}_{\mathrm{i}} - \mathbf{P} - d_{\mathrm{i}}\hat{\boldsymbol{\omega}}_{\boldsymbol{o}}) \tag{C.6}$$

Using Pythagoras the tangential component can easily be computed.

$$y_{\mathrm{t}}^2 = r^2 - x_{\mathrm{s}}^2 \tag{C.7}$$

x_{s} and y_{t} can then be substituted into C.1 to determine the power on the receiver cell, P_{R}.

Total power on a cell is given by the sum of the power from all of the discretised cells in the collector system. The speed of computation can be increased by vectorising these calculations.

$$P_{\mathrm{tot}} = \sum_{i=1}^{n} P_{\mathrm{R,i}} \tag{C.8}$$

Appendix D

Characterisation of the reflective surface

To evaluate the quality of the reflective surface an optical characterization system is typically used. Such a system provides a surface normal vector at each location that the camera views on the reflective surface [153]. This Appendix investigates the calculation procedure for determining the slope error terms from the normal vector data. This section is specifically included since the author could not find such procedure in existing literature.

The surface slope error is typically defined as the standard deviation of a normal probability distribution describing the angular deviation, ϵ, of the normal vector of the heliostat's reflective surface, $\hat{\mathbf{n}}'$, with regard to the one of an ideal reference surface, $\hat{\mathbf{n}}$, as defined in Figure D.1.

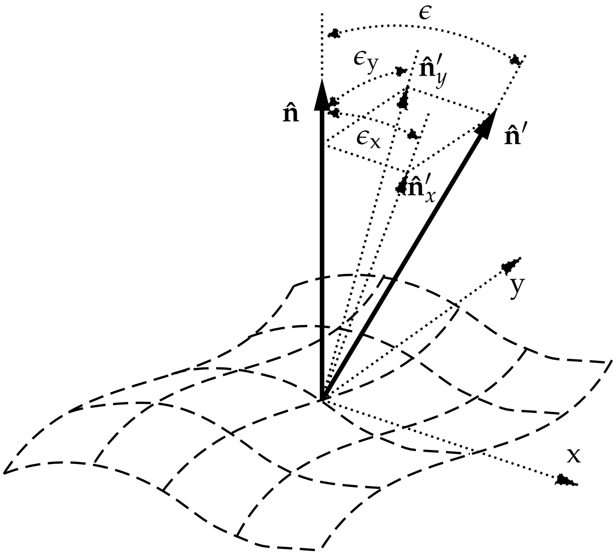

Figure D.1: Components of the normal vector error

Initially only $\hat{\mathbf{n}}'$ is known and $\hat{\mathbf{n}}$ must still be determined. To do this the normal vector data is fitted to the derivative of the ideal surface. The objective function is the RMS of ϵ. In this work a sphere was fitted to the data, although Yellowhair and Andraka [153] fit the normal vector data to a paraboloid. The fit first used both a Genetic Algorithm to find the global minima for this highly non-linear dataset. Afterwards the Nelder-Mead Simplex Method is applied to pinpoint the minima. The radius of curvature of the fitted sphere is used as the radius of curvature of the facet.

It is useful to understand the actual distribution of the errors on the reflective surface. Figure D.2 plots the empirical distribution function (EDF) of the angular error, ϵ, and its components, ϵ_x and ϵ_y. Additional plots in Figure D.2 are discussed later on.

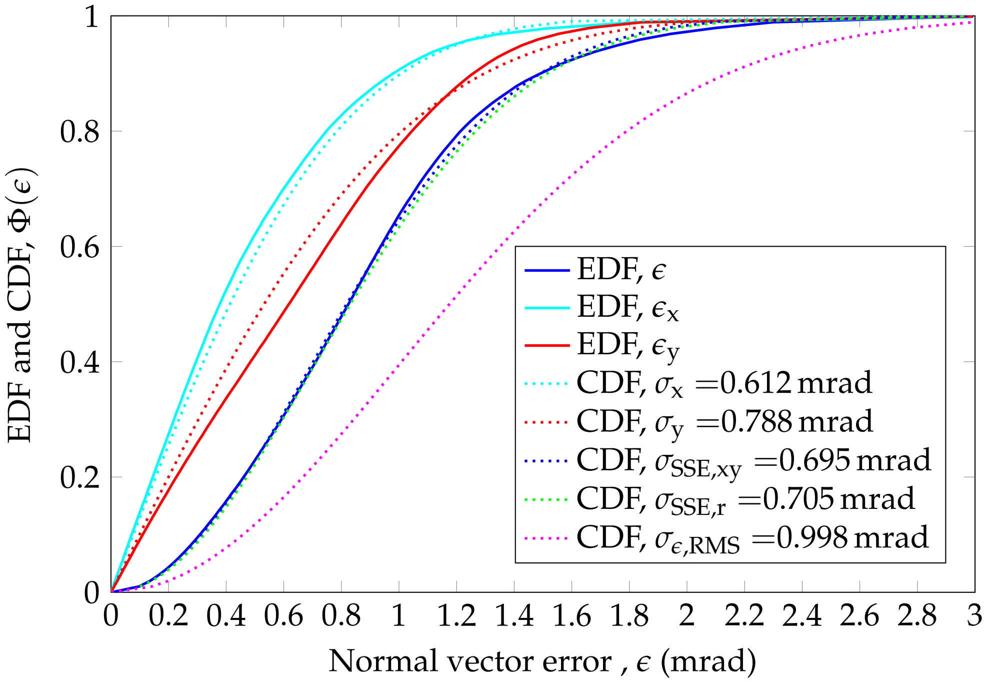

Figure D.2: Empirical distribution functions (EDF) and cumulative distribution functions (CDF) of the normal vector errors of the facet shown in Figure 9.8

D.1 Parameter estimation using component errors

Pettit [130] suggest that the errors have a circular Gaussian distribution. The variance of the components are given by the RMS of the component errors if this distribution holds. Applying this to the facet showed previously in Figure 9.8, values for $\sigma_{SSE,x}$ and $\sigma_{SSE,y}$ of 0.612 mrad and 0.788 mrad are determined.

$$\sigma_{\mathrm{x}}^2 = \frac{1}{n}\sum_{i=1}^{n}\epsilon_{\mathrm{x,i}}^2 \qquad \text{and} \qquad \sigma_{\mathrm{y}}^2 = \frac{1}{n}\sum_{i=1}^{n}\epsilon_{\mathrm{y,i}}^2 \tag{D.1}$$

The probability distribution function (PDF) for a bivariate Gaussian distribution is given by the product of the two univariate Gaussian distributions.

$$\mathrm{PDF}_{\mathrm{x,y}}(\epsilon_{\mathrm{x}}, \epsilon_{\mathrm{y}}) = \frac{1}{2\pi\left(\sigma_x\sigma_y\right)}\exp\left(\frac{-\left(\sigma_y^2\epsilon_{\mathrm{x}}^2 + \sigma_x^2\epsilon_{\mathrm{y}}^2\right)}{2\left(\sigma_x^2\sigma_y^2\right)}\right) \tag{D.2}$$

Approximating $\sigma_x \approx \sigma_y$ the equation simplifies down to its radial form. σ_{SSE} can be computed as the geometric mean of the components $\sigma_{\mathrm{SSE}} = \sqrt{\sigma_{\mathrm{x}} \cdot \sigma_{\mathrm{y}}}$ as defined previously in Equation 4.12 and results in 0.695 mrad.

$$\mathrm{PDF}_{\mathrm{x,y}}(\epsilon) = \frac{1}{2\pi\sigma_{\mathrm{SSE}}^2}\exp\left(\frac{-\epsilon^2}{2\sigma_{\mathrm{SSE}}^2}\right) \tag{D.3}$$

The polar integration of the function results in the cumulative distribution function (CDF) of ϵ. Figure D.2 shows that together the error components do approximate a circular Gaussian distribution as suggested by Pettit [130].

$$\mathrm{CDF}_{\mathrm{x,y}}(\epsilon) = 1 - \exp\left(-\frac{\epsilon^2}{2\sigma_{\mathrm{SSE}}^2}\right) \tag{D.4}$$

D.2 Parameter estimation using radial errors

The PDF of the radial error, ϵ, can be achieved by integrating Equation D.3 angularly from 0 to 2π which results in the Rayleigh distribution.

$$\mathrm{PDF}_{\mathrm{r}}(\epsilon) = \frac{\epsilon}{\sigma_{\mathrm{SSE}}^2}\exp\left(\frac{-\epsilon^2}{2\sigma_{\mathrm{SSE}}^2}\right) \tag{D.5}$$

As expected the CDF of the Rayleigh distribution is the same as that of the Circular Gaussian given in Equation D.4. σ_{SSE} is given by the maximum likelihood indicator of the Rayleigh parameter. Using this method σ_{SSE} is determined to be 0.705 mrad and plotted in Figure D.2.

$$\sigma_{\mathrm{SSE}}^2 = \frac{1}{2n}\sum_{i=1}^{n}\epsilon_{\mathrm{i}}^2 \tag{D.6}$$

Note that this is not the same as the RMS functions used in Equation D.1, the denominator contains an additional 2. The RMS of the radial error would overestimate the parameter at 0.998 mrad also shown in Figure D.2.

Appendix E

The Monte-Carlo ray tracer

The functionality of the individual components of the developed ray tracer are elaborated on here.

E.1 Software environment

The ray tracing model was written in the Matlab software environment. Matlab has numerous inbuilt functions negating the need to recode basic functions. Although Matlab is significantly slower than C++ for this application, the computation time was of lesser importance and the user friendly interface was chosen.

E.2 Defining coordinate systems

For convenience, all inputs for the ray tracer are given in the global coordinate system. This system, however, is impractical for ray tracing computations. Complex profiles need to be dealt with, some of which require differentiation to determine the profile normals. It is desirable that the profile be dealt with without the need for a transformation.

Therefore, it is convenient that the ray tracing occurs in a local coordinate system. The sun and target vectors can then be rotated around the complex profile, given that the light source is well defined and the target position is known. This approach reduces computational time because it requires only the transformation of two vectors rather than the transformation of the large number of hit point coordinates and corresponding normals.

In order to move between coordinate systems, vectors undergo a transformation which requires translation and rotation in the Euclidean space. Vector rotation and translation can be incorporated into a single transformation by a multiplication of transformation matrices.

The heliostat's physical position and orientation in the Euclidean space is determined by its placement relative to the tower, the choice of the tracking mechanism and the sun position, which was determined previously. Since the ray tracing will occur in a local coordinate system, the heliostat surface is already appropriately described. A single transformation matrix is used to transform vectors from the global to a local coordinate system, dependent on the orientation.

E.3 Creating hit points

The reflective surface profile of the heliostat is relatively flat, $z \ll (x, y)$. As a result, the random nature of the ray intercepts can be approximated to occur in the xy plane of the reflective surface. Matlab has a built in function that provides random numbers between 0 and 1 from which the hit point distribution over the surface is determined. Hit point selection is non-trivial and several approaches are possible: regular, random and stratified sampling [141].

In regular sampling the points are selected using a grid based pattern (Figure E.1a). Regular sampling does not conform to Monte Carlo theory, and regular artefacts such as Moiré patterns may arise. These artefacts may be avoided by using random sampling (Figure E.1b). The disadvantage of random sampling is that noise can be quite objectionable due to increased density of points in certain areas. This effect can only be reduced through increasing sample sizes. The disadvantages of both regular and random sampling can be cleverly avoided by using stratified sampling. Stratified sampling uses the randomly placed samples which perturbs a regular grid as seen in Figure E.1c below.

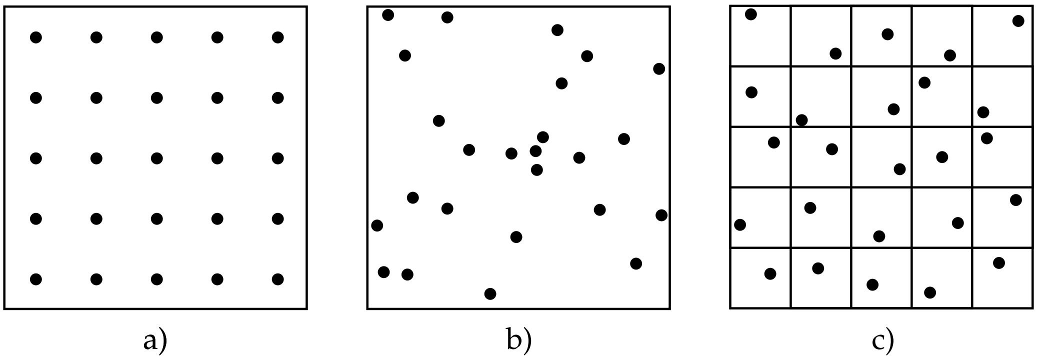

a) b) c)

Figure E.1: Sampling theories: a) regular sampling, b) random sampling and c) stratified sampling

All three sampling methods were coded and are implemented in the ray tracer; however, the effects were negligible for the high number of rays used in modelling. For all results presented in this thesis stratified sampling was used.

E.4 Profile normals

The profile normal dictates the direction of the reflected ray, and thus a normal vector needs to be computed at each hit point. Within the body of work, surface profiles are described in different ways, each requiring the surface normal vectors to be computed. Surface normal vectors are generally solved by using the cross product of the directional derivatives [188].

Simple profiles are easily described as a surface in the Euclidean space by a Cartesian equation, $\mathbf{z}(x, y)$, and the surface normal is given by directional derivatives.

$$\hat{\mathbf{n}}(x,y) = \frac{\partial \mathbf{z}}{\partial x} \times \frac{\partial \mathbf{z}}{\partial y} = \begin{bmatrix} f_x(x,y) \\ f_y(x,y) \\ -1 \end{bmatrix} \tag{E.1}$$

Parametric or non-continuous equations are often non-differentiable. Here the instantaneous rate of change, $D_u f(x,y)$, can be calculated in the required direction, $\mathbf{u} = \langle a, b \rangle$, which approaches the directional derivative as $h \to 0$. Again the cross product of the directional derivatives will give the surface normal.

$$D_u f(x,y) = \lim_{h \to 0} \frac{f(x + ah, y + bh) - f(x,y)}{h} \tag{E.2}$$

During experimentation, facet profiles were characterised using a Coordinate Measuring Machine (CMM) (Section 9.4.1, p. 115). Here the surface is given as a point cloud which also required ray tracing. Points were linked using Delaunay triangulation. This maximizes the minimum angle of all the angles of the triangles in the triangulation, thus avoiding thin or elongated triangles. The normal of a triangle is very easily calculated by the cross product of its vertices.

$$\hat{\mathbf{n}} = (\mathbf{P}_1 - \mathbf{P}_2) \times (\mathbf{P}_1 - \mathbf{P}_3) \tag{E.3}$$

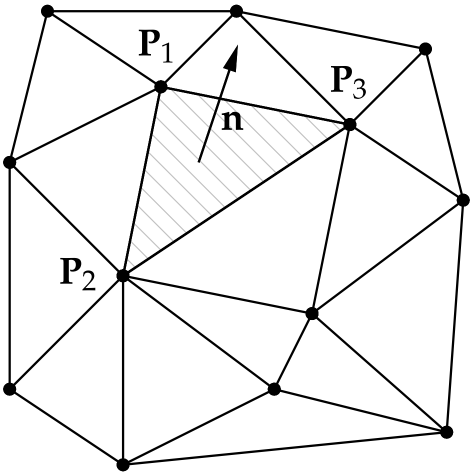

Figure E.2: Surface normal from a Delaunay triangulation

E.5 Dealing with errors

The aberrations experienced in the system are referred to as errors. Errors are incorporated into the ray tracer by offsetting the normals or reflected vectors in a Monte Carlo fashion. Random numbers are generated according to a distribution describing the statistical behaviour of light due to the aberration.

Random number generators for common probability distribution functions are trivial. However, if the probability density function was given as an analytical expression, the method given by [189] was used. All errors are dealt with individually in the sections below.

E.5.1 Surface slope errors

SSE account for optical accuracy of the profile and are made up of macro and micro errors. Macro errors account for the deviation of the surface normal from the ideal; the micro errors account for the specularity of the surface (Figure 4.3, p. 32). Both are modelled as Gaussian distributions, and the resulting standard deviation of the reflected ray is given as the square of their sums.

E.5.2 Tracking errors

The imperfections of the heliostat drives result in a misorientation of the heliostat. Misalignments occur in both axes of rotation and are known as tracking errors. Tracking errors are modelled using Gaussian distributions and specified as standard deviations for both the first and second axes. Tracking errors can be accounted for by adjusting the incidence vector since the entire profile is similarly affected by the tracking errors.

E.5.3 Gravitational errors

Much interest is given to cost reducing heliostats. Heliostats are required to be as light as possible to reduce the material usage, but may also reduce the stiffness of the structure. Reduced stiffness increases the structural deformation under gravitation and leads to changes in the surface profile and optical losses. A balance between optical performance and structural cost is essential. An option to model the effects of the gravitational deformation on optical performance was included in the ray tracer.

Each heliostat design has a unique structure on which deformation is dependent and simplifying assumptions are required. The model assumes a T-type heliostat with a torque tube in the second axis of rotation. The trusses are mounted perpendicular to the torque tube, and the facets are mounted on the trusses (Figure E.3).

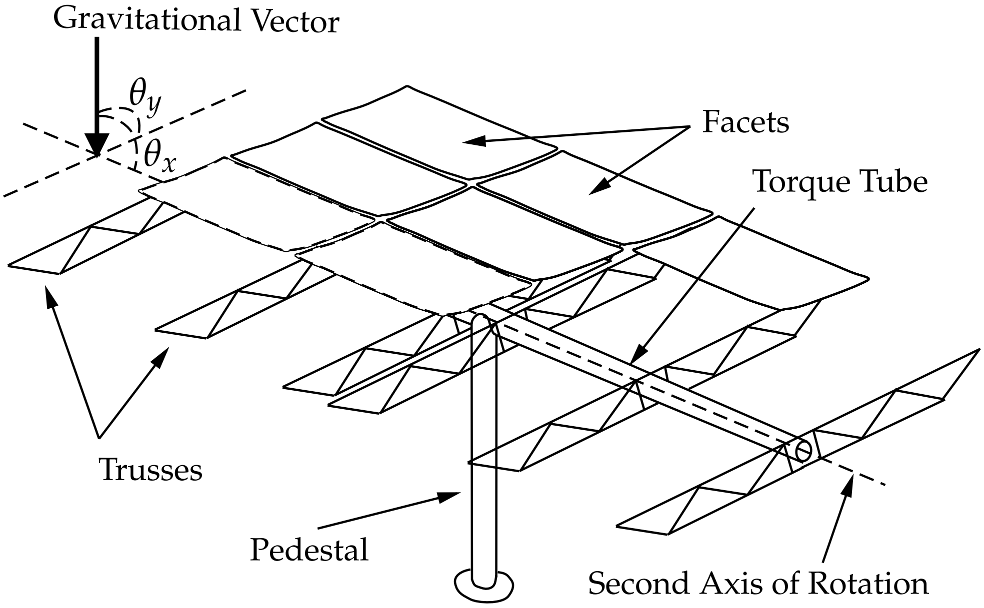

Figure E.3: Structural assumtions for gravitational loading

The model assumes that the area moment of inertias, I, of the torque tube and trusses remain constant for the length, L, of the beams. Deflection, δ, is calculated by assuming a uniformly distributed load, w, on a cantilevered beam. Since the loading is dependent on the instantaneous orientation of the heliostat relative to the gravitational vector, only the component of the gravitational vector normal to the plane of reflection was taken into account. The angular deviation, θ, is the derivative of the deflection.

$$\delta = \frac{w}{24EI}\left(x^4 + 6L^2x^2 - 4Lx^3\right) \tag{E.4}$$

$$\theta = \frac{w}{6EI}\left(x^3 + 3L^2x - 3Lx^2\right) \tag{E.5}$$

Since the heliostat is calibrated in a certain orientation, the facets and the heliostat structure are pre-stressed. The difference between the deformation of the pre-stressed heliostat and the deformation in the current position is seen optically. The difference in angular deviation is used to create a transformation matrix which is in turn used to rotate the normals. An exaggeration of the effect on the normals is depicted in Figure E.4.

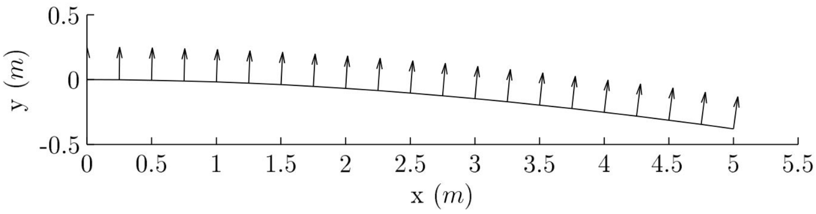

Figure E.4: Normal vectors of a cantilevered beam under uniformly distributed load

E.6 Number of rays

The numerical approach of using multiple rays to simulate an effect relies on random numbers. The entire model must be sufficiently random to avoid the formation of patterns. Enough random numbers must also be used to avoid random number effects. Several iterations is conducted to find the number of rays for which the model results stabilize.

List of References

[1] Kolb, G.J., Ho, C.K., Mancini, T.R. and Gary, J.A.: Power tower technology roadmap and cost reduction plan. Tech. Rep., SAND-2011-2419, Sandia National Laboratories, Albuquerque, NM, 2011.

[2] Kribus, A., Krupkin, V., Yogev, A. and Spirkl, W.: Performance limits of heliostat fields. *Journal of Solar Energy Engineering*, vol. 120, no. 4, pp. 240–246, 1998.

[3] Kistner, R. and Price, H.W.: Financing solar thermal power plants. Tech. Rep., NREL/CP-550-25901, National Renewable Energy Laboratory, Maui, HI, 1999.

[4] Kolb, G.J., Jones, S.A., Donnelly, M.W., Gorman, D., Thomas, R., Davenport, R. and Lumia, R.: Heliostat cost reduction study. Tech. Rep., SAND-2007-3293, Sandia National Laboratories, Albuquerque, NM, 2007.

[5] Tyner, C. and Wasyluk, D.: eSolar's modular, scalable molten salt power tower reference plant design. *Energy Procedia*, vol. 49, pp. 1563–1572, 2014.

[6] European Commission: SOLGATE - Solar hybrid gas turbine electric power system - Project Report. Tech. Rep., ENK5-CT-200-00333, European Commission, Brussels, 2005.

[7] Spelling, J.: *Hybrid solar gas-turbine power plants - a thermoeconomic analysis*. Ph.D. Thesis, Department of Energy Technology, KTH Royal Institute of Technology, Stockholm, Sweden, 2013.

[8] Australian Renewable Energy Agency: Solar air turbine project: Final report. Tech. Rep., Commonwealth Scientific Industrial Research Organisation, Newcastle, NSW, 2014.

[9] Segal, A. and Epstein, M.: Comparative performances of 'tower-top' and 'tower-reflector' central solar recievers. *Solar Energy*, vol. 65, no. 4, pp. 207–226, 1999.

[10] Karni, J., Kribus, A., Doron, P., Rubin, R., Fiterman, A. and Sagie, D.: The DIAPR: a high-pressure, high-temperature solar receiver. *Journal of Solar Energy Engineering*, vol. 119, no. 1, pp. 74–78, 1997.

[11] Lubkoll, M., Backström, T.W.V. and Kröger, D.G.: Survey on pressurized air receiver development. In: *Proceedings of the Southern African Solar Energy Conference*. Port Elizabeth, South Africa, 2014.

[12] Schmitz, M., Schwarzbözl, P., Buck, R. and Pitz-Paal, R.: Assessment of the potential improvement due to multiple apertures in central receiver systems with secondary concentrators. *Solar Energy*, vol. 80, no. 1, pp. 111–120, 2006.

[13] Kröger, D.G.: SUNSPOT: the Stellenbosch University solar power thermodynamic cycle. Tech. Rep., University of Stellenbosch, Stellenbosch, South Africa, 2012.

[14] Helio100: The TIA Helio100 technology development project [Online] (Accessed 2016-09-14). 2016.
Available at: `helio100.sun.ac.za`

[15] Luo, Y., Du, X., Yang, L., Xu, C. and Yang, Y.: Study on the allowable flux Density for a solar central dual-receiver. *Energy Procedia*, vol. 69, pp. 138–147, 2015.

[16] Vant-Hull, L.L.: The role of "allowable flux density" in the design and operation of molten-salt solar central receivers. *Journal of Solar Energy Engineering*, vol. 124, no. 2, pp. 165–169, 2002.

[17] Avila-Marin, A.L.: Volumetric receivers in solar thermal power plants with central receiver system technology: a review. *Solar Energy*, vol. 85, no. 5, pp. 891–910, 2011.

[18] Ho, C.K. and Iverson, B.D.: Review of high-temperature central receiver designs for concentrating solar power. *Renewable and Sustainable Energy Reviews*, vol. 29, pp. 835–846, 2014.

[19] Welford, W.T. and Winston, R.: *High collection nonimaging optics*. Academic Press, New York, NY, 1989.

[20] Stine, W.B. and Geyer, M.: *Power from the sun*. Published online at www. powerfromthesun. net, 2001.

[21] Rabl, A.: Tower reflector for solar power plant. *Solar Energy*, vol. 18, no. 3, pp. 269–271, 1976.

[22] Kribus, A., Zaibel, R., Carey, D., Segal, A. and Karni, J.: A solar driven combined cycle power plant. *Solar Energy*, vol. 62, no. 2, pp. 121–129, 1998.

[23] Vant-Hull, L.L.: Issues with beam-down concepts. *Energy Procedia*, vol. 49, no. SolarPACES 2013, pp. 257–264, 2014.

[24] AORA Solar Ltd.: AORA tulip system [Online] (Accessed 2016-09-20). 2016.
Available at: `www.aora-solar.com`

[25] Lovegrove, K. and Stein, W.: *Concentrating solar power technology*. Woodhead Publishing Ltd., Cambridge, UK, 2012.

[26] Falcone, P.K.: A handbook for solar central receiver design. Tech. Rep., SAND-86-8009, Sandia National Laboratories, Livermore, CA, 1986.

[27] Kistler, B.L.: A user's manual for DELSOL3: a computer code for calculating the optical performance and optimal system design for solar thermal central receiver plants. Tech. Rep., SAND-86-8018, Sandia National Laboratories, Livermore, CA, 1986.

[28] Fernaández, V., Silva, M. and Romero, M.: Win Delsol 1.0. In: *Proceedings of the 15th Task III Meeting within IEA SolarPACES on Solar Technology and Applications*. Almeria, Spain, 2001.

[29] Garcia, P., Ferriere, A. and Bezian, J.J.: Codes for solar flux calculation dedicated to central receiver system applications: A comparative review. *Solar Energy*, vol. 82, no. 3, pp. 189–197, 2008.

[30] Mutuberria, A., Pascual, J., Guisado, M.V. and Mallor, F.: Comparison of heliostat field layout design methodologies and impact on power plant efficiency. *Energy Procedia*, vol. 69, pp. 1360–1370, 2015.

[31] Collado, F.J.: One-point fitting of the flux density produced by a heliostat. *Solar Energy*, vol. 84, no. 4, pp. 673–684, 2010.

[32] Igel, E.A. and Hughes, R.L.: Optical analysis of solar facility heliostat. *Solar Energy*, vol. 22, no. 3, pp. 283–295, 1979.

[33] Schramek, P. and Mills, D.R.: Heliostats for maximum ground coverage. *Energy*, vol. 29, no. 5, pp. 701–713, 2004.

[34] Hoffschmidt, B., Alexopoulos, S., Göttsche, J., Sauerborn, M. and Kaufhold, O.: High concentration solar collectors. In: *Comprehensive renewable energy*. Elsevier, Oxford, UK, 2012.

[35] Kennedy, C.E. and Terwilliger, K.: Optical durability of candidate solar reflectors. *Journal of Solar Energy Engineering*, vol. 127, no. 1, pp. 262–269, 2004.

[36] Landman, W.A. and Gauché, P.: Sensitivity analysis of a curved heliostat profile. In: *Proceedings of the SolarPACES Conference*. Marrakech, Morocco, 2012.

[37] Diver, R.B. and Grossman, J.W.: Sandwich construction solar structural facets. Tech. Rep., SAND98-2845C, Sandia National Laboratories, Albuquerque, NM, 1998.

[38] Chen, Y.T., Kribus, A., Lim, B.H., Lim, C.S., Chong, K.K., Karni, J., Buck, R., Pfahl, A. and Bligh, T.P.: Comparison of two sun tracking methods in the application of a heliostat field. *Journal of Solar Energy Engineering*, vol. 126, no. 1, pp. 638–644, 2004.

[39] Zaibel, R., Dagan, E., Karni, J. and Ries, H.: An astigmatic corrected target-aligned heliostat for high concentration. *Solar Energy Materials and Solar Cells*, vol. 37, no. 2, pp. 191–202, 1995.

[40] Cordes, S., Prosinecki, T.C. and Wieghardt, K.: An Approach to Competitive Heliostats. In: *Proceedings of the SolarPACES Conference*. Marrakech, Morocco, 2012.

[41] Chong, K.K.: Optical analysis for simplified astigmatic correction of non-imaging focusing heliostat. *Solar Energy*, vol. 84, no. 8, pp. 1356–1365, 2010.

[42] Pfahl, A., Randt, M., Holze, C. and Unterschütz, S.: Autonomous light-weight heliostat with rim drives. *Solar Energy*, vol. 92, pp. 230–240, 2013.

[43] Pfahl, A.: Survey of heliostat concepts for cost reduction. *Journal of Solar Energy Engineering*, vol. 136, no. 1, pp. 014501 1–9, 2013.

[44] Coventry, J. and Pye, J.: Heliostat cost reduction - where to now? *Energy Procedia*, vol. 49, pp. 60–70, 2014.

[45] Gary, J., Turchi, C. and Siegel, N.: CSP and the DOE Sunshot initiative. In: *Proceedings of the SolarPACES Conference*. Granada, Spain, 2011.

[46] Weinrebe, G., Von Reeken, F., Wöhrbach, M., Plaz, T., Göcke, V. and Balz, M.: Towards holistic power tower system optimization. *Energy Procedia*, vol. 49, pp. 1573–1581, 2014.

[47] Mavis, C.L.: A description and assessment of heliostat technology. Tech. Rep., SAND-87-8025, Sandia National Laboratories, Livermore, CA, 1989.

[48] Dietrich, J.J., Knowles, R.K., Stone, K.W., Steinmeyer, D.A. and Nourse, J.H.: Second-generation heliostat optimisation studies. Tech. Rep., SAND-82-8175, Martin Marietta, Denver, CO, 1982.

[49] Larmuth, J.N.: *Heliostat cost reduction methods applied to a small heliostat*. M.Sc. Thesis, Department of Mechanical and Mechatronic Engineering, Stellenbosch University, Stellenbosch, South Africa, 2015.

[50] BrightSource: First heliostat placed on a pylon [Online] (Accessed 2011-07-06). 2011.
Available at: `www.ivanpahsolar.com`

[51] Schell, S.: Design and evaluation of esolar's heliostat fields. *Solar Energy*, vol. 85, no. 4, pp. 614–619, 2011.

[52] National Renewable Energy Laboratory: Concentrating solar power projects database [Online] (Accessed 2015-03-20). 2015.
Available at: `www.nrel.gov/csp/solarpaces/power-tower.cfm`

[53] Blackmon, J.B.: Parametric determination of heliostat minimum cost per unit area. *Solar Energy*, vol. 97, pp. 342–349, 2013.

[54] Sargent & Lundy: Assessment of parabolic trough and power tower solar technology cost and performance forecasts. Tech. Rep., NREL/SR-550-34440, National Renewable Energy Laboratory, Golden, CO, 2003.

[55] Bender, W., Chalifoux, B. and Schneider, D.: Suspension heliostat material efficiency. In: *Proceedings of the SolarPACES Conference*. Granada, Spain, 2011.

[56] Ho, C.K.: Software and codes for analysis of concentrating solar power technologies. Tech. Rep., SAND-2008-8053, Sandia National Laboratories, Albuquerque, NM, 2008.

[57] Bode, S.J. and Gauché, P.: Review of optical software for use in concentrating solar power systems. In: *Proceedings of the Southern African Solar Energy Conference*. Stellenbosch, South Africa, 2012.

[58] Yellowhair, J., Christian, J.M. and Ho, C.K.: Evaluation of solar optical modeling tools for modeling complex receiver geometries. In: *Proceedings of the ASME International Energy Sustainability Conference collocated with the ASME International Fuel Cell Science, Engineering and Technology Conference*. Boston, MA, 2014.

[59] Li, L., Coventry, J., Bader, R., Pye, J. and Lipiński, W.: Optics of solar central receiver systems: a review. *Optics Express*, vol. 24, no. 14, pp. A985–A1007, 2016.

[60] Lipps, F.W.: Four different views of the heliostat flux density integral. *Solar Energy*, vol. 18, pp. 555–560, 1976.

[61] Lipps, F.W.: An analytical integration of the solar flux density due to rectangular mirrors. *Journal of Solar Energy*, vol. 74, 1974.

[62] Walzel, M.D., Lipps, F.W. and Vant-Hull, L.L.: A solar flux density calculation for a solar tower concentrator using a two-dimensional hermite function expansion. *Solar Energy*, vol. 19, no. 3, pp. 239–253, 1977.

[63] Lipps, F.W.: A numerical approach to the flux density integral for reflected sunlight. *Solar Energy*, vol. 24, no. 5, pp. 461–469, 1980.

[64] Lipps, F.W. and Walzel, M.D.: An analytic evaluation of the flux density due to sunlight reflected from a flat mirror having a polygonal boundary. *Solar Energy*, vol. 21, pp. 113–121, 1978.

[65] Lipps, F.W. and Vant-Hull, L.L.: A cellwise method for the optimization of large central receiver systems. *Solar Energy*, vol. 20, pp. 505–516, 1978.

[66] Gilman, P., Blair, N., Mehos, M., Christensen, C., Janzou, S. and Cameron, C.: Solar Advisor Model: user guide for version 2.0. Tech. Rep., NREL/TP-670-43704, National Renewable Energy Laboratory, Golden, CO, 2008.

[67] Biggs, F. and Vittitoe, C.N.: The Helios model for optical behaviour of reflecting solar concentrators. Tech. Rep., SAND-76-0347, Sandia National Laboratories, Albuquerque, NM, 1979.

[68] Schwarzbözl, P., Schmitz, M. and Pitz-Paal, R.: Visual HFLCAL - A software tool for layout and optimisation of heliostat fields. In: *Proceedings of the SolarPACES Conference*. Berlin, Germany, 2009.

[69] Biggs, F. and Vittitoe, C.N.: HELIOS: A computational model for solar concentrators. Tech. Rep., SAND-77-1185C, Sandia National Laboratories, Albuquerque, NM, 1977.

[70] Collado, F.J., Gómez, A. and Turégano, J.A.: An analytic function for the flux density due to sunlight reflected from a heliostat. *Solar Energy*, vol. 37, no. 3, pp. 215–234, 1986.

[71] Hennet, J.C. and Abatut, J.L.: An analytical method for reflected flux density calculations. *Solar Energy*, vol. 32, no. 3, pp. 357–363, 1984.

[72] Harris, J.A. and Duff, W.S.: Focal plane flux distributions produced by solar concentrating reflectors. *Solar Energy*, vol. 27, no. 5, pp. 403–411, 1981.

[73] Pettit, R.B., Vittitoe, C.N. and Biggs, F.: Simplified calculational procedure for determining the amount of intercepted sunlight in an imaging solar concentrator. *Journal of Solar Energy Engineering*, vol. 105, no. 1, pp. 101–107, 1983.

[74] Elsayed, M.M. and Fathalah, K.A.: Solar flux density distribution using a separation of variables/superposition technique. *Renewable Energy*, vol. 4, no. 1, pp. 77–87, 1994.

[75] King, D.: Beam quality and tracking-accuracy evaluation of second-generation and Barstow production heliostats. Tech. Rep., SAND-82-0181, Sandia National Laboratories, Albuquerque, NM, 1982.

[76] Besarati, S.M., Goswami, D.Y. and Stefanakos, E.K.: Optimal heliostat aiming strategy for uniform distribution of heat flux on the receiver of a solar power tower plant. *Energy Conversion and Management*, vol. 84, pp. 234–243, 2014.

[77] Salomé, A., Chhel, F., Flamant, G., Ferrière, A. and Thiery, F.: Control of the flux distribution on a solar tower receiver using an optimized aiming point strategy: Application to THEMIS solar tower. *Solar Energy*, vol. 94, pp. 352–366, 2013.

[78] Grobler, A.: *Aiming strategies for small central receiver*. M.Sc. Thesis, Department of Mechanical and Mechatronic Engineering, Stellenbosch University, Stellenbosch, South Africa, 2015.

[79] Huang, W., Li, H., Li, L., Hu, P. and Chen, Z.: Gauss - Legendre integration of an analytical function to calculate the optical efficiency of a heliostat. *Solar Energy*, vol. 92, pp. 7–14, 2013.

[80] Loomis, J., Weinstein, L., Boriskina, S.V., Huang, X., Chiloyan, V. and Chen, G.: Diverging polygon-based modeling (DPBM) of concentrated solar flux distributions. *Solar Energy*, vol. 122, pp. 24–35, 2015.

[81] Guo, M. and Wang, Z.: On the analysis of an elliptical Gaussian flux image and its equivalent circular Gaussian flux images. *Solar Energy*, vol. 85, pp. 1144–1163, 2011.

[82] Leonardi, E. and D'Aguanno, B.: CRS4-2: A numerical code for the calculation of the solar power collected in a central receiver system. *Energy*, vol. 36, no. 8, pp. 4828–4837, 2011.

[83] Georgiou, M.D., Bonanos, A.M. and Georgiadis, J.G.: Caustics as an alternate of ray tracing to evaluate heliostat mirrors. In: *Conference Papers in Energy*. Hindawi Publishing Corporation, 2013.

[84] Belhomme, B., Pitz-Paal, R., Schwarzbözl, P. and Ulmer, S.: A new fast ray tracing tool for high-precision simulation of heliostat fields. *Journal of Solar Energy Engineering*, vol. 131, no. 3, pp. 031002 1–8, 2009.

[85] Kajiya, J.T.: The rendering equation. In: *ACM Siggraph Computer Graphics*, vol. 20, pp. 143–150. ACM, Dallas, TX, 1986.

[86] Metropolis, N. and Ulam, S.: The Monte Carlo method. *Journal of the American Statistical Association*, vol. 44, no. 247, pp. 335–341, 1949.

[87] Hammersley, J.M. and Handscomb, D.C.: *Monte Carlo methods*. Fletcher & Son Ltd., Norwich, UK, 1964.

[88] De la Torre, J., Baud, G., Bézian, J.J., Blanco, S., Caliot, C., Cornet, J.F., Coustet, C., Dauchet, J., El Hafi, M., Eymet, V., Fournier, R., Gautrais, J., Gourmel, O., Joseph, D., Meilhac, N., Pajot, A., Paulin, M., Perez, P., Piaud, B., Roger, M., Rolland, J., Veynandt, F. and Weitz, S.: Monte Carlo advances and concentrated solar applications. *Solar Energy*, vol. 103, pp. 653–681, 2014.

[89] Glassner, A.S.: *Principles of digital image synthesis*. Morgan Kaufmann Publishers, Inc., San Francisco, CA, 1995.

[90] Suffern, K.: *Ray tracing from the ground up*. A K Peters Ltd., Wellesley, MA, 2007.

[91] Lafortune, E.: *Mathematical models and Monte Carlo algorithms for physically based rendering*. Ph.D. Thesis, Department of Computer Science, Faculty of Engineering, Katholieke Universiteit, Leuven, Belgium, 1996.

[92] Izygon, M., Armstrong, P., Nilsson, C. and Vu, N.: TieSOL - A GPU-based suite of software for central receiver solar power plants. In: *Proceedings of the SolarPACES Conference*. Granada, Spain, 2011.

[93] Hoedt, A.D.: *Efficient ray tracing of dynamic scenes on the GPU*. M.Sc. Thesis, Department of Computer Science, Aarhus University, Aarhus, Denmark, 2011.

[94] Roccia, J.P.: Hybrid CPU/GPU KD-Tree construction for versatile ray tracing. In: *Proceedings of the Eurographics Symposium on Rendering*. Cagliari, Italy, 2012.

[95] Wendelin, T., Dobos, A. and Lewandowski, A.: SolTrace: A ray-tracing code for complex solar optical systems. Tech. Rep., NREL TP-5500-59163, National Renewable Energy Laboratory, Golden, CO, 2013.

[96] Daly, J.C.: Solar concentrator flux distributions using backward ray tracing. *Applied Optics*, vol. 18, no. 15, pp. 2696–2699, 1979.

[97] Leary, P.L. and Hankins, J.D.: User's guide for MIRVAL: a computer code for comparing designs of heliostat-receiver optics for central receiver solar power plants. Tech. Rep., SAND-77-8280, Sandia National Laboratories, Livermore, CA, 1979.

[98] Blanco, M.J., Mutuberria, A., Garcia, P., Gastesi, R. and Martin, V.: Preliminary validation of Tonatiuh. In: *Proceedings of the SolarPACES Conference*. Berlin, Germany, 2009.

[99] De la Torre, J.: *Calculs de sensibilités par méthode de Monte-Carlo, pour la conception de procédés à énergie solaire concentrée*. Ph.D. Thesis, Institut National Polytechnique de Toulouse, Université De Toulouse, Toulouse, France, 2011.

[100] Caliot, C., Benoit, H., Guillot, E., Sans, J.-L., Ferriere, A., Flamant, G., Coustet, C. and Piaud, B.: Validation of a Monte Carlo integral formulation applied to solar facility simulations and use of sensitivities. *Journal of Solar Energy Engineering*, vol. 137, no. 2, pp. 021019 1–8, 2015.

[101] Roccia, J.P., Piaud, B., Coustet, C., Caliot, C., Guillot, E., Flamant, G. and Delatorre, J.: SOLFAST, a ray-tracing Monte-Carlo software for solar concentrating facilities. *Journal of Physics: Conference Series (Online)*, vol. 369, no. 1, p. 2029, 2012.

[102] Bode, S.J.: *Development of a ray-tracer for concentrating solar power systems*. Ph.D. Thesis, Department of Mechanical and Mechatronic Engineering, Stellenbosch University, Stellenbosch, South Africa, 2013.

[103] Landman, W.A. and Gauché, P.: Influence of canting mechanism and facet profile on heliostat field performance. *Energy Procedia*, vol. 49, pp. 126–135, 2014.

[104] Bajorski, P.: *Statistics for imaging, optics, and photonics*. John Wiley & Sons, Inc., Hoboken, NJ, 2012.

[105] Prosch, L. and Stevens, C.: Proposed commercial concentrated solar power (CSP) facility. Tech. Rep., SEIA Report 30085, WSP Environment & Energy South Africa, Johannesburg, GP, 2012.

[106] Michalsky, J.J.: The astronomical almanac's algorithm for approximate solar position (1950-2050). *Solar Energy*, vol. 40, pp. 227–235, 1988.

[107] Reda, I. and Andreas, A.: Solar position algorithm for solar radiation applications. *Solar Energy*, vol. 76, no. 5, pp. 577–589, 2004.

[108] Grena, R.: An algorithm for the computation of the solar position. *Solar Energy*, vol. 82, pp. 462–470, 2008.

[109] Augsburger, G.: *Thermo-economic optimisation of large solar tower power plants*. Ph.D. Thesis, À La Faculté Des Sciences Et Techniques De L'ingénieur, École Polytechnique Fédérale De Lausanne, Lausanne, Switzerland, 2013.

[110] MIDC: NREL Measurement and Instrumentation Data Center [Online] (Accessed 2016-09-14). 2016.
Available at: `www.nrel.gov/midc/`

[111] Wilbert, S.: *Determination of circumsolar radiation and its effect on concentrating solar power*. Ph.D. Thesis, Fakultät fur Maschinenwesen der Rheinisch-Westfälischen, Technischen Hochschule Aachen, Aachen, Germany, 2014.

[112] Liou, K.N.: *An introduction to atmospheric radiation*, vol. 84. 2nd edn. Academic Press, San Diego, CA, 2002.

[113] Iqbal, M.: *An introduction to solar radiation*. Academic Press, Don Mills, Ontario, 1983.

[114] Watt., A.D.: Circumsolar radiation. Tech. Rep., SAND-80-7009, Watt Engineering Ltd., Cedaredge, CO, 1980.

[115] Vittitoe, C.N. and Biggs, F.: User's guide to HELIOS: a computer program for modeling the optical behavior of reflecting solar concentrators. Tech. Rep., SAND-91-1180, Sandia National Laboratories, Albuquerque, NM, 1981.

[116] Radiation Commission: IAMAP, A preliminary cloudless standard atmosphere for radiation computation. Tech. Rep., WCP-112, WMO/TD, World Meteorological Organization, Geneva, 1986.

[117] Kuiper, G.P.: *The Photosphere, the sun, the solar system*. University if Chicargo Press, Chicargo, IL, 1953.

[118] Pierce, A.K. and Slaughter, C.D.: Solar limb darkening. *Solar Physics*, vol. 51, no. 1, pp. 24–41, 1977.

[119] Allen, C.W. and Cox, A.N.: *Allen's astrophysical quantities*. Athlone Press, London, UK, 2000.

[120] Rabl, A. and Bendt, P.: Effect of circumsolar radiation on performance of focusing collectors. *Journal of Solar Energy Engineering*, vol. 104, no. 3, pp. 237–250, 1982.

[121] Neumann, A., Von der Au, B. and Heller, P.: Measurement of circumsolar radiation at the Plataforma Solar de Almería (Spain) and at DLR (Germany). In: *Proceedings of the ASME International Solar Energy Conference*. Albuquerque, NM, 1998.

[122] Grether, D. and Hunt, A.: Description of the LBL reduced data base and standard profiles. Tech. Rep., Lawrence Berkeley Laboratories, Berkeley, CA, 1977.

[123] Winter, C.J., Sizmann, R.L. and Vant-Hull, L.L.: *Solar power plants: fundamentals, technology, systems, economics*. Springer-Verlag, Berlin, Germany, 1991.

[124] Buie, D., Monger, A.G. and Dey, C.J.: Sunshape distributions for terrestrial solar simulations. *Solar Energy*, vol. 74, no. 2, pp. 113–122, 2003.

[125] Schubnell, M., Keller, J. and Imhof, A.: Flux density distribution in the focal region of a solar concentrator system. *Journal of Solar Energy Engineering*, vol. 113, no. 2, pp. 112–116, 1991.

[126] Schubnell, M.: Influence of circumsolar radiation on aperture, operating temperature and efficiency of a solar cavity receiver. *Solar Energy Materials and Solar Cells*, vol. 27, no. 3, pp. 233–242, 1992.

[127] Schubnell, M.: Sunshape and its influence on the flux distribution in imaging solar concentrators. *Journal of Solar Energy Engineering*, vol. 114, no. 4, pp. 260–226, 1992.

[128] Steinfeld, A. and Schubnell, M.: Optimum aperture size and operating temperature of a solar cavity-receiver. *Solar Energy*, vol. 50, no. 1, pp. 19–25, 1993.

[129] Alcaniz, C., Martínez, N., Heras, C. and Salinas, I.: Study of the influence of specularity on the efficiency of solar reflectors. *Energy Procedia*, vol. 69, pp. 14–23, 2015.

[130] Pettit, R.B.: Characterization of the reflected beam profile of solar mirror materials. *Solar Energy*, vol. 19, no. 6, pp. 733–741, 1977.

[131] Gee, R., Brost, R., Zhu, G. and Jorgensen, G.: An improved method for characterizing reflector specularity for parabolic trough concentrators. In: *Proceedings of the SolarPACES Conference*. Perpignan, France, 2010.

[132] Pitman, C.L. and Vant-Hull, L.L.: Performance of optimized solar central receiver systems as a function of receiver thermal loss per unit area. *Solar energy*, vol. 37, no. 6, pp. 457–468, 1986.

[133] Hottel, H.C.: A simple model for estimating the transmittance of direct solar radiation through clear atmospheres. *Solar Energy*, vol. 18, no. 2, pp. 129–134, 1976.

[134] Sengupta, M. and Wagner, M.: Atmospheric attenuation in central receiver systems from dni measurements. In: *Proceedings of the SolarPACES Conference*. Marrakech, Morocco, 2012.

[135] Coddington, H.: *An elementary treatise on optics*. 2nd edn. Deighton and Sons, Cambridge, UK, 1925.

[136] Parrott, L.E.: Theoretical upper limit to the conversion efficiency of solar energy. *Solar Energy*, vol. 21, pp. 227–229, 1978.

[137] Buck, R. and Teufel, E.: Comparison and optimization of heliostat canting methods. *Journal of Solar Energy*, vol. 131, no. 1, pp. 11001 1–8, 2009.

[138] Battleson, K.W.: Solar power tower design guide: solar thermal central receiver power systems, a source of electricity and/or process heat. Tech. Rep., SAND-81-8005, Sandia National Laboratories, Albuquerque, NM, 1981.

[139] Brueggemann, H.P.: *Conic mirrors*. Focal Press, London, UK, 1968.

[140] Noone, C.J.: *Optimization of central receiver concentrated solar thermal: site selection, heliostat layout & canting*. M.Sc. Thesis, Department of Mechanical Engineering, Massachusetts Institute of Technology, Boston, MA, 2011.

[141] Shirley, P. and Morley, R.K.: *Realistic ray tracing*. AK Peters, Ltd., Wellesley, MA, 2003.

[142] Wendelin, T.: SolTRACE: a new optical modeling tool for concentrating solar optics. In: *Proceedings of the ASME International Solar Energy Conference*. Kohala Coast, HI, 2003.

[143] Malan, K.J.: *A heliostat field control system*. M.Sc. Thesis, Department of Mechanical and Mechatronic Engineering, Stellenbosch University, Stellenbosch, South Africa, 2014.

[144] Landman, W.A. and Gauché, P.: Method for determining a continuous aberration free heliostat surface. In: *Proceedings of the Southern African Solar Energy Conference*. Stellenbosch, South Africa, 2012.

[145] Jones, S.A., Edgar, R.M. and Houser, R.M.: Recent results on the optical performance of solar two heliostats. Tech. Rep., SAND-94-2776C, Sandia National Laboratories, Albuquerque, NM, 1994.

[146] Chen, Y.T., Lim, B.H. and Lim, C.S.: Off-axis aberration correction surface in solar energy application. *Solar Energy*, vol. 80, no. 3, pp. 268–271, 2006.

[147] Frankot, R.T. and Chellappa, R.: A method for enforcing integrability in shape form shading algorithms. *IEEE Transactions on Pattern Analysis and Machine Intelligence*, vol. 10, no. 4, pp. 439–451, 1988.

[148] Jones, S.A.: A comparison of on-axis and off-axis heliostat alignment strategies. Tech. Rep., SAND-96-0566C, Sandia National Laboratories, Albuquerque, NM, 1996.

[149] Landman, W.A., Grobler, A., Gauché, P. and Dinter, F.: Incidence angle effects on circular Gaussian flux density distributions for heliostat imaging. *Solar Energy*, vol. 126, pp. 156–167, 2016.

[150] Rabl, A.: *Active solar collectors and their applications*. Oxford University Press, Oxford, UK, 1985.

[151] GeoModel Solar: Full time series sample data [Online] (Accessed 2015-06-04). 2015.
Available at: `http://geomodelsolar.eu/data/full-time-series`

[152] Mancini, T.R.: Catalog of solar heliostats. Tech. Rep., Task No. III - 1/00, Task III: Solar Technology and Applications, SolarPaces, Cologne, Germany, 2000.

[153] Yellowhair, J. and Andraka, C.E.: Evaluation of advanced heliostat reflective facets on cost and performance. *Energy Procedia*, vol. 49, pp. 265–274, 2014.

[154] Huss, S., Traeger, Y.D., Shvets, Z., Rojansky, M., Stoyanoff, S. and Garber, J.: Evaluating effects of wind loads in heliostat design. In: *Proceedings of the SolarPACES Conference*. Granada, Spain, 2011.

[155] Siala, F.M.F. and Elayeb, M.E.: Mathematical formulation of a graphical method for a no-blocking heliostat field layout. *Renewable energy*, vol. 23, no. 1, pp. 77–92, 2001.

[156] SolarPACES: Specifications for determination of the heliostat qualification parameters. Tech. Rep., Draft document for SolarPACES Task III, Cologne, Germany, 2014.

[157] Shealy, D.L. and Hoffnagle, J.a.: Laser beam shaping profiles and propagation. *Applied Optics*, vol. 45, no. 21, pp. 5118–5131, 2006.

[158] Nemes, G.: New asymptotic expansion for the Gamma function. *Archiv der Mathematik*, vol. 95, no. 2, pp. 161–169, 2010.

[159] Sassi, G.: Some notes on shadow and blockage effect. *Solar Energy*, vol. 3, no. 31, pp. 331–333, 1983.

[160] Yellowhair, J.: A cost/performance evaluation of advanced low-cost heliostat reflective facets. In: *Proceedings of the ASME 2013 7th International Conference on Energy Sustainability*. Minneapolis, MN, 2013.

[161] Landman, W.A., Gauché, P., Malan, K., Larmuth, J.N., Bode, S.J., Mouzouris, M., Dreijer, J. and Kotze, J.P.: On the development of a local heliostat technology for the concentrating solar power industry. In: *Proceedings of the PowerGen-Africa Conference*. Cape Town, South Africa, 2015.

[162] Sansom, C., Comley, P., Bhattacharyya, D. and Macerol, N.: A comparison of polymer film and glass collectors for concentrating solar power. *Energy Procedia*, vol. 49, pp. 209–219, 2014.

[163] Ho, C.K., Sment, J., Yuan, J. and A., S.C.: Characterization of metallized polymer films for long-distance heliostat applications. In: *Proceedings of the SolarPACES Conference*. Marrakech, Morocco, 2012.

[164] Naude, H.: Personal communication between Naude, H. and Landman, W.A. 2012.

[165] Chan, S.L.: Basic structural design considerations and properties of glass and aluminum structures. In: *Advanced Facade Engineering and Technology*. Hong Kong, China, 2006.

[166] Björkman, N.: *Heliostat design*. Master Thesis, Department of Industrial Engineering and Management, KTH Royal Institute of Technology, Stockholm, Sweden, 2014.

[167] So, A.K.W., Lai, B.S.L. and Chan, S.L.: Economical design of glass and aluminum panels by the large deflection theory. In: *HKIE Transactions*. Hong Kong Institution of Engineers, Hong Kong, China, 2013.

[168] Strachan, J.W. and Houser, R.M.: Testing and evaluation of large-area heliostats for solar thermal applications. Tech. Rep., SAND-92-1381-UC-235, Sandia National Laboratories, Albuquerque, NM, 1993.

[169] Nelson, J.E., Lubliner, J. and Mast, T.S.: Telescope mirror supports: plate deflections on point supports. In: *SPIE Advanced Technology Optical Telescopes*, vol. 332, pp. 212–228. Society of Photo-Optical Instrumentation Engineers, 1982.

[170] Lopez, C.W. and Stone, K.W.: Performance of the Southern California Edison Company stirling dish. Tech. Rep., SAND-93-7098, Sandia National Laboratories, Albuquerque, NM, 1993.

[171] Pérez, L. and Maria, J.: Heliostat facet, European Patent, EP-2-244-0-34-A2, 17 March 2010.

[172] ToughTrough GmbH: Innovative solar mirror technology [Online] (Accessed 2016-09-18). 2016.
Available at: `www.toughtrough.com`

[173] Rioglass Solar: Heliostat mirrors [Online] (Accessed 2016-09-18). 2016.
Available at: `www.rioglass.com/?page{_}id=2249`

[174] Swanson, S.R.: *Introduction to design and analysis with advanced composite materials*. Prentice Hall, Upper Saddle River, NJ, 1997.

[175] Droomer, L.: Personal communication between Droomer, L. and Landman, W.A. 2012.

[176] Braasch, J.: Personal communication between Braasch, J. and Landman, W.A. 2013.

[177] Peterka, J. and Derickson, R.: Wind load design methods for ground based heliostats and parabolic dish collectors. Tech. Rep., SAND-92âĂŞ7009. Sandia National Laboratories, Albuquerque, NM, 1992.

[178] Pfahl, A., Buselmeier, M. and Zaschke, M.: Wind loads on heliostats and photovoltaic trackers of various aspect ratios. *Solar Energy*, vol. 85, pp. 2185–2201, 2011.

[179] Pfahl, A., Buselmeier, M. and Zaschke, M.: Determination of wind loads on heliostats. In: *Proceedings of the SolarPACES Conference*. Marrakech, Morocco, 2012.

[180] Malan, K., Dreijer, J. and Gauché, P.: Heliostat control system for lowest cost power tower. In: *Proceedings of the SolarPACES Conference*. Cape Town, South Africa, 2015.

[181] Pilavachi, P.A.: Mini- and micro-gas turbines for combined heat and power. *Applied Thermal Engineering*, vol. 22, no. 18, pp. 2003–2014, 2002.

[182] Turbec: T100 microturbine system: technical description. Tech. Rep., D 14127-03 Version 3, Corporeno, Italy, 2009.

[183] Kribus, A., Doron, P., Rubin, R., Reuven, R., Taragan, E., Duchan, S. and Karni, J.: Performance of the directly-irradiated annular pressurized receiver (DIAPR) operating at 20 bar and 1,200 C. *Journal of Solar Energy Engineering*, vol. 123, no. 1, pp. 10–17, 2001.

[184] Welford, W.T. and Winston, R.: *The optics of nonimaging concentrators*. Academic Press, New York, NY, 1978.

[185] Pitz-Paal, R., Botero, N.B. and Steinfeld, A.: Heliostat field layout optimization for high-temperature solar thermochemical processing. *Solar Energy*, vol. 85, no. 2, pp. 334–343, 2011.

[186] standard, I.: Lasers and laser-related equipment - Test methods for laser widths, divergence angle and beam propagation factor. *ISO 111 46-1*, 2003.

[187] Chen, Y.T., Lim, B.H. and Lim, C.S.: General sun tracking formula for heliostats with arbitrarily oriented axes. *Journal of Solar Energy Engineering*, vol. 128, no. 2, pp. 245–250, 2006.

[188] Nocedal, J. and Wright, S.J.: *Numerical optimization*. Springer-Verlag New York, Inc., New York, NY, 2006.

[189] Hu, Y.: 1-D random number generation with any analytical expression probability density function [Online] (accesssed 2014-09-22). 2014.
Available at: `www.mathworks.com/matlabcentral/fileexchange/40598`